DISSERTATION

submitted to the
Combined Faculties for the Natural Sciences and for Mathematics
of the Ruperto-Carola University of Heidelberg, Germany
for the degree of

Doctor of Natural Sciences

Put forward by

Dipl.-Phys. Aleksandra Adametz

born in Neustadt, Poland

Oral examination: July 6th, 2011

Measurement of $\boldsymbol{\tau}$ decays into a charged hadron accompanied by neutral $\boldsymbol{\pi}$-mesons and determination of the CKM matrix element $|\boldsymbol{V_{us}}|$

Referees: Prof. Dr. Ulrich Uwer

Prof. Dr. Hans-Christian Schultz-Coulon

Abstract

This thesis presents the branching fraction measurement of the $\tau^- \to K^-(n\pi^0)\nu_\tau$ $(n = 0, 1, 2, 3)$ and $\tau^- \to \pi^-(n\pi^0)\nu_\tau$ $(n = 3, 4)$ decays. The measurement is based on a data sample of 435 million τ pairs produced in e^+e^- collisions and collected with the *BABAR* detector in 1999–2008. The analysis is validated using precisely known τ decays as control modes. The measured branching fractions are $\mathcal{B}(\tau^- \to K^-\nu_\tau) = (7.100 \pm 0.033 \pm 0.156) \times 10^{-3}$, $\mathcal{B}(\tau^- \to K^-\pi^0\nu_\tau) = (5.000 \pm 0.020 \pm 0.139) \times 10^{-3}$, $\mathcal{B}(\tau^- \to K^-(2\pi^0)\nu_\tau) = (5.654 \pm 0.144 \pm 0.323) \times 10^{-4}$, $\mathcal{B}(\tau^- \to K^-(3\pi^0)\nu_\tau) = (1.642 \pm 0.279 \pm 0.375) \times 10^{-4}$, $\mathcal{B}(\tau^- \to \pi^-(3\pi^0)\nu_\tau) = (1.216 \pm 0.010 \pm 0.047) \times 10^{-2}$, $\mathcal{B}(\tau^- \to \pi^-(4\pi^0)\nu_\tau) = (1.041 \pm 0.067 \pm 0.090) \times 10^{-3}$, where the first uncertainty is statistical and the second systematic. The branching fraction $\mathcal{B}(\tau^- \to \pi^-(4\pi^0)\nu_\tau)$ is measured for the first time. The precision of the results is comparable or significantly improved with respect to previous measurements. The branching fraction $\mathcal{B}(\tau^- \to K^-\nu_\tau)$ is combined with a lattice QCD calculation of the kaon decay constant to obtain the Cabibbo-Kobayashi-Maskawa matrix element $|V_{us}| = 0.2224 \pm 0.0025(\text{exp}) \pm 0.0029(\text{theo})$. The branching fractions of the τ decays into a kaon are combined with the current world averages. The resulting averages are used in the determination of the total τ branching fraction, $\mathcal{B}_\text{s}$, into strangeness $|S| = 1$ final states. $\mathcal{B}_\text{s}$ is used in conjunction with $|V_{ud}|$ and a small $SU(3)$-symmetry breaking correction to compute $|V_{us}| = 0.2176 \pm 0.0025(\text{exp}) \pm 0.0010(\text{theo})$.

Kurzfassung

In dieser Arbeit wird die Messung der Verzweigungsverhältnisse der $\tau^- \to K^-(n\pi^0)\nu_\tau$ $(n = 0, 1, 2, 3)$ und $\tau^- \to \pi^-(n\pi^0)\nu_\tau$ $(n = 3, 4)$ Zerfälle vorgestellt. Die Messung basiert auf einem Datensatz von 435 Millionen τ-Paaren, die in e^+e^- Kollisionen produziert und mit dem *BABAR*-Detektor in den Jahren 1999–2008 aufgezeichnet wurden. Die Analyse wird mit gut bekannten τ-Zerfällen validiert, die als Kontrollkanäle verwendet werden. Die gemessenen Verzweigungsverhältnisse sind $\mathcal{B}(\tau^- \to K^-\nu_\tau) = (7.100 \pm 0.033 \pm 0.156) \times 10^{-3}$, $\mathcal{B}(\tau^- \to K^-\pi^0\nu_\tau) = (5.000 \pm 0.020 \pm 0.139) \times 10^{-3}$, $\mathcal{B}(\tau^- \to K^-(2\pi^0)\nu_\tau) = (5.654 \pm 0.144 \pm 0.323) \times 10^{-4}$, $\mathcal{B}(\tau^- \to K^-(3\pi^0)\nu_\tau) = (1.642 \pm 0.279 \pm 0.375) \times 10^{-4}$, $\mathcal{B}(\tau^- \to \pi^-(3\pi^0)\nu_\tau) = (1.216 \pm 0.010 \pm 0.047) \times 10^{-2}$, $\mathcal{B}(\tau^- \to \pi^-(4\pi^0)\nu_\tau) = (1.041 \pm 0.067 \pm 0.090) \times 10^{-3}$, wobei die erste Unsicherheit statistisch und die zweite systematisch ist. Das $\tau^- \to \pi^-(4\pi^0)\nu_\tau$ Verzweigungsverhältnis wird erstmalig gemessen. Die Genauigkeit der Ergebnisse ist hinsichtlich früherer Messungen vergleichbar oder signifikant verbessert. Das Verzweigungsverhältnis $\mathcal{B}(\tau^- \to K^-\nu_\tau)$ wird in Verbindung mit einer QCD-Rechnung der Kaon-Zerfallskonstante zur Bestimmung des Cabibbo-Kobayashi-Maskawa Matrixelements $|V_{us}| = 0.2224 \pm 0.0025(\text{exp}) \pm 0.0029(\text{theo})$ verwendet. Die Verzweigungsverhältnisse der τ-Zerfälle in ein Kaon werden mit den Weltmittelwerten kombiniert. Die resultierenden Mittelwerte werden in der Bestimmung des Gesamtverzweigungsverhältnisses $\mathcal{B}_\text{s}$ für Endzustände mit Strangeness $|S| = 1$ verwendet. Aus $\mathcal{B}_\text{s}$ zusammen mit $|V_{ud}|$ und einer kleinen, die $SU(3)$-Symmetrie brechenden Korrektur wird $|V_{us}| = 0.2176 \pm 0.0025(\text{exp}) \pm 0.0010(\text{theo})$ berechnet.

Contents

1. Introduction 1

2. Theory of hadronic τ decays and experimental status 3

2.1. The Standard Model of particle physics 3
  2.1.1. The strong interaction 4
  2.1.2. The electroweak interaction 4
2.2. Leptonic τ decays 7
2.3. Hadronic τ decays 10
  2.3.1. Spectral functions of hadronic τ decays 10
  2.3.2. Spectral moments 11
  2.3.3. Determination of R_{had} from the leptonic τ decays 13
  2.3.4. Exclusive branching fractions of hadronic τ decays 14
  2.3.5. Theoretical prediction of the $\tau^- \to K^-\nu_\tau$ branching fraction . . 17
2.4. The CKM matrix element V_{us} 17
  2.4.1. $|V_{us}|$ from the unitarity condition of the CKM matrix 17
  2.4.2. $|V_{us}|$ from hyperon decays 18
  2.4.3. $|V_{us}|$ from semileptonic kaon decays 19
  2.4.4. $|V_{us}|$ from leptonic kaon decays 19
  2.4.5. $|V_{us}|$ from the $\tau^- \to K^-\nu_\tau$ and $\tau^- \to \pi^-\nu_\tau$ decays 20
  2.4.6. $|V_{us}|$ from the $\tau^- \to K^-\nu_\tau$ decay 20
  2.4.7. $|V_{us}|$ from inclusive $\tau \to s$ decays 21

3. The *BABAR* experiment 23

3.1. The PEP-II collider 23
3.2. The *BABAR* detector 25
  3.2.1. Silicon vertex tracker 25
  3.2.2. Drift chamber 27
  3.2.3. Detector of internally reflected Cherenkov light 28
  3.2.4. The electromagnetic calorimeter 30
  3.2.5. Magnet coil and instrumented flux return 31
3.3. The data sample 32
  3.3.1. Data sample 32
  3.3.2. Simulated event sample 32

4. Analysis overview 35

4.1. Goal of the measurement 35
4.2. Additional control decay modes 35

4.3. Event selection 36
4.4. Corrections of the simulation 36
  4.4.1. Charged particle identification corrections 37
  4.4.2. Correction of hadronic split-offs 37
  4.4.3. π^0 reconstruction efficiency correction 37
4.5. Determination of the branching fractions 38
4.6. Determination of $|V_{us}|$ 38

5. Particle Selection **39**
5.1. Charged particle reconstruction 39
  5.1.1. Reconstruction of tracks 39
  5.1.2. Selection of tracks 39
5.2. Charged particle identification 40
  5.2.1. Variables used for particle identification 40
  5.2.2. Particle identification algorithms at *BABAR* 43
  5.2.3. Identification of electrons, muons, pions, and kaons. 44
  5.2.4. PID selector sequence 48
  5.2.5. Particle identification efficiency correction 50
5.3. Neutral particles 52
  5.3.1. Reconstruction of photons 52
  5.3.2. Reconstruction of neutral pions. 53

6. Event selection **55**
6.1. Characteristics of $e^+e^- \to \tau^+\tau^-$ events 55
6.2. Selection of $e^+e^- \to \tau^+\tau^-$ events 57
  6.2.1. Lepton tag 58
  6.2.2. Event topology 60
  6.2.3. Charge conservation 63
  6.2.4. Missing mass 63
6.3. Selection of $\tau^- \to \mathbf{K}^-/\pi^-(\mathbf{n}\pi^\mathbf{0})\nu_\tau$ decays 66
  6.3.1. Separation of the selected $e^+e^- \to \tau^+\tau^-$ events in signal mode samples 66
  6.3.2. Cross feed rejection 67
  6.3.3. Background rejection 70
  6.3.4. Distributions of selected events 77

7. Charged pion and kaon identification **87**
7.1. Motivation 87
7.2. Method 87
7.3. Selection of the pion and kaon PID control samples 88
  7.3.1. Selection of $\tau^- \to t^-t^+t^-\nu_\tau$ decays 88
  7.3.2. Determination of the control track 90
  7.3.3. Selected $\tau^- \to \pi^-\pi^+\pi^-\nu_\tau$ and $\tau^- \to \pi^-K^+K^-\nu_\tau$ samples 91
7.4. Determination of the pion and kaon PID correction 92

8. Split-off correction 95
8.1. Introduction 95
8.2. Determination of the split-off correction 97

9. π^0 reconstruction efficiency correction 100
9.1. Motivation 100
9.2. Correction method 100
9.3. Determination of the π^0 efficiency correction 102
9.3.1. $\tau^- \to t^-\nu_\tau$ and $\tau^- \to t^-\pi^0\nu_\tau$ event samples 102
9.4. Determination of the correction values 104
9.5. Application of the π^0 correction 106
9.6. Uncertainty of the π^0 correction 106
9.6.1. Determination of systematic uncertainties 106
9.6.2. Sources of systematic uncertainties 107
9.6.3. Summary of the systematic uncertainties of the π^0 correction . . 110
9.6.4. Tests of possible remaining dependencies of the π^0 correction . . 110
9.6.5. Consistency check: Branching fractions determined in the $\tau^- \to t^-\nu_\tau$, $\tau^- \to t^-\pi^0\nu_\tau$, and $\tau^- \to t^-(2\pi^0)\nu_\tau$ samples 112

10. Determination of the branching fractions 114
10.1. Number of selected events 114
10.2. Calculation of the branching fractions 114
10.2.1. Definition of signal events for the branching fraction calculation 116
10.2.2. Branching fraction determination for control decays 117
10.2.3. Branching fraction determination for the signal decays 118
10.2.4. Statistical uncertainty of the signal branching fractions 119
10.3. Measured branching fractions 120
10.3.1. Control decays 121
10.3.2. Signal decays 121
10.4. Systematic uncertainties 121
10.4.1. Determination method of systematic uncertainties 122
10.4.2. Statistical uncertainty of the simulated event sample 123
10.4.3. Uncertainty of the background decays branching fractions 127
10.4.4. Particle identification uncertainty 128
10.4.5. Uncertainty of the number of τ pairs 130
10.4.6. Uncertainty of the track efficiency 132
10.4.7. Uncertainty of the split-off correction 133
10.4.8. Uncertainty of the π^0 reconstruction efficiency 134
10.4.9. Uncertainty due to $\tau^- \to \pi^-(5\pi^0)\nu_\tau$ and $\tau^- \to K^-(4\pi^0)\nu_\tau$ background decays. 135
10.4.10. Summary of systematic uncertainties 138
10.5. Stability checks of the results 142
10.5.1. Stability checks for the control modes 144
10.5.2. Stability checks for the signal modes 146

11. Summary, discussion of the results and determination of $|V_{us}|$ 153
11.1. Summary of the branching fraction measurements 153
11.2. Comparison of the obtained branching fractions with earlier published results 154
11.2.1. $\tau^- \to K^-\nu_\tau$ 156
11.2.2. $\tau^- \to K^-\pi^0\nu_\tau$ 157
11.2.3. $\tau^- \to K^-(2\pi^0)\nu_\tau$ 157
11.2.4. $\tau^- \to K^-(3\pi^0)\nu_\tau$ 157
11.2.5. $\tau^- \to \pi^-(3\pi^0)\nu_\tau$ 158
11.2.6. $\tau^- \to \pi^-(4\pi^0)\nu_\tau$ 158
11.2.7. Summary 158
11.3. Determination of $|V_{us}|$ 159
11.3.1. $|V_{us}|$ from the $\tau^- \to K^-\nu_\tau$ decay 160
11.3.2. $|V_{us}|$ from the inclusive sum of strange τ decays 160
11.4. Conclusion and outlook 161

A. Missing mass in τ decays 163

B. Pion and kaon identification correction weights 165

C. Effect of background in the branching fraction calculation 170

List of Figures 171

List of Tables 173

Bibliography 175

Acknowledgment 180

1. Introduction

The τ lepton is the heaviest known lepton in the Standard Model [1, 2, 3] of particle physics with a mass of $1.78\,\mathrm{GeV}/c^2$ [4]. It is the only lepton that can decay into hadrons. Hadronic τ decays can be used for a variety of Standard Model tests [5]. The invariant mass spectra of the hadronic final states offer the possibility for investigations of QCD dynamics. Predictions of the pion and kaon decay constants from lattice QCD can be tested. Furthermore, the strong coupling constant α_S can be measured at the scale of the τ mass. This analysis is focused on the determination of the coupling strength of the W^- exchange boson[1] to a $\overline{u}s$ quark current, a fundamental parameter of the Standard Model. It is described by the element V_{us} of the Cabibbo-Kobayashi-Maskawa (CKM) quark-mixing matrix [6].

Figure 1.1 shows the Feynman diagram of a hadronic τ decay into a hadronic final state with $S = 1$, where S is the strangeness quantum number. Strange τ decays are suppressed by the factor $|V_{us}|^2/|V_{ud}|^2 \approx 5\%$ [4], where V_{ud} describes the coupling strength of the W^- to a $\overline{u}d$ quark current, with respect to the hadronic τ decays with $S = 0$.

Experimentally, $|V_{us}|$ can be determined from the branching fractions of τ decays into an odd number of kaons. It can be either obtained from exclusive τ decays using predictions for the hadron decay constants [7], or from the inclusive $\tau^- \to X_\mathrm{s}^-\nu_\tau$ branching fraction [8], where X_s^- is a final state with $S = 1$, independently from the hadron decay constants. The inclusive branching fraction is determined from the sum of all measured exclusive strange τ branching fractions.

The vast majority of available hadronic τ decay measurements was performed by the ALEPH, DELPHI, OPAL, and CLEO experiments [4]. The results for strange τ decays were limited by the statistical precision [5]. In recent years, several new measurements of τ decays have been performed by the *BABAR* and Belle experiments which recorded very large τ-pair data sample in e^+e^- collisions at center-of-mass-energies of $10.58\,\mathrm{GeV}$.

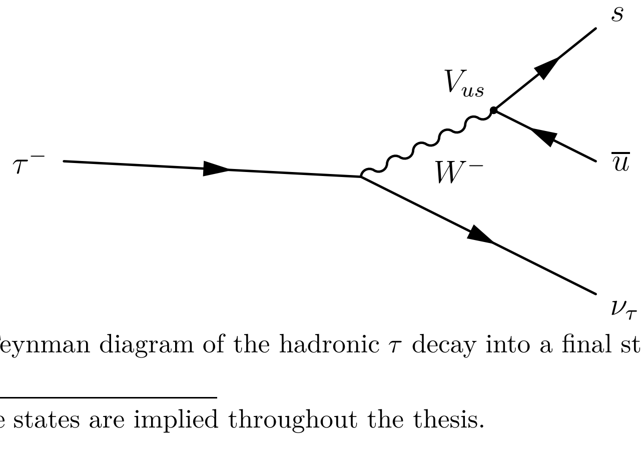

Figure 1.1.: Feynman diagram of the hadronic τ decay into a final state with $|S| = 1$.

---

[1] Charge-conjugate states are implied throughout the thesis.

The sum of the current world average branching fractions of strange τ decays results in a $|V_{us}|$ value which deviates by more than 3σ from the prediction derived from the unitarity conditions of the CKM matrix. It also deviates from the $|V_{us}|$ measurements in leptonic and semileptonic kaon decays which are experimentally and theoretically complementary [9]. With these measurements a relative $|V_{us}|$ uncertainty of $\approx 0.6\%$, limited by the theoretical uncertainty, is achieved. The $|V_{us}|$ determination from inclusive strange τ decays has a total relative uncertainty of $\approx 1.4\%$ and is limited by the experimental uncertainty of the individual branching fraction measurements. A measurement of strange τ decays with an improved precision is therefore an essential step to understand the observed deviation. This thesis contributes to this effort.

The τ dataset of 435 million τ-pairs recorded by the *BABAR* experiment is used to measure simultaneously the branching fractions of the decays

$$\begin{aligned}
&\tau^- \to K^-\nu_\tau, \\
&\tau^- \to K^-\pi^0\nu_\tau, \\
&\tau^- \to K^-(2\pi^0)\nu_\tau, \\
&\tau^- \to K^-(3\pi^0)\nu_\tau, \\
&\tau^- \to \pi^-(3\pi^0)\nu_\tau, \\
&\tau^- \to \pi^-(4\pi^0)\nu_\tau.
\end{aligned} \tag{1.1}$$

The first four branching fractions contribute to the inclusive strange τ decay branching fraction. The $\tau^- \to \pi^-(3\pi^0)\nu_\tau$ has so far only been measured by the ALEPH collaboration, and the $\tau^- \to \pi^-(4\pi^0)\nu_\tau$ is measured for the first time in this work.

In this thesis, τ decays are selected from the recorded *BABAR* e^+e^- dataset. Several criteria are applied to reduce background events. From the numbers of selected signal events the branching fractions are determined taking into account that signal decays can be misidentified as other signal modes, and, thus, can contribute to the background. Simulated events are used to develop the selection criteria and to obtain signal and background efficiencies. Various corrections to the simulation are derived using control samples to improve the description of the data. Preliminary results for the six branching fractions were already presented in the doctoral thesis of Stefan Schenk [10] which has been used as a starting point for this analysis. In this thesis a similar event selection strategy is used, and also the method to simultaneously determine the branching fractions and their uncertainties (Chapter 10) is adopted. However, the analysis is significantly expanded. Besides modifications to the event selection criteria, the well known $\tau^- \to \pi^-\nu_\tau$ and $\tau^- \to \mu^-\overline{\nu}_\mu\nu_\tau$ modes are selected as additional control modes used to cross check the event selection. Furthermore, different approaches to derive corrections of simulated events related to the π^0 reconstruction efficiency as well as to hadronic shower fluctuations are used. Moreover, the identification of charged particles is revised, and a correction of the simulated kaon and pion identification efficiency is developed using control samples with τ decays into three charged particles.

2. Theory of hadronic τ decays and experimental status

In this chapter a brief overview of the Standard Model of particle physics is given, followed by an introduction to the theoretical background of the analysis presented in this thesis and the experimental status of hadronic τ decays. Furthermore, various methods to determine the magnitude of the Cabibbo-Kobayashi-Maskawa matrix element V_{us} are presented with particular focus on the determination of $|V_{us}|$ from strange hadronic τ decays.

2.1. The Standard Model of particle physics

The Standard Model of particle physics [1, 2, 3] is a gauge theory which describes the fundamental particles and their interactions. Three of the four known fundamental forces are included in the standard model: the strong, the electromagnetic, and the weak interaction (see Table 2.1). The fourth known interaction, gravity, could not yet be incorporated.

The interactions are mediated by gauge bosons with spin 1. These exchange particles are the massless gluons for the strong interaction, the massless photon for the electromagnetic interaction, and the massive $W^{\pm}$ and Z^0 bosons for the weak interaction.

The elementary particles which are the building blocks of matter are the fermions with spin-1/2. For each fermion also an anti-fermion exists. Fermions are divided in two groups: leptons (three charged leptons and three neutral leptons, the neutrinos) and quarks. The quarks and leptons are ordered in three families. Table 2.2 lists the fermions with their masses. Neutrinos are massless in the original version of the

Table 2.1.: Fundamental forces in the Standard Model of particle physics. The strong, the electromagnetic, and the weak interactions are mediated by the gluons, the photon, and the massive $W^{\pm}$ and Z^0 bosons, respectively.

Interaction	Exchange boson	Boson mass
Strong	Gluon ($g_1 ... g_8$)	0
Electromagnetic	Photon	0
Weak	$W^{\pm}$, Z^0	80 GeV/c^2, 91 GeV/c^2

Table 2.2.: Fundamental particles in the Standard Model of particle physics. The masses of the particles given in brackets are taken from [4].

Family	Quarks		Leptons	
	up-type	down-type	charged	neutral
1	u (2 MeV/c^2)	d (5 MeV/c^2)	e (511 keV/c^2)	ν_e (< 2 eV/c^2)
2	c (1.25 GeV/c^2)	s (95 MeV/c^2)	μ (106 MeV/c^2)	ν_μ (< 0.19 MeV/c^2)
3	t (174 GeV/c^2)	b (4.2 GeV/c^2)	τ (1.78 GeV/c^2)	ν_τ (<18.2 MeV/c^2)

Standard Model. However, as summarized in [11], various experiments have measured neutrino oscillations indicating that neutrinos have mass which requires an extension of the Standard Model.

The Standard Model contains one additional particle, the Higgs boson, which is a spin-0 particle, which generates the mass of all other particles through its coupling to the boson and fermion fields. The Higgs is the only particle whose existence has not yet been experimentally confirmed.

2.1.1. The strong interaction

The quarks carry color charge, which is the charge of the strong interaction. Three values of color charge exist which are usually denoted as *red*, *green*, and *blue*. Quarks can be grouped in triplets of the $SU_C(3)$ color symmetry group . This results in 8 exchange particles, the gluons, which also carry color. Due to the possible gluon-gluon coupling the coupling constant α_S increases with the decrease of the q^2-value and with large distances of the quarks which therefore only exist in bound states.

2.1.2. The electroweak interaction

Table 2.3 lists the fermions with their weak quantum numbers. The quarks and charged leptons can be either left-handed (L) or right-handed (R) since the chiral symmetry is broken for massive particles. Neutrinos which are massless in the Standard Model do not have a right-handed component. The weak interaction only couples left-handed particles. Left-handed fermions are grouped in doublets of $SU(2)_L$ gauge group, which describes the symmetry of the weak isospin T. Right-handed particles are $SU(2)_L$ singlets. Glashow, Salman, and Weinberg [1, 2, 3] found that the weak and the electromagnetic interactions can be unified by considering a combined $SU(2)_L \times U(1)_Y$ gauge group, where Y is the hypercharge given by $Y = 2(Q - T_3)$, with Q being the electric charge and T_3 the third component of T.

The main subject of this thesis are τ leptons which can only decay weakly in the Standard Model. The τ decays proceed through the exchange of a W^- boson. The

Table 2.3.: Fundamental particles in the Standard Model of Particle Physics. The particles are characterized by the charge Q, the weak isospin T, its third component T_3, and the hypercharge Y. The *prime* indicates the quark eigenstates with respect to the weak interaction which are different from the mass eigenstates. The indices L and R denote left-handed and right-handed fermions.

			Q/e	T	T_3	Y
	Quarks					
$\begin{pmatrix} u \\ d' \end{pmatrix}_L$	$\begin{pmatrix} c \\ s' \end{pmatrix}_L$	$\begin{pmatrix} t \\ b' \end{pmatrix}_L$	$+\frac{2}{3}$	$\frac{1}{2}$	$+\frac{1}{2}$	$+\frac{1}{3}$
			$-\frac{1}{3}$	$\frac{1}{2}$	$-\frac{1}{2}$	$+\frac{1}{3}$
u_R	c_R	t_R	$+\frac{2}{3}$	0	0	$+\frac{4}{3}$
d_R	s_R	b_R	$-\frac{1}{3}$	0	0	$-\frac{2}{3}$
	Leptons					
$\begin{pmatrix} \nu_e \\ e \end{pmatrix}_L$	$\begin{pmatrix} \nu_\mu \\ \mu \end{pmatrix}_L$	$\begin{pmatrix} \nu_\tau \\ \tau \end{pmatrix}_L$	0	$\frac{1}{2}$	$+\frac{1}{2}$	-1
			-1	$\frac{1}{2}$	$-\frac{1}{2}$	-1
e_R	μ_R	τ_R	-1	0	0	-2

part of the Standard Model Lagrangian [12] which describes the interaction of quarks and leptons with the W^- is

$$\mathcal{L}_{\mathrm{CC}} = -\frac{g}{\sqrt{2}} \left(j^{\mu}_{\mathrm{CC}} \mathbf{W}^{+}_{\mu} + j^{\mu\dagger}_{\mathrm{CC}} \mathbf{W}^{-}_{\mu} \right) \tag{2.1}$$

where g is the weak coupling constant, $\mathbf{W}^{\pm}_{\mu}$ denote the $W^{\pm}$ fields, and j^{μ}_{CC} is the charged current which can be written as follows:

$$j^{\mathrm{CC}}_{\mu} = (\overline{\nu}_{eL}, \overline{\nu}_{\mu L}, \overline{\nu}_{\tau L})\gamma_\mu \begin{pmatrix} e_L \\ \mu_L \\ \tau_L \end{pmatrix} + (\overline{u}_L, \overline{c}_L, \overline{t}_L)\gamma_\mu \boldsymbol{V} \begin{pmatrix} d_L \\ s_L \\ b_L \end{pmatrix}, \tag{2.2}$$

where the index L denotes left-handed fermions, and γ_μ are Dirac matrices. The first term is the charged current for charged leptons and neutrinos, and the second term for quarks. The matrix $\boldsymbol{V}$ describes a transformation of the mass eigenstates (d, s, b) into the eigenstates of the weak interaction (d', s', b'):

$$\begin{pmatrix} d' \\ s' \\ b' \end{pmatrix} = \begin{pmatrix} V_{ud} & V_{us} & V_{ub} \\ V_{cd} & V_{cs} & V_{cb} \\ V_{td} & V_{ts} & V_{tb}. \end{pmatrix} \begin{pmatrix} d \\ s \\ b \end{pmatrix}. \tag{2.3}$$

This matrix is called the Cabibbo-Kobayashi-Maskawa (CKM) matrix [6] and is denoted as $\boldsymbol{V}_{\mathrm{CKM}}$ in the following. $\boldsymbol{V}_{\mathrm{CKM}}$ allows for transitions not only within one quark family but also between different quark families. The CKM matrix is the origin of the *flavor changing charged currents* observed in weak decays. A similar matrix occurs in the lepton term if massive neutrinos are considered. The mixing matrix in the lepton sector is called *Pontecorvo-Maki-Nakagawa-Sakata* (PMNK) matrix [13].

The complex $\boldsymbol{V}_{\mathrm{CKM}}$ elements V_{ij} multiplied with $\frac{g}{\sqrt{2}}$ are the coupling constants of the quarks i and j to the W^- boson. Since the sum of the transition probabilities, which are proportional to $|V_{ij}|^2$, of a quark i into any quark j has to be equal to one, $\boldsymbol{V}_{\mathrm{CKM}}$ has to be unitary, i. e., $\boldsymbol{V}_{\mathrm{CKM}}\boldsymbol{V}_{\mathrm{CKM}}{}^{\dagger} = 1$.

Properties of the CKM matrix

The unitarity of the CKM matrix is expressed by the following conditions on the matrix elements:

$$\sum_{i=1}^{3} V_{ij}V_{ik}^{*} = \delta_{jk}, \quad \sum_{j=1}^{3} V_{ij}V_{kj}^{*} = \delta_{ik} \quad \text{with} \quad \delta_{ij} = \begin{cases} 0 \text{ if } i \neq j \\ 1 \text{ if } i = j \end{cases}. \tag{2.4}$$

A complex 3×3 matrix like $\boldsymbol{V}_{\mathrm{CKM}}$ has in principal 18 free parameters. This number is reduced to 9 by the unitarity conditions. Moreover, 5 phases can be absorbed into quark fields leaving a final number of four free parameters. These four parameters are free parameters of the Standard Model. The Standard Model can therefore be tested by the measurements of the CKM matrix elements and their relations. Any deviations from the unitarity conditions of the CKM matrix are a hint for physics beyond the description of the Standard Model.

The CKM matrix which describes a rotation in flavor space can be parametrized by identifying the four free parameters as three Euler angles, Θ_{12}, Θ_{23}, and Θ_{13}, and a phase δ_{13}. $\boldsymbol{V}_{\mathrm{CKM}}$ can be then described by three rotation matrices, where one matrix contains a phase factor $e^{-i\delta_{13}}$:

$$\boldsymbol{V}_{\mathrm{CKM}} = \begin{pmatrix} 1 & 0 & 0 \\ 0 & c_{23} & s_{23} \\ 0 & -s_{23} & c_{23} \end{pmatrix} \begin{pmatrix} c_{13} & 0 & s_{13}e^{-i\delta_{13}} \\ 0 & 1 & 0 \\ -s_{13}e^{i\delta_{13}} & 0 & c_{13} \end{pmatrix} \begin{pmatrix} c_{12} & s_{12} & 0 \\ -s_{12} & c_{12} & 0 \\ 0 & 0 & 1 \end{pmatrix}, \tag{2.5}$$

where $s_{ij} = \sin\Theta_{ij}$ and $c_{ij} = \cos\Theta_{ij}$. The complex phase δ_{13} is the only source of CP violation in the Standard Model [6].

The elements of the CKM matrix show a hierarchy [4]. While the diagonal elements of $\boldsymbol{V}_{\mathrm{CKM}}$ are close to one, their size decreases with the distance to the diagonal. This means that transitions of quarks within one family are most probable, while transitions between the first and third family have the smallest probability. This hierarchy is reflected in the Wolfenstein parametrization which is an expansion of $\boldsymbol{V}_{\mathrm{CKM}}$ in the parameter $\lambda = s_{12}$. In order $\mathcal{O}(\lambda^4)$ the matrix is given by:

$$\boldsymbol{V}_{\mathrm{CKM}} = \begin{pmatrix} 1 - \lambda^2/2 & \lambda & A\lambda^3(\rho - i\eta) \\ -\lambda & 1 - \lambda^2/2 & A\lambda^2 \\ A\lambda^3(1 - \rho - i\eta) & -A\lambda^2 & 1 \end{pmatrix} + \mathcal{O}(4) \tag{2.6}$$

where A, ρ, and η are the three remaining free parameters in this parametrization.

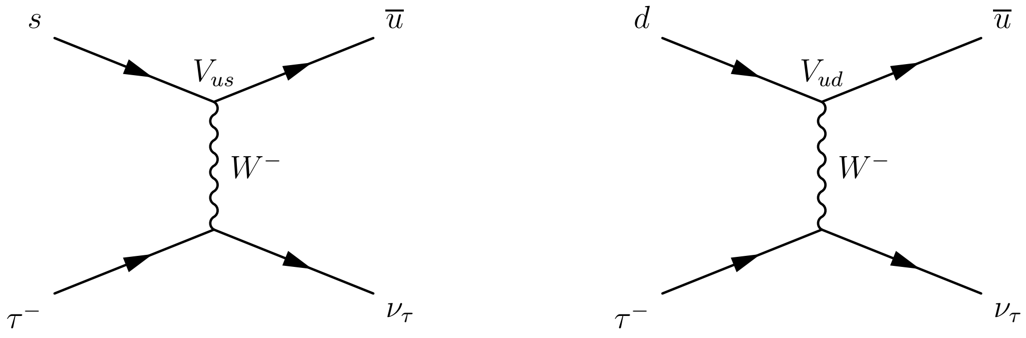

(a) $\tau^- \to \overline{u}s\nu_\tau$ **(b)** $\tau^- \to \overline{u}d\nu_\tau$

Figure 2.1.: Feynman diagrams of hadronic charged current transitions occurring in τ decays. Charge conjugate transitions are implied.

CKM matrix elements in hadronic τ decays

The CKM matrix elements which are relevant for hadronic τ decays are V_{ud} and V_{us}. Kinematically only the τ decays to the light quarks are possible. The matrix elements enter the decay amplitudes as coupling strength. The square of these elements correspond to the probabilities of the quark transitions $u \leftrightarrow d$ and $u \leftrightarrow s$ shown in Figure 2.1 The unitarity condition of the $\boldsymbol{V}_{\mathrm{CKM}}$ which contains both elements is

$$|V_{ud}|^2 + |V_{us}|^2 + |V_{ub}|^2 = 1, \tag{2.7}$$

where the size of $|V_{ub}|$ is negligible compared with the other two elements.

V_{ud} is the best known CKM matrix element [4]. The most precise value of the magnitude of V_{ud}, $|V_{ud}|$, has been measured in superallowed $0^+ \to 0^+$ nuclear beta decays [14]:

$$|V_{ud}| = 0.97425 \pm 0.00022, \tag{2.8}$$

where the relative uncertainty amounts to 0.02%.

The magnitude of V_{us}, $|V_{us}|$, which corresponds to the parameter $\lambda \approx 0.22$ of the Wolfenstein parametrization is discussed in detail in Section 2.4, since this element can be obtained using the branching fractions measured in this analysis.

In the next sections an experimental and theoretical overview of τ decays is given.

2.2. Leptonic τ decays

This section discusses the leptonic decays of the τ which contribute to approximately one third to the total τ decay width.

Measured branching fractions

The Feynman diagram of leptonic τ decays is shown in Figure 2.2. The branching fractions $\mathcal{B}(\tau^- \to e^-\overline{\nu}_e\nu_\tau)$ and $\mathcal{B}(\tau^- \to \mu^-\overline{\nu}_\mu\nu_\tau)$ are the most precisely known τ decay

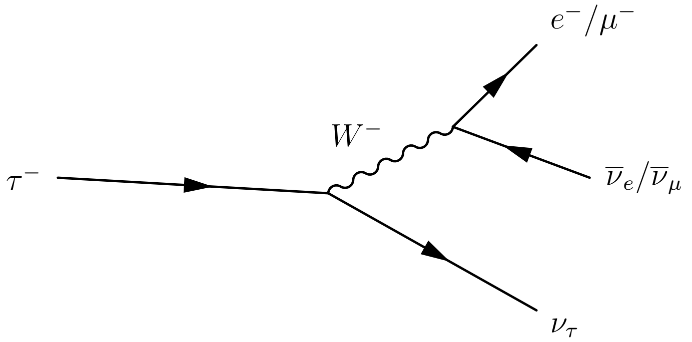

Figure 2.2.: Feynman diagram of the leptonic τ decay $\tau^- \to l^-\overline{\nu}_l\nu_\tau$ with $l^- = e^-, \mu^-$.

branching fractions. Their current world averages [4] are

$$\begin{aligned}\mathcal{B}(\tau^- \to e^-\overline{\nu}_e\nu_\tau) &= (17.82 \pm 0.05)\%,\\ \mathcal{B}(\tau^- \to \mu^-\overline{\nu}_\mu\nu_\tau) &= (17.33 \pm 0.05)\%.\end{aligned} \tag{2.9}$$

The relative precision of both averages is 0.3%.

Besides the direct measurements, $\mathcal{B}(\tau^- \to e^-\overline{\nu}_e\nu_\tau)$ can be determined from the masses and the lifetimes of the τ and μ as well as from the measured $\mathcal{B}(\tau^- \to \mu^-\overline{\nu}_\mu\nu_\tau)$. This determinations are presented in the next paragraphs.

Leptonic decay widths

According to [5] the partial widths of $L = \mu, \tau$ lepton decays into leptons $l = e, \mu$ can be computed from

$$\Gamma(L \to l\nu_l\nu_\tau(\gamma)) = \frac{G_F G_l m_L^5}{192\pi^3} f\left(\frac{m_l^2}{m_L^2}\right) \delta_W^L \delta_\gamma^L, \tag{2.10}$$

where m_l and m_L are the masses of the leptons, and the different terms are

$$\begin{aligned}
G_F &= \frac{g_w^2}{4\sqrt{2}M_W^2},\\
\delta_W^L &= 1 + \frac{3}{5}\frac{m_L^2}{M_W^2} \quad \text{with} \quad \begin{cases}\delta_W^\tau = 1 + 2.9 \times 10^{-4}\\ \delta_W^\mu = 1 + 1.0 \times 10^{-6},\end{cases}\\
\delta_\gamma^L &= 1 + \frac{\alpha(m_L)}{2\pi}\left(\frac{25}{4} - \pi^2\right) \quad \text{with} \quad \begin{cases}\delta_\gamma^\tau = 1 - 43.2 \times 10^{-4}\\ \delta_\gamma^\mu = 1 + 42.4 \times 10^{-4},\end{cases}\\
f(x) &= 1 - 8x + 8x^3 - x^4 - 12x^2 \ln x
\end{aligned} \tag{2.11}$$

where g_w is the weak couplings, M_W is the mass of the W boson, and $\alpha(m_L)$ is the electromagnetic coupling constant at the mass scale of the lepton, and G_F is the Fermi coupling constant.

$\mathcal{B}(\tau^- \to e^-\overline{\nu}_e\nu_\tau)$ from masses and lifetimes of the τ and μ

The $\mathcal{B}(\tau^- \to e^-\overline{\nu}_e\nu_\tau)$ can be expressed as follows using Equation 2.10 and by assuming μ-τ universality, i. e., $g_\mu = g_\tau$:

$$\begin{aligned} \mathcal{B}(\tau^- \to e^-\overline{\nu}_e\nu_\tau) &= \frac{\Gamma(\tau^- \to e^-\overline{\nu}_e\nu_\tau)}{\Gamma_\tau} \\ &= \frac{\Gamma(\mu^- \to e^-\overline{\nu}_e\nu_\mu)}{\Gamma_\tau}\left(\frac{m_\tau}{m_\mu}\right)^5 \frac{f(m_e^2/m_\tau^2)}{f(m_e^2/m_\mu^2)}\frac{\delta_W^\tau\delta_\gamma^\tau}{\delta_W^\mu\delta_\gamma^\mu} \end{aligned} \tag{2.12}$$

where Γ_τ is the total τ decay width. The total decay width is related with the lifetime, τ, of the decaying particle through $\Gamma = \frac{\hbar}{\tau}$. By using the latter relation and $\Gamma(\mu^- \to e^-\overline{\nu}_e\nu_\mu) = \Gamma_\mu$, Equation 2.12 can be written as

$$\mathcal{B}(\tau^- \to e^-\overline{\nu}_e\nu_\tau) = \frac{\tau_\tau}{\tau_\mu}\left(\frac{m_\tau}{m_\mu}\right)^5 \frac{f(m_e^2/m_\tau^2)}{f(m_e^2/m_\mu^2)}\frac{\delta_W^\tau\delta_\gamma^\tau}{\delta_W^\mu\delta_\gamma^\mu}. \tag{2.13}$$

The value of $\mathcal{B}(\tau^- \to e^-\overline{\nu}_e\nu_\tau)$ obtained from $m_\tau = 1776.82 \pm 0.16\,\mathrm{MeV}/c^2$, $m_\mu = 105.6583668 \pm 0.0000038\,\mathrm{MeV}/c^2$, $\tau_\tau = (290.6 \pm 1.0) \times 10^{-15}s$, and $\tau_\mu = (2.197034 \pm 0.000021) \times 10^{-6}s$ taken from [4] is

$$\mathcal{B}(\tau^- \to e^-\overline{\nu}_e\nu_\tau) = (17.796 \pm 0.061)\%, \tag{2.14}$$

which is consistent with the current world average of the direct measurements.

$\mathcal{B}(\tau^- \to e^-\overline{\nu}_e\nu_\tau)$ from the measured $\mathcal{B}(\tau^- \to \mu^-\overline{\nu}_\mu\nu_\tau)$

Equation 2.10 can be used to express $\mathcal{B}(\tau^- \to e^-\overline{\nu}_e\nu_\tau)$ with $\mathcal{B}(\tau^- \to \mu^-\overline{\nu}_\mu\nu_\tau)$:

$$\mathcal{B}(\tau^- \to e^-\overline{\nu}_e\nu_\tau) = \frac{1}{r_e^\mu}\mathcal{B}(\tau^- \to \mu^-\overline{\nu}_\mu\nu_\tau), \tag{2.15}$$

where r_e^μ is a kinematic factor correcting for different masses of:

$$r_e^\mu = \frac{f(m_\mu^2/m_\tau^2)}{f(m_e^2/m_\tau^2)}. \tag{2.16}$$

The value of $\mathcal{B}(\tau^- \to e^-\overline{\nu}_e\nu_\tau)$ obtained with m_τ, m_μ, and $\mathcal{B}(\tau^- \to \mu^-\overline{\nu}_\mu\nu_\tau)$ taken from [4] is

$$\mathcal{B}(\tau^- \to e^-\overline{\nu}_e\nu_\tau) = (17.819 \pm 0.051)\%, \tag{2.17}$$

which is also consistent with the direct measurements.

Average $\mathcal{B}(\tau^- \to e^-\overline{\nu}_e\nu_\tau)$

The $\mathcal{B}(\tau^- \to e^-\overline{\nu}_e\nu_\tau)$ values determined from the masses and the lifetimes of the τ and μ and from the measured $\mathcal{B}(\tau^- \to \mu^-\overline{\nu}_\mu\nu_\tau)$ are computed under the assumption of lepton universality. The branching fraction obtained by combining these results with the world average of direct measurements amounts to

$$\mathcal{B}(\tau^- \to e^-\overline{\nu}_e\nu_\tau)_{\mathrm{uni}} = (17.817 \pm 0.031)\%, \tag{2.18}$$

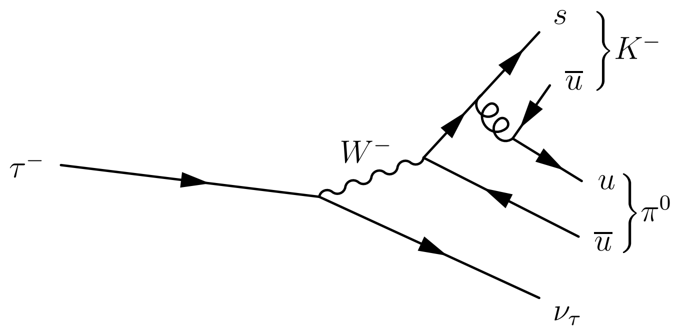

Figure 2.3.: Feynman diagram of the $\tau^- \to K^-\pi^0\nu_\tau$ decay.

and is denoted as the *universality-improved* $\mathcal{B}(\tau^- \to e^-\overline{\nu}_e\nu_\tau)_{\text{uni}}$. $\mathcal{B}(\tau^- \to e^-\overline{\nu}_e\nu_\tau)_{\text{uni}}$ is the most precise value of the $\tau^- \to e^-\overline{\nu}_e\nu_\tau$ branching fraction.

As will be discussed in Section 11, the leptonic branching fractions are used to derive the total hadronic τ decay width ratio, R_{had}, which enters the determination of the CKM matrix $|V_{us}|$ from inclusive strange τ decays. To minimize the uncertainty of $|V_{us}|$ the $\mathcal{B}(\tau^- \to e^-\overline{\nu}_e\nu_\tau)_{\text{uni}}$ will be used in the calculation of R_{had}.

2.3. Hadronic τ decays

In this section, an overview of the experimental and theoretical status of hadronic τ decays is presented. A detailed review of hadronic τ decays is given in [5].

The τ is the only lepton which can decay into hadrons due to its sufficiently large mass. τ decays of the type

$$\tau^- \to X^-_{\text{had}}\nu_\tau \tag{2.19}$$

where X^-_{had} denotes one or more hadrons, are called *hadronic* τ decays. Decays of this type can proceed through intermediate short-lived resonances (e. g., a_1,ω, ρ) and result in final-state hadronic systems that can contain charged and neutral kaons and pions, as well as η mesons. Hadronic τ decays into final states with strangeness quantum number $|S| = 1$, i. e., decays that contain an odd number of kaons in the final state, are denoted in the following as *strange* τ decays. Correspondingly, hadronic τ decays with $S = 0$ are called *non-strange* τ decays. As an example of a hadronic τ decay, the Feynman diagram of the $\tau^- \to K^-\pi^0\nu_\tau$ decay is shown in Figure 2.3.

2.3.1. Spectral functions of hadronic τ decays

The hadronic final states X_{had} in τ decays are described by so-called *spectral functions.* These functions describe the probability to create X_{had} as a function of the invariant mass, m_{had}. Depending on the spin J of the hadronic system which is indicated by the subscript, and, depending on the vector (V) or axial-vector (A) nature of X_{had}, the spectral functions, v_0, v_1, a_0, and a_1 are defined as:

$$\begin{aligned} f_1(s) = &\frac{m_\tau^2}{6|V_{ij}|^2 S_{EW}} \frac{\mathcal{B}(\tau \to X^-(J=1)\nu_\tau)}{\mathcal{B}(\tau^- \to e^- \overline{\nu}_e \nu_\tau)} \\ &\times \frac{1}{N_X}\frac{dN_X}{ds}\left[\left(1-\frac{s}{m_\tau^2}\right)^2\left(1+\frac{2s}{m_\tau^2}\right)\right]^{-1}, \end{aligned} \tag{2.20}$$

$$\begin{aligned} f_0(s) = &\frac{m_\tau^2}{6|V_{ij}|^2 S_{EW}} \frac{\mathcal{B}(\tau \to X^-(J=0)\nu_\tau)}{\mathcal{B}(\tau^- \to e^- \overline{\nu}_e \nu_\tau)} \\ &\times \frac{1}{N_X}\frac{dN_X}{ds}\left(1-\frac{s}{m_\tau^2}\right)^{-2}, \end{aligned} \tag{2.21}$$

where $X^- = V^-$ if $f_i(s) = v_i$ or $X^- = A^-$ if $f_i(s) = a_i$, $s = m_{\mathrm{had}}^2$, $|V_{ij}| = |V_{ud}|$ for non-strange decays, $|V_{ij}| = |V_{us}|$ for strange decays, and S_{EW} is a short-distance electroweak radiative correction. The term $\frac{1}{N_X}\frac{dN_X}{ds}$ is the normalized invariant mass squared distribution of the hadronic final state which is multiplied with a kinematic factor and with the ratio of the branching fractions of the considered decay and the $\tau^- \to e^- \overline{\nu}_e \nu_\tau$ decay.

Spectral functions are an important input for QCD studies at a τ-mass scale. They also carry information on α_S, and, for X_{had} with $|S| = 1$, can be used to determine the strange quark mass [5]. Spectral functions have been measured by the ALEPH and OPAL experiments leading to a determination of α_S and m_S.

Analyses of invariant mass spectra in τ decays are also carried out by the B factories. For example, preliminary results of invariant hadronic mass distributions in the $\tau^- \to K_S^0 \pi^- \nu_\tau$ decays have been presented in [15]. In this analysis, the main goal is the precise measurement of six hadronic τ decay branching fractions. This measurements is an essential step towards the determination of the invariant mass spectra of these decays.

2.3.2. Spectral moments

Information on the shape of the spectral functions can be derived from *spectral moments* which are defined as

$$R_{\mathrm{had}}^{kl} = \int_0^{m_\tau^2} ds \left(1-\frac{s}{m_\tau^2}\right)^k \left(\frac{s}{m_\tau^2}\right)^l \frac{dR_{\mathrm{had}}}{ds}, \tag{2.22}$$

where $s = m_{\mathrm{had}}^2$, R_{had} is the total hadronic τ decay ratio defined as the hadronic τ decay width divided by the electronic τ decay width:

$$R_{\mathrm{had}} = \frac{\Gamma(\tau \to X_{\mathrm{had}}^- \nu_\tau)}{\Gamma(\tau^- \to e^- \overline{\nu}_e \nu_\tau)}. \tag{2.23}$$

As can be seen in Equation 2.22, the first spectral moment $R_{\mathrm{had}}^{00} = R_{\mathrm{had}}$.

The spectral moments can be separated into their strange and non-strange components:

$$R^{kl}_{\text{had}} = R^{kl}_{\text{ns}} + R^{kl}_{\text{s}} \tag{2.24}$$

Within the framework of the *Operator Product Expansion* (OPE) [8] the contributions $R^{kl}_x = R^{kl}_{\text{s}}, R^{kl}_{\text{ns}}$ to the total hadronic rate can be written as

$$R^{kl}_x = N_C |V_{ij}|^2 S_{EW} \left(1 + \delta^{kl(0)} + \delta^{kl(')} + \delta^{kl(2,m_q)} + \sum_{D=4,6,\ldots} \delta^{kl(D,m_q)}\right), \tag{2.25}$$

where $N_C = 3$ is the number of color charges in QCD, $|V_{ij}| = |V_{ud}|$ for non-strange decays, $|V_{ij}| = |V_{us}|$ for strange decays, S_{EW} is a short-distance electroweak radiative correction, $\delta^{kl(')}$ is a residual small non-logarithmic electroweak correction which is neglected in the following. The perturbative contributions $\delta^{kl(0)}$ and $\delta^{kl(2,m_q)}$ depend on $\alpha_S(m_\tau^2)$, and on $\alpha_S(m_\tau^2)$ and the quark masses m_q, respectively. The remaining contributions which depend on quark masses to the dimension $D = 4, 6, ...$, contain non-perturbative terms.

When investigating spectral moments the theoretical uncertainty can be reduced by considering the difference, δR^{kl}_τ, of the strange and non-strange contributions normalized by the corresponding CKM matrix elements:

$$\delta R^{kl}_\tau = \frac{R^{kl}_{\text{ns}}}{|V_{ud}|^2} - \frac{R^{kl}_{\text{s}}}{|V_{us}|^2}. \tag{2.26}$$

The theoretical description of this $SU(3)$-breaking relation can be derived from Equation 2.25:

$$\delta R^{kl}_\tau = 3 S_{EW} \left(-\delta^{kl(2,m_S)} + \sum_{D=4,6,\ldots} \overline{\delta}^{\;kl(D,m_q)}\right), \tag{2.27}$$

where the contribution $\delta^{kl(0)}$ to the mass dimension $D = 0$ cancels in the difference, and the quark masses of the light quarks u and d are assumed to be negligible compared to the strange quark mass, i. e., $m_u = m_d = 0$, leaving only the strange quark mass contribution $\delta^{kl(2,m_s)}$ in mass dimension $D = 2$. Moreover, some terms in higher mass dimensions also cancel resulting in a modified $\overline{\delta}^{\;kl(D,m_q)}$. According to [5] the term $\delta^{kl(2,m_s)}$ exhibits a problematic convergence behavior which deteriorates with increasing k, and is subject to many theoretical investigations (for example [16]). Moreover, large correlations between the moments have been found which makes the simultaneous extraction of information from the moments difficult.

$|V_{us}|$ and m_s from spectral moments

As can be seen in Equations 2.26 and 2.27, the magnitude of the CKM matrix element V_{us} and the strange quark mass m_s can be determined by the measurement of the spectral moments and $|V_{ud}|$. Due to the problematic behavior of moments with $k > 0$ only the first moment R^{00} is considered in the following. Three possibilities arise from the above relations:

1. In principle, an optimal approach would be a simultaneous determination of $|V_{us}|$

and m_s in a fit of the spectral moments. This approach is currently limited by the uncertainties of the experimental input data, which could be improved by future measurements of hadronic τ decays by the B factories.

2. m_s can be determined by using $|V_{us}|$ from independent measurements as input. According to [5] higher k-moments[1] are more sensitive to m_s than the first moment. Moreover, one of the dominant uncertainties of m_s obtained from R^{00} in that way is the uncertainty of $|V_{us}|$ which makes this approach less favorable compared with the reverse approach described next.

3. $|V_{us}|$ can be determined by using m_s obtained from non-τ sources as input. The first moments R_{s}^{00} and R_{ns}^{00} are particularly sensitive to $|V_{us}|$ [5]. Using these moments the best theoretical precision on $|V_{us}|$ is achieved. $|V_{us}|$ is obtained from the relation:
$$|V_{us}| = \sqrt{\frac{R_{\mathrm{s}}^{00}}{\frac{R_{\mathrm{ns}}^{00}}{|V_{ud}|^2} - \delta R_{\tau}^{00}}}, \tag{2.28}$$
This approach has the advantage that even a relatively large uncertainty of δR_{τ}^{00} has a small impact on the resulting uncertainty of $|V_{us}|$. This is due to the small size of δR_{τ}^{00} compared to $\frac{R_{\tau,\mathrm{ns}}^{00}}{|V_{ud}|^2} \approx 3.6$. According to [8] δR_{τ}^{00} amounts to
$$\delta R_{\tau}^{00} = 0.240 \pm 0.032 \tag{2.29}$$
where $m_s(2\,\mathrm{GeV}) = (94 \pm 6)\,\mathrm{MeV}/c^2$ has been used for the strange quark mass. This approach to determine $|V_{us}|$ is used in this analysis. Currently it is limited by experimental uncertainties.

In the next sections an experimental status of $R_{\tau,\mathrm{ns}}^{00}$ and $R_{\tau,\mathrm{s}}^{00}$ is presented.

2.3.3. Determination of R_{had} from the leptonic τ decays

Inclusive branching fraction of hadronic τ decays

The branching fraction of hadronic τ decays, $\mathcal{B}_{\mathrm{had}} = \mathcal{B}(\tau \to X_{\mathrm{had}}^{-}\nu_\tau)$, can be determined very precisely from the leptonic τ branching fractions (Section 2.2):
$$\mathcal{B}_{\mathrm{had}} = 1 - \mathcal{B}(\tau^- \to e^-\overline{\nu}_e\nu_\tau) - \mathcal{B}(\tau^- \to \mu^-\overline{\nu}_\mu\nu_\tau). \tag{2.30}$$
With Equation 2.15 and using the universality improved branching fraction $\mathcal{B}(\tau^- \to e^-\overline{\nu}_e\nu_\tau)_{\mathrm{uni}}$ the hadronic branching fraction amounts to:
$$\mathcal{B}_{\mathrm{had}} = 1 - (1 + r_e^{\mu})\mathcal{B}(\tau^- \to e^-\overline{\nu}_e\nu_\tau)_{\mathrm{uni}} = (65.85 \pm 0.06)\% \tag{2.31}$$

---

[1] Moments with $k > 0$ have been used by the ALEPH collaboration [5] to determine m_s. The results of this measurements are consistent with m_s determined in non-τ analysis. However, the obtained uncertainties are not competitive with the other results.

Hadronic τ decay width ratio

Similarly to the hadronic τ branching fraction, the partial hadronic τ decay width ratio defined as:

$$R_\tau = \frac{\Gamma(\tau \to X^-_{\mathrm{had}}\nu_\tau)}{\Gamma(\tau^- \to e^-\overline{\nu}_e\nu_\tau)} \tag{2.32}$$

can also be obtained from the leptonic branching fractions:

$$\begin{aligned} R_\tau &= \frac{1 - \mathcal{B}(\tau^- \to e^-\overline{\nu}_e\nu_\tau) - \mathcal{B}(\tau^- \to \mu^-\overline{\nu}_\mu\nu_\tau)}{BR(\tau^- \to e^-\overline{\nu}_e\nu_\tau)} \\ &= \frac{1}{\mathcal{B}(\tau^- \to e^-\overline{\nu}_e\nu_\tau)_{\mathrm{uni}}} - (1 + r^\mu_e) \\ &= 3.6401 \pm 0.0098. \end{aligned} \tag{2.33}$$

This result can be compared with the prediction arising from the Equation 2.24 and Equation 2.25 by neglecting all electroweak corrections:

$$R_\tau \approx N_C|V_{ud}|^2 + N_C|V_{us}|^2 = 3 \tag{2.34}$$

where $N_C = 3$, the unitarity of the CKM matrix is assumed, i. e., $|V_{ud}|^2 + |V_{us}|^2 + |V_{ud}|^2 = 1$. $|V_{ub}|$ is negligible compared with the other two CKM matrix elements, and is therefore ignored. This comparison gives an estimate of the contribution of the radiative corrections to R_τ of about 20%.

2.3.4. Exclusive branching fractions of hadronic τ decays

In this section, the experimental status of exclusive hadronic τ branching fraction determinations is presented.

Hadronic τ decay modes

About 87% of the total hadronic τ branching fraction $\mathcal{B}_{\mathrm{had}}$ originate from only five different τ decays which are listed in Table 2.4 with the current world averages of their branching fractions. The sum of these branching fractions is known with a relative uncertainty of 1.7%. Other non-strange τ decays contribute with approximately 9% to $\mathcal{B}_{\mathrm{had}}$. The fraction of Cabibbo-suppressed strange τ decays is about 4% with an relative uncertainty of 2.7%. A list of strange decay modes is given in Table 2.5.

Measurments of hadronic τ decays before B factories

The vast majority of hadronic τ branching fraction measurements have been performed by the LEP experiments ALEPH, DELPHI, and OPAL, as well as by the CLEO experiment. For the τ decays with large branching fractions (Table 2.4), small relative systematic uncertainties on the order of 1% have been achieved. Typically, the statistical uncertainties of these measurements are of similar size as the systematic uncertainties. Smaller branching fractions have also been measured (down to 10^{-4}), however, with degrading precision.

Table 2.4.: Branching fractions of the five most frequent hadronic τ decays. The listed values are the current world averages [4], except for the $\tau^- \to \pi^-\pi^+\pi^-\pi^0\nu_\tau$ decay, where the PDG fit result is listed.

Decay	$\mathcal{B}$ [%]	$\Delta\mathcal{B}/\mathcal{B}$ [%]
$\tau^- \to \pi^-\nu_\tau$	10.828 ± 0.105	1.0
$\tau^- \to \pi^-\pi^0\nu_\tau$	25.46 ± 0.12	0.5
$\tau^- \to \pi^-(2\pi^0)\nu_\tau$	9.239 ± 0.124	1.3
$\tau^- \to \pi^-\pi^+\pi^-\nu_\tau$	9.041 ± 0.970	1.1
$\tau^- \to \pi^-\pi^+\pi^-\pi^0\nu_\tau$	2.70 ± 0.08	3.0
Total	57.268 ± 0.994	1.7

Table 2.5.: Branching fractions of strange τ decays. The listed values are the current world averages [4]. The first four listed branching fractions are measured in this analysis.

Decay	$\mathcal{B}$ [%]	$\Delta\mathcal{B}/\mathcal{B}$ [%]
$\tau^- \to K^-\nu_\tau$	0.685 ± 0.023	3.4
$\tau^- \to K^-\pi^0\nu_\tau$	0.426 ± 0.016	3.8
$\tau^- \to K^-(2\pi^0)\nu_\tau$	0.058 ± 0.024	41.4
$\tau^- \to K^-(3\pi^0)\nu_\tau$	0.037 ± 0.024	64.9
$\tau^- \to \pi^-\overline{K}^0\nu_\tau$	0.831 ± 0.030	3.6
$\tau^- \to \pi^-\overline{K}^0\pi^0\nu_\tau$	0.360 ± 0.040	11.1
$\tau^- \to \pi^-\overline{K}^0\pi^0\pi^0\nu_\tau$	0.026 ± 0.024	92.3
$\tau^- \to \overline{K}^0h^-h^-h^+\nu_\tau$	0.023 ± 0.020	88.0
$\tau^- \to K^-\pi^+\pi^-\nu_\tau$ (ex. K^0)	0.280 ± 0.019	6.8
$\tau^- \to K^-\pi^+\pi^-\pi^0\nu_\tau$ (ex. K^0,ω)	0.037 ± 0.009	24.3
$\tau^- \to K^-\phi(\to KK)\nu_\tau$	0.004 ± 0.001	25.0
$\tau^- \to K^-\eta\nu_\tau$	0.016 ± 0.001	6.3
$\tau^- \to K^-\eta\pi^0\nu_\tau$	0.005 ± 0.001	20.0
$\tau^- \to \pi^-\overline{K}^0\eta\nu_\tau$	0.009 ± 0.002	22.2
$\tau^- \to K^-\omega\nu_\tau$	0.041 ± 0.009	22.0
Total	2.838 ± 0.077	2.7

Measurements of hadronic τ decays at the B factories

In the last 4 years, hadronic τ decay branching fraction measurements have also been published by the B-factory experiments, BABAR and Belle. The 2010 edition of the PDG listings contains 22 results from the B factories. Among these results, six branching fractions were measured for the first time.

The τ-pair datasets recorded at the B factories are significantly larger than the data collected by the experiments listed above. For example, about 0.33×10^6 τ decays have been used by the ALEPH collaboration in [17], while this analysis which uses the BABAR dataset exploits more than 400×10^6 τ pairs. This large dataset leads to small statistical uncertainties even for τ decays with small branching fractions ($\mathcal{O}(10^{-4})$). The systematic uncertainties of the BABAR measurements are dominated by the effects related to the reconstruction of photons and π^0's. In the ALEPH measurements, these uncertainties are smaller due to the good performance of the ALEPH large-coverage electromagnetic calorimeter. A measurement of the $\tau^- \to \pi^-\pi^0\nu_\tau$ and $\tau^- \to \pi^-(2\pi^0)\nu_\tau$ decays by BABAR would not be competitive with the ALEPH results. The potential of the BABAR experiment lies in the measurement of τ decays with smaller branching fractions which have been so far limited by their statistical uncertainties.

The $\tau^- \to \pi^-(3\pi^0)\nu_\tau$ and $\tau^- \to \pi^-(4\pi^0)\nu_\tau$ decay modes

The non-strange $\tau^- \to \pi^-(3\pi^0)\nu_\tau$ and $\tau^- \to \pi^-(4\pi^0)\nu_\tau$ decay modes are measured in this analysis. The branching fraction of the $\tau^- \to \pi^-(3\pi^0)\nu_\tau$ decay was previously only measured by the ALEPH collaboration with a relative uncertainty of 9% ($\mathcal{B}(\tau^- \to \pi^-(3\pi^0)\nu_\tau) = (0.98 \pm 0.09)\%$). The $\tau^- \to \pi^-(4\pi^0)\nu_\tau$ branching fraction is measured for the first time in this analysis. An estimate for the expected size of this branching fraction can be derived from the branching fraction of $\tau^- \to h^-(4\pi^0)\nu_\tau$ decays, where h can be either a charged pion or kaon, ($\mathcal{B}(\tau^- \to h^-(4\pi^0)\nu_\tau) = (1.12 \pm 0.51) \times 10^{-3}$), which was measured by the ALEPH collaboration. Typically, the branching fraction of a τ decay into a kaon is smaller by a factor of $10 - 100$ compared to the branching fraction of a decay into a pion and the same number of π^0's, i. e., one expects roughly $\mathcal{B}(\tau^- \to \pi^-(4\pi^0)\nu_\tau) \approx 1 \times 10^{-3}$.

Strange τ decays

The Cabibbo-suppressed strange τ decays are of particular importance because they can be used to determine the magnitude of the CKM matrix element V_{us} (Section 2.4). The sum of all measured strange branching fractions which are listed in Table 2.5 amounts to

$$\mathcal{B}_\mathrm{s} = (2.838 \pm 0.077) \times 10^{-2} \tag{2.35}$$

where a fraction of almost 70% comes from the three most frequent decays $\tau^- \to K^-\nu_\tau$, $\tau^- \to K^-\pi^0\nu_\tau$, $\tau^- \to \pi^-\overline{K}^0\nu_\tau$ which are known with a relative precision of about 3.5%. The first two decays are measured in this analysis. In addition, the branching fractions of the $\tau^- \to K^-(2\pi^0)\nu_\tau$ and $\tau^- \to K^-(3\pi^0)\nu_\tau$ decays are determined in this work. These decays contribute only with the relatively small fraction of 3.3% to $\mathcal{B}_\mathrm{s}$. However, their present relative uncertainties are 40% and 65%, respectively. Thus, a reduction of these uncertainties would lead to an improved knowledge of $\mathcal{B}_\mathrm{s}$.

Recently, the Belle collaboration published a result for the $\tau^- \to K^-\pi^+\pi^-\nu_\tau$ branching fraction which has not yet been taken into account in the world average, and thus has not been included in the above value of $\mathcal{B}_\mathrm{s}$. The current world average for the $\tau^- \to K^-\pi^+\pi^-\nu_\tau$ branching fraction is dominated by the *BABAR* measurement, $\mathcal{B}(\tau^- \to K^-\pi^+\pi^-\nu_\tau) = (0.273 \pm 0.009)\%$ [18]. The new Belle result $\mathcal{B}(\tau^- \to K^-\pi^+\pi^-\nu_\tau) = (0.330 \pm 0.017)\%$ [19] deviates by 3.0σ from the *BABAR* measurement. If the Belle result is taken into account $\mathcal{B}_\mathrm{s} = (2.849 \pm 0.076) \times 10^{-2}$.

2.3.5. Theoretical prediction of the $\tau^- \to K^-\nu_\tau$ branching fraction

The measured branching fraction of the $\tau^- \to K^-\nu_\tau$ decays can be compared with an indirect determination from the branching fraction of the $K^- \to \mu^-\overline{\nu}_\mu$ decay. Assuming τ-μ universality, $\mathcal{B}(\tau^- \to K^-\nu_\tau)$ can be computed from [5]:

$$\begin{aligned}\mathcal{B}(\tau^- \to K^-\nu_\tau)_\mathrm{uni} &= \mathcal{B}(K^- \to \mu^-\overline{\nu}_\mu)\frac{\tau_\tau}{\tau_K}\frac{m_\tau^3}{2m_K m_\mu^2}\left(\frac{1-m_K^2/m_\tau^2}{1-m_\mu^2/m_K^2}\right)^2\delta_{\tau/K} \\ &= (0.717 \pm 0.004)\%,\end{aligned} \tag{2.36}$$

where $\delta_{\tau/K} = 1.00090 \pm 0.0022$ is a radiative correction. The lifetimes, masses, and the $K^- \to \mu^-\overline{\nu}_\mu$ branching fraction are taken from the PDG 2010 publication [4]: $\tau_K = (1.2379 \pm 0.0021) \times 10^{-8}$, $m_K = 493.696 \pm 0.013\,\mathrm{MeV}/c^2$, and $\mathcal{B}(K^- \to \mu^-\overline{\nu}_\mu) = 0.6360 \pm 0.0016$, (the values of the other quantities have been already listed above).

The current world average for $\mathcal{B}(\tau^- \to K^-\nu_\tau)$ (Table 2.5) is 1.4σ smaller than the predicted value.

2.4. The CKM matrix element V_{us}

In this section, various methods to determine the magnitude of the CKM matrix element V_{us} are discussed. A comparison of the $|V_{us}|$ values determined with these methods is presented in Figure 2.4.

2.4.1. $|V_{us}|$ from the unitarity condition of the CKM matrix

The unitarity conditions of the CKM matrix are given in Equation 2.4. The condition which involves $|V_{us}|$ is:

$$|V_{ud}|^2 + |V_{us}|^2 + |V_{ub}|^2 = 1, \tag{2.37}$$

where $|V_{ub}|$ is negligible. From this condition together with the precise value of $|V_{ud}|$ given in Equation 2.8 the most precise value of $|V_{us}|$ can be determined:

$$|V_{us}| = \sqrt{1-|V_{ud}|^2} = 0.2255 \pm 0.0010, \qquad \Delta^{rel} = 0.44\%, \tag{2.38}$$

where $\Delta^{rel} := \Delta|V_{us}|/|V_{us}|$. The uncertainty of this value is indicated by the yellow band in Figure 2.4.

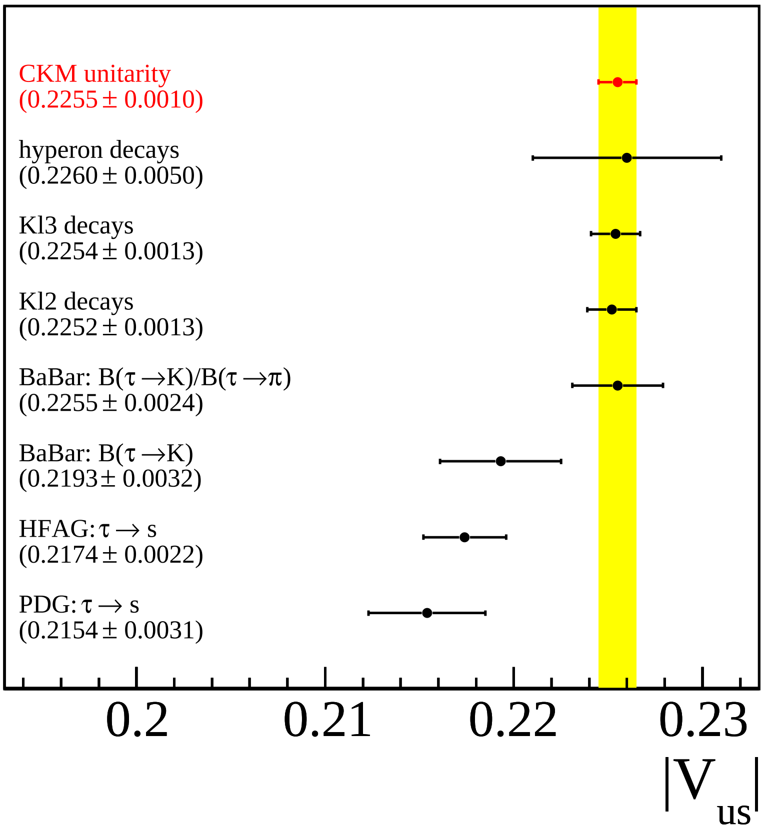

Figure 2.4.: Comparison of different $|V_{us}|$ measurements. $|V_{us}|$ obtained from the unitarity condition of the CKM matrix is shown as red circle. The uncertainty of this result is displayed as the yellow band. The black circles show different $|V_{us}|$ values measured with various methods described in Section 2.4.

2.4.2. $|V_{us}|$ from hyperon decays

The second value of $|V_{us}|$ presented in Figure 2.4 has been obtained in semileptonic hyperon[2] decays. The measured hyperon decay width Γ is related with $|V_{us}|$ through

$$\Gamma \propto |\tilde{f}_1 V_{us}|^2 \tag{2.39}$$

where $\tilde{f}_1$ is a form factor. The uncertainty of the form factor obtained in theoretical calculations dominates the uncertainty of the obtained $|V_{us}|$ value [20]:

$$|V_{us}| = 0.2260 \pm 0.0050, \qquad \Delta^{rel} = 2.2\%. \tag{2.40}$$

This result is consistent with $|V_{us}|$ determined from the unitarity condition of the CKM matrix, but due to the large theoretical uncertainty the result is not competitive with other results presented in Figure 2.4.

---

[2] Hyperons are barions with at least one strange constituent quark, e. g., $\Sigma^-, \Lambda^-, \Xi^0$.

2.4.3. $|V_{us}|$ from semileptonic kaon decays

$|V_{us}|$ can be determined from the semileptonic kaon decays $K \to \pi e^- \overline{\nu}_e$ and $K \to \pi \mu^- \overline{\nu}_\mu$ [9] . Such decays are denoted as $Kl3$ decays where $l = e, \mu$. The width of these decays is given by:

$$\Gamma_{Kl3} = \frac{G_F^2 m_K^5}{192\pi^3} S_{EW}(1 + \delta_K^l + \delta_{SU2}) C^2 |V_{us}|^2 |f_+(0)|^2 I_K^l, \tag{2.41}$$

where G_F is the Fermi constant, m_K is the kaon mass, S_{EW} is a short-distance electroweak radiative correction, δ_K^l is the long-distance QED radiative correction which depends on the lepton type, $f_+^2(0)$ is the form factor at $q^2 = 0$ for the $l\nu$ system, and I_K^l is the phase-space integral, δ_{SU2} and C^2 account for the difference between neutral and charged kaon decays.

Experimentally, the branching fractions of the $Kl3$ decays are measured to obtain

$$|V_{us}| \times |f_+(0)| = 0.2163 \pm 0.0005 \tag{2.42}$$

where the quoted value has been presented in [9]. With the lattice QCD estimate $|f_+(0)| = 0.959 \pm 0.005$ [9], $|V_{us}|$ amounts to

$$|V_{us}| = 0.2254 \pm 0.0013, \qquad \Delta^{rel} = 0.6\%. \tag{2.43}$$

The relative theoretical uncertainty of $|V_{us}|$ coming from the form factor estimate is $\Delta_{th}^{rel} = 0.48\%$. The uncertainty of $|V_{us}|$ from $Kl3$ decays is dominated by the accuracy of theoretical prediction of the from factor.

2.4.4. $|V_{us}|$ from leptonic kaon decays

$|V_{us}|$ can be determined from the ratio of leptonic kaon decays ($K^- \to l^- \overline{\nu}_l$) to leptonic pion decays ($\pi^- \to l^- \overline{\nu}_l$). The decays are called $Kl2$ and $\pi l2$ decays, respectively. The ratio of the corresponding decay widths can be written as

$$\frac{\Gamma_{Kl3}}{\Gamma_{\pi l2}} = \frac{|V_{us}|^2}{|V_{ud}|^2} \frac{f_K^2}{f_\pi^2} \frac{m_K(1 - m_l^2/m_K^2)^2}{m_\pi(1 - m_l^2/m_\pi^2)^2} (1 - \delta_{EM}), \tag{2.44}$$

where f_K/f_π is the ratio of the kaon and pion decay constants, and δ_{EM} is a long-distance QED radiative correction.

Measured leptonic kaon decay branching fractions have been used in [9] to derive the product

$$\frac{|V_{us}|^2}{|V_{ud}|^2} \times \frac{f_K^2}{f_\pi^2} = 0.2758 \pm 0.0005. \tag{2.45}$$

The ratio of decay constants $f_K/f_\pi = 1.193 \pm 0.006$ [9] has been estimated in lattice QCD calculations, and leads to

$$\frac{|V_{us}|^2}{|V_{ud}|^2} = 0.2312 \pm 0.0013. \tag{2.46}$$

With the $|V_{ud}|$ value given in Equation 2.8 this results in

$$|V_{us}| = 0.2252 \pm 0.0013, \qquad \Delta^{rel} = 0.6\%. \tag{2.47}$$

with $\Delta^{rel}_{th} = 0.50\%$. This $|V_{us}|$ value is also consistent with the value derived from CKM unitarity. This method to determine $|V_{us}|$ is limited by the theoretical uncertainty, similarly to $|V_{us}|$ from the semileptonic kaon decays.

2.4.5. $|V_{us}|$ from the $\tau^- \to K^-\nu_\tau$ and $\tau^- \to \pi^-\nu_\tau$ decays

An alternative approach to determine $|V_{us}|$ is to measure the ratio of the $\tau^- \to K^-\nu_\tau$ and $\tau^- \to \pi^-\nu_\tau$ decays which is given by

$$\frac{\Gamma_{\tau^- \to K^-\nu_\tau}}{\Gamma_{\tau^- \to \pi^-\nu_\tau}} = \frac{|V_{us}|^2}{|V_{ud}|^2}\frac{f_K^2}{f_\pi^2}\frac{(1-m_K^2/m_\tau^2)^2}{(1-m_\pi^2/m_\tau^2)^2}(1-\delta_{LD}), \tag{2.48}$$

where δ_{LD} is a long-distance QED correction.

From the experimental point of view this method is complementary to the determination of $|V_{us}|$ from kaon decays. However, the same theoretical uncertainty as for the leptonic kaon decays related to the ratio f_K/f_π has to be considered resulting in $\Delta^{rel}_{th} \approx 0.50\%$. In a recent *BABAR* analysis [7], $|V_{us}|$ has been determined with this method. $f_K/f_\pi = 1.189 \pm 0.007$ [21] has been used to obtain

$$|V_{us}| = 0.2255 \pm 0.0031, \qquad \Delta^{rel} = 1.4\%, \tag{2.49}$$

where the central value is numerically identical to $|V_{us}|$ from the unitarity condition (Equation 2.38), and the uncertainty does not yet reach the precision of the $Kl3$ and $Kl2$ decays.

2.4.6. $|V_{us}|$ from the $\tau^- \to K^-\nu_\tau$ decay

In the same *BABAR* analysis $|V_{us}|$ has also been determined from the relation

$$\mathcal{B}(\tau^- \to K^-\nu_\tau) = \frac{G_F^2 f_K^2 |V_{us}|^2 m_\tau^3 \tau_\tau}{16\pi\hbar}\left(1 - \frac{m_K^2}{m_\tau^2}\right)^2 S_{EW}, \tag{2.50}$$

where τ_τ is the τ lifetime, to

$$|V_{us}| = 0.2193 \pm 0.0032, \qquad \Delta^{rel} = 1.6\%. \tag{2.51}$$

The relative theoretical uncertainty of $|V_{us}|$, $\Delta^{rel}_{th} = 1.27\%$ [22], comes from the uncertainty of the kaon decay constant $f_K = 157 \pm 2\,\text{MeV}$ which is theoretically predicted with a larger uncertainty as the decay constants ratio f_K/f_π. The obtained $|V_{us}|$ value lies within 2σ with respect to $|V_{us}|$ resulting from the unitarity of the CKM matrix. In Chapter 11, this method is used to determine $|V_{us}|$ from the $\mathcal{B}(\tau^- \to K^-\nu_\tau)$ measured in this analysis.

2.4.7. $|V_{us}|$ from inclusive $\tau \to s$ decays

As discussed in Section 2.3.2, $|V_{us}|$ can be determined from the spectral moments measured in hadronic strange τ decays. The smallest theoretical uncertainty of $|V_{us}|$ arises from the first moments which are identical to the hadronic τ decay width ratios R_{ns} and R_{s}. $|V_{us}|$ is therefore determined from

$$|V_{us}| = \sqrt{\frac{R_{\mathrm{s}}}{\frac{R_{\mathrm{ns}}}{|V_{ud}|^2} - \delta_\tau}} \tag{2.52}$$

where $\delta_\tau = 0.240 \pm 0.032$ is a theoretical $SU(3)$-symmetry breaking correction (see also Section 2.3.2) which would vanish if the d and s quarks had the same masses. The theoretical uncertainty of $|V_{us}|$ determined with this method amounts to $\Delta^{rel}_{th} = 0.46\%$, and is of different nature than in all other methods presented in this section. The inclusive character of the ratios R_{ns} and R_{s} has the advantage that the above relation does not depend on form factors and decay constants whose uncertainties dominate the theoretical uncertainties of the other $|V_{us}|$ determination methods. This method is therefore complementary to the $|V_{us}|$ determinations from $Kl3$ and $Kl2$ decays from both the experimental and theoretical point of view.

The strange decay rate R_{s} can be obtained from the sum of exclusive strange τ decay branching fractions divided by the branching fraction of the $\tau^- \to e^-\overline{\nu}_e\nu_\tau$ decay. A list of these decays is given in Table 2.5 with their current world average branching fractions as listed by the PDG [4]. From the sum of the branching fractions one obtains

$$R_{\mathrm{s}} = 0.1590 \pm 0.0043. \tag{2.53}$$

The non-strange decay rate R_{ns} can in principle also be determined by calculating the sum of all non-strange hadronic τ decays. Since R_{ns} amounts to 96% of the hadronic τ decay rate, this has the disadvantage of a relatively large uncertainty on R_{ns}, which enters the uncertainty of $|V_{us}|$, coming from the individual branching fraction measurements. A more convenient way to determine R_{ns} with a minimal uncertainty is to use

$$R_{\mathrm{ns}} = R_{\mathrm{had}} - R_{\mathrm{s}} = 3.4811 \pm 0.0107 \tag{2.54}$$

where $R_{\mathrm{had}} = 3.6401 \pm 0.0098$ is calculated from the precisely known leptonic τ decay branching fractions (see Equation 2.18). The $|V_{us}|$ value calculated from the above rates and δ_τ is

$$|V_{us}| = 0.2154 \pm 0.0031, \qquad \Delta^{rel} = 1.4\%. \tag{2.55}$$

The Heavy Flavor Averaging (HFAG) Tau group has recently presented a slightly larger and more precise value of the strange decay width ratio, $R_{\mathrm{s}}^{\mathrm{HFAG}} = 0.1613 \pm 0.0028$ [23]. This value has been determined in a fit which constrains the sum of the measured branching fractions to one and which not only takes the branching fractions considered in the PDG 2010 publication [4] into account, but includes in addition recent results of the B Factories (some of them being preliminary). Moreover, correlations between different results are accounted for in the fit. The resulting value of $|V_{us}|$ is

$$|V_{us}|_{\text{HFAG}} = 0.2174 \pm 0.0022, \qquad \Delta^{rel} = 1.0\%. \tag{2.56}$$

Both $|V_{us}|$ values are smaller than the $|V_{us}|$ value predicted by CKM unitarity by more than 3σ. The observed deviation is lively discussed in the τ-physics community. In principle, four different origins for the deviation are possible:

1. The magnitude of the CKM matrix element V_{ud}.
   The most precise value of $|V_{ud}|$ (Equation 2.8), which is used for the determination of $|V_{us}|$, comes from the measurements of superallowed beta decays in various nuclei. The experimental uncertainty is very small, since $|V_{ud}|$ is determined in various precise measurements with different nuclei. Theoretical input to the $|V_{ud}|$ determination was so far found to be in agreement with experimental tests [24].

2. The theoretical correction δ_τ.
   As has been already mentioned in Section 2.3.2, δ_τ is subject to various theoretical investigations. However, due to the small size of δ_τ with respect to the ratio $R_{\text{ns}}/|V_{ud}|^2$ even large changes of δ_τ (even doubling the correction) cannot fully account for the observed deviation.

3. Experimental result for R_{s}.
   The measured value of R_{s} might be too small. This can be either due to underestimated branching fractions or to missing modes of strange τ decays. Therefore, the investigation of previously measured decays and not yet measured decays by the B factories could potentially resolve the $|V_{us}|$ puzzle. This thesis is part of the current efforts to improve the accuracy of R_{s}.

4. New physics.
   In principle, a deviation from the unitarity condition of the CKM matrix might be a hint for new physics. However, with the current experimental status, studies are not yet focused on this possibility.

3. The *BABAR* experiment

The *BABAR* experiments [25] was operated at the *Positron Electron Project* (PEP-II) e^+e^- collider [26] of the SLAC National Accelerator Laboratory in California. It was primarily designed to provide optimal conditions for studies of B mesons. During the data taking period from October 1999 to April 2008, *BABAR* recorded a large dataset corresponding to an integrated luminosity of $\mathcal{L} = 531.43\,\mathrm{fb}^{-1}$ [27]. About 80% of the data was taken at a center-of-mass energy slightly above the B meson production threshold. The cross section for B-meson pair production at this energy is $\sigma_{BB} = 1.05\,\mathrm{nb}$ [28], i. e., about 560×10^6 B-meson pairs were recorded. The *BABAR* collaboration successfully carried out a huge number of different B-meson decay analyses. In particular, the existence of CP violation in B decays was confirmed.

Due to a τ-pair production cross section, $\sigma_{\tau\tau} = 0.919\,\mathrm{nb}$ [29], which is almost as large as σ_{BB}, the *BABAR* dataset also contains almost 490×10^6 τ-lepton pairs which are exploited in this analysis.

This chapter gives an overview of the *BABAR* experiment. In the first section, the PEP-II collider is briefly described, than the design of the major components of the *BABAR* detector is summarized. If not mentioned otherwise, the information is taken from [25]. In the last section, the dataset as well as the simulated event sample exploited in this analysis are presented.

3.1. The PEP-II collider

The PEP-II e^+e^- collider [26] with a circumference of 2.2 km consist of two storage rings, the High Energy Ring (HER) and the Low Energy Ring (LER), which makes it possible to store electrons and positrons with different energies. Electrons and positrons are accelerated in the linear accelerator (Linac), injected into the storage rings, and brought to collision in the interaction region within the *BABAR* detector. PEP-II was designed to provide a luminosity of $3 \times 10^{33}\,\mathrm{cm}^{-1}\,\mathrm{s}^{-1}$. Significantly larger luminosities were achieved over the years with a peak luminosity of $12 \times 10^{33}\,\mathrm{cm}^{-1}\,\mathrm{s}^{-1}$ [30]. A schematic view of the PEP-II facility is shown in Figure 3.1.

The main part of the data delivered by PEP-II was produced in collisions of electrons with an energy of 9.0 GeV and positrons with an energy of 3.1 GeV resulting in a center-of-mass energy of 10.85 GeV. This energy corresponds to the mass of the $\Upsilon(4S)$ resonance decaying with a branching fraction of $\approx 96\%$ into B-meson pairs. Due to the asymmetric beam energies the $\Upsilon(4S)$ is boosted with $\beta\gamma = 0.56$. A fraction of $\approx 10\%$ of the data was taken 40 MeV below the $\Upsilon(4S)$ resonance. This dataset was mainly intended for studies of background processes for the B-meson measurements. The reduced center-of-mass energy does not affect $e^+e^- \to \tau^+\tau^-$ events. Therefore, this data

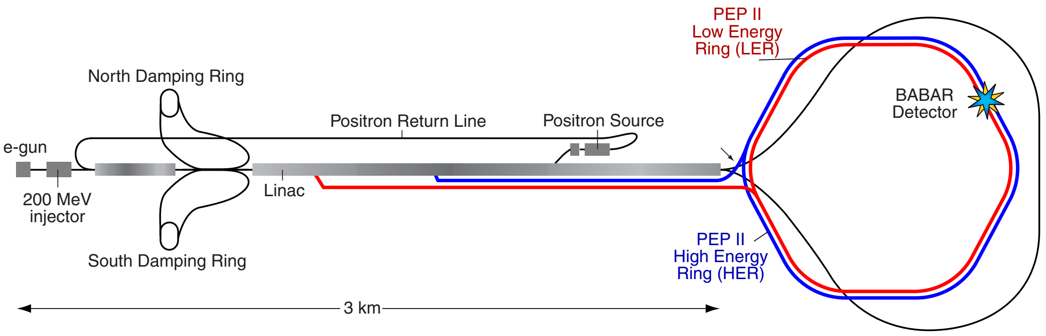

Figure 3.1.: Schematic view of the linear accelerator (Linac) and the PEP-II collider with the two individual storage rings. The high energy ring (HER) is shown in blue, and the low energy ring (LER) in red. The location of the *BABAR* detector at the beam-crossing point is marked with the star. The image is taken from [31]

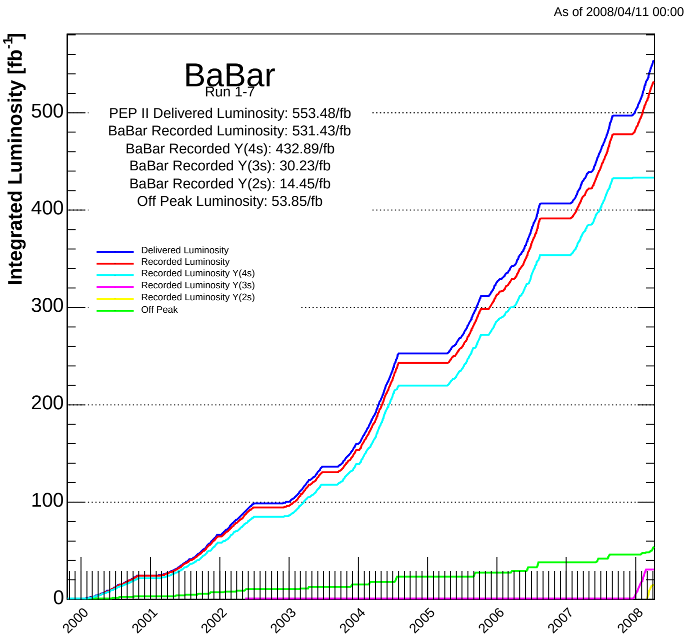

Figure 3.2.: Integrated luminosity as a function of the *BABAR* operation time. The different curves show the integrated luminosity delivered by PEP-II (blue) and the total luminosity recorded by *BABAR* (red). The curves with other colors show the integrated luminosities recorded at different center-of-mass energies. The image is taken from [27].

sample is also used in τ decay studies. The total *BABAR* dataset was divided according to the data taking periods with constant experimental conditions into six *runs*. In the last year of operation, an additional run (run 7) was performed at center-of-mass energies corresponding to the $\Upsilon(2S)$ and $\Upsilon(3S)$ resonances. Figure 3.2 shows the recorded integrated luminosity as a function of the operation time of the *BABAR* experiment.

3.2. The *BABAR* detector

The *BABAR* detector was located at the crossing of the electron and positron beams of PEP-II. Due to the asymmetric beam energies, the particles produced in the e^+e^- collisions were boosted in *forward* direction, i. e., in the flight direction of the e^-. Therefore, the detector was not symmetric. Figure 3.3 shows a schematic view of the detector along the beam line. The beam interaction point, IP, is shifted in the backward direction with respect to the geometrical center, ℄ , of the detector, which leads to a larger acceptance region of the detector in forward direction. The coverage is further increased by the asymmetric design of some of the subdetectors. The two innermost subdetectors are the silicon vertex tracker (SVT) and the drift chamber (DCH) used for the reconstruction of charged particle trajectories. The next subdetector is the Cherenkov detector (DIRC) which is the most important charged particle identification device. It is surrounded by the crystal electromagnetic calorimeter (EMC). These inner detector components are located within a superconducting magnet coil which provides a 1.5 T magnetic field parallel to the beam direction. The outermost component is the instrumented flux return (IFR) used to identify muons. In the following, the subdetectors are described in more detail.

3.2.1. Silicon vertex tracker

The silicon vertex tracker is the innermost detector component of the *BABAR* detector. It is used together with the drift chamber to reconstruct the trajectories of charged particles which are curved due to the magnetic field. From the measured curvature the particle momentum can be derived. Both detector components also contribute to the identification of charged particles through the measurement of the specific energy loss dE/dx.

The SVT is in particular designed for the reconstruction of secondary vertices in particle decays near the interaction point, and to reconstruct the angles of the charged particles. It is located as close as possible to the water-cooled beryllium beam pipe which has an outer radius of 27.9 mm. The SVT covers a polar angle of 20°–150° with respect to the beam line. It is composed of five radially arranged layers of double-sided silicon strip detectors with 150×10^3 readout channels in total. Each layer consists of overlapping modules to provide a full azimuthal coverage. The strip detectors on the inner side of a layer are arranged in parallel to the beam line to measure the azimuth coordinate of the particle trajectories. The outer strip detectors are orthogonal to the beam axis and thus measure the trajectory position along the z-axis (defined as the tangent to the IP along the beam line). The innermost layer has a radius of 32 mm,

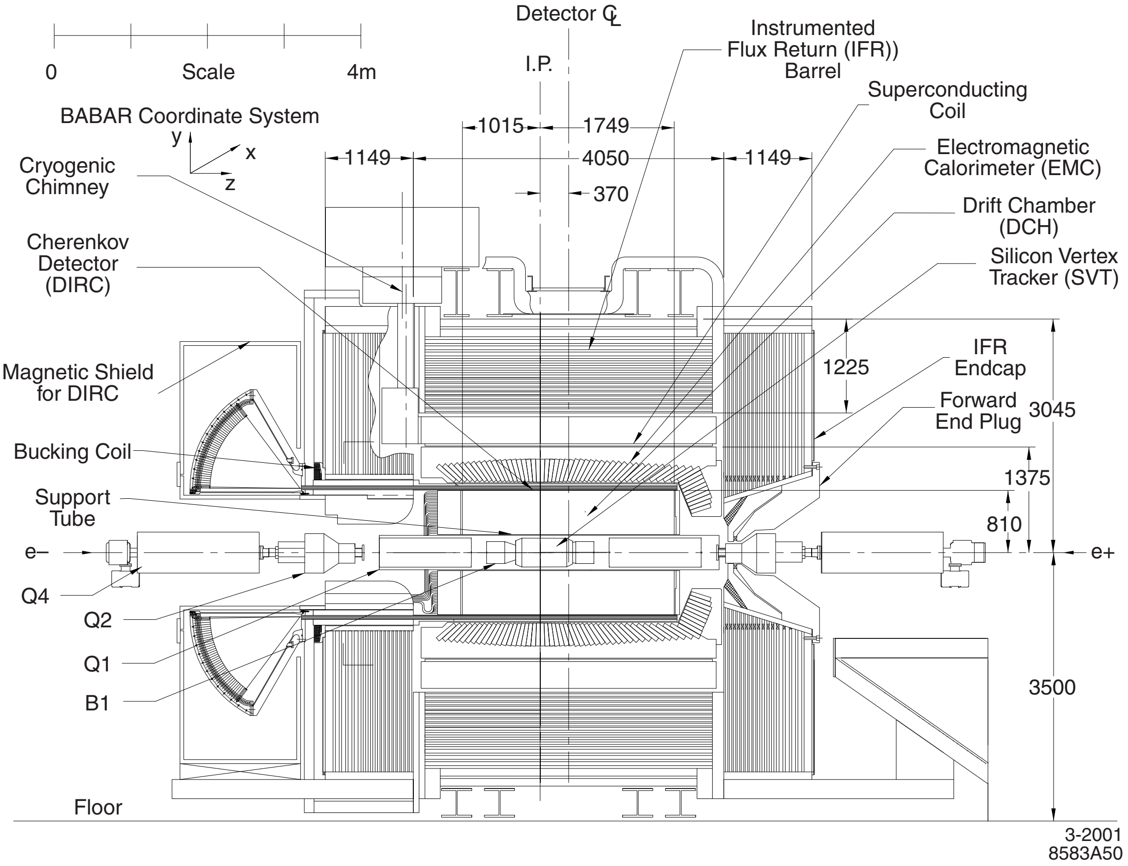

Figure 3.3.: Schematic longitudinal view of the *BABAR* detector. All major detector components are shown. The direction of the electron beam is from left to right in the figure, and is denoted as the *forward* direction. The direction of the positron beam is called the *backward* direction. The particles collide in the interaction point (IP), which is shifted with respect to the geometrical center, ℄, of the detector. The dimensions are given in mm. The image is taken from [25]

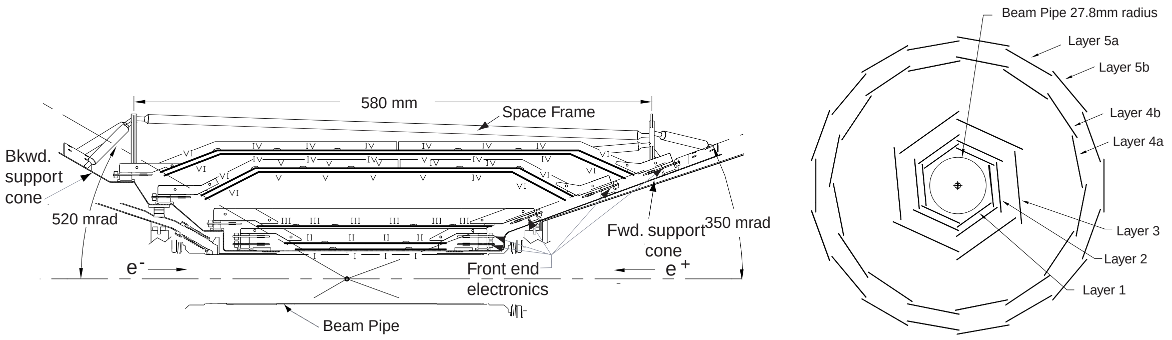

(a) Longitudinal view. **(b)** Radial view.

Figure 3.4.: Schematic view of the silicon vertex tracker (SVT). (a) shows a longitudinal view. The roman numbers denote different types of silicon strip sensors. (b) shows the radial view of the 5 layers centered around the beam pipe. The images are taken from [25].

the next two layers are close to the first. Layer 4 and 5 have a larger distance to the beam pipe with an outer radius of 144 μm. The SVT is surrounded by the ≈ 4.5 m long support tube which permeates the *BABAR* detector.

The SVT was designed to provide a minimum trajectory reconstruction efficiency of 70% for particles with transverse momenta down to 50 MeV/c. The minimum spacial resolution was required to be ≈ 100 μm in plane perpendicular to the beam line, and 80 μm in in z-direction. These design goals were achieved.

3.2.2. Drift chamber

The drift chamber is the second tracking device. It is predominantly used for the reconstruction of the curvature of the particle trajectories, and thus for the measurement of the particle momenta. In addition, the DCH is used for the identification of charged particles with momenta below 700 MeV/c through the measurement of the specific energy loss dE/dx.

The cylindrical DCH is a multi-wire proportional chamber with 7104 readout channels in total. It is almost 3 m long with an inner radius of 23.6 cm and an outer radius of 80.9 cm. The DCH covers an polar angle region between 17.2° and 152.6°. It consists of 40 radial layers of hexagonal cells filled with a helium-isobutane (80:20) gas mixture. To provide a longitudinal position measurement, 24 of the layers are tilted with a small angle with respect to the other layers. For particles with a transverse momentum larger than 180 MeV/c, 40 separate spatial and dE/dx measurements are possible, due to the 40 layers.

For particles with momenta below 750 MeV/c a dE/dx resolution of 7.5% is achieved. The spatial resolution as a function of the transverse momentum, p_T, is parametrized as

$$\frac{\sigma_{p_T}}{p_T} = (0.13 \pm 0.01)\% \cdot p_T[\,\mathrm{GeV}/c] + (0.45 \pm 0.03)\%. \tag{3.1}$$

The achieved spatial resolution in longitudinal direction is ≈ 1 mm.

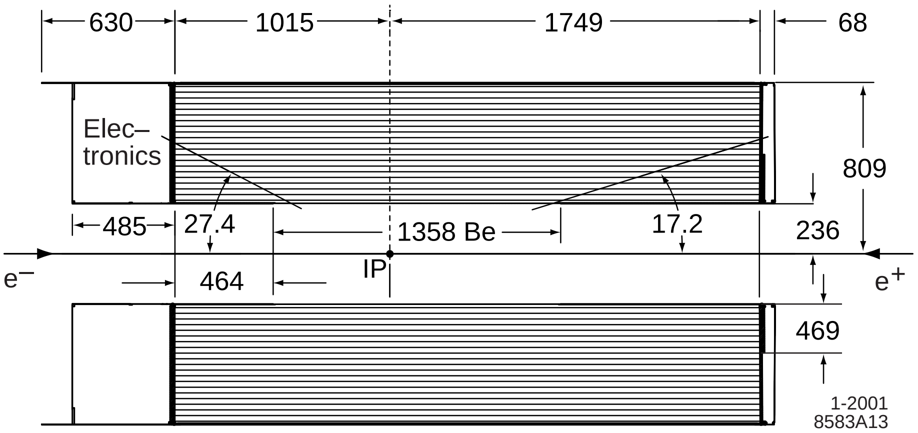

Figure 3.5.: Schematic longitudinal view of the drift chamber DCH. The vertical hashing indicated the orientation of the wires. The dimensions are given in mm. The image is taken from [25].

3.2.3. Detector of internally reflected Cherenkov light

The detector of internally reflected Cherenkov light is a ring-imagining Cherenkov detector (Figure 3.6a). It is the main particle identification device and is designed to provide a $\approx 4\sigma$ separation of charged pions and kaons with momenta between 0.7–4.2 GeV/c, where the upper bound is close to the kinematic limit.

A special geometrical design was chosen for the DIRC to reduce the amount of material in front of the electromagnetic calorimeter. This requirement was necessary to minimize a degradation of the EMC energy resolution resulting from electromagnetic showers already induced in the DIRC and thus not being fully contained in the EMC. In addition, a thin DIRC was required to minimize the inner radius, and thus the volume, of the electromagnetic calorimeter, leading to a reduction of the cost for the EMC crystals.

The active part of the DIRC consists of 144 bars with a 17×35 mm rectangular cross section and a length of 4.9 m which are made of synthetic, fused silica with a mean refractive index n = 1.473. The bars are arranged in 12 bar boxes resulting in a duodecagonal shape of the DIRC barrel. The radial view of a bar box is shown in Figure 3.6b. The total thickness (in radial direction) including support structures is 8 cm which corresponds to 0.17 radiation lengths at normal incidence. The DIRC readout, i. e., the standoff box filled with about 6000 l of purified water and instrumented with 10572 photomultiplier tubes, is located at the rear end of the *BABAR* detector, i. e., in the direction opposite to the boost in the e^+e^- collisions.

The working principle of the DIRC is shown in Figure 3.7. A charged particle traversing a DIRC bar with the velocity $\beta = v/c \leq \frac{1}{n}$ (where n is the refractive index of the material) emits Cherenkov light under the Cherenkov angle θ_C given by

$$\cos\theta_C = \frac{1}{n}\sqrt{1 + \left(\frac{m}{p}\right)^2} = \frac{1}{\beta n} \tag{3.2}$$

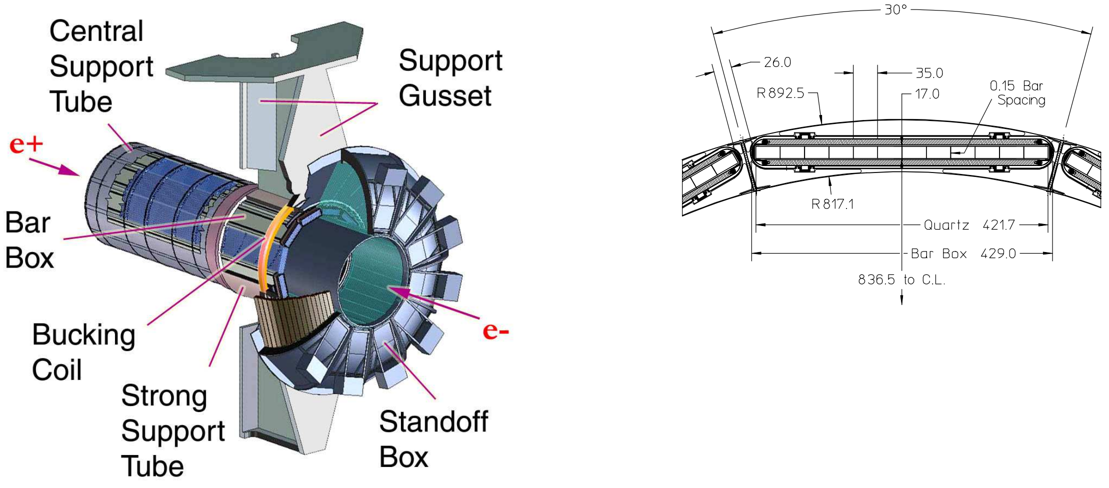

(a) Schematic view of the DIRC **(b)** Schematic view of a DIRC bar box

Figure 3.6.: (a) shows an illustration of the DIRC. Besides the 12 bar boxes arranged in a polygonal barrel, the standoff box containing the readout devices and support structures are shown. (b) shows the cross section of a bar box which consists of 12 individual quartz bars. The dimensions are given in mm. The images are taken from [25].

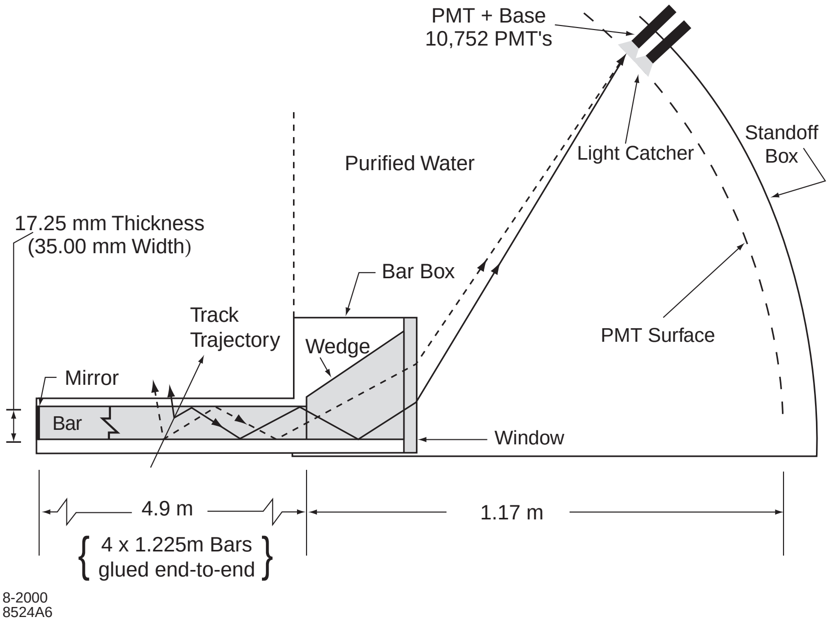

Figure 3.7.: Illustration of the DIRC working principle. A charged particle which traverses the DIRC bar is indicated by the arrow. The paths of the emitted Cherenkov photons are indicated by the dashed and solid lines. The image is taken from [25].

The emitted Cherenkov photons are trapped by internal reflection and transported to the rear or forward end of the bar. In the latter case, mirrors assembled at the forward end are used to direct the Cherenkov photons to the readout devices, which are located only at the rear end. At this end of the DIRC bar, the Cherenkov photons enter the standoff box and propagate to the photomulipliers mounted at the rear of the box.

The internal reflection preserves the original Cherenkov angle. It can be therefore reconstructed, up to an 16-fold ambiguity which arises from the DIRC geometry, from the coordinates of the detected photons, i. e., from the position of the responsive photomultiplier, and from the angle and position of the intersection of the charged particle with the DIRC bar. The latter are extrapolated from the trajectory measured in the tracking devices. The ambiguities arise from the different possible path's of the Cherenkov photons through the DIRC bar. For example, the photons can either propagate directly to the rear end of a bar, or first propagate to the mirrors at the front end. Since the DIRC also provides time information with a measured resolution of 1.7 ns, the ambiguities can be resolved by comparing the expected and the measured arrival time of the Cherenkov photons in the photomultipliers. The time information is also used to improve the assignment of detected Cherenkov photons to the correct charged particle in the event, and to reduce beam background.

3.2.4. The electromagnetic calorimeter

The electromagnetic calorimeter has been designed to measure the energy, the position, and the transverse shape of electromagnetic showers. It is also used to obtain information from the energy deposited by muons and hadrons.

It was built from 6580 crystals of thallium-doped cesium iodide (CsI(Tl)) with a high light yield ($50000\gamma/\,\mathrm{MeV}$) short radiation length (1.85 cm) and a small Molière radius (3.8 cm). These material allows for a high energy and angular resolution, fully contained showers, and a compact design of the EMC. The length of the crystals varies between 29.6 cm and 32.4 cm which corresponds to an electromagnetic interaction length ranging from $16.0X_0$ to $17.5X_0$. The area of the crystal front face is $4.7 \times 4.7\,\mathrm{cm}^2$, while the area of the back face is $6.1 \times 6.0\,\mathrm{cm}^2$. The crystals are readout by silicon photodiodes mounted at the back face which operate well within the 1.5 T magnetic field.

Figure 3.8 shows the longitudinal cross section of the upper half of the EMC. Due to the boosted center-of-mass system, the EMC is asymmetric in z-direction. It consists of two main sections, the barrel and the endcap. The cylindrical barrel, which has an inner radius of 91 cm and which covers the polar angle region $29.9^\circ < \theta < 140.8^\circ$ consists of 48 rings, each containing 120 crystals. The conic endcap ($15.8^\circ < \theta < 26.9^\circ$) has 8 rings with a decreasing number of crystals with the ring radius.

In general, an electromagnetic shower induced by a particle interacting with the EMC material extends over several crystals, i. e., the energy of the particle is deposited in a group of neighboring crystals. Such a group is called a cluster. The cluster reconstruction algorithm is described in detail in [25] and is summarized in Section 8.1. The particle energy, E, is reconstructed by adding the energies deposited in the individual crystals contained in the cluster, and the intersection point of the particle with the calorimeter is determined by the position of the cluster centroid. The achieved energy

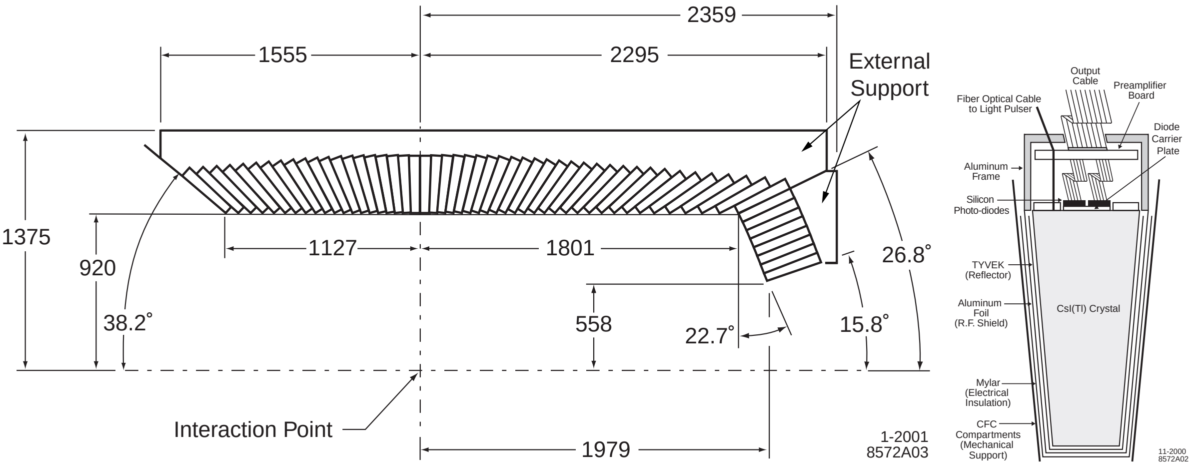

(a) Longitudinal view of the upper EMC half. **(b)** Crystal

Figure 3.8.: In (a) a schematic longitudinal view of the upper half of the electromagnetic calorimeter (EMC) is shown. The EMC consists of 56 crystal rings. (b) shows an individual crystal with the readout electronics. The dimensions are given in mm and °. The images are taken from [25].

resolution, σ_E can be parametrized by

$$\frac{\sigma_E}{E} = \frac{(2.32 \pm 0.30)\%}{\sqrt[4]{E(\,\mathrm{GeV})}} \oplus (1.85 \pm 0.12)\% \tag{3.3}$$

where the terms are added in quadrature. The angular resolution is equal for both the polar angle θ and the azimuthal angle ϕ. It is parametrized by

$$\sigma_\theta = \sigma_\phi = \left(\frac{3.87 \pm 0.07}{\sqrt{E(\,\mathrm{GeV})}} + 0.00 \pm 0.004 \right) \mathrm{mrad}. \tag{3.4}$$

3.2.5. Magnet coil and instrumented flux return

All inner detector components described so far are surrounded by the super-conducting magnet coil with a weight of 6.5 t, an inner radius of 1.40 m and an outer radius of 1.73 m. It creates a 1.5 T magnetic field which is parallel to the beam line. The iron flux return of the magnet is the outermost detector component. It is designed for the detection of muons, and neutral long-lived hadrons like the K_L^0.

An schematic view of the IFR is shown in Figure 3.9. It consists of three major parts, the barrel and the forward and backward end doors. The barrel consists of 19 radially-arranged iron layers, while the end doors have 18 layers each oriented perpendicular to the beam line. The thickness of the layers increases from 2 cm for the inner layers to 10 cm for the outermost layer. The gaps between the layers were instrumented with resistive plate chambers (RPC's) during the data taking periods (runs) 1–4. Due to significantly degrading performance the RPC were replaced by limited streamer tubes (LST) for the remaining operation time of the BABAR detector.

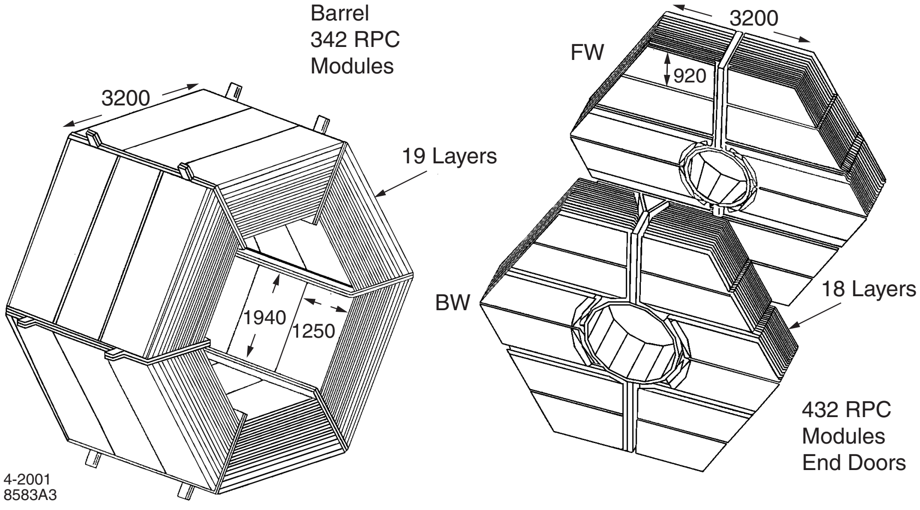

Figure 3.9.: Schematic view of the instrumented flux return (IFR). The barrel section is shown on the left. The two end doors are displayed on the right. The resistive plate champers (RPC) were replaced by limited streamer tubes (LST) after the fourth data taking period. The dimensions are given in mm. The image is taken from [25].

3.3. The data sample

3.3.1. Data sample

In this analysis, two *BABAR* datasets recorded at different energies are used. The first dataset was recorded at the $\Upsilon(4S)$ resonance (OnPeak), i. e., at a center-of-mass energy of 10.58 GeV. The second dataset which corresponds to about 10% of the total dataset, was recorded 40 MeV below the $\Upsilon(4S)$ (OffPeak). The average τ-pair cross section for the two samples is $\sigma_{\tau\tau} = (0.919 \pm 0.003)\,\mathrm{nb}$ [29]. No distinction is made between the two datasets. The total dataset used in this analysis corresponds to an integrated luminosity[1] of

$$\mathcal{L} = 473.9\,\mathrm{fb}^{-1}. \tag{3.5}$$

The integrated luminosity recorded during each run is listed in Table 3.1.

3.3.2. Simulated event sample

Monte Carlo simulated events are used in this analysis to develop selection criteria, and to determine selection efficiencies of signal and background events. Exactly the same selection criteria are applied to simulated events as to the data events. This includes the trigger requirements, all (loose) preselection criteria for τ-pairs, and the criteria specific to the signal decays selected in this analysis. The following processes are considered:

---

[1] The integrated luminosity is determined from the measurement of the number of $e^+e^- \to e^+e^-$, $e^+e^- \to \mu^+\mu^-$, and two-photon events [32].

Table 3.1.: Integrated lumiminosity of the dataset used in this analysis for each run, and separately for the OnPeak and OffPeak datasets.

Run	$\mathcal{L}_{\text{OnPeak}}\ [\text{fb}^{-1}]$	$\mathcal{L}_{\text{OffPeak}}\ [\text{fb}^{-1}]$
1	20.6	2.6
2	62.1	7.0
3	32.9	2.5
4	100.8	10.2
5	133.9	14.5
6	79.0	7.9
Total	429.1	44.8

$$\begin{aligned} &e^+e^- \to \tau^+\tau^- \\ &e^+e^- \to \mu^+\mu^- \\ &e^+e^- \to q\overline{q} \quad \text{with} \quad q = u, d, s, c, b. \end{aligned} \tag{3.6}$$

The first two processes are generated with `kk2f` [33]. τ decays are described by the `TAUOLA` library [34]. The branching fractions of τ decays implemented in `TAUOLA` are the world averages of 2002. These branching fractions are reweighted within this analysis to the current world averages taken from PDG 2010 [4]. All $e^+e^- \to q\overline{q}$ processes are generated with `EvtGen` [35]. The interaction of the generated particles with the detector is simulated with `GEANT4` [36].

Bhabha events, i. e., $e^+e^- \to e^+e^-$ events, are an important background in this analysis. Due to the very large cross section of $\approx 40\,\text{nb}$ [28], it is difficult to generate the appropriate number of events to account for rare topologies which possibly could mimic the signal decays. Instead of simulating these events special care is taken to suppress all Bhabha events from the selection.

Simulated events are produced by taking the detector conditions at a given time into account. All simulated events are overlaid with randomly triggered events with no physics content. Such events do only contain the beam background and detector noise as present at the given time. Thus, samples of simulated events are available for the different runs. In the branching fraction measurement presented in this thesis, the numbers of generated events are scaled to match the integrated data luminosity separately for each run. Table 3.2 lists the numbers of generated events for each process and for each run. In addition, the cross sections of the considered processes are listed.

The $e^+e^- \to \tau^+\tau^-$ sample generated as described above is denoted as the *generic* τ sample. It does not contain τ decays which have small branching fractions with large uncertainties. To also take this decays into account in this analysis, so called *dedicated* τ decay samples have been generated (Table 3.3). In such a dedicated sample one of the two τ's decays in the considered channel, while the other τ decays according to the `TAUOLA` implementation. The dedicated decay samples are generated in dependence of

Table 3.2.: Cross sections and numbers of generated events for the different run. The uncertainty of the cross sections of the $e^+e^- \to q\overline{q}$ processes is not listed in the table, because the fraction of these processed selected in this analysis is very small, i. e., the uncertainty can be neglected.

$e^-e^- \to$	$\tau^+\tau^-$	$\mu^+\mu^-$	$u\overline{u}$,$d\overline{d}$,$s\overline{s}$	$c\overline{c}$	$b\overline{b}$
σ [nb]	0.919 ± 0.003	1.147 ± 0.004	2.09	1.30	1.05
Run	N [$\times 10^6$]	N [$\times 10^6$]	N [$\times 10^6$]	N [$\times 10^6$]	N [$\times 10^6$]
1	64.6	46.2	160.5	55.2	69.7
2	163.3	136.0	473.2	164.7	109.7
3	59.2	76.0	275.9	88.3	113.9
4	180.0	121.6	416.1	267.3	336.6
5	237.1	153.5	514.3	344.2	431.0
6	139.2	94.1	327.0	208.6	265.5

Table 3.3.: Branching fractions [4] and numbers of generated signal and background τ decays which are not included in the generic τ-pair sample. This samples are denoted as *dedicated* simulated samples. (*) The branching fraction of the $\tau^- \to \pi^-(4\pi^0)\nu_\tau$ decay has not been measured yet. The given number is the $\tau^- \to h^-(4\pi^0)\nu_\tau$ branching fraction.

Decay	$\mathcal{B}$ [$\times 10^{-4}$]	Generated events [$\times 10^3$]
$\tau^- \to K^-(3\pi^0)\nu_\tau$	3.7 ± 2.4	8004
$\tau^- \to \pi^-(4\pi^0)\nu_\tau$	11.2 ± 5.1*	8010
$\tau^- \to \pi^-\eta\pi^0\pi^0\nu_\tau$	1.5 ± 0.5	844
$\tau^- \to K^-\eta\nu_\tau$	1.61 ± 0.10	8311
$\tau^- \to K^-\eta\pi^0\nu_\tau$	0.48 ± 0.12	723
$\tau^- \to \pi^-\overline{K}^0\eta\nu_\tau$	0.93 ± 0.15	706

the detector conditions in the same way as the generic sample. In Table 3.3 the total number of the generated events in a dedicated sample, i. e., the sum for the runs 1–6, is listed.

4. Analysis overview

This section provides an overview of the strategy of the measurement. The different steps of the analysis chain are described in detail in the following chapters.

4.1. Goal of the measurement

The goal of the analysis is the measurement of the branching fractions of the decays

$$\begin{aligned}
&\tau^- \to \pi^-(3\pi^0)\nu_\tau \\
&\tau^- \to \pi^-(4\pi^0)\nu_\tau \\
&\tau^- \to K^-\nu_\tau \\
&\tau^- \to K^-\pi^0\nu_\tau \\
&\tau^- \to K^-(2\pi^0)\nu_\tau \\
&\tau^- \to K^-(3\pi^0)\nu_\tau,
\end{aligned} \tag{4.1}$$

which are denoted as signal decays in the following.

4.2. Additional control decay modes

In addition to the above signal modes the following τ control modes are used to develop selection criteria for the signal decays, and to derive corrections to be applied to the simulation:

$$\begin{aligned}
&\tau^- \to \pi^-\nu_\tau \\
&\tau^- \to \pi^-\pi^0\nu_\tau \\
&\tau^- \to \pi^-(2\pi^0)\nu_\tau \\
&\tau^- \to \mu^-\overline{\nu}_\mu\nu_\tau.
\end{aligned} \tag{4.2}$$

The numbers of selected events in the control samples are about 10–100 times larger than the numbers of selected signal events due to the relatively large branching fractions [4] of the control decays:

$$\begin{aligned}
\mathcal{B}(\tau^- \to \pi^-\nu_\tau) &= (10.83 \pm 0.11)\% \\
\mathcal{B}(\tau^- \to \pi^-\pi^0\nu_\tau) &= (25.46 \pm 0.12)\% \\
\mathcal{B}(\tau^- \to \pi^-(2\pi^0)\nu_\tau) &= (9.24 \pm 0.12)\% \\
\mathcal{B}(\tau^- \to \mu^-\overline{\nu}_\mu\nu_\tau) &= (17.33 \pm 0.05)\%.
\end{aligned} \tag{4.3}$$

The control decays have very similar properties as the signal decays. All control and signal decays have one charged particle in the final state. The only difference between the control decays $\tau^- \to \pi^-(n\pi^0)\nu_\tau$ and the signal decays $\tau^- \to K^-(n\pi^0)\nu_\tau$ with $n = 0, 1, 2$ is the charged particle type. Therefore, the majority of the selection criteria can be directly transfered from the control decays to the signal decays. The $\tau^- \to \pi^-\pi^0\nu_\tau$ and $\tau^- \to \pi^-(2\pi^0)\nu_\tau$ modes are used to develop the selection criteria related to neutral pions. The branching fraction of each of the control decays is determined and compared with the precisely known world average [4] to validate the analysis.

4.3. Event selection

The first step of the analysis is the selection of $e^+e^- \to \tau^+\tau^-$ events.

In contrast to $e^+e^- \to q\overline{q}$ events, this type of events is characterized by low particle multiplicity and a jet-like topology. These properties are used to suppress quark-pair events. In addition, $e^+e^- \to \tau^+\tau^-$ events contain at least two neutrinos which cannot be directly reconstructed in the detector. The missing momentum from the neutrinos can be used to distinguish τ-pair events from $e^+e^- \to \ell^+\ell^-$ events with $\ell = e, \mu$, whose kinematics are fully determined by the measurement of the two charged leptons in the final state. Topological event properties are also used to suppress two-photon processes.

In the next step signal decays are selected from the $e^+e^- \to \tau^+\tau^-$ event sample by applying a so-called *lepton tag*. One of the two τ's is required to decay into a charged lepton, i. e., an electron or a muon, and two neutrinos. Any other reconstructed particle is then associated with the decay of the other τ in the event. Since all signal decays contain one charged particle, the application of a lepton tag results in exactly two charged particles reconstructed per event.

The decays measured in this analysis contain different numbers of π^0's. Neutral pions cannot be detected directly in the *BABAR* detector. They are reconstructed in the mode $\pi^0 \to \gamma\gamma$ ($\mathcal{B}(\pi^0 \to \gamma\gamma) \approx 99\%$) from the two photons which are detected in the calorimeter.

Signal decay modes with the same number of π^0's can only be discriminated by the type of the charged particle. A good performance of the pion and kaon identification is therefore crucial for this analysis.

The event selection is finalized by removing remaining background events from the selected signal samples with appropriate requirements which are specific for the considered signal mode.

4.4. Corrections of the simulation

The reconstruction and identification efficiencies for the final-state particles of the τ decays are determined from the Monte Carlo simulation. Thus a good description of the data by the simulation is very important. However, it is known that the simulated event samples do not model some characteristics of the data with a precision that is sufficient for this analysis. The development of correction methods to improve the simulation is a major challenge in this analysis.

4.4.1. Charged particle identification corrections

For the presented measurement it is necessary to determine for each reconstructed track if it is created by an electron, muon, kaon or pion. This particle identification (PID) is performed with selection tools (PID selectors) provided by the *BABAR* collaboration. It is known that the selection efficiency for these tools is different for data and simulation. The *BABAR* PID Group provides correction factors for each PID selector to be applied to the simulated events. In this analysis, however, an independent determination of correction factors has been performed for the pion and kaon identification using τ control samples to achieve the necessary precision. As further control samples the decays

$$\begin{aligned}\tau^- &\to \pi^-\pi^+\pi^-\nu_\tau,\\ \tau^- &\to \pi^- K^+ K^- \nu_\tau\end{aligned} \tag{4.4}$$

are used.

4.4.2. Correction of hadronic split-offs

Separated neutrons from hadronic showers in the calorimeter can be the source of spurious photons, so-called split-offs. The amount of wrongly identified photons from split-offs is not well modeled in the simulation. The differences between data and simulation are studied using

$$\begin{aligned}\tau^- &\to \mu^-\overline{\nu}_\mu\nu_\tau,\\ \tau^- &\to \pi^-\nu_\tau,\end{aligned} \tag{4.5}$$

decays and are corrected.

4.4.3. π^0 reconstruction efficiency correction

The signal decays contain up to four π^0's. The uncertainty of the π^0 reconstruction efficiency is one of the dominant uncertainties of the branching fraction measurement. The discrepancy between data and simulation has been so far corrected within the *BABAR* collaboration by using a correction factor of $(-2 \pm 3)\%$ [37] for each π^0. A systematic uncertainty of 3% per π^0 is large compared to other systematic effects in this analysis and would dominate the uncertainty of this measurement. The following decays are used to determine a π^0 correction factor with a significantly smaller uncertainty:

$$\begin{aligned}\tau^- &\to t^-\nu_\tau,\\ \tau^- &\to t^-\pi^0\nu_\tau,\end{aligned} \tag{4.6}$$

where t denotes a charged particle whose track has been reconstructed and which fails the electron identification criteria. It is important that t is not explicitly identified as a muon, pion, or kaon.

4.5. Determination of the branching fractions

To account for signal decays that have been wrongly reconstructed in one of the other signal modes (*signal cross-feed*) a simultaneous determination of all signal branching fractions is performed. The branching fractions are determined with a migration-matrix technique [10] which takes the migration of selected events from one mode to another into account.

The fraction of background events in a selected signal event sample is estimated using Monte Carlo simulation and is subtracted from the data.

4.6. Determination of $|V_{us}|$

The magnitude of the Cabibbo-Kobayashi-Maskawa matrix element V_{us} is determined from the measured $\tau^- \to K^-\nu_\tau$ branching fraction combined with a lattice QCD calculation of the kaon decay constant.

$|V_{us}|$ is also determined from the total branching fraction, $\mathcal{B}_{\mathrm{s}}$, of exclusive τ decays into final-states with strangeness $|S| = 1$. The signal decays measured in this analysis with kaons in the final-state contribute to $\mathcal{B}_{\mathrm{s}}$. For each strange signal decay an average branching fraction is calculated by averaging the result obtained in this analysis with previously published results by the *BABAR* collaboration and with results from other experiments. The resulting average branching fractions are then used to update $\mathcal{B}_{\mathrm{s}}$ and to calculate a new value of $|V_{us}|$.

5. Particle Selection

In this analysis four different types of charged particles, electrons, muons, kaons and pions, are selected. Moreover, neutral pions, which mainly decay into two photons, are reconstructed from their decay products. The *BABAR* collaboration provides sophisticated particle reconstruction and identification algorithms [38], which are used in this work. The underlying methods are described in this chapter together with additional selection criteria used in this analysis.

5.1. Charged particle reconstruction

5.1.1. Reconstruction of tracks

The trajectories of charged particles are reconstructed in the silicon vertex tracker (SVT) and the drift chamber (DCH) of the *BABAR* detector. Both sub-detectors are described in detail in Sections 3.2.1 and 3.2.2.

Hits measured in both sub-detectors are used as input to a sequence of optimized track finding algorithms. The algorithms use detailed information about the detector material distribution and of the exact field map of the $1.5\,T$ magnetic field, which surrounds the tracking detectors. The measured space points are fitted by a track model. Due to the magnetic field the fitted trajectories are constrained to a helix shape with its origin in the intersection point (IP) or in a fitted secondary vertex. The radius of the helix-shaped particle trajectory is proportional to the momentum of the particle. Therefore, the particle momentum is determined from the measured radius. A reconstructed charged particle trajectory is denoted as *track* in the following.

5.1.2. Selection of tracks

A prerequisite of this analysis is to reconstruct charged decay products of the τ lepton, and to separate them from charged particles produced in particle interactions with the detector material or in subsequent decays of daughter particles of the τ.

Due to the lifetime, $\tau_\tau = (290.6 \pm 1.0) \times 10^{-15}$ s, of the τ lepton, the vast majority of τ leptons already decays in the beam pipe of the *BABAR* detector[1]. The origin of the decay products trajectories is therefore consistent with the position of the primary vertex of the event. This τ-pair event property is used to reject tracks of particles produced in interactions with the detector material, e. g., photon conversions ($\gamma \rightarrow e^+e^-$). Each

---

[1] The flight length of a τ with a momentum $p = 1.8\,\text{GeV}/c$ which decays after the time $t = \tau_\tau$ is $s = \frac{p}{m_\tau} ct = 87\,\mu\text{m}$. The outer radius of the beam pipe is 27.9 mm [25].

reconstructed track has to fulfill the following requirements:

$$\begin{aligned} |d0| &< 1.5\,\mathrm{cm} \\ |z0| &< 2.5\,\mathrm{cm} \end{aligned} \tag{5.1}$$

where $|d0|$ and $|z0|$ are the distance of closest approach in the xy-plane and along the z-axis between the track and the primary vertex, respectively. In addition to this criterion, track pairs with an invariant mass consistent with either zero or the mass of a longer-lived particle, such as the K_S^0, which is frequently produced in τ decays, are discarded. Tracks which fulfill the above criteria are reconstructed in data with an efficiency [39] of

$$\epsilon_t^{\mathrm{Data}} = 93.923 \pm 0.224. \tag{5.2}$$

The track reconstruction efficiency [39] in simulated events, ϵ_t^{MC}, is consistent with the one measured in data within uncertainties:

$$\frac{\epsilon_t^{\mathrm{Data}}}{\epsilon_t^{\mathrm{MC}}} = 0.9996 \pm 0.0017 \tag{5.3}$$

No correction is therefore applied to simulated events. However, the uncertainty is taken into account in the determination of the total systematic uncertainty of the branching fraction measurement.

5.2. Charged particle identification

5.2.1. Variables used for particle identification

The type of a charged particle is identified by studying the particle's signature in several components of the *BABAR* detector and combining the obtained information. The tracking devices are used to measure the momentum and the specific energy loss, dE/dx, of the traversing particle. The Cherenkov detector provides a good pion-kaon separation by measurement of the emitted Cherenkov light. The deposited energy and the shape of showers induced in the electromagnetic calorimeter are used to distinguish between electrons, muons and hadrons. Finally, energy deposits in the instrumented flux return are used to distinguish between muons and hadrons.

Specific energy loss

In addition to the position of energy deposits along a charged particle trajectory also the magnitude of the energy loss per unit path length, dE/dx, is measured in the tracking system.

Muons, pions, and kaons with momenta as observed in the *BABAR* experiment lose energy through ionization and atomic excitation of the detector material. The specific energy loss is related to the particle velocity, $\beta = \frac{v}{c}$, through the Bethe-Bloch equation [4]:

$$-\frac{\mathrm{d}E}{\mathrm{d}x} = \kappa z^2 \cdot \frac{Z}{A} \cdot \frac{1}{\beta^2} \left[\frac{1}{2} \ln \frac{2 m_e c^2 \gamma^2 \beta^2}{I^2} E_{\mathrm{kin}}^{\mathrm{max}} - \beta^2 - \frac{\delta}{2} \right], \tag{5.4}$$

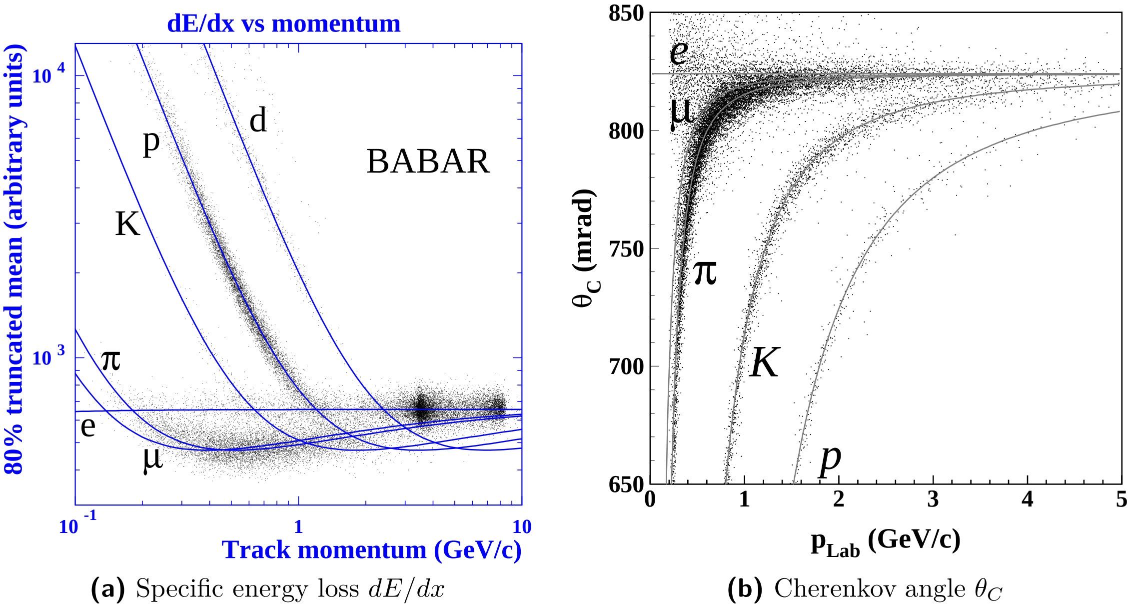

(a) Specific energy loss dE/dx

(b) Cherenkov angle θ_C

Figure 5.1.: Specific energy loss, dE/dx (a), and the Cherenkov angle, θ_C (b), as a function of the particle momentum determined in multi-hadron events. The grey lines show the predicted values for the different particle types. The figures are taken from [40].

where $E_{\text{kin}}^{\text{max}}$ is the maximum kinetic energy, m_e is the electron mass, Z and A are the atomic and mass numbers of the absorber material, I is the mean excitation energy, ze is the charge of the incident particle, and $\kappa = 4\pi N_A r_e^2 m_e c^2$, where N_A is the Avogadro number. The energy loss of electrons is not described by the Bethe-Bloch equation. The dominating process is bremsstrahlung for this case.

Figure 5.1a shows the energy loss, dE/dx, as a function of the particle momentum $p = m\gamma\beta$ for different particle types. The magnitude of the energy loss varies for different particles types in the same momentum region due to the different masses of the particles. The particle type can therefore be determined by measuring the energy loss and the momentum of the particle. A sufficient separation of pions and kaons using this method is only possible up to momenta of about 0.7 GeV. The type of particles with momenta above this threshold is determined with the Cherenkov detector (DIRC) of the *BABAR* experiment .

Cherenkov angle

The Cherenkov detector (Section 3.2.3) is the most important device of the *BABAR* detector to separate pions and kaon. Charged particles that traverse the quartz bars of the DIRC with a velocity larger than the velocity of light in the material emit Cherenkov photons at an angle θ_C with

$$\cos(\theta_C) = \frac{1}{n\beta}, \tag{5.5}$$

where β is the velocity of the particle, and n is the refraction index of the traversed material.

The value of the Cherenkov angle differs for particles with the same momentum but different masses. Figure 5.1b shows θ_C as a function of the particle momentum and illustrates the pion-kaon separation power. Kaons can be well separated from pions in the momentum region 0.7-4 GeV/c, which corresponds to the momentum range of kaons and pions selected in this analysis.

Energy deposits in the electromagnetic calorimeter

The ratio of the energy deposited in the electromagnetic calorimeter, E_{EMC}, and of the particle momentum, p, depends on the particle type. Electrons deposit all their energy in the calorimeter, which leads to $E_{\mathrm{EMC}}/p = 1$. Muons are almost minimum-ionizing particles, and therefore $E_{\mathrm{EMC}} \ll p$. Hadrons, e. g.. kaons and pions, induce hadronic showers which are not fully contained in the electromagnetic calorimeter leading to ratios $E_{\mathrm{EMC}}/p \leq 0.8$.

Shower shape

Particles types can also be distinguished by the shapes of the showers induced in the electromagnetic calorimeter. Electrons produce more compact showers in the calorimeter than hadrons. Muons do not deposit much energy in the calorimeter, since they are almost minimum-ionizing particles.
The extension of a shower can be measured in transversal direction, since showers extend over several crystals of the EMC. A longitudinal measurement of the shower shape is not performed.

The lateral moment, LAT, is used as a measure of the lateral extension of a shower:

$$LAT := \frac{\sum\limits_{i=3}^{N_{\mathrm{Crystal}}} E_i r_i^2}{E_1 r_0^2 + E_2 r_0^2 + \sum\limits_{i=3}^{N_{\mathrm{Crystal}}} E_i r_i^2} \in [0, 1) \tag{5.6}$$

where E_i is the energy deposited in crystal i, N_{Crystal} is the number of the crystals contained in an EMC cluster, ordered such that $E_1 < E_2 < ... < E_{N_{\mathrm{Crystal}}}$, r_i is the distance between the cluster centroid and the position of crystal i, and $r_0 = 5\,\mathrm{cm}$ denotes the average distance between two crystals.

Muons usually deposit energy in only one or two crystals, which leads to $LAT = 0$. Electrons deposit most of their energy in two or three crystals. Since the two highest energy deposits E_1 and E_2 are excluded in the sum in the nominator of Equation 5.6 LAT is small for electrons. The LAT for hadronic showers which have a broader energy distribution is typically larger than for electrons.

Energy deposits in the instrumented flux return

The trajectories of tracks measured in the tracking system are extrapolated into the instrumented flux return, which is the outer most component of the BABAR detector.

The signature of an electron is a measured track without energy deposits in the layers of the IFR *(IFR hits)* along its extrapolated trajectory, since electrons are fully absorbed in the calorimeter. Hadrons and muons reach the IFR. Hadrons produce broad hadronic showers, and deposit their energy in the inner layers of the IFR. In contrast to that muons traverse all layers. The number of IFR layers with hits is therefore larger for muons than for hadrons and can thus be used to identify muons.

5.2.2. Particle identification algorithms at *BABAR*

The *BABAR* collaboration provides various identification algorithms to determine the type of a reconstructed particle. These algorithms are called *PID selectors*. PID selectors are available for all particle types selected in this analysis, i. e., electrons, muons, pions, and kaons[2]. All PID selectors use combinations of the measured particle properties presented in Section 5.2.1 to determine the particle type.

Different identification techniques are implemented in the various PID selectors provided by the *BABAR* collaboration. There are four basic approaches:

- Requirements for a certain particle type are imposed separately on each measured quantity [41].
- A likelihood variable is calculated for a particle type [42].
- A neural network is trained on control samples for the considered particle type [43].
- Bootstrap aggregate (bagged) decision trees [44] are trained on control samples.

Independently of the implemented approach all PID selectors return only two possible values: the track is identified as a certain type or it is not identified as this type. This standardization is achieved by built-in thresholds values for the different output types of the basic approaches. For example, in the likelihood-based approach the track is identified as a certain type if the determined likelihood is above a predefined value.

For each identification method of a certain particle type a set of different built-in threshold values is implemented. The chosen values define the *tightness level* of a selector. The tightness of a selector determines the balance between identification efficiency, ϵ_a, and misidentification fraction, $\eta_{a\text{-as-}b}$, where $a, b = e, \mu, K, \pi$ with $a \neq b$.

The identification efficiency of a PID selector `A` for the particle type a is given by

$$\epsilon_a^{\mathtt{A}} = \frac{N_a^{\mathtt{A}}}{N_a} \tag{5.7}$$

where N_a is the number of particles of type a in a data sample, and $N_a^{\mathtt{A}}$ is the number of correctly identified particles.

Accordingly, the probability to misidentify a particle of type b as a particle of type a with the selector `A` is defined as

$$\eta_{b\text{-as-}a}^{\mathtt{A}} = \frac{N_b^{\mathtt{A}}}{N_b} \tag{5.8}$$

where N_b is the number of particles of type b, and $N_b^{\mathtt{A}}$ is the number of these particles misidentified as type a.

In the following section, the PID selectors used in this analysis are presented.

---

[2] The *BABAR* collaboration also provides PID selectors for protons.

5.2.3. Identification of electrons, muons, pions, and kaons.

Underlying identification algorithm

The charged particles are identified with a set of PID selectors recommended by the *BABAR* PID Group for the usage with the *BABAR* software release[3] used in this analysis. The identification of electrons, pions, and kaons is performed with a selector group[4] which uses bagged decision tree algorithms for each particle type. The output of each of these algorithms is combined using an Error Correcting Output Code (ECOC) technique [45]. The identification of muons is not included in this group. A separate muon selector[5] [44] is used which is also based on the bagged decision tree technique, but which uses a different combination of measured quantities. This set of quantities includes information measured in the IFR. A detailed description of the PID selectors can be found in [38].

Tightness of the PID selectors

The tightness level of the PID selectors is chosen to minimize misidentification probabilities.

Electrons and muons produce clean signatures in the detector and can be well separated from the other particle types. Low misidentification probabilities are already achieved with relatively loose identification criteria. This means that a low *tightness level* of the PID selectors is chosen, leading to a high identification efficiency.

Signal decays with a charged kaon can only be distinguished from the corresponding decays with a charged pion by the application of PID selectors. The branching fractions of the signal decays with a π^- and n π^0's are about 10–100 times larger than those of decays with kaons and the same number of π^0's. A low misidentification probability of pions as kaons in therefore crucial. PID selectors with tight selection criteria are chosen for kaons and pions.

The particle identification efficiencies and misidentification probabilities of PID selectors are determined using data control samples as well as simulated events. The control decays are described in the next paragraph.

PID control samples

A control sample contains tracks of known type. The type of the tracks is determined independently of the PID algorithms, e. g., the type is identified from kinematic considerations and conservation laws.

Control track samples are used to measure particle identification efficiencies and misidentification probabilities of PID selectors. The values determined for the PID selectors used in this analysis are discussed in the next paragraph. Moreover, control samples [46] are used to derive correction factors to account for differences between data and simulation in the identification performance (Section 5.2.5).

For pions as well as for kaons two different control samples are used. The standard control samples for pions and kaons provided by the *BABAR* collaboration are used to

---

[3] The version name of the used *BABAR* software release is `analysis-51`.

[4] The electron, pion and kaon selectors are named `eKMVeryLoose`, `KKMTight`, and `piKMTight`.

[5] The muon selector is named `muBDTVeryLoose`.

determine the efficiencies and misidentification fractions of available pion and kaon PID selectors. Among these PID selectors, the selectors with an optimal identification performance are chosen. Additional control samples of τ decays into three charged particles are used to determine kaon and pion identification correction factors to be applied to simulated events.

The standard control samples used by the *BABAR* collaboration for pions and kaons contain the decay chain

$$D^{*+} \to \pi^+_{\text{soft}} D^0 (\to \pi^+ K^-). \tag{5.9}$$

This decay is reconstructed by selecting two particles with an invariant mass consistent with the D^0 mass. The momentum of the third particle has to be $< 0.5\,\text{GeV}/c$ to identify that particle as the *soft* pion π^+_{soft}. The invariant mass of the three particles which fulfill that criteria has to be consistent with the mass of a D^{*+} meson. The pion in the D^0 decay has the same charge as the reconstructed π^+_{soft}, since the $D^0 \to \pi^- K^+$ decay is doubly Cabibbo suppressed, and is thus negligible. The pion control sample is therefore selected in the following way: The track with the same charge as the soft pion is marked as the pion control track. No PID selector is applied to identify the type of this track. The kaon control sample is selected similarly: The control track is the track with the charge opposite to the charge of the π^+_{soft}.

The standard control samples which originate from high-multiplicity hadronic events are not used in this analysis to derive PID correction factors, because the particle identification performance depends on the average particle multiplicity. This has been shown in [47] for the identification performance of electrons. Typically, in low-multiplicity events a better performance of the particle identification is achieved. For example, the measurement of the Cherenkov angle depends on the occupancy of the DIRC. The larger the number of charged particles traversing a DIRC segment the more difficult is the assignment of detected Cherenkov photons to the particles, and thus the determination of the Cherenkov angle. The PID correction factors are derived from a comparison of the PID performance in data and simulation, and can therefore also depend on the particle multiplicity. Thus, they should be determined in control samples with a topology as similar as possible to the topology of signal events to achieve an optimal correction of the simulation. For this analysis, control samples of $e^+e^- \to \tau^+\tau^-$ events are selected, where a tag lepton (Section 6.2.1) is required and the other τ decay is

$$\begin{aligned} &\tau^- \to \pi^-\pi^+\pi^-\nu_\tau \quad \text{(pion control sample)},\\ &\tau^- \to \pi^- K^+ K^- \nu_\tau \quad \text{(kaon control sample)}. \end{aligned} \tag{5.10}$$

These events contain only four reconstructed particles. Their topology is similar to the topology of the signal decays. The selection of these decays and the determination of the correction factors for simulated events is described in Chapter 7.

The control samples for electrons and muons which are provided by the *BABAR* collaboration are samples of $e^+e^- \to e^+e^-(\gamma)$ processes and $e^+e^- \to \mu^+\mu^-(\gamma)$ processes, respectively. The type of the control track is determined from lepton-flavor conservation and four-momentum conservation. These control samples have a very similar topology

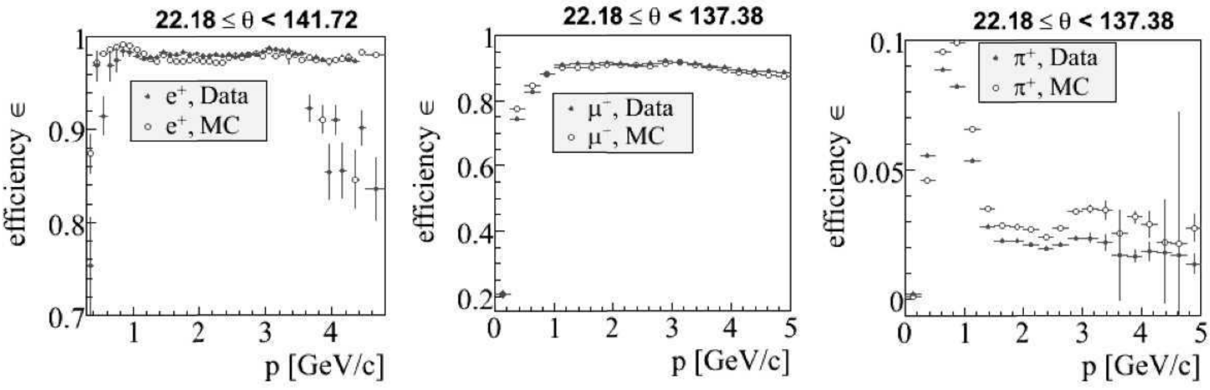

(a) ϵ_{e^+} **(b)** ϵ_{μ^+} **(c)** $\eta_{\pi^+\text{-}as\text{-}\mu^+}$

Figure 5.2.: Identification efficiencies, ϵ_{e^+}, (a), and ϵ_{μ^+} (b) of the electron and muon PID selector used in this analysis. In addition, the pion misidentification rate, $\eta_{\pi^+\text{-}as\text{-}\mu^+}$ is shown in (c). All distributions are displayed as a function of the track momentum in data (filled circles) and simulation (open circles). The figures are taken from [38].

to τ pair events, i. e., the electron and muon PID correction factors are determined by using these samples.

Electrons

Figure 5.2a shows the positron[6] identification efficiency as a function of the particle momentum for the electron PID selector used in this analysis. The electron identification efficiency is about 98%. The misidentification fraction of pions as electrons (not shown in the figure) is $\eta_{\pi\text{-as-}e} \leq 0.9\%$ for pion momenta below 1 GeV. The probability is significantly smaller for pions with larger momenta. Misidentification fractions of other particles as electrons are negligible.

Muons

The efficiency of the muon identification, ϵ_μ, is shown in Figure 5.2b. For small muon momenta below 1 GeV/c, ϵ_μ lies in the region 70-90%, while $\epsilon_\mu \approx 90\%$ is achieved for higher momenta. The misidentification probability of pions (Figure 5.2c) shows the opposite behavior: The probability reaches almost 10% for low momenta and significantly decreases to about 3% above 1 GeV/c. The misidentification of pions is the dominant misidentification effect, because pions and muons are difficult to distinguished using information from the tracking systems and the DIRC. The separation relies almost only on IFR information.

Kaons

The identification performance of the kaon is illustrated in Figure 5.3. The kaon identification efficiency is $\epsilon_K = 80 - 90\%$. The misidentification probabilities of pions and muons as kaons are $1 - 2\%$ in both cases.

---

[6] The figures shown in this section, which display the identification efficiencies and the misidentification fractions, have been produced for positively charged particles. The corresponding distributions for negatively charged particles can be found in [38]. The separation according to the charge is performed to account for possible charge asymmetries.

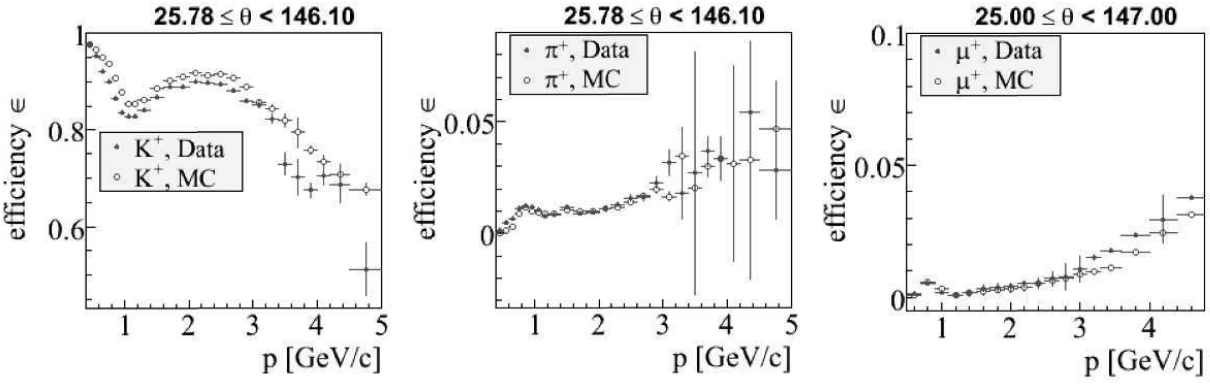

(a) ϵ_{K^+} **(b)** $\eta_{\pi^+\text{-}as\text{-}K^+}$ **(c)** $\eta_{\mu^+\text{-}as\text{-}K^+}$

Figure 5.3.: The identification efficiency, ϵ_{K^+} (a), the pion misidentification rate, $\eta_{\pi^+\text{-}as\text{-}K^+}$ (b), and the muon misidentification rate, $\eta_{\mu^+\text{-}as\text{-}K^+}$ (c), of the kaon PID selector used in this analysis as a function of the track momentum in data (filled circles) and simulation (open circles). The figures are taken from [38].

Pions

The identification efficiency for pions is 95% (Figure 5.4). The kaon misidentification probability of ≈ 2-5% is not shown in the figure, since a negligibly small number of kaons enter the pion decay mode samples, due to $\frac{\mathcal{B}(\tau^-\to\pi^-(n\pi^0)\nu_\tau)}{\mathcal{B}(\tau^-\to K^-(n\pi^0)\nu_\tau)} \approx 10$. The misidentification probability of an electron as a pion is small: $\eta_{e\text{-as-}\pi} \approx 1\%$. In contrast to that, the misidentification probability for muons is very large, $\eta_{\mu\text{-as-}\pi} \approx 97\%$. The chosen pion PID selector does not use any IFR information. Therefore, pions and muons cannot be distinguished using this selector. Nevertheless, the fraction of muons misidentified as pions is strongly suppressed in this analysis by the special application order of PID selectors. This is described in detail in Section 5.2.4.

Additional lepton identification criteria

In addition to the criteria implemented in the PID selectors, the momentum of electrons and muons selected in this analysis is required to be

$$p_{e/\mu} > 1\,\mathrm{GeV}/c. \tag{5.11}$$

to avoid the increase in the misidentification probabilities at smaller momenta.

Additional kaon identification criteria

Kaon identification requirements which are applied in addition to the kaon selector have been developed in [10] to improve the agreement of data and simulation.

Kaons with small momenta, i. e., $p_K \leq 0.7\,\mathrm{GeV}/c$, are identified by using only the dE/dx measurement in the tracking devices, which increases the probability to misidentify another particle as a kaon. Therefore, charged particles are only identified as kaons if the Cherenkov angle, θ_C, has been reconstructed. This criterion is technically implemented by requiring

$$\theta_C > 0.1\,\mathrm{rad}. \tag{5.12}$$

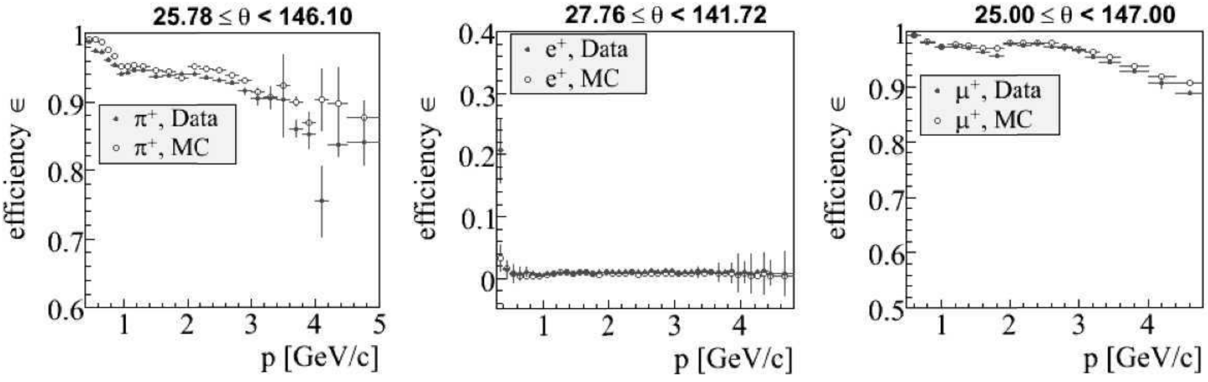

(a) ϵ_{π^+} **(b)** $\eta_{e^+\text{-}as\text{-}\pi^+}$ **(c)** $\eta_{\mu^+\text{-}as\text{-}\pi^+}$

Figure 5.4.: The identification efficiency, ϵ_{π^+} (a), the electron misidentification rate, $\eta_{e^+\text{-}as\text{-}\pi^+}$ (b), and the muon misidentification rate, $\eta_{\mu^+\text{-}as\text{-}\pi^+}$ (c), of the pion PID selector used in this analysis as a function of the track momentum in data (filled circles) and simulation (open circles). The figures are taken from [38].

Kaons can decay shortly before the DIRC. The Cherenkov angle is then measured for the kaon decay products and not for the kaon. It has been observed in [10] that typically $\theta_C \approx 0.8\,\text{rad}$ in this case. Such kaons are rejected by the following requirement:

$$\theta_C < 0.65\,\text{rad} + 0.125\text{p}\frac{\text{rad}}{\text{GeV/c}}. \tag{5.13}$$

Additional charged track identification criteria

A good quality of the charged particle identification is further ensured by restricting the polar angle of the particle trajectory to

$$0.45 < \theta_{\text{track}} < 2.36\,\text{rad}, \tag{5.14}$$

which corresponds to the overlapping acceptance region of the DIRC and DCH. The DIRC covers a smaller polar angle region than the tracking system. The performance of the identification is also improved by requiring a minimal transverse momentum

$$p^T_{\text{track}} > 250\,\text{MeV}/c \tag{5.15}$$

of charged particles to ensure that the particle trajectories are inside the DIRC acceptance.

5.2.4. PID selector sequence

For the decays selected in this analysis, each selected event contains exactly two charged tracks due to the application of the lepton-tag technique, which is described below in Section 6.2.1. One of the tracks is either identified as an electron or muon (*tag lepton*). The other track has to fulfill the criteria of a pion or kaon (*signal track*). Events of the type ($\tau^+ \to e^+\nu_e\overline{\nu}_\tau$ and $\tau^- \to \mu^-\overline{\nu}_\mu\nu_\tau$) are also selected if the respective particles are identified.

The two selected tracks, t_1 and t_2, are not distinguishable before the particle identification algorithms are applied, i. e., t_1 can be the tag lepton and t_2 the signal track, and vice versa. It has to be tested for both tracks that they fulfill the criteria for a tag lepton and for a signal track. Each of the four PID selectors – the electron, muon, kaon, and pion PID selector – is applied to each track.

For reasons of readability the four PID selectors are denoted as

$$\begin{aligned} \text{muon selector:} \quad & \texttt{muon} \\ \text{electron selector:} \quad & \texttt{electron} \\ \text{kaon selector:} \quad & \texttt{kaon} \\ \text{pion selector:} \quad & \texttt{pion} \end{aligned} \tag{5.16}$$

in the following.

The PID selectors are applied to each of the two tracks, t_i, in the following order:

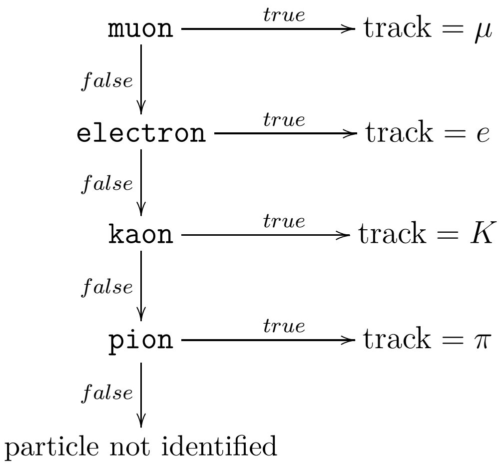

The first selector applied to the track is the muon selector. The track is identified as a muon if the selector returns the value *true*, and the procedure is closed. If the particle is not identified as a muon, the electron selector is applied. The procedure is repeated for the kaon selector and finalized with the application of the pion selector. This sequence leads to explicit *particle identification vetos* for all particle types except the muon. That means, for example, that identified electrons, kaons, and pions failed the selection criteria of a muon, i. e.. they are vetoed if they are a muon. The following selector combinations are effectively applied to the particles selected in this analysis:

$$\begin{aligned} \mu : \quad & \texttt{muon} \\ e : \quad & \texttt{electron} \wedge \texttt{!muon} \\ K : \quad & \texttt{kaon} \wedge \texttt{!electron} \wedge \texttt{!muon} \\ \pi : \quad & \texttt{pion} \wedge \texttt{!kaon} \wedge \texttt{!electron} \wedge \texttt{!muon} \end{aligned} \tag{5.17}$$

These special combinations of PID selectors have to be considered when correcting the simulation for deviations between data and simulation. Correction factors that are determined separately for each of the selectors have to be combined correctly. This is described in Section 5.2.5.

The order of the selectors is chosen to minimize the fraction of misidentified particles in the decay mode samples. Since all decays measured in this analysis contain a hadron, the lepton PID selectors are applied at first, which suppresses the number of leptonic τ decays misidentified as a decay into a hadron. Muons are selected before electrons, since the muon misidentification probability $\eta_{\mu\text{-as-}e}$ is larger then the inverse probability, $\eta_{e\text{-as-}\mu}$. Moreover, the application of a muon veto before the identification of a pion strongly suppresses the very large $\eta_{\mu\text{-as-}\pi} \approx 97\%$ due to the high muon identification efficiency.

In principle, the order of the kaon and pion PID selectors could be chosen arbitrary. These PID selectors which use the same identification method and have the same tightness level are designed to be *exclusive*. This means that a track identified with one of these PID selectors fails the requirements of the other. However, a correction (see Section 5.2.5) of simulated events is necessary for each applied PID selector leading to the uncertainty of the identification procedure. The kaon is identified first to avoid the larger uncertainty arising from a pion veto[7].

5.2.5. Particle identification efficiency correction

The misidentification probability of muons as electrons is shown in Figure 5.2 as a function of the muon momentum for data as well as for simulated events. Clear deviations are visible between these two distributions. Deviations between data and simulation also exist in the other distributions of efficiencies and misidentification probabilities shown in Section 5.2.3.

The BABAR collaboration provides tables with correction factors for simulation to account for these differences. Control samples are used to measure the identification efficiencies (Equation 5.7) and misidentification probabilities (Equation 5.8) for all PID selectors. The correction factors for simulated events are then defined as the ratios of the PID selector efficiency determined in data, ϵ_a^{Data}, and the efficiency obtained for simulated events, ϵ_a^{MC}, :

$$w_{a\text{-as-}a} = \frac{\epsilon_a^{\text{Data}}}{\epsilon_a^{\text{MC}}}. \tag{5.18}$$

Respective ratios are also defined for the misidentification probabilities

$$w_{b\text{-as-}a} = \frac{\eta_{b\text{-as-}a}^{\text{Data}}}{\eta_{b\text{-as-}a}^{\text{MC}}}, \tag{5.19}$$

---

[7] The main goal of this analysis is the precise measurement of $\tau^- \to K^-(n\pi^0)\nu_\tau$ decays which can be used to determine the CKM-matrix element $|V_{us}|$. Therefore, a small uncertainty of the branching fractions of these decays is preferred over a small uncertainty of $\mathcal{B}(\tau^- \to \pi^-(3\pi^0)\nu_\tau)$ and $\mathcal{B}(\tau^- \to \pi^-(4\pi^0)\nu_\tau)$ also measured in this analysis.

where $a, b = e, \mu, \pi, K$ with $a \neq b$. The correction factors do not only depend on the true particle type, i, and the reconstructed type, j, of the particle $(i, j = e, \mu, \pi, K)$. They are also determined in dependence of the particle charge, momentum, polar angle, and azimuthal angle:

$$w_{i\text{-as-}j} = w_{i\text{-as-}j}(q, p, \theta, \phi). \tag{5.20}$$

The determined ratios are used as correction factors applied to simulated events as event weights. These weights are denoted as *PID weights*.

Each simulated event is weighted with a combination of PID weights according to the applied PID selectors. The signal events contain two charged tracks t_1 and t_2, i. e., two PID weights are applied to obtain the total weight:

$$w^{id} = w^{t_1}_{i\text{-as-}j} \cdot w^{t_2}_{k\text{-as-}l} \qquad i, j, k, l = e, \mu, \pi, K, \tag{5.21}$$

As described in Section 5.2.4 PID selectors are also used to veto particles. Deviations of data and simulation also have to be corrected in this case. The corrections are done by applying *PID veto weights* defined as

$$w^{veto}_{a\text{-as-}a} = \frac{1 - \epsilon^{\text{Data}}_a}{1 - \epsilon^{\text{MC}}_a} \quad \text{and} \quad w^{veto}_{b\text{-as-}a} = \frac{1 - \eta^{\text{Data}}_{b\text{-as-}a}}{1 - \eta^{\text{MC}}_{b\text{-as-}a}}. \tag{5.22}$$

The total veto weight, w^{veto}_{track}, applied to an identified track t depends on the particle type, since a sequence of different PID selectors is applied to each particle type. According to Equation 5.17 the following weight combinations have to be applied for the different particle types:

$$\begin{aligned} \mu: \quad & w^{veto}_{\mu} = 1, \\ e: \quad & w^{veto}_{e} = w^{veto}_{i\text{-as-}\mu}, \\ K: \quad & w^{veto}_{K} = w^{veto}_{i\text{-as-}\mu} \cdot w^{veto}_{i\text{-as-}e} \\ \pi: \quad & w^{veto}_{\pi} = w^{veto}_{i\text{-as-}\mu} \cdot w^{veto}_{i\text{-as-}e} \cdot w^{veto}_{i\text{-as-}K} \end{aligned} \tag{5.23}$$

The total weight, w^{PID}_{event} which is applied to each simulated event to account for differences in the particle identification performance is then

$$w^{\text{PID}}_{event} = w^{id} \cdot w^{veto}_{t_1} \cdot w^{veto}_{t_2}. \tag{5.24}$$

Statistical limitation of the *BABAR* PID tables

The PID weights for the identification of pions and kaons, and the misidentification of pions as kaons which are determined using τ control samples in Chapter 7 are available for all occurring values of track momentum, $p_{K/\pi}$, polar angle, $\theta_{K/\pi}$, and azimuthal angle, $\phi_{K/\pi}$. The particle identification and misidentification tables provided by the *BABAR* collaboration are used to obtain all other PID weights $w_{i\text{-as-}j}$. The identification tables cover a large region of (p, θ, ϕ). In rare cases however, i. e., for a fraction $< 1\times10^{-4}$ of the correctly identified electrons and muons, selected tracks are outside this region. In some (p, θ, ϕ) intervals, in particular at large momenta $p \gtrapprox 4\,\text{GeV}/c$, the number of control tracks is very small. PID weights cannot be determined in these intervals. The PID weights are set to $w = 1.0$ which is the mean of the PID weight distribution applied to selected electrons as well as muons. The uncertainty of the PID weights, which contributes to the uncertainty of the measured signal decay branching fractions (Chapter 10), is estimated by the RMS of the PID weight distributions.

The misidentification tables, e. g., the PID weights for the misidentification of electrons as muons, are produced with the same control samples as the identification tables. In general, the misidentification probabilities are significantly smaller than the identification efficiencies leading to larger statistical uncertainties of misidentification weights. This results in a larger fraction of intervals without reliable PID weights. These PID weights and their uncertainties are also replaced in the same way as described above. This is valid, since the absolute fraction of applied misidentification weights is small.

The same replacement is also applied in case of veto weights. The vast majority of occurring veto weights are misidentification veto weights. For example, following the selector sequence described in Section 5.2.4, a true electron will typically be not identified as a muon and than be correctly identified which results in the weight combination $w^{veto}_{e\text{-as-}\mu} \cdot w_{e\text{-as-}e}$. The probability to misidentify an electron as a muon, $\eta_{e\text{-as-}\mu}$, is on the order of 1% resulting in $w^{veto}_{e\text{-as-}\mu} = \frac{1-\eta^{\mathrm{Data}}_{e\text{-as-}\mu}}{1-\eta^{\mathrm{MC}}_{e\text{-as-}\mu}} \approx 1$. For small misidentification probabilities, the uncertainty $\Delta w_{e\text{-as-}\mu} \approx \sqrt{(\Delta\eta^{\mathrm{Data}}_{e\text{-as-}\mu})^2 + (\Delta\eta^{\mathrm{MC}}_{e\text{-as-}\mu})^2}$. Since $\eta_{e\text{-as-}\mu}$ is not determined in many intervals of the PID tables the uncertainty is estimated by the RMS of the muon PID weight distribution.

5.3. Neutral particles

Almost all signal decays and control decays have neutral pions in the final state. π^0's decay before they reach the calorimeter and cannot be detected directly with the *BABAR* detector. They are reconstructed in the decay channel $\pi^0 \to \gamma\gamma$ with $\mathcal{B}(\pi^0 \to \gamma\gamma) = (98.823 \pm 0.034)\%$, where the two produced photons are detected with the electromagnetic calorimeter. The applied photon quality criteria, and the reconstruction of the π^0 from the two detected photons are described in this section.

5.3.1. Reconstruction of photons

The signature of a photon candidate is a measured cluster (Section 3.2.4) in the electromagnetic calorimeter (EMC) without an associated charged track reconstructed in the tracking devices. The cluster energy, E_{cluster}, is given by the sum of the energy deposits in all crystals assigned to the cluster. The minimum energy of a cluster is $E^{\mathrm{min}}_{\mathrm{cluster}} = 30\,\mathrm{MeV}/c^2$. In this analysis tighter photon selection criteria are imposed to ensure a high purity of photons originating from a π^0 decay.

Calorimeter acceptance

Only fully reconstructed electromagnetic showers are considered as photon candidates. An electromagnetic shower induced by a photon extends over several crystals of the electromagnetic calorimeter. A fraction of 99% of the energy is deposited in a cylinder with a radius corresponding to 3.5 Molière radii. The Molière radius in cesium iodide is $R_M(CsI(Th)) \approx 3.8\,\mathrm{cm}$, while the average distance between two crystals of the EMC is $r_0 = 5\,\mathrm{cm}$. Hence, electromagnetic showers are fully contained in a 3×3 crystals area. The EMC is build of crystal rings in azimuthal direction, and therefore full coverage is ensured in ϕ. In polar direction the acceptance region is limited to $0.277 < \theta < 2.456\,\mathrm{rad}$. Photon candidates in the endcap[8] region ($0.277 < \theta < 0.473\,\mathrm{rad}$) of the calorimeter are discarded, due to the large uncertainty of the calibration in this calorimeter region. The full containment of photon showers in the calorimeter is ensured by also requiring an maximum θ given by the acceptance edge minus three crystal rings:

$$0.473 < \theta_\gamma < 2.360\,\mathrm{rad}. \tag{5.25}$$

Photon shower extension

The extension of a shower is used to suppress spurious photons from hot calorimeter channels and energy deposits due to fluctuations in hadronic showers. A typical signature of such photon candidates are *neutral* EMC clusters, i. e., clusters without an associated track, with one or two crystals. In contrast, photon showers extend over several crystals of the calorimeter. Therefore, real photon candidate clusters have to consist of more than one or two crystals resulting in a non-vanishing lateral moment (Equation 5.6). Technically, this criterion is ensured by requiring:

$$LAT_\gamma > 0.0001 \tag{5.26}$$

Photon energy

Photons not originating from π^0 decays can be beam-background photons or photons produced in particle interactions with the detector material. This type of photons tends to have small energies. Photon candidates selected in this analysis are required to have

$$E_\gamma > 75\,\mathrm{MeV} \tag{5.27}$$

The photon selection criteria are summarized in Table 5.1.

5.3.2. Reconstruction of neutral pions.

The four-momentum of a π^0 candidate, $\widehat{p}_{\gamma\gamma}$, is determined from two photons from the $\pi^0 \to \gamma\gamma$ decay as

$$\widehat{p}_{\gamma\gamma} = \widehat{p}_{\gamma_1} + \widehat{p}_{\gamma_2} \tag{5.28}$$

where

$$\widehat{p} = \begin{pmatrix} E \\ \vec{p} \end{pmatrix}. \tag{5.29}$$

---

[8] The electromagnetic calorimeter of the BABAR detector is asymmetric. The calorimeter barrel covers central polar angle values. In forward direction ($\theta < 0.473\,\mathrm{rad}$) the acceptance region is increased by additional crystal rings–the calorimeter endcap. (Section 3.2.4)

In events which contain more than two photons, each photon is combined with every other photon. The maximum number of selected π^0 candidates, $n_{\gamma\gamma}$, is

$$n_{\gamma\gamma} = \frac{(2n_{\pi^0} + n^{\gamma}_{\text{other}})!}{2!(2n_{\pi^0} + n^{\gamma}_{\text{other}} - 2)!}. \tag{5.30}$$

where n_{π^0} is the number of true π^0's, and $n^{\gamma}_{\text{other}}$ is the number of other photons also reconstructed in the event. For example, $n_{\gamma\gamma} = 3$ for 3 photons and $n_{\gamma\gamma} = 6$ for 4 photons.

A π^0 candidate is selected if the invariant two-photon mass $m_{\gamma\gamma} = \sqrt{E^2 - |\vec{p}|^2}$ is consistent with the π^0 mass, $m^0_\pi \approx 135\,\text{MeV}/c^2$ [4]:

$$90 < m_{\gamma\gamma} < 165\,\text{MeV}/c^2. \tag{5.31}$$

This criterion does not remove all wrong two-photon combinations. Remaining additional π^0 candidates with a mass in the required interval are denoted as *combinatorial π^0 background.* This background can be divided in two categories:

1. **Two-photon combinations containing non-π^0 photons**
   This type of spurious π^0 candidates is already suppressed by the selection requirements imposed on photons (Section 5.3.1). They are further suppressed by requiring
   $$p_{\gamma\gamma} > 200\,\text{MeV}/c, \tag{5.32}$$
   where $p_{\gamma\gamma}$ is the momentum of the selected π^0 candidate.
2. **π^0 candidates containing a photon originating from a different π^0.**
   Two π^0 candidates can share a photon. The π^0 candidate with the larger momentum is selected.

Table 5.1.: Neutral particle reconstruction criteria.

Photon	
Energy	$E_\gamma > 75\,\text{MeV}/c^2$
Lateral Moment	$LAT > 0.0001$
Polar angle	$0.473 < \theta_\gamma < 2.36\,\text{rad}$
π^0	
Inv. mass	$90 < m_{\gamma\gamma} < 165\,\text{MeV}/c^2$
Energy	$E_{\gamma\gamma} > 200\,\text{MeV}/c^2$
Candidates sharing a photon	reject candidate with smaller momentum

Table 5.1 summarizes the photons selection criteria and the requirements imposed on selected neutral pions.

6. Event selection

The first step to select events containing the τ decays to be measured is to distinguish $e^+e^- \to \tau^+\tau^-$ events from other types of events, which are produced in e^+e^- collisions at the *BABAR* experiment. In this chapter the characteristic signature of τ pairs is described and compared with typical features of other events. The differences are used to select $e^+e^- \to \tau^+\tau^-$ events. In the next step, the τ signal decays are reconstructed and separated from other τ decays. The applied selection criteria are described in Section 6.3.

6.1. Characteristics of $e^+e^- \to \tau^+\tau^-$ events

In this section, an overview of the basic characteristics of $e^+e^- \to \tau^+\tau^-$ events is presented.

The center-of-mass energy of e^+e^- collisions at PEP-II is $\sqrt{s} = 10.58\,\mathrm{GeV}$ for the *On-Peak* data sample and $\sqrt{s} = 10.54\,\mathrm{GeV}$ for the *Off-Peak* data sample (Section 3.3.1). The former energy is slightly higher than the threshold for B meson pair production, since the mass of a B meson is $m_B = 5.28\,\mathrm{GeV}/c^2$. Therefore, B mesons decay almost at rest in the *BABAR* detector. As a consequence, their decay products are distributed isotropically in the center-of-mass frame. In contrast, τ leptons from τ-pair events are boosted due to their smaller mass, $m_\tau = 1.78\,\mathrm{GeV}/c^2$. This leads to a jet-like topology of $e^+e^- \to \tau^+\tau^-$ events. The very different topologies of $e^+e^- \to \tau^+\tau^-$ and $e^+e^- \to B\overline{B}$ events are illustrated in Figure 6.1. The figure shows *BABAR* event displays for the two types of events.

In addition to the different spatial distribution of the final state particles, the number of charged particles, n_t, in τ-pair events is much smaller than n_t of a typical $e^+e^- \to q\overline{q}$ event.

An important property of τ-pair events is the presence of at least two neutrinos. Neutrinos escape undetected which leads to missing mass in the event. The magnitude of the missing mass, m_{miss}, can be used to separate $e^+e^- \to \tau^+\tau^-$ events from other low-multiplicity events like $e^+e^- \to e^+e^-(\gamma)$ or $e^+e^- \to \mu^+\mu^-(\gamma)$ events (see Figure 6.2a), if all particles are reconstructed, i. e., $m_{\mathrm{miss}} = 0$.

The direction of the missing momentum can be used to discriminate between τ-pair events from so-called two-photon events, $e^+e^- \to e^+e^- f\bar{f}$, where f denotes a fermion (see Figure 6.2b). The two fermions are either charged leptons, i. e., $f\bar{f} = e^+e^-, \mu^+\mu^-$, or quarks ($f\bar{f} = q\overline{q}$), which hadronize.

In this analysis only events which contain two charged particles are selected (Section 6.2.1). A two-photon event, which has four charged particles in the final state,

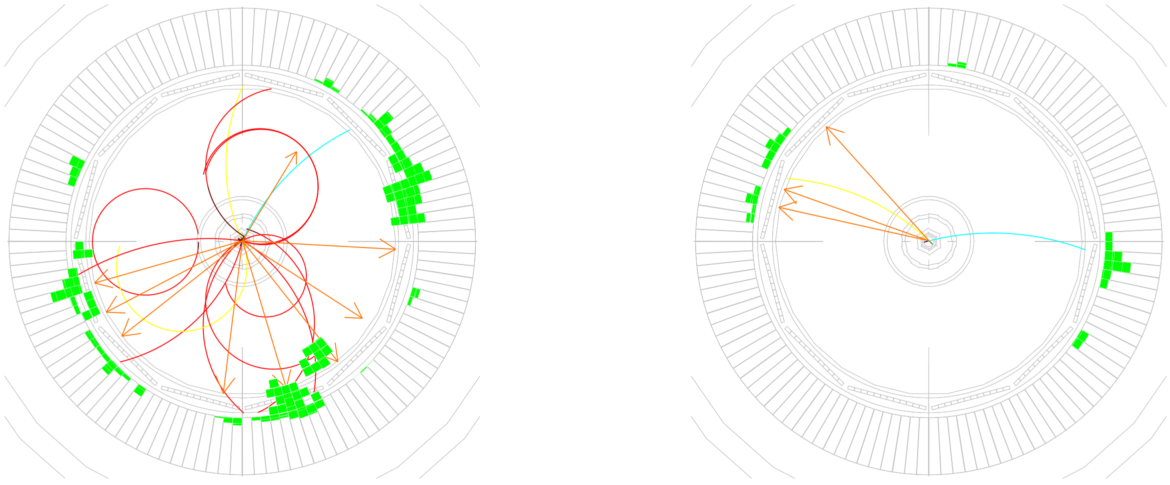

(a) $e^+e^- \to B^0\ \overline{B}^0$ **(b)** $e^+e^- \to \tau^+\tau^-$

Figure 6.1.: *BABAR* event displays showing two different kinds of simulated events (radial view). Reconstructed trajectories of charged particles are displayed as curved lines: pions (red), kaons (yellow) and electrons (light blue). The size of the green markers corresponds to the energy deposited in the electromagnetic calorimeter. The momentum direction of reconstructed π^0's is indicated by the orange arrows. (a) shows a typical $e^+e^- \to B^0$ $\overline{B}^0$ event with a large number of isotropically distributed final state particles. In (b) a $e^+e^- \to \tau^+\tau^-$ event with subsequent decays $\tau^+ \to e^+\nu_e\overline{\nu}_\tau$ and $\tau^- \to K^-(3\pi^0)\nu_\tau$ is shown. The event illustrates the characteristic low-multiplicity jet-like topology of τ pair events . Both illustrations are taken from [10]

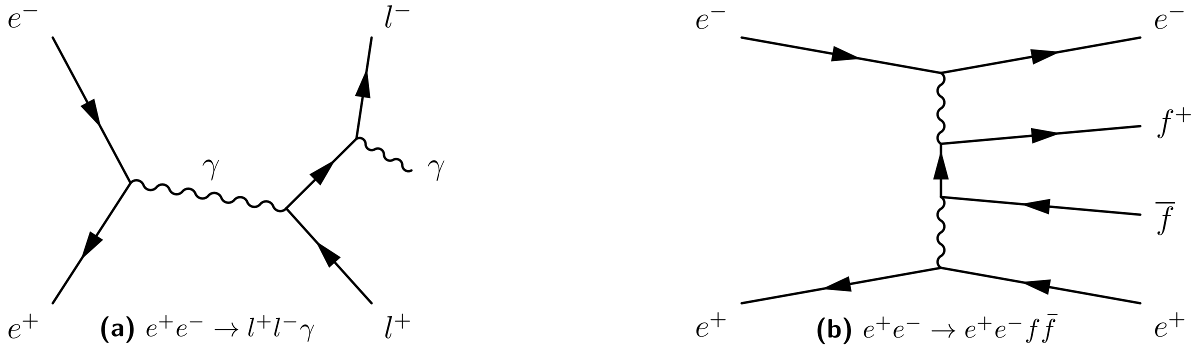

(a) $e^+e^- \to l^+l^-\gamma$ **(b)** $e^+e^- \to e^+e^-f\bar{f}$

Figure 6.2.: Feynman diagrams of the processes $e^+e^- \to l^+l^-\gamma$ (a) and $e^+e^- \to e^+e^-f\bar{f}$ (b).

can be only misidentified as a τ-pair event, if two of the charge particle trajectories are outside the acceptance of the tracking system, i. e., for small or large polar angles. Typically the high-energy final-state electrons are scattered at small angles and escape detection, while the trajectories of the fermion pair lie within the detector acceptance.

In addition, the missing mass calculated from the missing momentum vector, $\vec{p}_{\mathrm{miss}}$, in two-photon events is large due to the energy carried away by the undetected electron and positron. Moreover, the transverse component of $\vec{p}_{\mathrm{miss}}$ is small in two photon events while it is moderate in $e^+e^- \to \tau^+\tau^-$ events. In summary, the following characteristics of $e^+e^- \to \tau^+\tau^-$ events are used to separate them from other event types:

- jet-like topology,
- low particle multiplicity,
- sizable missing momentum within the detector acceptance

6.2. Selection of $e^+e^- \to \tau^+\tau^-$ events

In this section, the observables and requirements imposed in the selection of τ-pair events are described. The next step of the analysis, the separation of signal decays from background decays, is presented in Section 6.3.

The selection is mainly derived from the control decays $\tau^- \to \pi^-\nu_\tau$, $\tau^- \to \pi^-\pi^0\nu_\tau$, $\tau^- \to \pi^-(2\pi^0)\nu_\tau$, and $\tau^- \to \mu^-\overline{\nu}_\mu\nu_\tau$ which have a very similar topology and kinematics as the signal decays. The control decays are well known which leads to a reliable description of the data by simulation. Moreover, the decays have relatively large branching fractions leading to small statistical uncertainties. Effective criteria to suppress background events can be therefore derived and systematic effects can be investigated with high accuracy.

The selection criteria are developed by comparing the distributions of certain quantities in data and in simulation. For such comparisons the simulated distributions have to be normalized correctly. The total simulated event sample contains samples of the $e^+e^- \to \tau^+\tau^-$, $e^+e^- \to \mu^+\mu^-$, and $e^+e^- \to q\overline{q}$ ($q = u, d, s, c, b$) processes (Equation 3.6). The number of generated events, N_i^{gen}, in each sample i has to be scaled such that it corresponds to the number of these processes, N_i^{expected}, expected in the e^+e^- collisions:

$$N_i^{\mathrm{gen}} \cdot S_i = N_i^{\mathrm{expected}}, \tag{6.1}$$

with the scaling factor

$$S_i = \frac{\sigma_i}{N_i^{\mathrm{gen}}} \cdot \mathcal{L}, \tag{6.2}$$

where σ_i is the cross section of the processes of type i and $\mathcal{L}$ is the integrated data luminosity[1]. For the determination of the branching fraction it would be enough to

---

[1] This scaling factor applies to the so-called *generic* simulated samples (Section 3.3.2). For the *dedicated* τ decay samples, S_i is modified appropriately with the branching fraction of the generated τ decay.

apply the S_i to the final numbers of selected simulated events. In practice, S_i is applied as a weight to each simulated event. This has the advantage that the simulated events can be displayed in histograms with an appropriate normalization.

The majority of the figures shown in this and the following chapters is of the same type. In the upper part of the figures (e. g., Figure 6.3) the distribution of a quantity is compared for data and simulated events. The data distribution is displayed as black circles with error bars. The stacked filled histograms are the simulated contributions of various decays represented by different colors and hatch styles which are explained in the legend. Each of these histograms is added to the previous histogram. The lower part of the figure shows the ratio of the distributions in data and simulation which is denoted as *data/MC ratio* in the following. The ratio is obtained by dividing the content of each bin in the data histogram by the sum of the simulated contributions in the corresponding bin. The data/MC ratio is very useful to visualize the agreement between data and simulated events.

The errors shown in the figures are the statistical uncertainties of the number of data and simulated events. Other uncertainty contributions are not taken into account.

If not mentioned otherwise all event selection criteria are imposed in the figures, and all corrections are applied to the selected simulated events. This includes the identification efficiency correction for electrons and muons described in Section 5.2.5, and the pion and kaon identification correction developed in Chapter 7. Also the split-off correction (Chapter 8), and the π^0 reconstruction efficiency correction (Chapter 9) are applied.

The branching fractions used in the simulation to describe the signal τ decays are scaled to the results measured in this analysis (Section 10).

Some of the displayed figures are so-called n–1 *distributions*, i. e., all selection criteria are applied except of the criterion imposed on the displayed quantity. For this type of figures, the criterion is illustrated with vertical lines in the figure.

All figures are produced with the data sample of the runs 1–6 corresponding to an integrated luminosity of $473.8\,\mathrm{fb}^{-1}$. For some of the figures the data sample is split into two sub-samples, the e-tag and μ-tag sample, which are explained in the next section. It is explicitly mentioned in the caption of a figure if the data sample is split.

6.2.1. Lepton tag

A powerful technique to select τ decays in $e^+e^- \to \tau^+\tau^-$ events is the so called *lepton-tag method*. An electron (e-tag) or muon (μ-tag) is reconstructed in the event. The e and μ is required to fulfill the particle identification criteria described in Section 5.2.3:

$$\text{Lepton tag:} \quad identified\ e\ or\ \mu\,. \tag{6.3}$$

The signal τ decays measured in this analysis have one[2] charged particle in the final state. Therefore, only events with exactly two reconstructed charged particles, the tag

---

[2] The pion and kaon identification correction developed in this work is determined using τ decays into three charged particles. The selection of these decays is described separately in Chapter 7

lepton and the signal track, are selected,

$$N_{\text{charged}} = 2. \tag{6.4}$$

This criterion strongly suppresses $e^+e^- \to q\overline{q}$ events, which usually contain a larger number of reconstructed charged particles.

A single reconstructed charged lepton is a distinct signature of a $\tau^- \to l^-(\gamma)\nu_\tau\overline{\nu}_e$ decay, since the branching fraction, $\mathcal{B}(\tau^- \to l^-(\gamma)X\nu_\tau\overline{\nu}_e)$, of τ decays into a charged lepton, neutrinos, and additional particles X is negligible [4]. This means that all reconstructed particles other than the tag lepton (and possibly radiated photons) originate from the other τ lepton, the *signal* τ , in the $e^+e^- \to \tau^+\tau^-$ event. The decay of the signal τ can be therefore reconstructed with high purity, since wrong combinations of final state particles from the two τ decays are avoided. The signal decays are selected among the decays of the signal τ. Only one signal τ decay is selected per $e^+e^- \to \tau^+\tau^-$ event.

A further information, which is deduced from the reconstructed tag lepton is the charge of the τ leptons. The tag lepton carries the same charge as its mother particle. The charge of the signal τ is opposite to the tag-lepton charge.

The requirement of a tag lepton reduces the selection efficiency of events containing a signal decay. However, the branching fraction $\mathcal{B}(\tau^- \to l^-\overline{\nu}_l\nu_\tau) \approx 34\%$ is sufficiently large, i. e., the efficiency is reduced by a factor of 1/3. Therefore the advantages of the tagging technique outweigh the reduction of the selection efficiency.

The following combinations of τ decays are selected in this analysis:

$$\begin{aligned}
\tau^+ \to e^+\nu_e\overline{\nu}_\tau \quad &\text{and} \quad \tau^- \to \pi^-(n\pi^0)\nu_\tau \ (n = 0, 1, 2, 3, 4),\\
\tau^+ \to \mu^+\nu_\mu\overline{\nu}_\tau \quad &\text{and} \quad \tau^- \to \pi^-(n\pi^0)\nu_\tau \ (n = 0, 1, 2, 3, 4),\\
\tau^+ \to e^+\nu_e\overline{\nu}_\tau \quad &\text{and} \quad \tau^- \to K^-(n\pi^0)\nu_\tau \ (n = 0, 1, 2, 3),\\
\tau^+ \to \mu^+\nu_\mu\overline{\nu}_\tau \quad &\text{and} \quad \tau^- \to K^-(n\pi^0)\nu_\tau \ (n = 0, 1, 2, 3).\\
\tau^+ \to e^+\nu_e\overline{\nu}_\tau \quad &\text{and} \quad \tau^- \to \mu^-\overline{\nu}_\mu\nu_\tau.
\end{aligned} \tag{6.5}$$

Events of the type ($\tau^+ \to e^+\nu_e\overline{\nu}_\tau$ and $\tau^- \to e^-\overline{\nu}_e\nu_\tau$) or ($\tau^+ \to \mu^+\nu_\mu\overline{\nu}_\tau$ and $\tau^- \to \mu^-\overline{\nu}_\mu\nu_\tau$) are not selected in this analysis, because of the potentially large background contribution from $e^+e^- \to e^+e^-$ and $e^+e^- \to \mu^+\mu^-$ events. An investigation of such event topologies is beyond the scope of this thesis.

In addition to the particle identification criteria mentioned above, the momentum of the tag lepton is required to be

$$p_{\text{tag-lepton}} > 1.0\,\text{GeV}/c. \tag{6.6}$$

In selected events of the type $\tau^+ \to e^+\nu_e\overline{\nu}_\tau$ and $\tau^- \to \mu^-\overline{\nu}_\mu\nu_\tau$ both final-state leptons have to fulfill the criteria of a tag lepton. The requirement is imposed to ensure an optimal identification performance, i. e., to minimize the systematic uncertainty arising from the uncertainty of the PID corrections (Section 5.2.5) in this momentum region. The momentum of the tag lepton for events with selected $\tau^- \to \pi^-\nu_\tau$ and $\tau^- \to \pi^-\pi^0\nu_\tau$

candidates is shown in Figure 6.3 separately for the e-tag and μ-tag event samples. A deviation from the expected value of 1 can be seen in the data/MC ratio in the momentum region below 1.0 GeV/c. This deviation is more pronounced in the μ-tag sample. In this momentum region the applied PID corrections, especially for muons, are determined with a large uncertainty and do not account for the observed deviations.

6.2.2. Event topology

The magnitude of the so-called thrust is used to quantify how jet-like the topology of an event is. The thrust T is defined as

$$T := \max_{\mathbf{n}_T} \left(\frac{\sum_i |\mathbf{p}_i^{\mathrm{CMS}} \cdot \mathbf{n}_T|}{\sum_i |\mathbf{p}_i^{\mathrm{CMS}}|} \right) \in [0.5, 1], \tag{6.7}$$

where $\mathbf{p}_i^{\mathrm{CMS}}$ is the momentum of the i^{th} reconstructed particle[3], where the index i runs over all particles, determined in the center-of-mass (CMS) frame, and $\mathbf{n}_T$ is the *thrust axis* of the event. The thrust axis is defined as the unit vector which maximizes the sum of the longitudinal projections of the $\mathbf{p}_i^{\mathrm{CMS}}$.

Figure 6.4 shows a schematic illustration of an $e^+e^- \to \tau^+\tau^-$ event as reconstructed in this analysis. The thrust axis is indicated by a blue line. The direction of the axis corresponds approximately to the momentum direction of the τ leptons. The difference is due to the presence of undetected neutrinos in the final state.

The plane perpendicular to the thrust axis is used to divide the event in two hemispheres. The hemisphere containing the tag lepton is called *tag hemisphere*. The other hemisphere is denoted as *signal hemisphere*. In this analysis, events with one track in each hemisphere are selected, i. e., a

$$\text{1-1 topology} \tag{6.8}$$

is required.

Events with an isotropic distribution of final-state particles tend to have lower thrust values, i. e., $T = 0.5$ for an ideally spherical event. For τ decays the thrust value is required to be

$$0.88 < T < 0.99. \tag{6.9}$$

The maximum value is imposed to discard $e^+e^- \to e^+e^-$ and $e^+e^- \to \mu^+\mu^-$ events. The angle between the final state particles in this type of events is 180°, which leads to $T = 1$. The distribution of the thrust T for selected $\tau^- \to \pi^-\nu_\tau$ and $\tau^- \to \pi^-\pi^0\nu_\tau$ events is shown in Figure 6.5.

---

[3] The thrust is calculated from neutral EMC clusters as defined in Section 5.3.1, from the tag lepton, from the signal track, and also from charged tracks originating from decays of K_S^0 mesons and longer-lived particles.

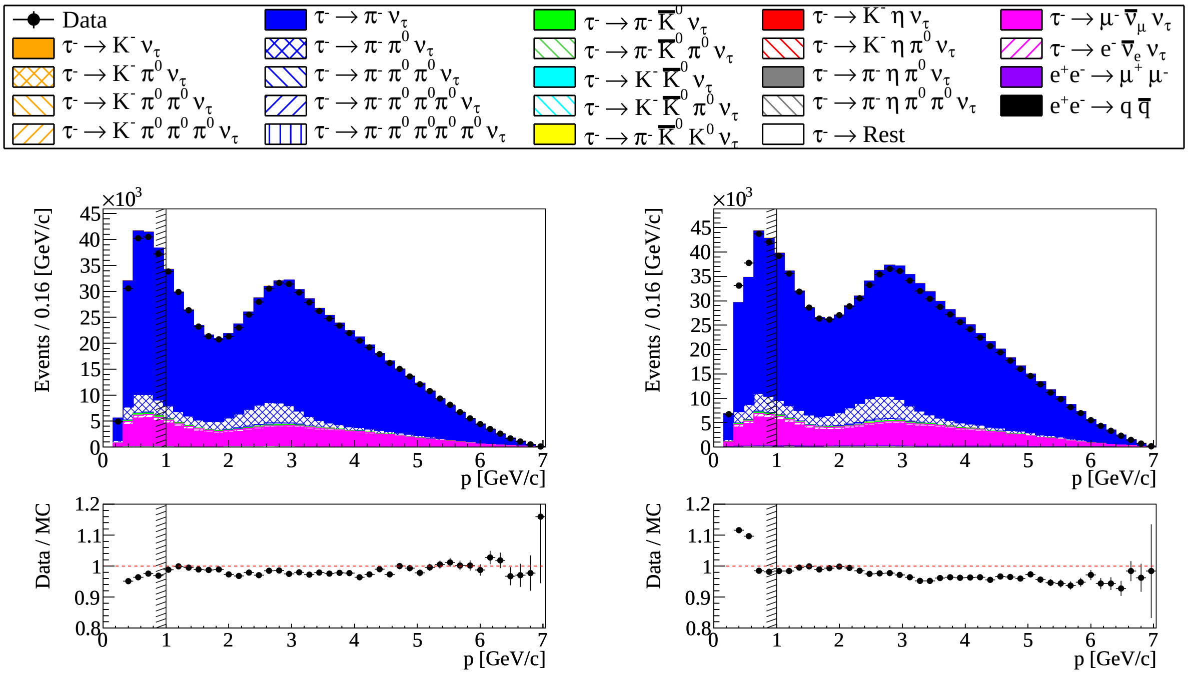

(a) $\tau^- \to \pi^- \nu_\tau$, e-tag

(b) $\tau^- \to \pi^- \nu_\tau$, μ-tag

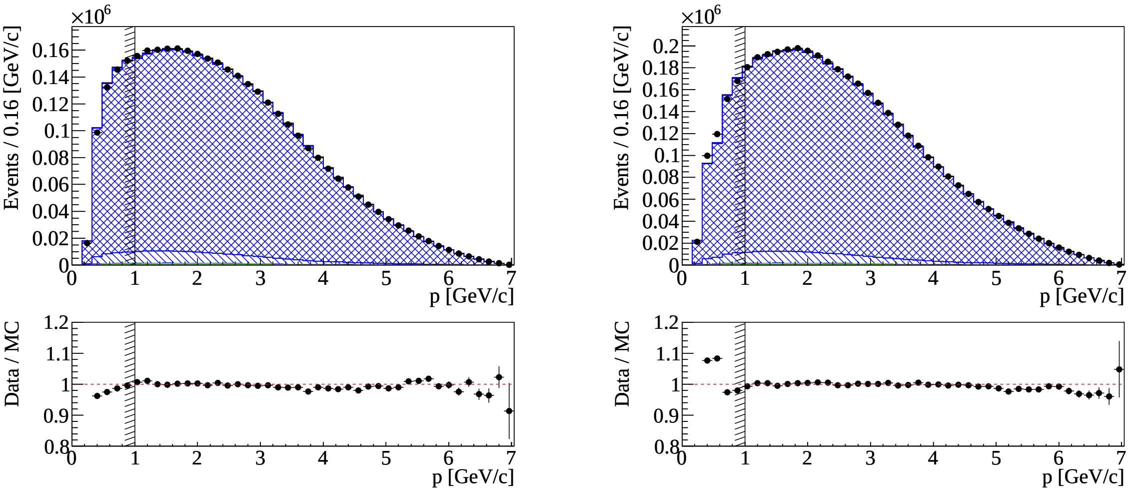

(c) $\tau^- \to \pi^- \pi^0 \nu_\tau$, e-tag

(d) $\tau^- \to \pi^- \pi^0 \nu_\tau$, μ-tag

Figure 6.3.: Distribution of the tag lepton momentum for selected $\tau^- \to \pi^- \nu_\tau$ and $\tau^- \to \pi^- \pi^0 \nu_\tau$ candidates, displayed separately for the e-tag and μ-tag samples. The data set (black circles) of the runs 1–6 is used which corresponds to and integrated luminosity of $473.8\,\mathrm{fb}^{-1}$. The different simulated processes are displayed as stacked histograms with different colors and hatch styles. The simulated samples are scaled such that the number of generated events of a certain process corresponds to the number of such events expected in the e^+e^- collisions. The vertical black line indicates the requirement imposed on the shown quantity.

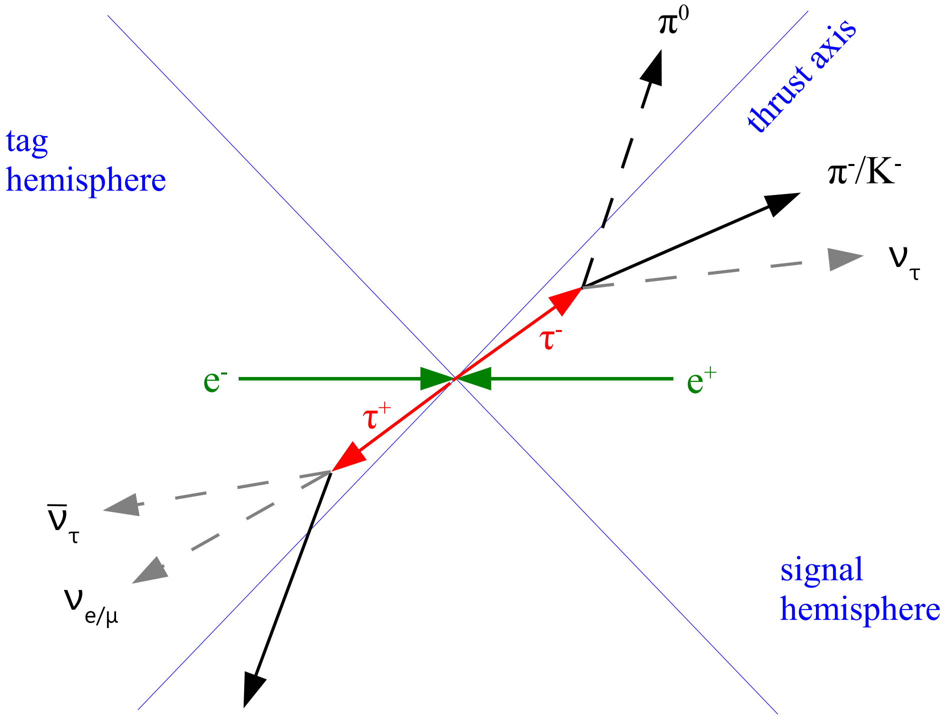

Figure 6.4.: A schematic illustration of a $e^+e^- \to \tau^+\tau^-$ event in the center-of-mass system of the τ leptons (red arrows). The displayed τ^+ lepton decays into a charged lepton, i. e., an electron or a muon, and two neutrinos. The other shown τ decay is $\tau^- \to h^-\pi^0\pi^0\nu_\tau$, where $h = \pi, K$. The τ leptons decay already inside the beam pipe, and therefore cannot be observed directly. Charged final state particles indicated by black solid lines are measured with the tracking devices. The π^0's (dashed lines) are reconstructed in their dominant decay channel, $\pi^0 \to \gamma\gamma$, from the photons measured with the electromagnetic calorimeter. The neutrinos (grey dashed lines) escape undetected. The event is divided in two hemispheres defined by a plane perpendicular to the thrust axis. This axis approximates the direction of the τ leptons, and is defined in Section 6.2.2. The so called signal hemisphere contains the reconstructed particles produced in the signal decay, i. e., the decay under study. The other hemisphere is called tag hemisphere, and contains the reconstructed charged lepton (tag lepton) originating from the decay of the second τ. The technique of tagging is explained in the text.

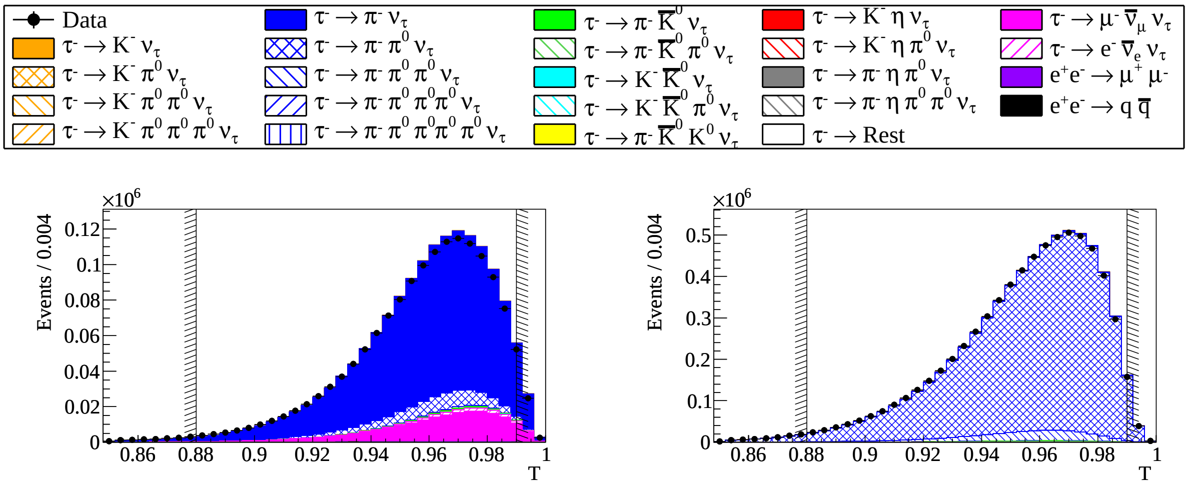

(a) $\tau^- \to \pi^- \nu_\tau$

(b) $\tau^- \to \pi^- \pi^0 \nu_\tau$

Figure 6.5.: Distribution of the thrust for selected $\tau^- \to \pi^- \nu_\tau$ and $\tau^- \to \pi^- \pi^0 \nu_\tau$ candidates.

6.2.3. Charge conservation

In correctly reconstructed $e^+e^- \to \tau^+\tau^-$ events where both τ's decay into one charged particle the sum of the charges amounts to $Q_{tot} = 0$. $e^+e^- \to q\bar{q}$ events are selected as τ-pair candidates if the quark fragmentation produces only few charged particles or if some charged particles are not reconstructed. In the latter case, Q_{tot} is not necessarily equal to zero. If particles are lost the total charge can be $Q = 0, -2, 2$, (because exactly two charged particles are reconstructed). Therefore, the following requirement is applied to suppress $e^+e^- \to q\bar{q}$ events:

$$Q_{tot} := \sum_{i=1}^{2} Q_i = 0 \tag{6.10}$$

where Q_i is the charge of the i^{th} particle .
Similarly, this requirement suppresses $e^+e^- \to \tau^+\tau^-$ events, where any of the two τ leptons decays into more than one charged particle, e. g., $\tau^- \to \pi^-\pi^+\pi^-\nu_\tau$, and two of the final state particles escape detection.

6.2.4. Missing mass

Every signal event contains three neutrinos. Neutrinos cannot be measured directly. However, the missing momentum four-vector, $\widehat{p}_{\text{miss}}$, can be calculated from the energy and direction of the initial-state particles, i. e., the electron and positron in e^+e^- collisions, and the reconstructed final-state particles:

$$\widehat{p}_{\text{miss}} = \widehat{p}_{ee} - \sum \widehat{p}_i, \tag{6.11}$$

where $\widehat{p}_{ee}$ is the momentum four-vector of the colliding electron and positron, and $\widehat{p}_i$ the momentum four-vector of each reconstructed particle.

The missing mass, which is sizable in τ-pair events because of the neutrinos, is calculated from the momentum four-vector according to

$$m_{\mathrm{miss}} = \sqrt{E_{\mathrm{miss}}^2 - p_{\mathrm{miss}}^2}. \tag{6.12}$$

Due to detector effects m_{miss} can take negative values.

The missing mass is used to reject $e^+e^- \to l^+l^-(\gamma)$ with $l = e, \mu$ events and two-photon events.

In $e^+e^- \to l^+l^-(\gamma)$ events m_{miss} is zero if all final-state particles are reconstructed. The vast majority of these events can be easily discarded by loose selection criteria applied on m_{miss} [4]. However, $e^+e^- \to l^+l^-(\gamma)$ events where a radiated photon is not detected are more difficult to be distinguished from τ events.

As listed in Section 3.3.2, Bhabha events are not included in the simulation used in this analysis. Due to the huge $e^+e^- \to e^+e^-(\gamma)$ production cross section of $\approx 40\,\mathrm{nb}$ ([28]) a very large number of $e^+e^- \to e^+e^-(\gamma)$ events would have to be generated to simulate a sufficiently large number of such special $e^+e^- \to e^+e^-(\gamma)$ that can be misidentified as τ-pair events. The production of such a large data sample is very CPU time and disk space consuming. A contamination of the $e^+e^- \to \tau^+\tau^-$ event sample with $e^+e^- \to e^+e^-(\gamma)$ events can therefore appear as an excess of data events. $e^+e^- \to \mu^+\mu^-(\gamma)$ events are included in the simulation.

The distributions shown in Figure 6.6 show a data excess in the small m_{miss} region which is attributes to the $e^+e^- \to e^+e^-(\gamma)$ events. The following criterion is applied to reject $e^+e^- \to l^+l^-(\gamma)$ events:

$$\begin{aligned} m_{\mathrm{miss}} &> 2.5\,\mathrm{GeV}/c^2 \quad \text{if} \quad n_{\pi^0} = 0, \\ m_{\mathrm{miss}} &> 1.0\,\mathrm{GeV}/c^2 \quad \text{if} \quad n_{\pi^0} > 0, \end{aligned} \tag{6.13}$$

where n_{π^0} is the number of reconstructed π^0's in the event. The threshold values of the missing mass are chosen differently for decays with π^0's because m_{miss} is reduced on average by the presence of an additional particle.

It should be further noted, that the probability to misidentify a $e^+e^- \to l^+l^-(\gamma)$ event with $l = e, \mu$ as an $e^+e^- \to \tau^+\tau^-$ event decreases with the number of reconstructed π^0's. Therefore, the observed data excess gets less significant with increasing n_{π^0}.

In two-photon events, the missing mass tends to have large values, because in most cases the scattered beam particles which carry most of the energy are not detected. To discard this type of events a maximum missing mass is required:

$$m_{\mathrm{miss}} < 7.5\,\mathrm{GeV}/c^2. \tag{6.14}$$

---

[4] In addition, selection criteria applied on the thrust (Figure 6.5) and the acoplanarity (Figure 6.11) also suppress $e^+e^- \to l^+l^-(\gamma)$ events in the π^0-less decays modes.

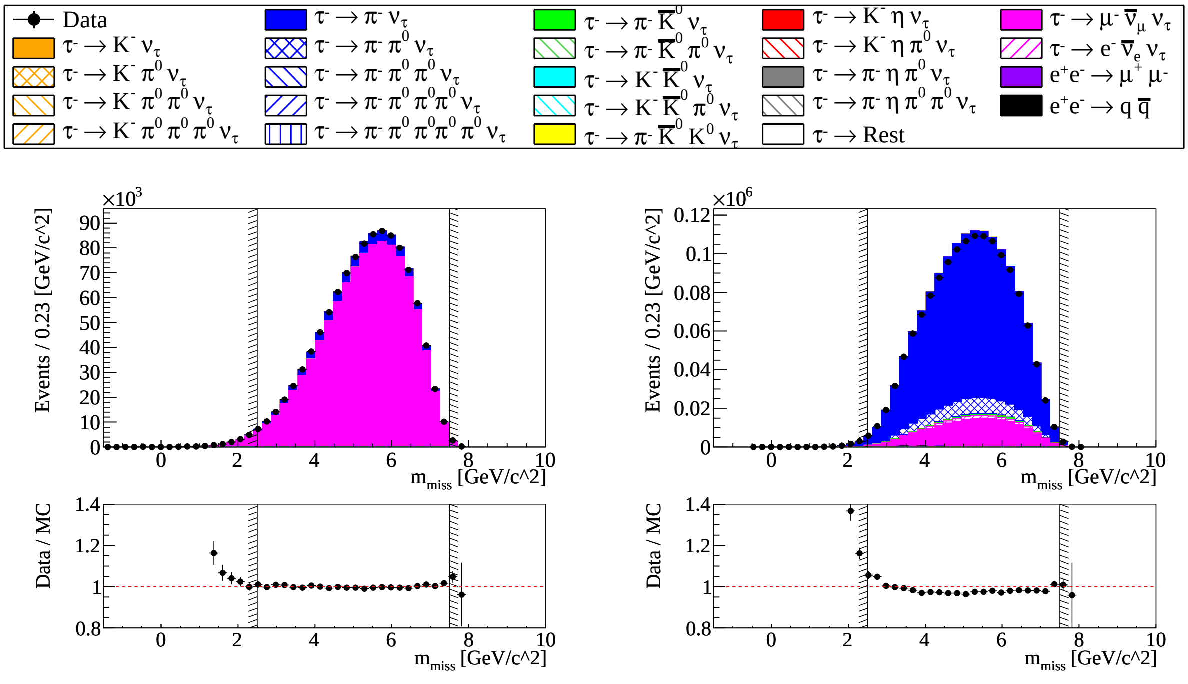

(a) $\tau^+ \to \mu^+ \nu_\mu \overline{\nu}_\tau$ **(b)** $\tau^- \to \pi^- \nu_\tau$

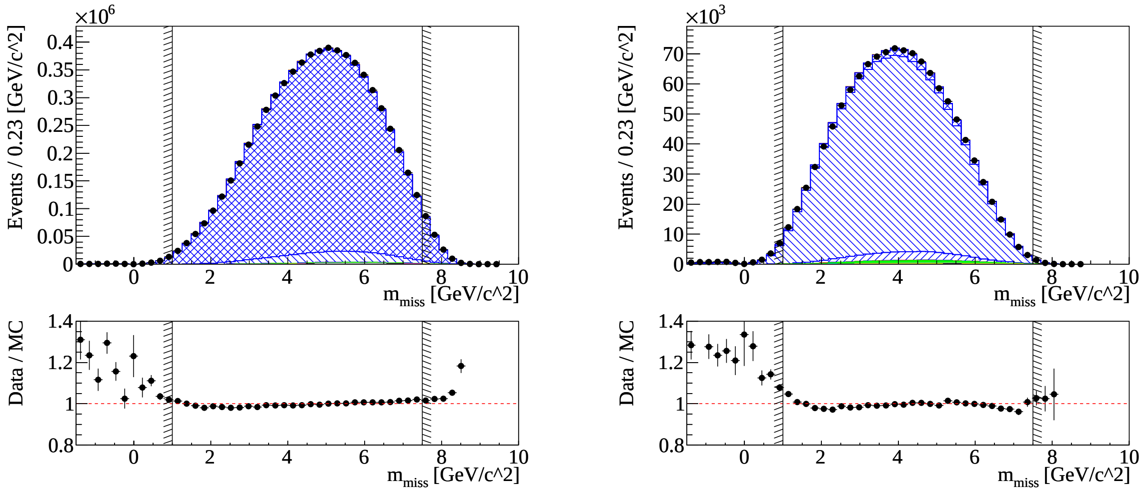

(c) $\tau^- \to \pi^- \pi^0 \nu_\tau$ **(d)** $\tau^- \to \pi^- (2\pi^0) \nu_\tau$

Figure 6.6.: Distribution of the missing mass, m_{miss}, for the different control modes.

6.3. Selection of $\tau^- \rightarrow \mathrm{K}^-/\pi^-(\mathrm{n}\pi^0)\nu_\tau$ decays

The selection of $e^+e^- \rightarrow \tau^+\tau^-$ events as well as the reconstruction of the lepton tag, i. e., the decays $\tau^- \rightarrow l^-\overline{\nu}_l\nu_\tau$, has already been described in Section 6.2. In this section, the reconstruction of the various control and signal decay modes is described. Additional criteria to reject remaining background events are discussed.

6.3.1. Separation of the selected $e^+e^- \rightarrow \tau^+\tau^-$ events in signal mode samples

The number and type of particles which fulfill the criteria described in Chapter 5 are used to sort the events according to the signal decay modes.

The charged track reconstructed in the signal hemisphere has to be identified as a charged pion or kaon:

$$\text{charged track in signal hemisphere: } \pi^- \;\; or \;\; K^- \tag{6.15}$$

The particle identification criteria and the identification efficiencies are described in Chapter 5. The events are further sorted into different decay modes according to the number of reconstructed π^0's:

$$\begin{aligned} n_{\pi^0} &= 0\text{-}4 \;\; (\text{if } \pi^-), \\ n_{\pi^0} &= 0\text{-}3 \;\; (\text{if } K^-). \end{aligned} \tag{6.16}$$

In addition, events of the type $\tau^+ \rightarrow e^+\nu_e\overline{\nu}_\tau$, $\tau^- \rightarrow \mu^-\overline{\nu}_\mu\nu_\tau$ are selected, where both leptons have to fulfill the criteria used to select a tag lepton. The decay $\tau^- \rightarrow \mu^-\overline{\nu}_\mu\nu_\tau$ is defined as the signal decay. In summary, events containing the following reconstructed decays are selected:

$$\begin{array}{l} \text{Signal decay modes} \\ \tau^- \rightarrow \pi^-(3\pi^0)\nu_\tau \\ \tau^- \rightarrow \pi^-(4\pi^0)\nu_\tau \\ \tau^- \rightarrow K^-\nu_\tau \\ \tau^- \rightarrow K^-\pi^0\nu_\tau \\ \tau^- \rightarrow K^-(2\pi^0)\nu_\tau \\ \tau^- \rightarrow K^-(3\pi^0)\nu_\tau \end{array} \tag{6.17}$$

$$\begin{array}{l} \text{Control decay modes} \\ \tau^- \rightarrow \mu^-\overline{\nu}_\mu\nu_\tau, \\ \tau^- \rightarrow \pi^-\nu_\tau \\ \tau^- \rightarrow \pi^-\pi^0\nu_\tau \\ \tau^- \rightarrow \pi^-(2\pi^0)\nu_\tau \end{array} \tag{6.18}$$

For each signal decay mode the background contribution can be divided in three categories:

1. Signal cross feed: Signal decays which are reconstructed in the wrong signal decay mode. For example, an event containing the $\tau^- \rightarrow K^-\pi^0\nu_\tau$ decay can enter the

$\tau^- \to K^-\nu_\tau$ decay mode sample if the π^0 escaped detection.

2. Cross feed from control modes: Control decays which are reconstructed as a signal decay. For example, a $\tau^- \to \pi^-\nu_\tau$ decay can be misidentified as a $\tau^- \to K^-\nu_\tau$ decay, due to the sizable pion-as-kaon misidentification probability (Chapter 7).

3. Background: Events in the signal mode samples which do not contain neither a true signal decay nor a control decay. Such events are either $e^+e^- \to q\overline{q}$, $e^+e^- \to l^+l^-$ with $l = e, \mu$, and two-photon events. Moreover, τ-pair events with τ decays other than the signal or control decays are included in this category. This are for example τ decays into more than one charged particle, e. g., the $\tau^- \to \pi^-\pi^+\pi^-\nu_\tau$ decay, where two pions were not reconstructed. Or events with τ decays into one charged particle and a K^0_S or η, which can decay further into neutral particles.

Criteria to reject remaining cross-feed events and background events are described in the next sections.

6.3.2. Cross feed rejection

Misidentification of pions as kaons

The first source of cross feed is the misidentification of charged pions as kaons, and vice versa. The latter case is less frequent, since the branching fractions of τ decays with kaons are about 10–100 times smaller than the branching fractions of decays with pions and the same number of π^0's.

The misidentification fraction of pions as kaons is significant. The kaon identification criteria applied in this analysis are chosen to minimize this fraction. They are described in Section 5.2.3.

Figure 6.7 shows the distribution of the kaon momentum, p_K, in the $\tau^- \to K^-\nu_\tau$ and $\tau^- \to K^-\pi^0\nu_\tau$ decay modes. The fraction of selected events containing τ decays into a pion, i. e., decays where a pion is misidentified as a kaon, is large at high p_K. Pions have on average larger momenta than kaons due to their smaller mass. The kaon momentum is required to be

$$p_K < 3.5\,\mathrm{GeV}/c. \tag{6.19}$$

The remaining fraction of cross feed due to the misidentification of pions as kaons is listed in Table 10.1 for each signal decay mode.

An additional benefit from this requirement is a reduction of the particle identification uncertainty. In this analysis, pion and kaon control samples are used to determine momentum-dependent correction factors for simulated events (Chapter 7) to account for differences between data and simulation in the PID performance. The control samples contain only a small number of control tracks with momenta above 3.5 GeV/c. Identification correction factors in this high-momentum region can only be determined with a large statistical uncertainty[5]. For this reason the same momentum restriction is

---

[5] The statistical uncertainty of the standard PID correction values provided by the *BABAR* PID-group is also large for high track momenta.

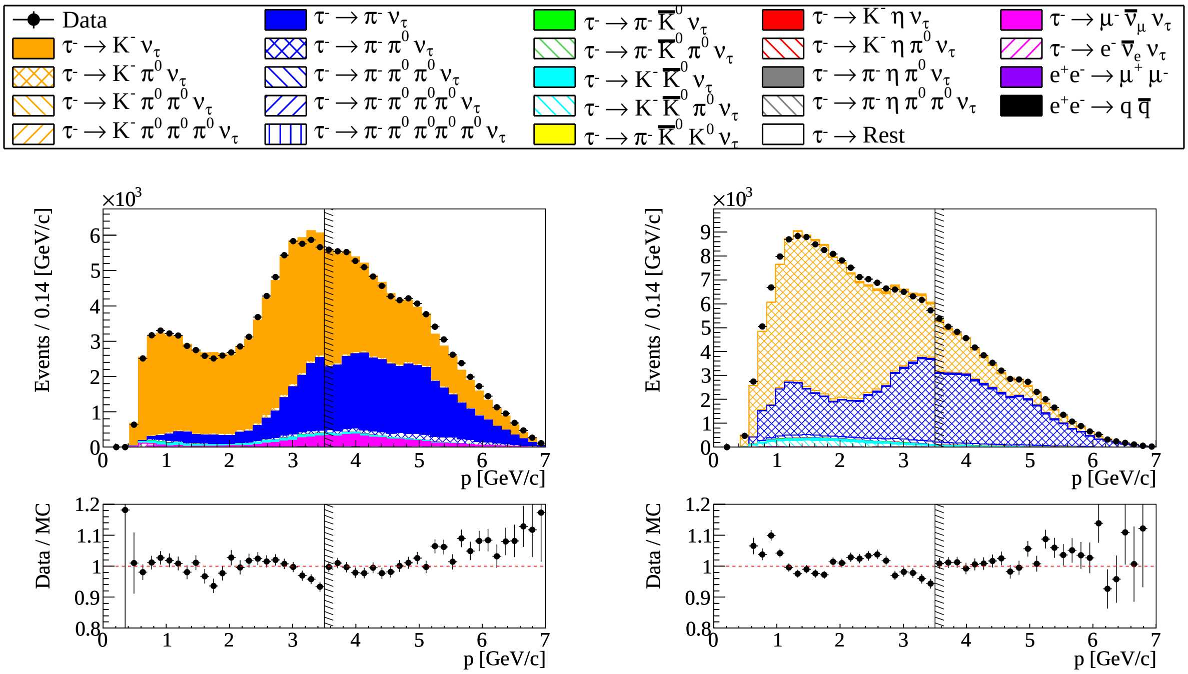

(a) $\tau^- \to K^-\nu_\tau$ **(b)** $\tau^- \to K^-\pi^0\nu_\tau$

Figure 6.7.: Distribution of the kaon momentum for selected $\tau^- \to K^-\nu_\tau$ and $\tau^- \to K^-\pi^0\nu_\tau$ candidates.

also used for pions:

$$p_\pi < 3.5\,\mathrm{GeV}/c, \tag{6.20}$$

The final-state particles in $e^+e^- \to l^+l^-(\gamma)$ events have on average larger momenta than particles produced in τ decays, because the latter contain at least one neutrino. The above requirement is therefore also imposed on the muon in selected $(\tau^+ \to e^+\nu_e\overline{\nu}_\tau$ and $\tau^- \to \mu^-\overline{\nu}_\mu\nu_\tau)$ candidates .

Additional π^0 candidates

A further source of cross feed are additional spurious π^0's. In that case, $\tau^- \to h(n\pi^0)\nu_\tau$ $(h = \pi^-/K^-)$ decays are reconstructed as $\tau^- \to h(n+m)\pi^0\nu_\tau$ decays, where m is the number of the spurious π^0's. A spurious π^0 can be reconstructed from random photons not originating from a π^0. Such photon candidates can be either background photons or split-offs. The latter are described in detail in Chapter 8. This type of cross feed is suppressed by the applied photon selection which discards background photons (Section 5.3.1).

Another type of spurious π^0's are π^0 candidates which contain photons radiated by the tag lepton, since the reconstruction of photon candidates is not restricted to the signal hemisphere. These cross-feed events are expected to have a large angle, $\alpha^{\mathrm{CMS}}_{\pi^0 h}$ with $h = \pi^-, K^-$, between the π^0 direction and the charged hadron direction in the signal hemisphere determined in the center-of-mass frame. The distribution of $\alpha^{\mathrm{CMS}}_{\pi^0 h}$ is shown in Figure 6.8 for the control mode $\tau^- \to \pi^-\pi^0\nu_\tau$ and for the $\tau^- \to K^-\pi^0\nu_\tau$ signal mode. The number of cross-feed events with $(n+m)$ π^0's is very small. Nevertheless,

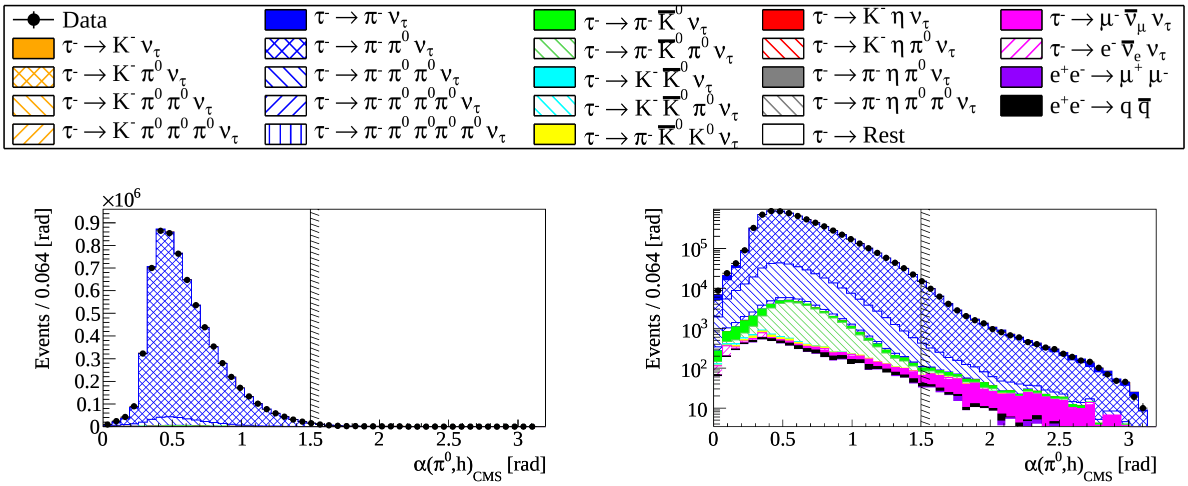

(a) $\tau^- \to \pi^- \pi^0 \nu_\tau$ **(b)** $\tau^- \to \pi^- \pi^0 \nu_\tau$ (logarithmic scale)

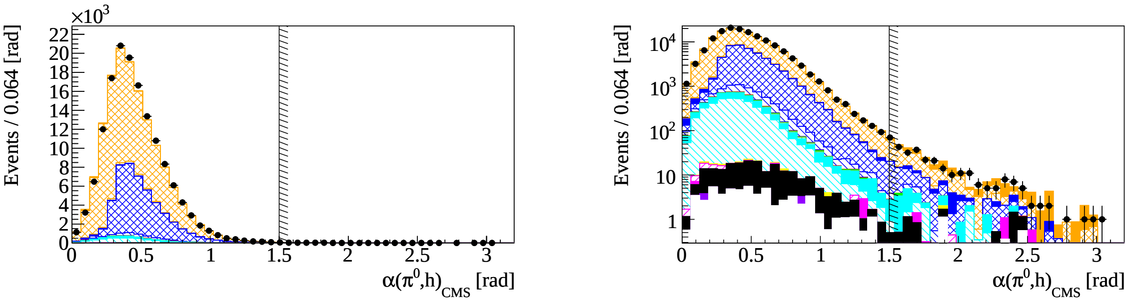

(c) $\tau^- \to K^- \pi^0 \nu_\tau$ **(d)** $\tau^- \to K^- \pi^0 \nu_\tau$ (logarithmic scale)

Figure 6.8.: Distribution of the angle between the π^0 direction and the hadron direction for selected $\tau^- \to \pi^- \pi^0 \nu_\tau$ and $\tau^- \to K^- \pi^0 \nu_\tau$ candidates.

the following requirement is imposed:

$$\alpha^{\text{CMS}}_{\pi^0 h} < 1.5\,\text{rad}. \tag{6.21}$$

Undetected π^0's

Finally, the last source of cross feed are lost π^0's. Neutral pions can be lost if one or both daughter photons are not detected. This can happen if a photon is outside the acceptance region of the calorimeter, or its measured energy is smaller than the minimal energy required in this analysis. In general, a $\tau^- \to hn\pi^0\nu_\tau$ decay is misidentified as an $\tau^- \to h(n-m)\pi^0\nu_\tau$ decay, where m is the number of missed π^0's.

Such events can contain photons not assigned to a π^0's candidate. In the following these photons are denoted as *additional photons*. An event contains additional photons if one of the two daughter photons of a missed π^0 is detected, or a remaining background photon is present. The distribution of the number of additional photons, $N_{\gamma_{add}}$, is shown in Figure 6.9 for the $\tau^- \to \pi^-\pi^0\nu_\tau$ and $\tau^- \to \pi^-(2\pi^0)\nu_\tau$ control modes. The fraction of cross feed events with more than one π^0 is 26% in the sample of selected $\tau^- \to \pi^-\pi^0\nu_\tau$

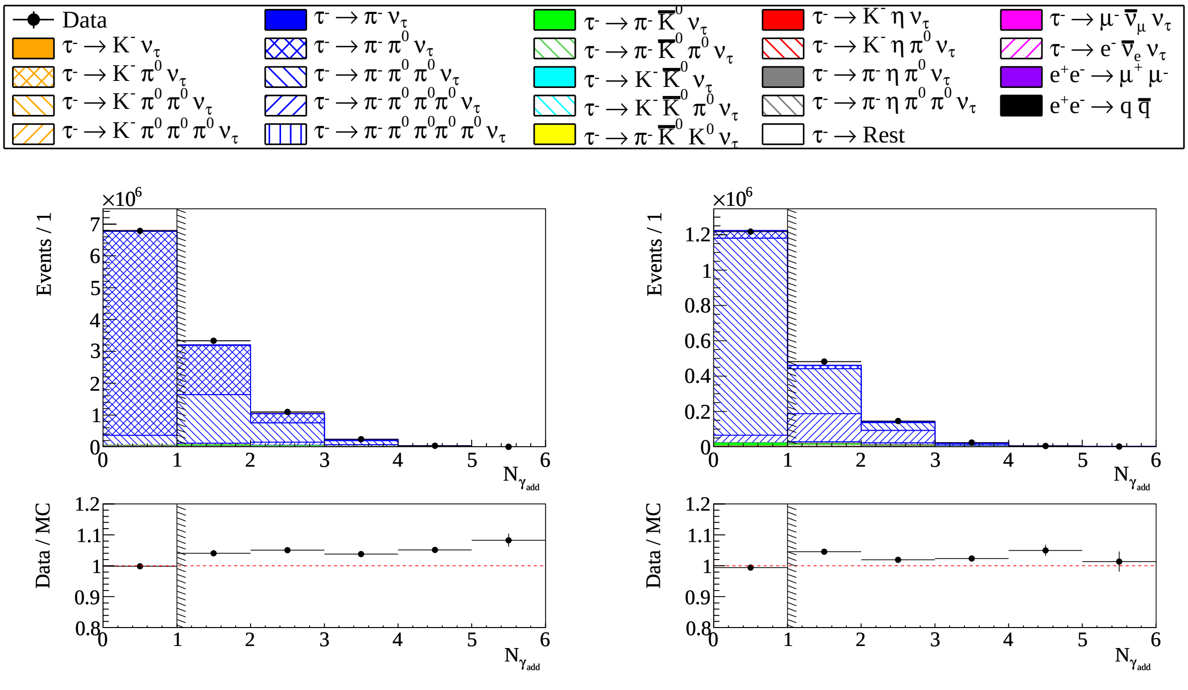

(a) $\tau^- \to \pi^-\pi^0\nu_\tau$

(b) $\tau^- \to \pi^-(2\pi^0)\nu_\tau$

Figure 6.9.: Distribution of the number of additional photons in the event, $N_{\gamma_{add}}$, for selected $\tau^- \to \pi^-\pi^0\nu_\tau$ and $\tau^- \to \pi^-(2\pi^0)\nu_\tau$ candidates.

candidates. This fraction decreases to 5% in events with $N_{\gamma_{add}} = 0$ (first interval of the distribution).

The data excess which can be seen in the data/MC ratio for $N_{\gamma_{add}} > 0$ is due to so called split-offs. This effect is discussed in detail in Chapter 8.
Events with

$$N_{\gamma_{add}} > 0 \tag{6.22}$$

are rejected to reduce the fraction of cross-feed events with (n+m) π^0's, where $m > 0$.

6.3.3. Background rejection

In this paragraph the criteria to reject remaining background events, i. e., events not containing any of the signal or control decays (Equation 6.18 and Equation 6.17), are presented.

Rejection of two-photon events

For $e^+e^- \to e^+e^- f\bar{f}$ events, where f denotes a fermion, the total transverse momentum in the center-of-mass frame is $p^T_{tot} = |(\vec{p}^{\,\text{CMS}}_{f+} + \vec{p}^{\,\text{CMS}}_{f-})^T|$. Since the undetected energetic electron and positron are scattered at small angles along the beam pipe, p^T_{tot} tends to have small values for two-photon event that are wrongly reconstructed as τ-pair events. The missing energy $E_{\text{miss}} = \sqrt{s} - p^{\text{CMS}}_{f+} - p^{\text{CMS}}_{f-}$, where $\sqrt{s}$ is the center-of-mass energy of the colliding electron and positron, is large. The following ratio is therefore small for wrongly reconstructed two-photon events:

$$\frac{p^T_{l,h}}{E_{\mathrm{miss}(l,h)}} = \frac{|(\vec{p}_l^{\,\mathrm{CMS}} + \vec{p}_h^{\,\mathrm{CMS}})^T|}{\sqrt{s} - p_l^{\mathrm{CMS}} - p_h^{\mathrm{CMS}}} \tag{6.23}$$

where l denotes the tag lepton and h is the charged hadron in the reconstructed event. This quantity is used to separate τ-pair events from two-photon events.

Figure 6.10 shows the distribution of this quantity for all π^0-less signal modes selected in this analysis, i. e., for the decay modes $\tau^- \to \mu^-\overline{\nu}_\mu\nu_\tau$, $\tau^- \to \pi^-\nu_\tau$, and $\tau^- \to K^-\nu_\tau$. In all three distributions a clear data event excess is visible at low values. This excess is attributed to two-photon events, which are not included in the simulation. No significant data excess is observed in decays with π^0's, e. g., $\tau^- \to \pi^-\pi^0\nu_\tau$ (also shown in Figure 6.10), since the presence of π^0's significantly suppresses two-photon background. The following criterion is imposed:

$$\begin{aligned} \frac{p^T_{l,h}}{E_{\mathrm{miss}(l,h)}} > 0.2 \quad \text{for} \quad & \tau^- \to \mu^-\overline{\nu}_\mu\nu_\tau, \\ & \tau^- \to \pi^-\nu_\tau, \\ & \tau^- \to K^-\nu_\tau. \end{aligned} \tag{6.24}$$

For decays with π^0's no requirement is applied.

Rejection of $e^+e^- \to l^+l^-$ events with $l = e, \mu$

Ignoring photon radiation, the angle between the final-state particles in $e^+e^- \to e^+e^-$ and $e^+e^- \to \mu^+\mu^-$ events is 180° in the center-of-mass frame. In the laboratory frame the particles are boosted in z-direction due to the different energies of the beam electron and positron. The back-to-back signature is conserved in the x-y plane, which is perpendicular to the boost direction. The acoplanarity

$$\Delta\phi_{12} = \begin{cases} |\phi_1 - \phi_2| & \text{if } |\phi_1 - \phi_2| \leq 180^\circ, \\ 360^\circ - |\phi_1 - \phi_2| & \text{if } |\phi_1 - \phi_2| > 180^\circ. \end{cases} \tag{6.25}$$

where ϕ_i are the azimuthal angles of the two charged final-state particles, is therefore $\Delta\phi_{12} = 180^\circ$ in $e^+e^- \to e^+e^-$ and $e^+e^- \to \mu^+\mu^-$ events. In signal events the value of the acoplanarity is smaller due to the presence of neutrinos and π^0's.

The distribution of the acoplanartiy is shown in Figure 6.11. The data excess in the distribution for the $\tau^- \to \pi^-\nu_\tau$ decay mode at large values is due to $e^+e^- \to e^+e^-$ events, which are not included in the simulation. No excess is present in events with π^0's, as can be seen in the distribution for the $\tau^- \to \pi^-\pi^0\nu_\tau$ control mode. To reject remaining two-photon events in signal decay modes without π^0's the acoplanarity is required to be

$$\begin{aligned} \Delta\phi_{12} < 2.95\,\mathrm{rad} \quad \text{for} \quad & \tau^- \to \mu^-\overline{\nu}_\mu\nu_\tau, \\ & \tau^- \to \pi^-\nu_\tau, \\ & \tau^- \to K^-\nu_\tau. \end{aligned} \tag{6.26}$$

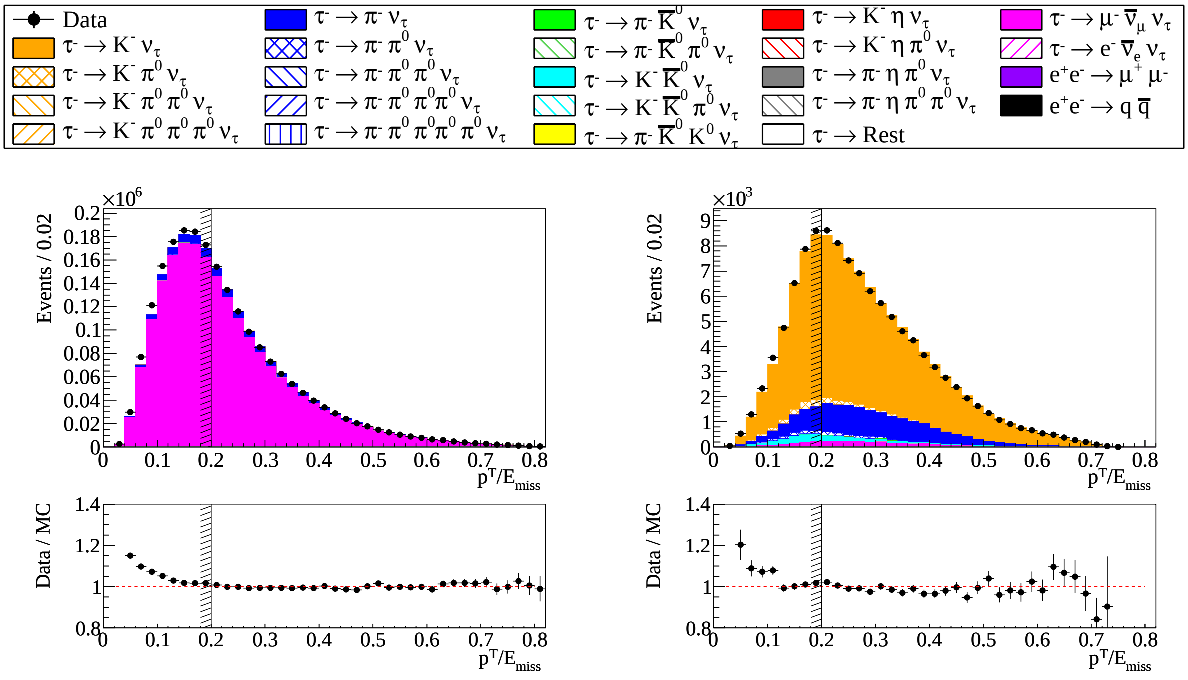

(a) $\tau^- \to \mu^- \overline{\nu}_\mu \nu_\tau$ **(b)** $\tau^- \to K^- \nu_\tau$

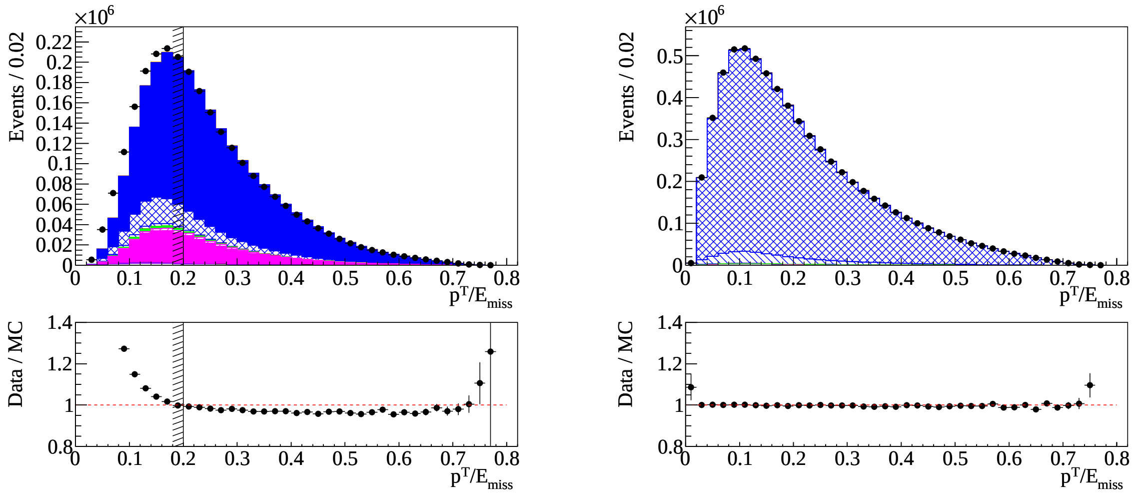

(c) $\tau^- \to \pi^- \nu_\tau$ **(d)** $\tau^- \to \pi^- \pi^0 \nu_\tau$

Figure 6.10.: Distribution of the ratio of the total transvers momentum and the missing energy for all reconstructed decay modes without π^0's in the final state, and for selected $\tau^- \to \pi^- \pi^0 \nu_\tau$ candidates. A minimum $p^T/E_{\text{miss}} = 0.2$ is required for the π^0-less modes.

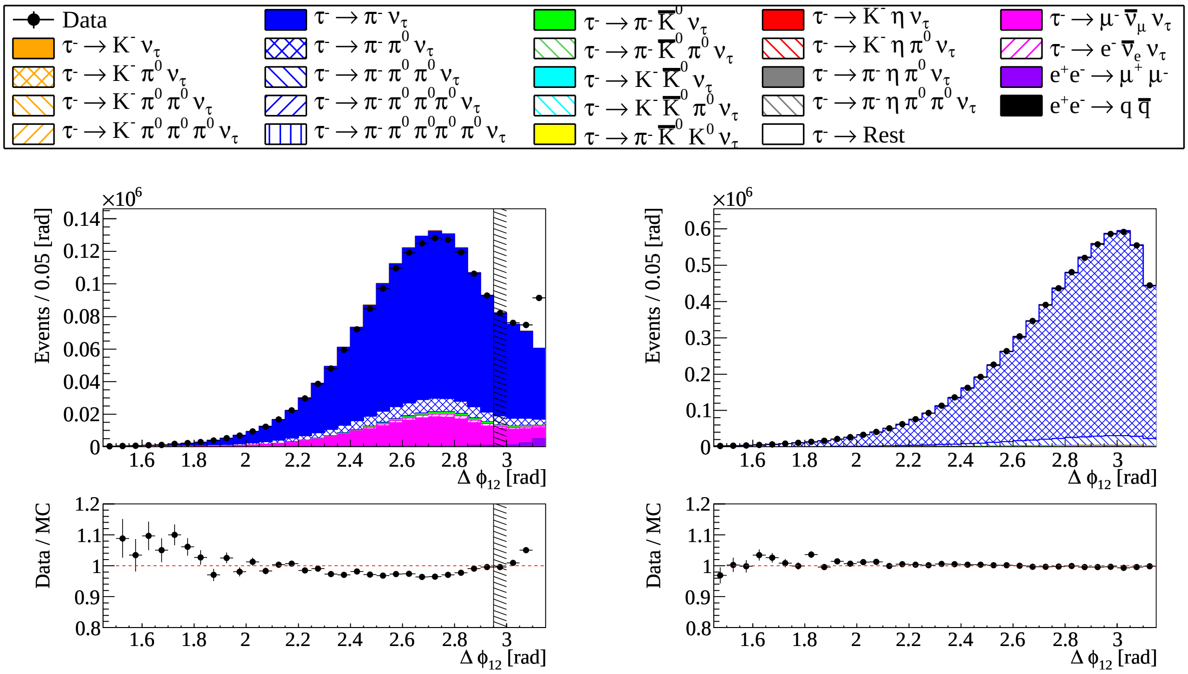

(a) $\tau^- \to \pi^- \nu_\tau$

(b) $\tau^- \to \pi^- \pi^0 \nu_\tau$

Figure 6.11.: Distribution of the acoplanarity, $\Delta\phi_{12}$, for $\tau^- \to \pi^- \nu_\tau$ and $\tau^- \to \pi^- \pi^0 \nu_\tau$ candidates.

Rejection of decays containing K^0 and η mesons

A type of τ-pair background that has a very similar signature as the signal events is due to τ decays into one charged particle, n π^0's, and additional K^0 or η mesons:

$$\begin{aligned} &\tau^- \to \pi^- \overline{K}^0 \nu_\tau \\ &\tau^- \to \pi^- \overline{K}^0 \pi^0 \nu_\tau \\ &\tau^- \to K^- \overline{K}^0 \nu_\tau \\ &\tau^- \to K^- \overline{K}^0 \pi^0 \nu_\tau \\ &\tau^- \to \pi^- \overline{K}^0 K^0 \nu_\tau \end{aligned} \tag{6.27}$$

$$\begin{aligned} &\tau^- \to K^- \eta \nu_\tau \\ &\tau^- \to K^- \eta \pi^0 \nu_\tau \\ &\tau^- \to \pi^- \eta \pi^0 \nu_\tau \\ &\tau^- \to \pi^- \eta \pi^0 \pi^0 \nu_\tau \end{aligned} \tag{6.28}$$

An event which contains a K^0_L can enter a signal decay mode if the K^0_L is not identified. Moreover, a decay with a K^0_S or η is selected as a signal decay with two or three additional π^0's, if the K^0_S decays in the channel $K^0_S \to \pi^0\pi^0$ and the η decay is $\eta \to \pi^0\pi^0\pi^0$, respectively. The decays with K^0's and η mesons are excluded in the branching fraction measurements in this analysis. Their contribution to the background is determined from simulation and subtracted from the data events. Some of the branching fractions of the decays with K^0's and η's, which are used in the simulation, are only known with a relatively large uncertainty (Table 10.4). Therefore, the reduction of this background is important. This is done by imposing requirements on two quantities, the invariant $n\pi^0$-mass and the missing mass in a τ decay.

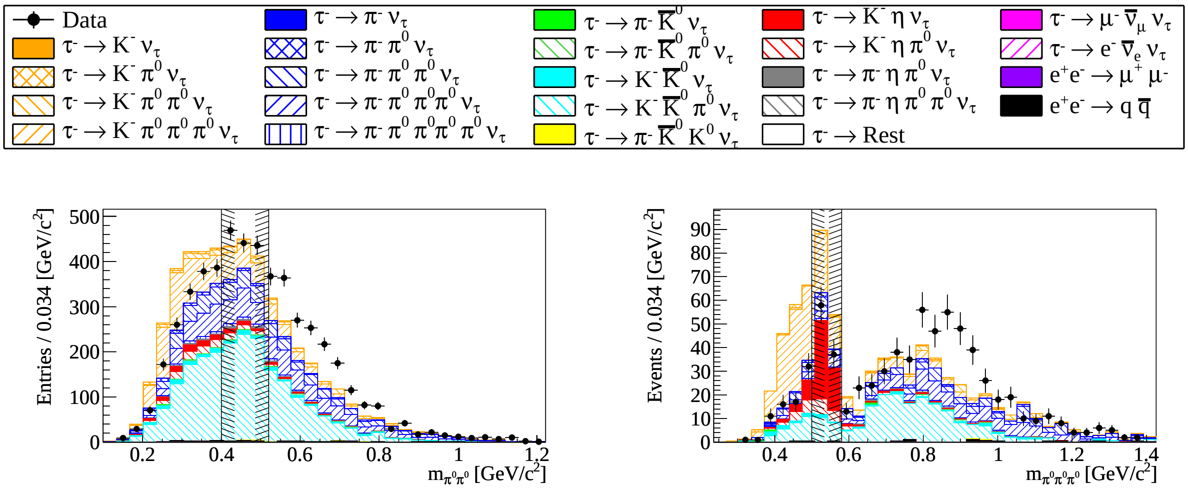

(a) $\tau^- \to K^-(3\pi^0)\nu_\tau$ **(b)** $\tau^- \to K^-(3\pi^0)\nu_\tau$

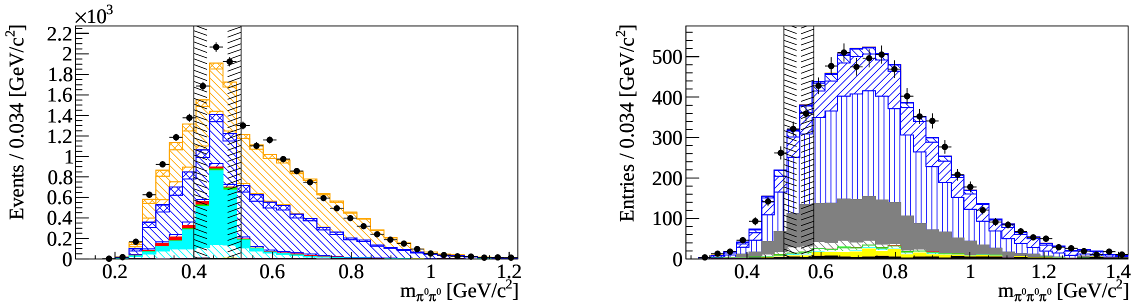

(c) $\tau^- \to K^-(2\pi^0)\nu_\tau$ **(d)** $\tau^- \to \pi^-(4\pi^0)\nu_\tau$

Figure 6.12.: Distribution of the invariant $\pi^0\pi^0$-mass, $m_{\pi^0\pi^0}$, and $\pi^0\pi^0\pi^0$-mass, $m_{\pi^0\pi^0\pi^0}$, for selected $\tau^- \to K^-(2\pi^0)\nu_\tau$, $\tau^- \to K^-(3\pi^0)\nu_\tau$, and $\tau^- \to \pi^-(4\pi^0)\nu_\tau$ candidates.

1. **Invariant $n\pi^0$-mass** Figure 6.12 shows the distributions of the invariant $\pi^0\pi^0$-mass, $m_{\pi^0\pi^0}$, for the $\tau^- \to K^-(2\pi^0)\nu_\tau$ and $\tau^- \to K^-(3\pi^0)\nu_\tau$ decay modes, and the invariant $\pi^0\pi^0\pi^0$-mass, $m_{\pi^0\pi^0\pi^0}$, for the $\tau^- \to K^-(3\pi^0)\nu_\tau$ and $\tau^- \to \pi^-(4\pi^0)\nu_\tau$ decay modes. The number of entries per event in each histogram corresponds to the number of possible two-π^0 (three-π^0) combinations.

In Figures 6.12c and 6.12b, which have one entry per event, clear peaks are visible in the $\pi^0\pi^0$-mass and $\pi^0\pi^0\pi^0$-mass distributions in the region of the K^0_S-mass, $m_{K^0_S} = 497.6\,\mathrm{MeV}/c^2$, and the η-mass, $m_\eta = 547.8\,\mathrm{MeV}/c^2$ [4]. This regions are excluded from selection. The distributions with more than one possible combination of π^0's do not contain clear peaks in the mass regions of the K^0_S and η, because of the uniform distribution of invariant mass values for random combinations of π^0's. Nevertheless, the mass regions of the K^0_S and η are also excluded in these distributions.

The imposed selection criteria are

$$
\begin{aligned}
&(m_{\pi^0\pi^0} < 0.40\,\mathrm{GeV}/c^2 \;||\; m_{\pi^0\pi^0} > 0.52\,\mathrm{GeV}/c^2) && \text{for } \tau^- \to K^-(2\pi^0)\nu_\tau, \\
& && \phantom{\text{for }}\tau^- \to K^-(3\pi^0)\nu_\tau, \\
&(m_{\pi^0\pi^0\pi^0} < 0.50\,\mathrm{GeV}/c^2 \;||\; m_{\pi^0\pi^0\pi^0} > 0.58\,\mathrm{GeV}/c^2) && \text{for } \tau^- \to K^-(3\pi^0)\nu_\tau, \\
& && \phantom{\text{for }}\tau^- \to \pi^-(4\pi^0)\nu_\tau.
\end{aligned}
$$

2. **Missing mass in a τ decay**

Events containing K^0 mesons, especially undetected K_L^0, are removed using an estimate of the missing mass in a τ decay, $m_{\text{miss}(\tau\text{-decay})}$. This quantity has been introduced in [10]. The squared missing mass in the τ decay is

$$m^2_{\text{miss}(\tau\text{-decay})} = E^2_{\text{miss}(\tau\text{-decay})} - p^2_{\text{miss}(\tau\text{-decay})} \tag{6.29}$$

where $E_{\text{miss}(\tau\text{decay})}$ and $p_{\text{miss}(\tau\text{-decay})}$ are the missing energy and momentum in the τ decay given by the four vector

$$\widehat{p}_{\text{miss}(\tau\text{-decay})} = \begin{pmatrix} E_{\text{miss}(\tau\text{-decay})} \\ \vec{p}_{\text{miss}(\tau\text{-decay})} \end{pmatrix} = \widehat{p}_\tau - \widehat{p}_{\pi/Kn\pi^0}. \tag{6.30}$$

While the momentum four-vector of the reconstructed final state particles

$$\widehat{p}_{\pi/Kn\pi^0} = \widehat{p}_{\pi/K} + \sum_{i=1}^{n} \widehat{p}_{\pi_i^0} \tag{6.31}$$

is measured, the four-momentum of the τ, $\widehat{p}_\tau$, has to be estimated. The energy of the τ^- is determined by the center-of-mass energy in the e^+e^- collisions

$$E_\tau = \sqrt{s/2}, \tag{6.32}$$

and the momentum magnitude is given by

$$p_\tau = \sqrt{(s/2)^2 - m_\tau^2}, \tag{6.33}$$

where $m_\tau = 1.78\,\mathrm{GeV}/c^2$ [4]. The direction of the τ momentum vector is, however, not known. As a rough estimate of the direction the thrust axis as defined in Section 6.2.2 is used. The momentum four-vector of the τ is therefore estimated by

$$\widehat{p}_\tau = (E_\tau, p_\tau \cdot \vec{n}_T). \tag{6.34}$$

The distribution of $m^2_{\text{miss}(\tau\text{-decay})}$ is shown in Figure 6.13 for the decay modes $\tau^- \to \pi^-(3\pi^0)\nu_\tau$, $\tau^- \to \pi^-(4\pi^0)\nu_\tau$, $\tau^- \to K^-\nu_\tau$, and $\tau^- \to K^-\pi^0\nu_\tau$, and in Figures A.1 and A.2 in the Appendix A for the other signal modes. The expected value of $m^2_{\text{miss}(\tau\text{-decay})}$ for signal decays should be in principle close to zero, since all final-state particles except for the neutrino are detected. However, due to the rough estimate of the τ direction the distribution of $m^2_{\text{miss}(\tau\text{-decay})}$

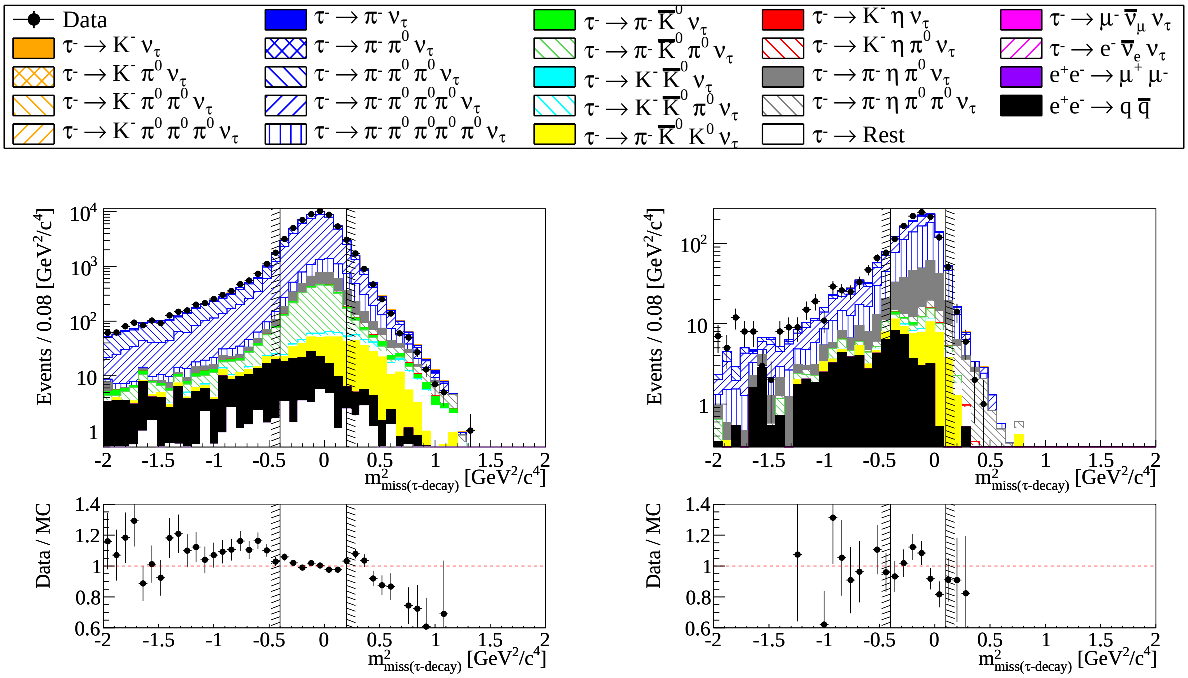

(a) $\tau^- \to \pi^-(3\pi^0)\nu_\tau$ **(b)** $\tau^- \to \pi^-(4\pi^0)\nu_\tau$

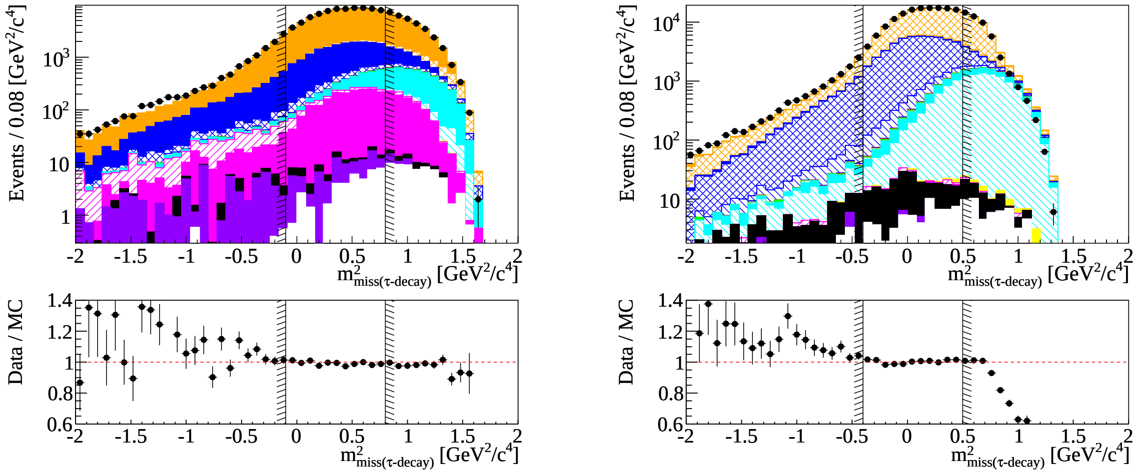

(c) $\tau^- \to K^-\nu_\tau$ **(d)** $\tau^- \to K^-\pi^0\nu_\tau$

Figure 6.13.: Distribution of the squared missing mass in the τ decay, $m_{\text{miss}(\tau-decay)}$ for selected $\tau^- \to \pi^-(3\pi^0)\nu_\tau$,$\tau^- \to \pi^-(4\pi^0)\nu_\tau$, $\tau^- \to K^-\nu_\tau$, and $\tau^- \to K^-\pi^0\nu_\tau$ candidates.

is broad. Nevertheless, background events with undetected particles, e. g., not reconstructed K_L^0 mesons, have larger $m_{\text{miss}(\tau\text{-decay})}$ values than signal events. A maximum $m^2_{\text{miss}(\tau\text{-decay})}$ is required to reject these events. Moreover, cross-feed events with wrongly reconstructed additional particles have negative $m^2_{\text{miss}(\tau\text{-decay})}$ values, e. g., $\tau^- \to \pi^-(2\pi^0)\nu_\tau$ events which are reconstructed as $\tau^- \to \pi^-(3\pi^0)\nu_\tau$ candidates. Therefore, in addition to the requirement of a maximum $m^2_{\text{miss}(\tau\text{-decay})}$, also a minimum $m^2_{\text{miss}(\tau\text{-decay})}$ is required. The applied criteria are

$$\begin{array}{llcll}
\tau^- \to \pi^-\nu_\tau & : 0.0 & < m^2_{\text{miss}(\tau\text{-decay})} < & 1.6 & \text{GeV}^2/c^4 \\
\tau^- \to \pi^-\pi^0\nu_\tau & : -0.4 & < m^2_{\text{miss}(\tau\text{-decay})} < & 1.0 & \text{GeV}^2/c^4 \\
\tau^- \to \pi^-(2\pi^0)\nu_\tau & : -0.4 & < m^2_{\text{miss}(\tau\text{-decay})} < & 0.7 & \text{GeV}^2/c^4 \\
\tau^- \to \pi^-(3\pi^0)\nu_\tau & : -0.4 & < m^2_{\text{miss}(\tau\text{-decay})} < & 0.2 & \text{GeV}^2/c^4 \\
\tau^- \to \pi^-(4\pi^0)\nu_\tau & : -0.4 & < m^2_{\text{miss}(\tau\text{-decay})} < & 0.1 & \text{GeV}^2/c^4 \\
\tau^- \to K^-\nu_\tau & : -0.1 & < m^2_{\text{miss}(\tau\text{-decay})} < & 0.8 & \text{GeV}^2/c^4 \\
\tau^- \to K^-\pi^0\nu_\tau & : -0.4 & < m^2_{\text{miss}(\tau\text{-decay})} < & 0.5 & \text{GeV}^2/c^4 \\
\tau^- \to K^-(2\pi^0)\nu_\tau & : -0.4 & < m^2_{\text{miss}(\tau\text{-decay})} < & 0.2 & \text{GeV}^2/c^4 \\
\tau^- \to K^-(3\pi^0)\nu_\tau & : -0.5 & < m^2_{\text{miss}(\tau\text{-decay})} & & \text{GeV}^2/c^4 \\
\tau^- \to \mu^-\overline{\nu}_\mu\nu_\tau & : 0.0 & < m^2_{\text{miss}(\tau\text{-decay})} & & \text{GeV}^2/c^4
\end{array} \tag{6.35}$$

Misidentified muons and electrons in the $\tau^- \to \pi^-\nu_\tau$ control decay mode

Figure 6.14a shows the pion momentum in the $\tau^- \to \pi^-\nu_\tau$ decay mode. A significant fraction of $\tau^- \to e^-\overline{\nu}_e\nu_\tau$ and $\tau^- \to \mu^-\overline{\nu}_\mu\nu_\tau$ events is visible in the distribution. In these events a muon or an electron are misidentifies as a pion. The largest contribution of these decays is found at low momentum values. The purity of the selected control decay mode $\tau^- \to \pi^-\nu_\tau$ is improved by requiring

$$p_\pi > 1.0\,\text{GeV}/c \quad \text{for} \quad \tau^- \to \pi^-\nu_\tau. \tag{6.36}$$

Since kaons can be better separated from electrons and muons than pions, this criterion is not imposed for the selection of the $\tau^- \to K^-\nu_\tau$ decay (Figure 6.14b).

6.3.4. Distributions of selected events

In this section, example distributions for the control and signal event samples selected according to the criteria summarized in Table 6.1 and Table 6.2 are shown and discussed.

Figure 6.15 shows the distribution of the tag-lepton momentum for all control modes[6].

---

[6] The the tag-lepton momentum distribution shows a minimum at approximately 2.0 GeV/c for the $\tau^- \to \mu^-\overline{\nu}_\mu\nu_\tau$ and $\tau^- \to \pi^-\nu_\tau$ control decays. A minimum is also visible in the momentum distribution of the tag lepton for the $\tau^- \to K^-\nu_\tau$ decay (Figure 6.16c), as well as in all signal track momentum distributions for the π^0-less decays (Figures 6.17 and 6.18). This structure results from the criterion applied on the $\frac{p^T_{l,h}}{E_{\text{miss},(l,h)}}$ ratio (Section 6.3.3). Events which contain charged tracks with momenta

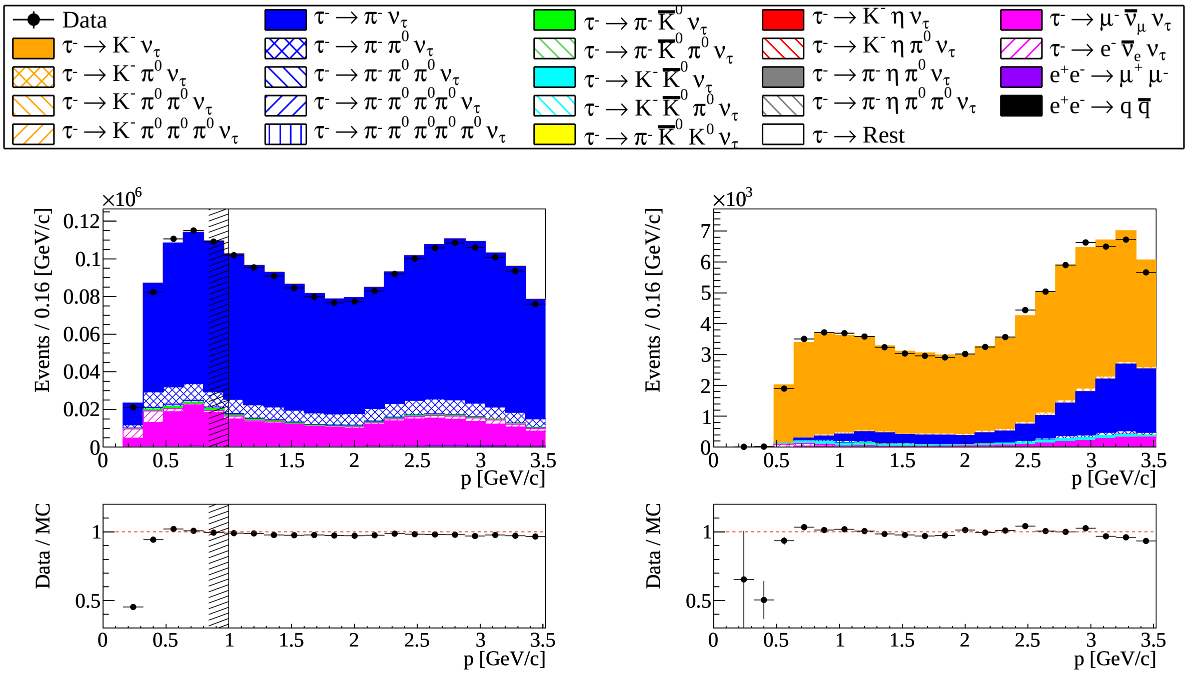

(a) $\tau^- \to \pi^- \nu_\tau$ **(b)** $\tau^- \to K^- \nu_\tau$

Figure 6.14.: Distribution of the pion and kaon momentum for selected $\tau^- \to \pi^- \nu_\tau$ and $\tau^- \to K^- \nu_\tau$ candidates.

The agreement between data and the simulation after all corrections considered in this analysis are applied is very good for all control modes except for the $\tau^- \to \pi^- \nu_\tau$ mode. In the $\tau^- \to \pi^- \nu_\tau$ mode, a 3% deviation from the expected event yield is observed. This deviation is discussed in Chapter 9 in the context of the π^0 correction, and in Section 10.5, where the results and systematic effects of this measurement are summarized. It is attributed to a large uncertainty of the separation of muons and pions in this decay mode.

Figure 6.16 displays the tag-lepton momentum for the signal decays. The description of data by the simulation is good[7] for the $\tau^- \to K^- \nu_\tau$, $\tau^- \to K^- \pi^0 \nu_\tau$, $\tau^- \to K^-(2\pi^0)\nu_\tau$, and $\tau^- \to \pi^-(3\pi^0)\nu_\tau$ decay modes. The number of selected $\tau^- \to \pi^-(4\pi^0)\nu_\tau$ and $\tau^- \to K^-(3\pi^0)\nu_\tau$ candidates is small. Therefore, the information content of the data/MC ratio is statistically limited.

Figures 6.17 and 6.18 show the distributions of the signal track momentum for all selected decay modes. A good agreement between data and the simulated distribution is observed for the $\tau^- \to \mu^- \overline{\nu}_\mu \nu_\tau$, $\tau^- \to \pi^- \nu_\tau$, and $\tau^- \to \pi^- \pi^0 \nu_\tau$ modes. For the modes with a kaon in the final state deviations are visible in the data/MC ratios which can

---

of similar magnitude are more often rejected by that requirement than events with a low-momentum track and a high-momentum track. The average track momentum is approximately 2 GeV/c. Therefore the minimum appears at this value.

[7] The branching fractions of the signal decays used in the simulation are scaled to the values measured in this analysis. The data/MC ratio distributions is therefore on average one. A good description of the data by the simulation is concluded if the ratio is uniform as a function of the shown quantity.

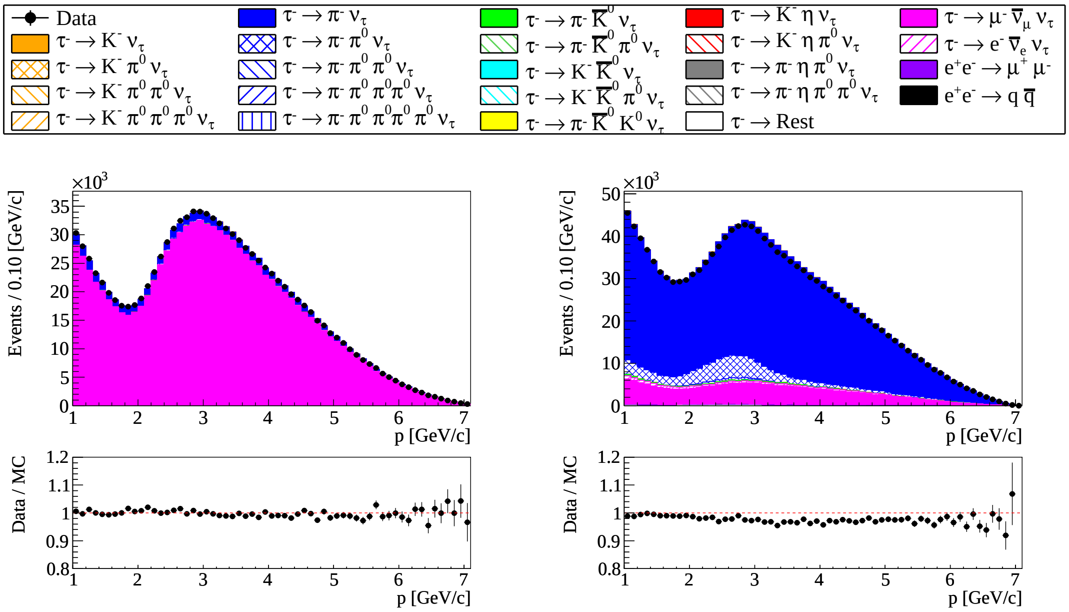

(a) $\tau^- \to \mu^- \overline{\nu}_\mu \nu_\tau$ **(b)** $\tau^- \to \pi^- \nu_\tau$

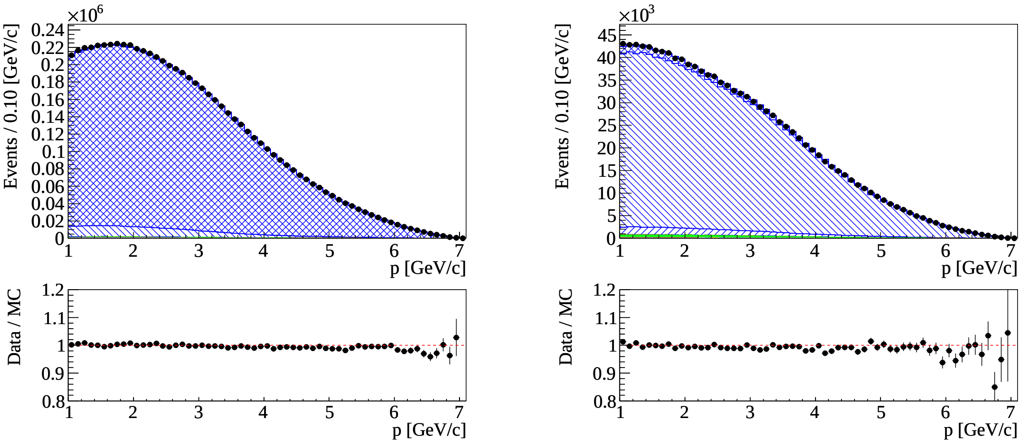

(c) $\tau^- \to \pi^- \pi^0 \nu_\tau$ **(d)** $\tau^- \to \pi^- (2\pi^0) \nu_\tau$

Figure 6.15.: Distribution of the tag lepton momentum for the control modes.

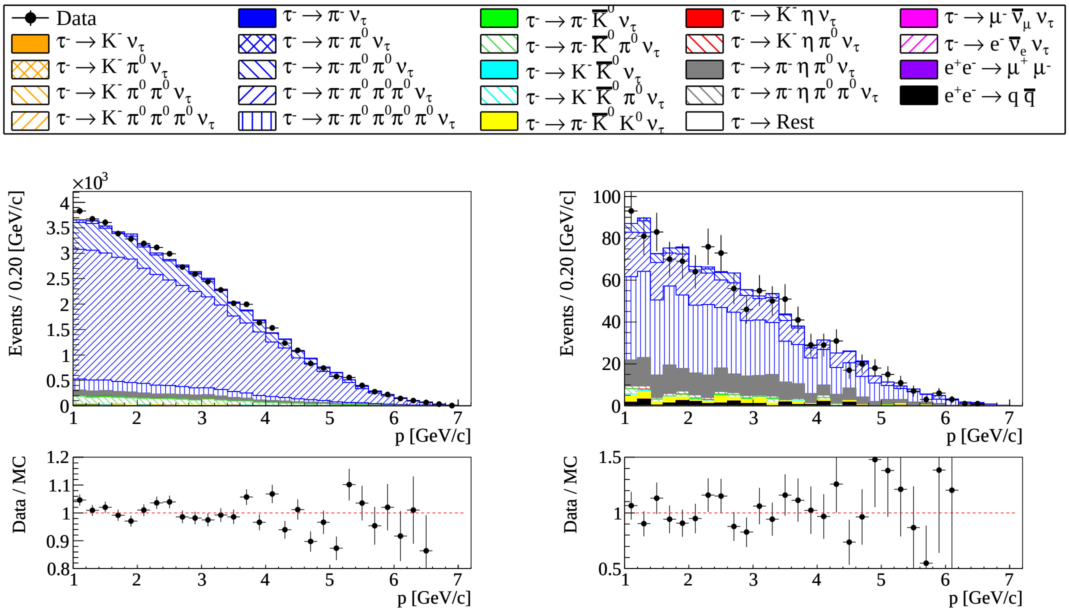

(a) $\tau^- \to \pi^-(3\pi^0)\nu_\tau$ **(b)** $\tau^- \to \pi^-(4\pi^0)\nu_\tau$

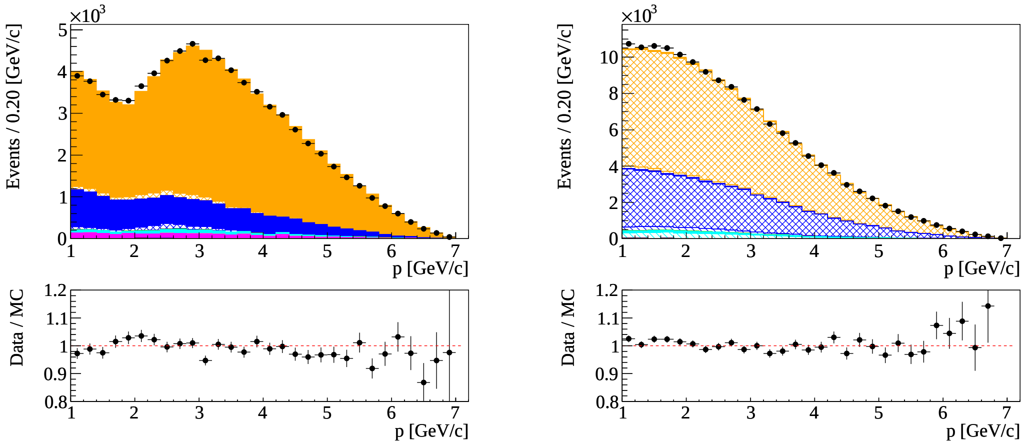

(c) $\tau^- \to K^-\nu_\tau$ **(d)** $\tau^- \to K^-\pi^0\nu_\tau$

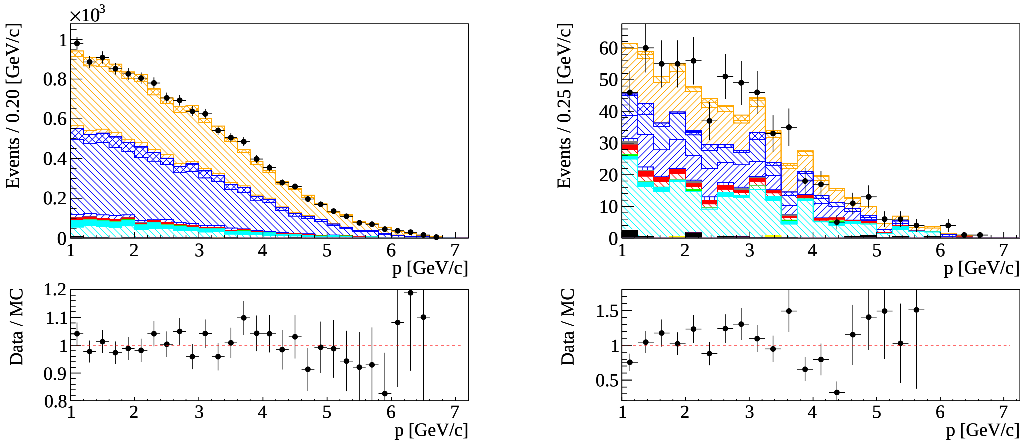

(e) $\tau^- \to K^-(2\pi^0)\nu_\tau$ **(f)** $\tau^- \to K^-(3\pi^0)\nu_\tau$

Figure 6.16.: Distribution of the tag lepton momentum for the signal modes.

Table 6.1.: Selection criteria applied to all decay modes.

Quantity	Selection criterion
Lepton tag	e-tag, μ-tag
Tag lepton momentum	$p_{\text{tag-lepton}} > 1\,\text{GeV}/c$
Signal track momentum	$p_{\pi,K,\mu} < 3.5\,\text{GeV}/c$
Topology	1-1
Thrust	0.88<T<0.99
Total charge	$Q_{tot} = 0$
Number of additional photons	$N_{\gamma^{add}} = 0$
Hadron-π^0 angle	$\alpha_{h\pi^0}^{\text{CMS}} < 1.5\,\text{rad}$

be explained with the relatively large uncertainty of the pion-as-kaon misidentification which is discussed in Chapter 7. The particle identification uncertainty is not taken into account in the figures.

Significant deviations are also visible in the data/MC ratio of the $\tau^- \to \pi^-(2\pi^0)\nu_\tau$ and $\tau^- \to \pi^-(3\pi^0)\nu_\tau$ decay modes. This effect is attributed to the insufficient modeling of the resonance structure in the $a_1(1260)$ decay [10]. The $\tau^- \to \pi^-(2\pi^0)\nu_\tau$ decay is dominated by the production of the $a_1(1260)$ resonance:

$$\tau^- \to a_1(1260)\nu_\tau \tag{6.37}$$

which also contributes to the resonance structure of the $\tau^- \to \pi^-(3\pi^0)\nu_\tau$ decay. The properties of this resonance are not well known. The subsequent decay of the $a_1(1260)$ has been studies by the CLEO collaboration in [48]. Besides the dominant contribution of the $a_1(1260) \to \rho^-\pi^0$ decay to the total width, significant contributions from the decays into $\sigma^-\pi^0$, $f_0(1370)\pi^0$, and $f_2(1270)\pi^0$ have been found in model-dependent fits to Dalitz plots. However, only the contribution from the ρ^- resonance is considered in the simulated $\tau^- \to \pi^-(2\pi^0)\nu_\tau$ sample used in this analysis:

$$a_1(1260) \to \rho^-(\to \pi\pi^0)\pi^0. \tag{6.38}$$

The observed deviations in the charged pion momentum distribution of the $\tau^- \to \pi^-(2\pi^0)\nu_\tau$ and $\tau^- \to \pi^-(3\pi^0)\nu_\tau$ decay modes are therefore explainable. The $\tau^- \to \pi^-(2\pi^0)\nu_\tau$ decay is used as a control mode and it contributes to the background of signal decays. The branching fraction of that decay determined in this analysis (Chapter 10) agrees with the reference value [4]. Therefore, the effect of the observed deviation on the event selection and thus on the signal branching fractions measurement is assumed to be negligible.

Figures 6.19 and 6.20 show the polar angle of the signal track for the control and signal modes. Also here the deviations due to the kaon identification uncertainty are visible. If the particle identification uncertainty is taken into account, the agreement between data and simulation is reasonable for all modes.

Table 6.2.: Decay-specific selection criteria applied in this analysis.

Quantity	Signal track				$N_{\pi^0} = 0$	$N_{\pi^0} = 1$	$N_{\pi^0} = 2$	$N_{\pi^0} = 3$	$N_{\pi^0} = 4$
particle momentum	π	p	$[\,\mathrm{GeV}/c]$	$>$	1.0	-	-	-	-
Missing mass	all	m_{miss}	$[\,\mathrm{GeV}/c^2]$	$>$	2.5	1.5	1.5	1.5	1.5
Missing mass	all	m_{miss}	$[\,\mathrm{GeV}/c^2]$	$<$	7.5	7.5	7.5	7.5	7.5
Acoplanyrity	all	$\Delta\phi_{12}^{\mathrm{CMS}}$	$[\,\mathrm{rad}]$	$<$	2.95	-	-	-	-
Transv. mom / missing energy	all	$\frac{p_{l,h}^T}{E_{\mathrm{miss}(l,h)}}$		$>$	0.2	-	-	-	-
Missing mass in τ decay	μ	$m^2_{\mathrm{miss}(\tau\text{-decay})}$	$[\,\mathrm{GeV}^2/c^4]$	$>$	0.0	-	-	-	-
Missing mass in τ decay	π	$m^2_{\mathrm{miss}(\tau\text{-decay})}$	$[\,\mathrm{GeV}^2/c^4]$	$>$	0.0	-0.4	-0.4	-0.4	-0.4
Missing mass in τ decay	K	$m^2_{\mathrm{miss}(\tau\text{-decay})}$	$[\,\mathrm{GeV}^2/c^4]$	$>$	-0.1	-0.4	-0.4	-0.4	-
Missing mass in τ decay	μ	$m^2_{\mathrm{miss}(\tau\text{-decay})}$	$[\,\mathrm{GeV}^2/c^4]$	$<$	-	-	-	-	-
Missing mass in τ decay	π	$m^2_{\mathrm{miss}(\tau\text{-decay})}$	$[\,\mathrm{GeV}^2/c^4]$	$<$	1.6	1.0	0.7	0.2	0.1
Missing mass in τ decay	K	$m^2_{\mathrm{miss}(\tau\text{-decay})}$	$[\,\mathrm{GeV}^2/c^4]$	$<$	0.8	0.5	0.2	-	-
Inv. $2\pi^0$ mass	π	$m_{\pi^0\pi^0}$	$[\,\mathrm{GeV}/c^2]$	$<$	-	-	-	-	-
Inv. $2\pi^0$ mass	K	$m_{\pi^0\pi^0}$	$[\,\mathrm{GeV}/c^2]$	$<$	-	-	0.40	0.40	-
Inv. $2\pi^0$ mass	π	$m_{\pi^0\pi^0}$	$[\,\mathrm{GeV}/c^2]$	$>$	-	-	-	-	-
Inv. $2\pi^0$ mass	K	$m_{\pi^0\pi^0}$	$[\,\mathrm{GeV}/c^2]$	$>$	-	-	0.52	0.52	-
Inv. $3\pi^0$ mass	π	$m_{\pi^0\pi^0\pi^0}$	$[GeV/c^2]$	$<$	-	-	-	-	0.50
Inv. $3\pi^0$ mass	K	$m_{\pi^0\pi^0\pi^0}$	$[GeV/c^2]$	$<$	-	-	-	0.50	-
Inv. $3\pi^0$ mass	π	$m_{\pi^0\pi^0\pi^0}$	$[GeV/c^2]$	$>$	-	-	-	-	0.58
Inv. $3\pi^0$ mass	K	$m_{\pi^0\pi^0\pi^0}$	$[GeV/c^2]$	$>$	-	-	-	0.58	-

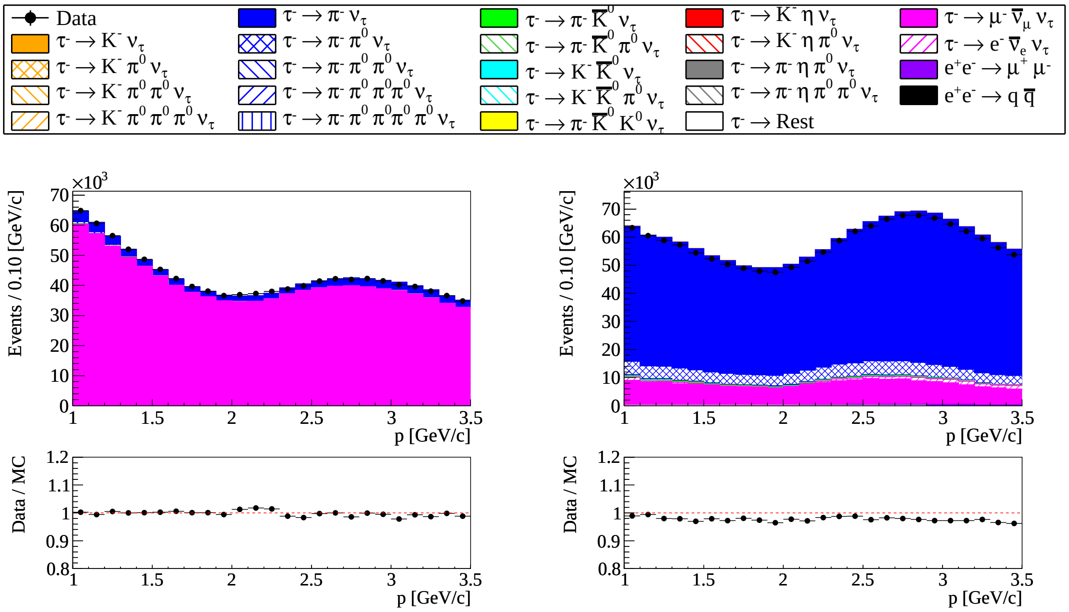

(a) $\tau^- \to \mu^-\overline{\nu}_\mu\nu_\tau$

(b) $\tau^- \to \pi^-\nu_\tau$

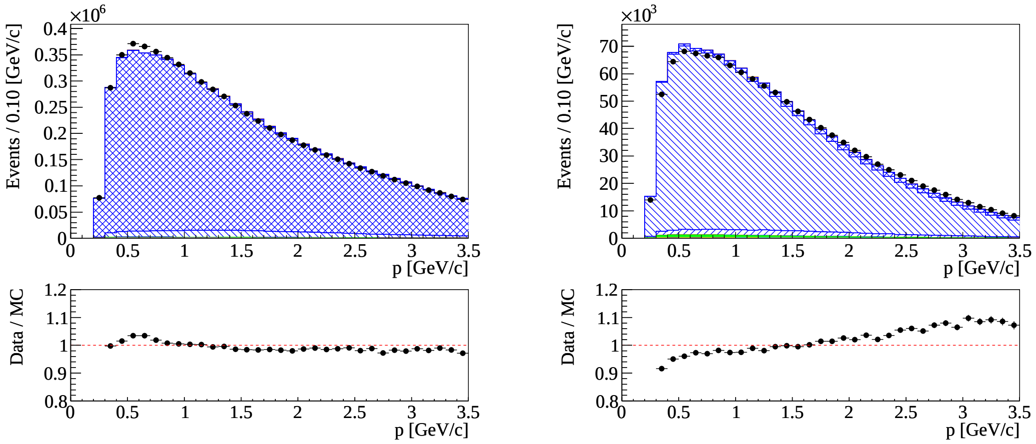

(c) $\tau^- \to \pi^-\pi^0\nu_\tau$

(d) $\tau^- \to \pi^-(2\pi^0)\nu_\tau$

Figure 6.17.: Distribution of the signal track momentum for the control modes.

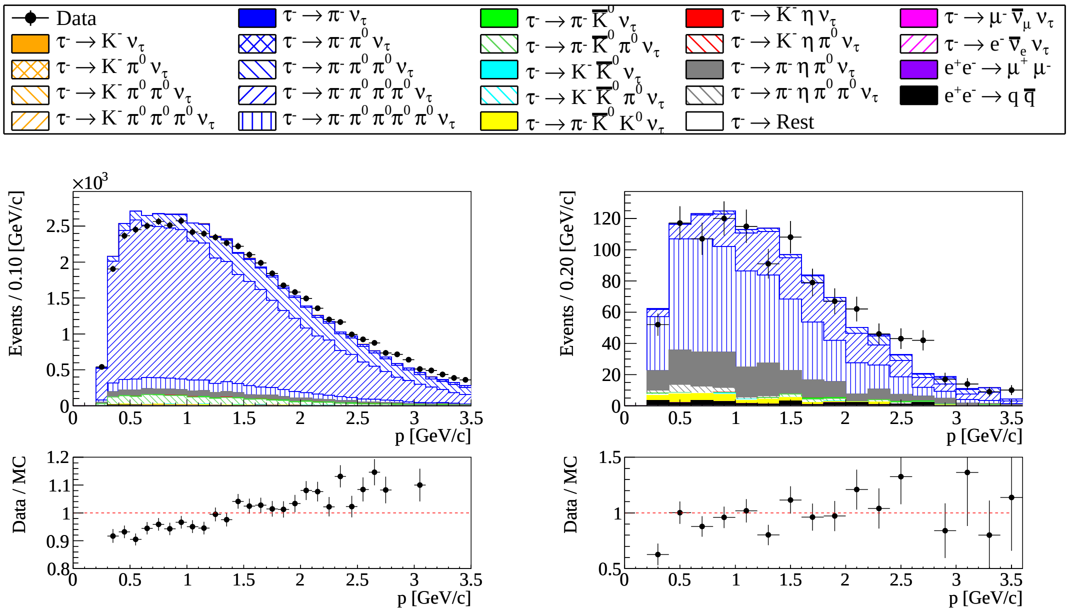

(a) $\tau^- \to \pi^-(3\pi^0)\nu_\tau$ **(b)** $\tau^- \to \pi^-(4\pi^0)\nu_\tau$

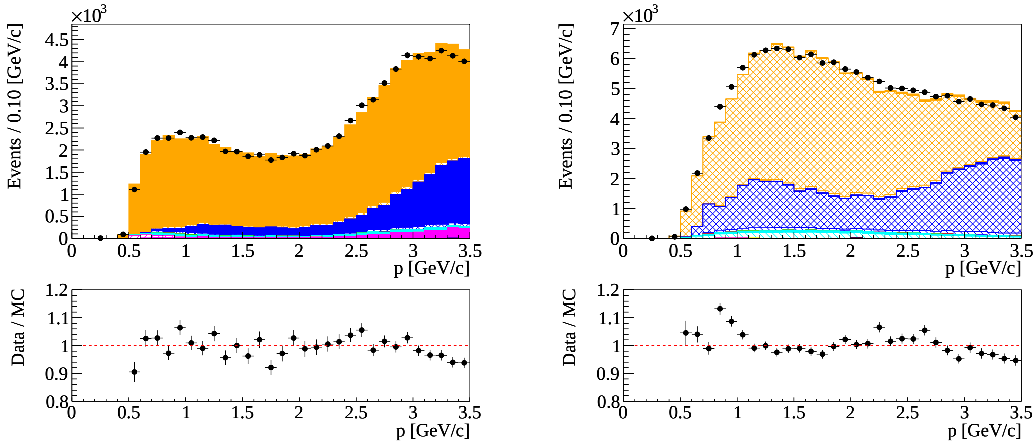

(c) $\tau^- \to K^-\nu_\tau$ **(d)** $\tau^- \to K^-\pi^0\nu_\tau$

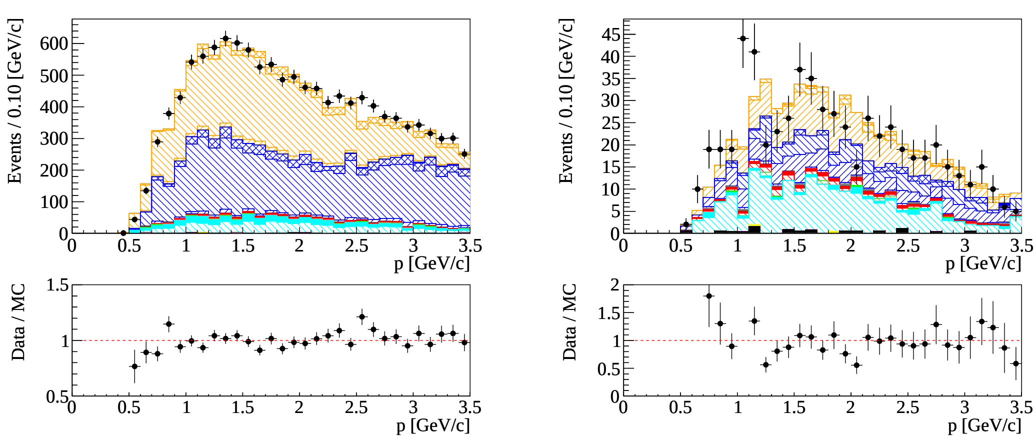

(e) $\tau^- \to K^-(2\pi^0)\nu_\tau$ **(f)** $\tau^- \to K^-(3\pi^0)\nu_\tau$

Figure 6.18.: Distribution of the signal track momentum for the signal modes.

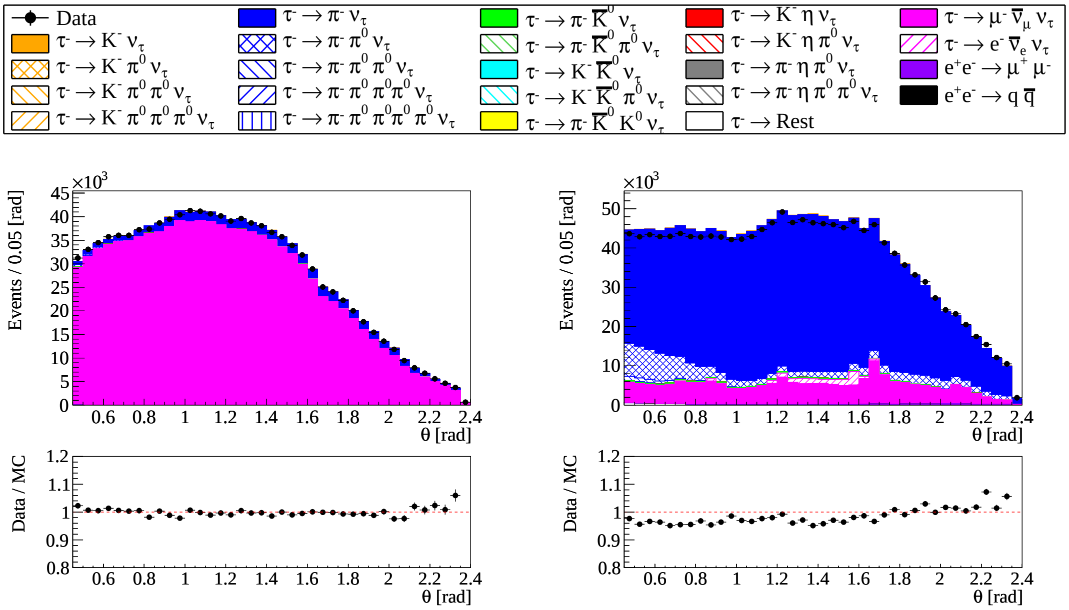

(a) $\tau^- \to \mu^-\overline{\nu}_\mu\nu_\tau$ **(b)** $\tau^- \to \pi^-\nu_\tau$

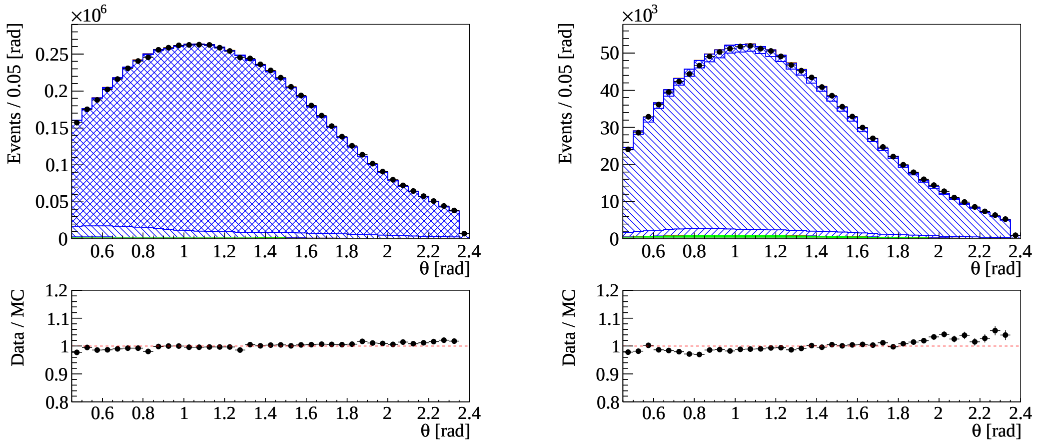

(c) $\tau^- \to \pi^-\pi^0\nu_\tau$ **(d)** $\tau^- \to \pi^-(2\pi^0)\nu_\tau$

Figure 6.19.: Distribution of the signal track polar angle for the control modes.

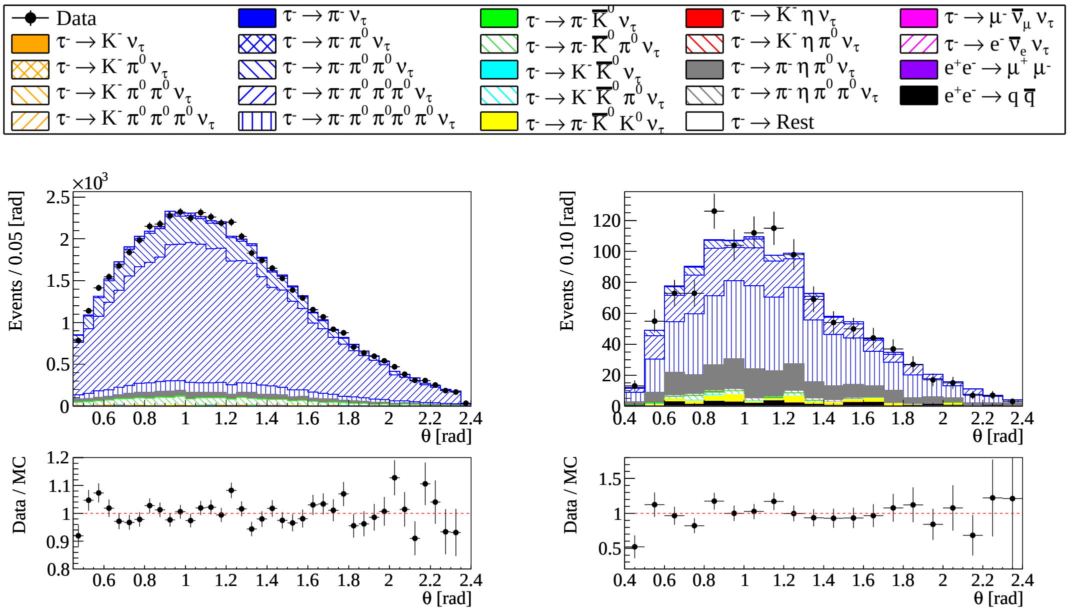

(a) $\tau^- \to \pi^-(3\pi^0)\nu_\tau$ **(b)** $\tau^- \to \pi^-(4\pi^0)\nu_\tau$

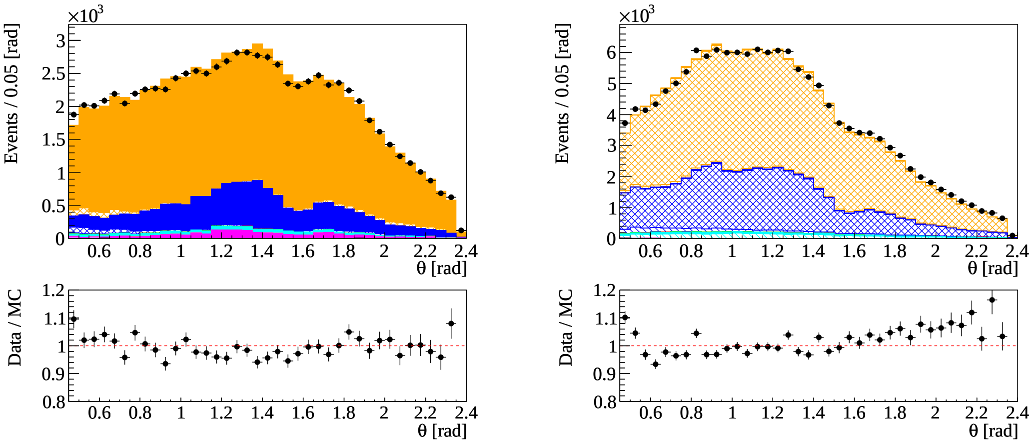

(c) $\tau^- \to K^-\nu_\tau$ **(d)** $\tau^- \to K^-\pi^0\nu_\tau$

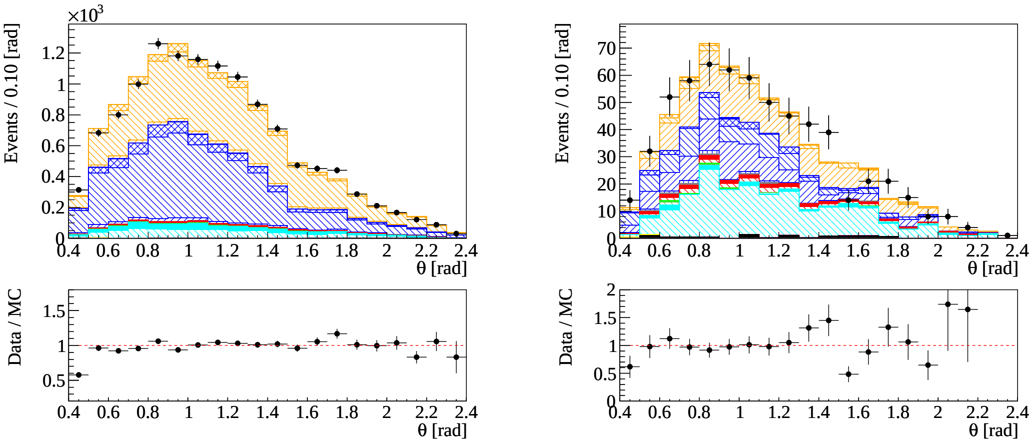

(e) $\tau^- \to K^-(2\pi^0)\nu_\tau$ **(f)** $\tau^- \to K^-(3\pi^0)\nu_\tau$

Figure 6.20.: Distribution of the signal track polar angle for the signal modes.

7. Charged pion and kaon identification

This chapter describes a study to determine the efficiency correction and the uncertainty of the particle identification algorithms for charged pions and kaons. The study is performed using control samples following a similar approach as described in [49].

7.1. Motivation

The reconstructed samples of the signal decays $\tau^- \to K^-(n\pi^0)\nu_\tau$ with $n = 0, 1, 2, 3$ contain a large fraction of cross feed events from the corresponding decay with a charged pion, e. g., in the $\tau^- \to K^-(2\pi^0)\nu_\tau$ mode 38% of the selected events are true $\tau^- \to \pi^-(2\pi^0)\nu_\tau$ events . The reasons for this large background are a sizable probability to misidentify a pion as a kaon for all kaon PID selectors, and the branching fractions for modes with a charged pion which are larger by a factor of 10–100 compared to the corresponding mode with a charged kaon. If the simulation fails to describe the particle identification properties correctly, in particular the pion-as-kaon misidentification, a large effect on the measured branching fractions for these modes is expected due to the large fraction of cross feed. This motivates the detailed PID study described in this chapter: The description of the particle identification in data by the simulation is studied with control samples which contain decays as similar as possible to the signal decays to derive correction factors for the simulated events.

7.2. Method

For studying the performance of a PID selector high-purity samples with tracks coming from the type of particle under study (*control tracks*) have to be selected. The particle type has to be determined from information not related to the studied PID algorithm.

After the selection of an event sample containing control tracks, the efficiency, $\epsilon_{\text{PID}}^{\text{Data}}$, of the selector is determined in data

$$\epsilon_{\text{PID}}^{\text{Data}} = \frac{N_{t^{sel}}^{\text{Data}}}{N_t^{\text{Data}}}, \tag{7.1}$$

where N_t^{Data} denotes the number of control tracks, t, available in the control sample, and $N_{t^{sel}}^{\text{Data}}$ is the number of control tracks, which fulfill the tested PID criteria. The efficiency $\epsilon_{\text{PID}}^{\text{Data}}$ is then compared with the efficiency, $\epsilon_{\text{PID}}^{\text{MC}}$, obtained from simulation. Event dependent correction factors for the simulation are determined from deviations between $\epsilon_{\mathrm{PID}}^{\mathrm{Data}}$ and $\epsilon_{\mathrm{PID}}^{\mathrm{MC}}$. The correction factors are applied as weights, w^{PID}, to the simulated events. The weights are given by

$$w^{\mathrm{PID}} = \frac{\epsilon_{\mathrm{PID}}^{\mathrm{Data}}}{\epsilon_{\mathrm{PID}}^{\mathrm{MC}}}. \tag{7.2}$$

The dependence of w^{PID} on the track momentum, polar angle and azimuthal angle is studied in Section 7.4.

7.3. Selection of the pion and kaon PID control samples

The *PID control decays* used to derive the correction factors to the kaon and pion PID in simulated events are

$$\tau^- \to \pi^-\pi^+\pi^-\nu_\tau \quad \text{(pion control channel)}, \tag{7.3}$$

$$\tau^- \to \pi^- K^+ K^- \nu_\tau \quad \text{(kaon control channel)}. \tag{7.4}$$

These decays are suitable as PID control decays because the type of one of the three final-state hadrons is constrained by identifying the type of the two other hadrons. The determination of the control track is described in detail in Section 7.3.2. In addition, these decays are chosen since they have a similar topology as the signal decays measured in this analysis. The branching fractions [4] of the PID control decays are sufficiently large for this study and are known with a good precision:

$$\mathcal{B}(\tau^- \to \pi^-\pi^+\pi^-\nu_\tau) = (9.00 \pm 0.06) \times 10^{-2} \qquad (\Delta\mathcal{B}/\mathcal{B} = 0.7\%), \tag{7.5}$$

$$\mathcal{B}(\tau^- \to \pi^- K^+ K^-\nu_\tau) = (1.40 \pm 0.05) \times 10^{-3} \qquad (\Delta\mathcal{B}/\mathcal{B} = 3.6\%). \tag{7.6}$$

The first step to obtain these control decays is the selection of events containing τ decays with three charged tracks:

$$\tau^- \to t^- t^+ t^- \nu_\tau. \tag{7.7}$$

The selection criteria used to separate events containing this type of decays from background events are described in the next section. In a second step the selected events are sorted in two categories by applying PID criteria to two of the three tracks in the decay to determine the control track.

7.3.1. Selection of $\tau^- \to t^- t^+ t^- \nu_\tau$ decays

The criteria used to select events of the type $\tau^- \to \pi^-\pi^+\pi^-\nu_\tau$ and $\tau^- \to \pi^- K^+ K^- \nu_\tau$ are chosen as similar as possible to the selection criteria used in the main analysis to guarantee that the obtained PID correction factors are applicable. Since the criteria are similar, however not identical they are briefly summarized in this section.

Event topology

For the pion and kaon particle identification study the same *BABAR* dataset as for the branching fraction measurement is used (Sections 3.3.1 and 3.3.2). The *BABAR* collaboration provides tools [50] to preselect events with a

1-3 topology.

The two hemispheres of the event, which are defined by the thrust axis (Section 6.2.2), contain one and three charged tracks, respectively. The hemisphere with three tracks is denoted as the signal hemisphere. All four selected tracks are consistent with originating from the interaction point, i. e., tracks originating from a secondary vertex are not considered.

Lepton tag

The track in the one-track hemisphere of the event has to be identified as an electron or a muon. The same identification criteria are used as described in Chapter 5.

Charge conservation in the event

The total charge of the event, i. e., the sum of all particle charges, is required to be $Q_{tot} = 0$. In addition, the sum of the charges of the signal tracks has to be equal to the charge of the tag lepton.

DIRC acceptance

All charged tracks have to be within the DIRC acceptance to ensure optimal particle identification performance:

$$0.45 < \theta_t < 2.36\,\text{rad}, \tag{7.8}$$

$$p_t^T > 250\,\text{MeV}/c, \tag{7.9}$$

where θ_t is the track polar angle, and p_t^T the track transverse momentum.

Missing mass

The missing mass of the event, as defined in Section 6.2.4, is required to be in the range

$$1.0 < m_{miss} < 7.5\,\text{GeV}/c^2 \tag{7.10}$$

to reject Bhabha and two-photon background events.

Ratio of the total transverse momentum and the missing energy

To suppress two-photon background the ratio of the total transverse momentum in the event and the missing energy (Section 6.3.3) has to be

$$\frac{\left(\sum_{i=1}^{4} \vec{p}_i^{\,\text{CMS}}\right)^T}{\sqrt{s} - \sum_{i=1}^{4} p_i^{\text{CMS}}} > 0.2 \tag{7.11}$$

where $\vec{p}_i^{\,\text{CMS}}$ is the momentum vector of the i^{th} track.

Invariant hadronic mass

The invariant mass, m_{ttt}, of the three tracks in the signal hemisphere is required to be

$$m_{ttt} < 1.82\,\mathrm{GeV}/c^2, \tag{7.12}$$

to suppress $e^+e^- \to e^+e^-(\gamma)$ and $e^+e^- \to \mu^+\mu^-(\gamma)$ backgrounds. This value is chosen to be slightly higher than the mass of the τ lepton, $m_{\tau^-} = 1.78\,\mathrm{GeV}/c^2$. Even tough the invariant mass of the hadrons cannot in principle be larger than the τ mass, detector resolution effects can lead to larger m_{ttt} values.

Photon selection

Clusters in the electromagnetic calorimeter are accepted as photons if

$$E_\gamma > 0.075\,\mathrm{GeV}, \tag{7.13}$$

$$E_\gamma > 0.200\,\mathrm{GeV} \quad \text{if} \quad d(\gamma, t) < 40\,\mathrm{cm}, \tag{7.14}$$

where $d(\gamma, t)$ is the distance between the photon cluster centroid and the track's intersection point on the calorimeter surface. This criterion takes into account that low-energy calorimeter clusters may originate from split-offs (Chapter 8). Events which contain photons are discarded:

$$N_\gamma = 0. \tag{7.15}$$

Pion and kaon identification

Two of the three tracks in the signal hemisphere have to pass the PID selectors for kaons and pions (Section 5.2.3). The additional kaon identification criteria described in Section 5.2.3 have to be also fulfilled. Particle identification is not applied to the third track. The method to choose the control track is described in the next section.

7.3.2. Determination of the control track

Pion control sample $\tau^- \to \pi^-\pi^+\pi^-\nu_\tau$

In the $\tau^- \to t^-t^+t^-\nu_\tau$ decay the track with the opposite charge than the τ lepton[1], i. e., the t^+ is used as the control track. The two tracks with the same charge, i. e., both t^-'s, are identified as pions using the pion PID selector, i. e., $\tau^- \to \pi^-t^+\pi^-\nu_\tau$ decays are selected.

The W^- boson in a τ^- decay couples to $\overline{u}d$ or $\overline{u}s$ quark pairs. Therefore only final states with strangeness $S = 0, -1$ are possible, i. e., the $\tau^- \to \pi^-K^+\pi^-\nu_\tau$ decay is not allowed. Thus the track t^+ must be a pion. In the following this track is used as the pion control track.

---

[1] The charge Q_τ of the τ is determined by the charge of the opposite-side tag lepton: $Q_\tau = -Q_{\text{tag-lepton}}$

Kaon control sample $\tau^- \to \pi^- K^+ K^- \nu_\tau$

In the kaon control sample the negatively charged kaon in the $\tau^- \to \pi^- K^+ K^- \nu_\tau$ decay is used as the control track. The identification of this track without the application of a PID selector starts with the identification of the positively charged track, t^+, in the $\tau^- \to t^- t^+ t^- \nu_\tau$ decay. This track must be identified as a kaon with the kaon PID selector. In a second step one of the negatively charged tracks must be identified as a pion with the pion PID selector, i. e., $\tau^- \to \pi^- K^+ t^- \nu_\tau$. By the selection of a positive kaon and a negative pion the potential background decays $\tau^- \to K^- \pi^+ \pi^- \nu_\tau$ and $\tau^- \to K^- K^+ K^- \nu_\tau$ are highly suppressed. The third track, t^-, must therefore be a kaon, and is used as the control track.

7.3.3. Selected $\tau^- \to \pi^- \pi^+ \pi^- \nu_\tau$ and $\tau^- \to \pi^- K^+ K^- \nu_\tau$ samples

Agreement between data and simulation

The ratios, $R_{\mathrm{MC}}^{\mathrm{Data}} = \frac{N_{sel}^{\mathrm{Data}}}{N_{sel}^{\mathrm{MC}}}$, of the selected numbers of events in data and simulation are

$$R_{\mathrm{MC}}^{\mathrm{Data}}(\tau^- \to \pi^- \pi^+ \pi^- \nu_\tau) = 0.992 \pm 0.001 \qquad (7.16)$$

$$R_{\mathrm{MC}}^{\mathrm{Data}}(\tau^- \to \pi^- K^+ K^- \nu_\tau) = 1.035 \pm 0.006, \qquad (7.17)$$

where the quoted uncertainty is only statistical. A lower limit for a systematic uncertainty can be roughly estimated from the uncertainty of the branching fraction used to simulate the decays which is $\Delta\mathcal{B}/\mathcal{B} = 0.7\%$ for the pion control decay, and $\Delta\mathcal{B}/\mathcal{B} = 3.6\%$ for the kaon control sample, and from the uncertainty of the track reconstruction efficiency. The latter is $\approx 0.2\%$ per track. Four tracks are selected in the control events, the resulting uncertainty contribution is therefore 0.8%[2]. Considering these uncertainties, the total event yield obtained in simulation is already in good agreement with the yield obtained in data for both control decays.

Figure 7.1 shows the distribution of the control track momentum for the two control channels. The deviations of the data/MC ratio between the different momentum intervals can be explained by the uncertainty of the particle identification. As has been described in the last section, the particle type of two of the three charged tracks in the control decays is identified with a PID selector. The correction factors which are derived in this study are not applied for these identified particles. Instead, the momentum-dependent standard correction factors provided by the *BABAR* PID Group are applied which have been determined in high-multiplicity D^0 decay control samples (Section 5.2.3), i. e., in events with a different topology than τ-pair events. Table 7.1 lists the ratios $R_{\mathrm{MC}}^{\mathrm{Data}} = \frac{N_{sel}^{\mathrm{Data}}}{N_{sel}^{\mathrm{MC}}}$ determined separately for each run and for each tag sample. As expected, the agreement between the e-tag and μ-tag is reasonable for all runs and both decay modes. The deviation between the different runs are attributed to the run-dependent PID efficiency uncertainty for the two tracks in the control decays which

---

[2] The uncertainty of the track reconstruction efficiency is fully correlated for the four tracks, i. e., the contributions of the four tracks are added.

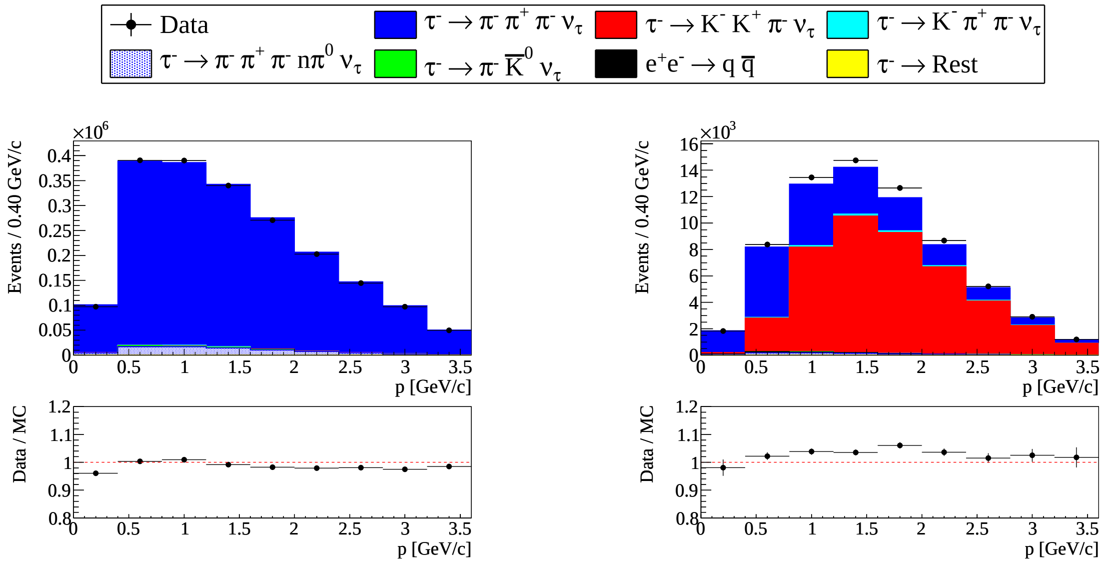

(a) $\tau^- \to \pi^-\pi^+\pi^-\nu_\tau$ **(b)** $\tau^- \to \pi^- K^+ K^- \nu_\tau$

Figure 7.1.: Momentum of the control track. In case of (a) the π^+ is used as the control track to measure the performance of the pion identification algorithm. The control track used to test the kaon identification is the K^- in (b).

are identified with PID selectors.

Purity of the control decays

Table 7.2 shows the composition of the reconstructed control samples in simulation in terms of the true decay modes. The pion control sample consists to 95% of true $\tau^- \to \pi^-\pi^+\pi^-\nu_\tau$ events. In addition, almost 4% of the selected events contain true decays with three pions and additional π^0's, where the control track corresponds to the correct type of track to be tested. The contribution from other channels is negligible.

For the $\tau^- \to \pi^- K^+ K^- \nu_\tau$ decay a purity of 66% is achieved. The background is dominated by $\tau^- \to \pi^-\pi^+\pi^-\nu_\tau$ decays, where a pion has been misidentified as a kaon. The branching fraction of this background is known to a sufficiently good precision of 0.7%, and can therefore be correctly accounted for in the PID study. The remaining background modes can be neglected.

7.4. Determination of the pion and kaon PID correction

According to Section 5.2.4 pions and kaons are identified in this analysis with a combination of PID selectors, which is referred to as *stacked selector* S:

$$\text{stacked kaon selector:} \quad S_K = \texttt{!muon} \wedge \texttt{!electron} \wedge \texttt{kaon} \tag{7.18}$$

$$\text{stacked pion selector:} \quad S_\pi = \texttt{!muon} \wedge \texttt{!electron} \wedge \texttt{!kaon} \wedge \texttt{pion} \tag{7.19}$$

where `muon`, `electron`, `kaon`, and `pion` denote the PID identification algorithms provided by the *BABAR* PID group and which are applied in the given order.

Table 7.1.: The ratio of selected data events and selected simulated events, $R_{\mathrm{MC}}^{\mathrm{Data}} = N_{sel}^{\mathrm{Data}}/N_{sel}^{\mathrm{MC}}$, for the PID control samples $\tau^- \to \pi^-\pi^+\pi^-\nu_\tau$ and $\tau^- \to \pi^-K^+K^-\nu_\tau$. $R_{\mathrm{MC}}^{\mathrm{Data}}$ is listed separately for each run and both tag lepton types. The given uncertainties are only statistical.

	$R_{\mathrm{MC}}^{\mathrm{Data}}$ [%]			
	$\tau^- \to \pi^-\pi^+\pi^-\nu_\tau$		$\tau^- \to \pi^-K^+K^-\nu_\tau$	
Run	e-tag	μ-tag	e-tag	μ-tag
1	97.3 ± 0.6	97.6 ± 0.6	94.1 ± 3.4	98.8 ± 3.3
2	98.2 ± 0.4	97.5 ± 0.3	101.6 ± 2.1	102.8 ± 2.0
3	97.4 ± 0.5	98.7 ± 0.5	99.6 ± 2.9	100.9 ± 2.7
4	98.4 ± 0.3	99.7 ± 0.3	101.3 ± 1.7	105.2 ± 1.6
5	99.0 ± 0.3	101.1 ± 0.3	105.3 ± 1.5	103.6 ± 1.4
6	99.7 ± 0.3	101.6 ± 0.3	109.2 ± 2.0	105.7 ± 1.9

Table 7.2.: Composition of the selected τ PID control samples in simulation.

Decay	$\tau^- \to \pi^-\pi^+\pi^-\nu_\tau$ N [%]	$\tau^- \to \pi^-K^+K^-\nu_\tau$ N [%]
$\tau^- \to \pi^-\pi^+\pi^-\nu_\tau$	95.31	31.58
$\tau^- \to \pi^-K^+K^-\nu_\tau$	0.13	65.60
$\tau^- \to \pi^-\pi^+\pi^-n\pi^0\nu_\tau$	3.84	1.18
$\tau^- \to K^-\pi^+\pi^-\nu_\tau$	0.21	0.99
$\tau^- \to \pi^-\overline{K}^0\nu_\tau$	0.36	0.13
$e^+e^- \to q\overline{q}$	0.04	0.45
rest	0.11	0.07

The particle identification performance of the stacked selectors S_K and S_π is measured with the method described in Section 5.2.3 using the control track samples selected as described in the last section.

The pion control sample, $\tau^- \to \pi^-\pi^+\pi^-\nu_\tau$, is used to determine the misidentification fractions $\epsilon_{\pi\text{-}as\text{-}K}^{\mathrm{Data}}$ and $\epsilon_{\pi\text{-}as\text{-}K}^{\mathrm{MC}}$ in data and simulation and the corresponding correction factors:

$$w_{\pi\text{-}as\text{-}K}^{\mathrm{PID}} = \frac{\epsilon_{\pi\text{-}as\text{-}K}^{\mathrm{Data}}}{\epsilon_{\pi\text{-}as\text{-}K}^{\mathrm{MC}}}. \tag{7.20}$$

This so-called *PID weight* $w_{\pi\text{-}as\text{-}K}^{\mathrm{PID}}$ (see also Section 5.2.5) is used as a correction for the π-as-K misidentification fraction in simulated events. Moreover, this control sample is used to determine the correction factors

$$w_{\pi\text{-}as\text{-}\pi}^{\mathrm{PID}} = \frac{\epsilon_{\pi\text{-}as\text{-}\pi}^{\mathrm{Data}}}{\epsilon_{\pi\text{-}as\text{-}\pi}^{\mathrm{MC}}} \tag{7.21}$$

of the pion identification efficiency $\epsilon_{\pi\text{-as-}\pi}$. In an analogous way, the corresponding correction factors for the kaon identification efficiency $\epsilon_{K\text{-as-}K}$

$$w^{\mathrm{PID}}_{K\text{-}as\text{-}K} = \frac{\epsilon^{\mathrm{Data}}_{K\text{-}as\text{-}K}}{\epsilon^{\mathrm{MC}}_{K\text{-}as\text{-}K}} \tag{7.22}$$

are obtained using the kaon control sample $\tau^- \to \pi^- K^+ K^- \nu_\tau$.

Figure 7.2 shows the $w^{\mathrm{PID}}_{\pi\text{-}as\text{-}K}$ correction in dependence of the control-track momentum, p_{control}, polar angle, $\theta_{\mathrm{control}}$, and azimuthal angle, ϕ_{control}. The track momentum range is limited to $p_{\mathrm{control}} < 3.6\,\mathrm{GeV}/c$, because the number of available control tracks is small for momenta above $3.6\,\mathrm{GeV}/c$. The distribution of $w^{\mathrm{PID}}_{\pi\text{-}as\text{-}K}$ in $\theta_{\mathrm{control}}$ and ϕ_{control} is uniform, i. e., the same correction value can be applied over the whole angular range. However, the values vary significantly with the momentum: The misidentification rate is about twice as large as the simulated rate for momenta between 0.4 GeV and 0.8 GeV. Above 0.8 GeV, the PID weights range from 0.95 to 1.2. Therefore, the correction $w^{\mathrm{PID}}_{\pi\text{-}as\text{-}K}$ is applied as a function of momentum. In addition, the correction values are determined separately for each run, to account for changing detector conditions. The distributions of $w^{\mathrm{PID}}_{\pi\text{-}as\text{-}K}$ for each run are given in Appendix B. The corrections $w^{\mathrm{PID}}_{\pi\text{-}as\text{-}\pi}$ and $w^{\mathrm{PID}}_{K\text{-}as\text{-}K}$ are determined in the same manner. The corresponding distributions are also given in Appendix B.

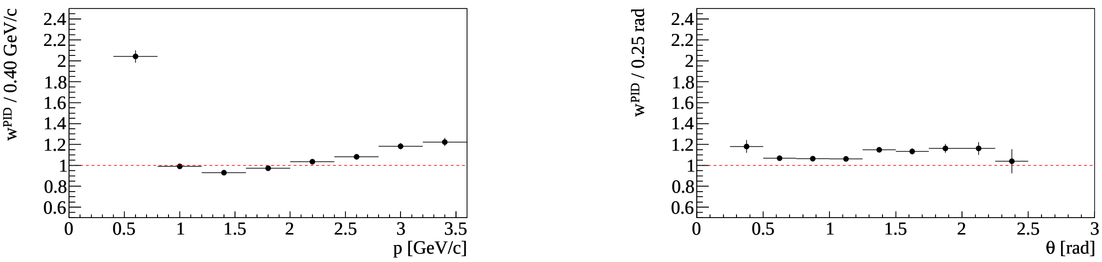

(a) Momentum p_{control} **(b)** Polar angle $\theta_{\mathrm{control}}$

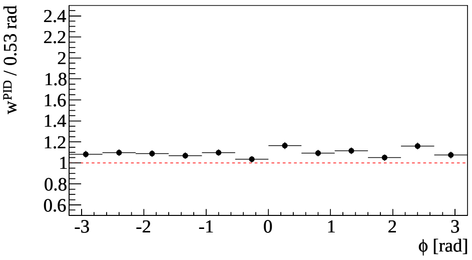

(c) Azimuthal angle ϕ_{control}

Figure 7.2.: Misidentification weights for a pion misidentified as a kaon, $w^{PID}_{\pi\text{-}as\text{-}K}$ in dependence of the control track momentum, polar angle and azimuthal angle. The whole data sample, i. e., runs 1-6, is used to obtain the shown weights. The error bars correspond to the statistical uncertainties of the weights.

8. Split-off correction

8.1. Introduction

Electrons and hadrons that reach the electromagnetic calorimeter interact with the material of the EMC and can produce showers. Showers are reconstructed as clusters which typically expand over several crystals. These clusters are formed by a cluster finding algorithm which uses a crystal with an energy deposit larger than $10\,\mathrm{MeV}/c^2$ as seed and adds in a first step neighboring crystals with energy deposits over a certain threshold to the cluster candidate. In the second step local energy maxima are identified in that cluster candidate. A cluster candidate with exactly one maximum is reconstructed as a cluster. If more that one local maximum are found the cluster candidate is split and separate clusters are formed around each of the local maxima. The algorithm is described in more detail in [25].

In hadronic showers, neutral particles like K^0's and neutrons can be produced. Such particles can pass trough several crystals of the calorimeter before interaction and possibly producing a further subshower. If the subshower has a separate local energy maximum, the hadronic shower is reconstructed as two separate clusters. For hadronic showers originating from a charged hadron, e. g., an charged pion or kaon, only one of the two clusters is associated to a track. The second cluster originating from the subshower is called a *split-off*. This signature is illustrated in Figure 8.1. Split-offs can be reconstructed as spurious photons. These spurious photons tend to have lower energies than real photons from π^0 decays and are reconstructed at small distances to the intersection of a pion or kaon trajectory with the calorimeter surfaces.

A study of split-offs at *BABAR* has been performed in [10] using the decay $\tau^- \to \pi^-\pi^0\nu_\tau$. Split-offs are not well described by the simulation, since hadronic shower shapes are difficult to model. It has been found in [10] and is confirmed in this study that more hadronic split-offs are produced in data than in simulation leading to a larger number of reconstructed photons.

As described in Section 6.3.2, events with reconstructed photons that are not associated with π^0's are rejected. Such additional photons can originate from τ decays with π^0's in the final state where one of the two daughter photons of a π^0 is not detected and thus the π^0 could not be reconstructed. They can also be beam-induced background photons[1], radiated photons, or split-offs. Due to the insufficient modeling of split-offs more data events than simulated events are rejected by requiring that $N_{\gamma_{add}} = 0$, where $N_{\gamma_{add}}$ is the number of additional photons.

In contrast to [10], the decay $\tau^- \to \pi^-\nu_\tau$ is used to determine a split-off correction

---

[1] As described in Section 3.3.2, simulated events are overlaid with randomly triggered events with no physics content. Thus, beam-induced background photons are correctly described by the simulation.

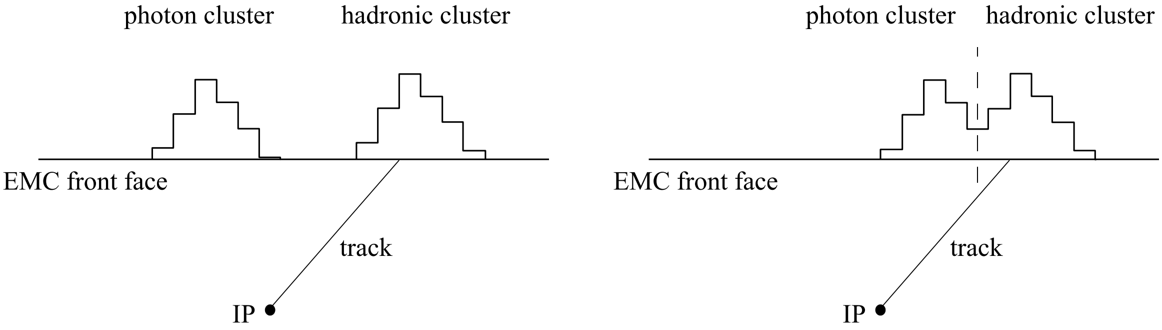

(a) Real photon (separate) **(b)** Real photon (overlap)

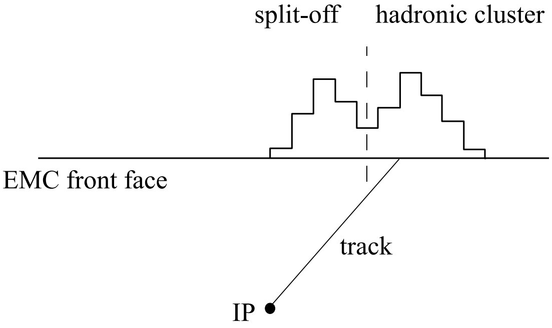

(c) Split-off

Figure 8.1.: Illustration of real photon signatures in (a) and (b) compared with a split-off signature in (c). The surface of the electromagnetic calorimeter is illustrated by the horizontal line. Each bin of the distributions corresponds to an energy deposit in a calorimeter crystal. In the three figures a track of a charged hadron is shown which points from the interaction point (IP) to the reconstructed calorimeter cluster originating from that particle. In (a) a real photon cluster is shown in addition to the hadronic cluster. The two clusters are well separated on the EMC surface. In (b) the photon shower overlaps with the hadronic shower resulting in a cluster candidate with two local maxima. The cluster candidate is split into separate clusters around the local maxima. The intersection of the track with the EMC surface determines which of the two clusters is assigned to the charged particle. (c) shows an area of contiguous energy deposits originating from a hadronic shower with two local energy maxima. This signature is also reconstructed as two separate clusters and cannot be distinguished from the signature in (b). The cluster not assigned to the charged particle can be wrongly identified as a photon. A similar illustration can be found in [10].

where possible effects due to the presence of π^0 daughter photons are excluded. Also the $\tau^- \to \mu^- \overline{\nu}_\mu \nu_\tau$ decay mode is used as a cross check.

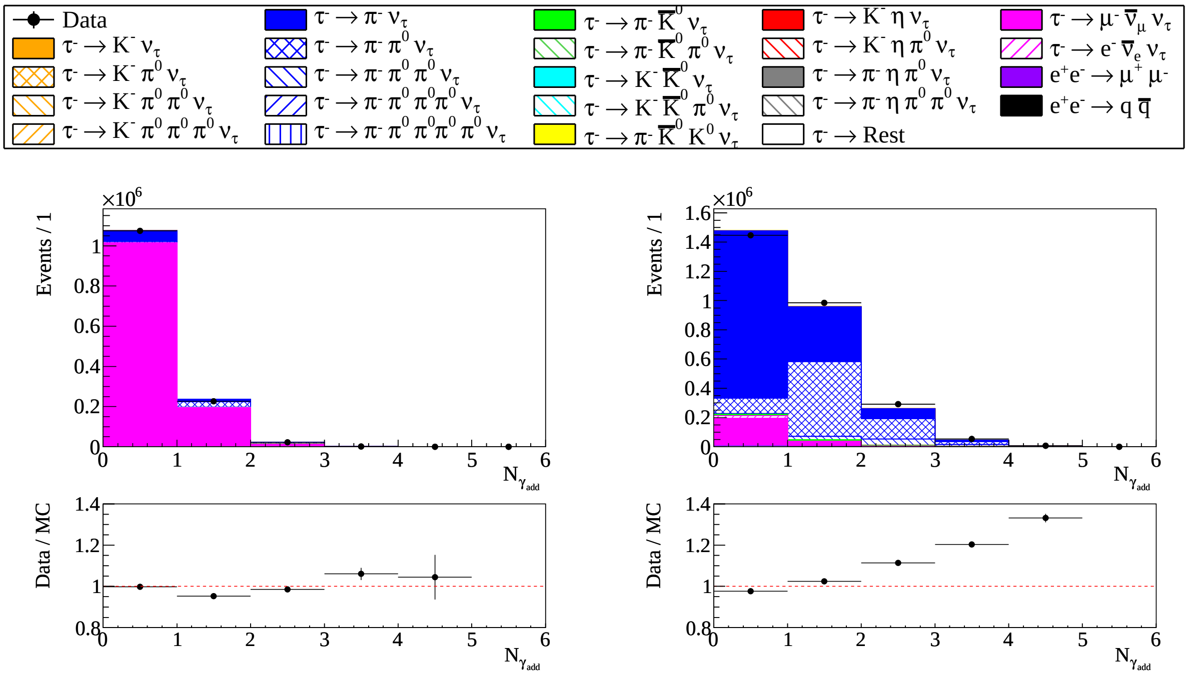

(a) $\tau^- \to \mu^- \overline{\nu}_\mu \nu_\tau$ **(b)** $\tau^- \to \pi^- \nu_\tau$

Figure 8.2.: Number of additional photons, $N_{\gamma_{add}}$, in the event for the decays $\tau^- \to \mu^- \overline{\nu}_\mu \nu_\tau$ and $\tau^- \to \pi^- \nu_\tau$.

8.2. Determination of the split-off correction

Figure 8.2 shows the number of additional photons in the event for the decays $\tau^- \to \mu^- \overline{\nu}_\mu \nu_\tau$ and $\tau^- \to \pi^- \nu_\tau$.

The number of additional photons is small in $\tau^- \to \mu^- \overline{\nu}_\mu \nu_\tau$ decays compared to the $\tau^- \to \pi^- \nu_\tau$ decays. This is expected, because the $\tau^- \to \mu^- \overline{\nu}_\mu \nu_\tau$ sample contains less $\tau^- \to \pi^- \pi^0 \nu_\tau$ cross-feed events than the $\tau^- \to \pi^- \nu_\tau$ sample, and the muon does not produce split-offs from hadronic showers.

The data/MC ratio is approximately constant for the $\tau^- \to \mu^- \overline{\nu}_\mu \nu_\tau$ decay mode. In contrast to that, the distribution for the $\tau^- \to \pi^- \nu_\tau$ decay shows an increase of the ratio with the number of additional photons. An overall data excess with respect to the first bin ($N_{\gamma_{add}} = 0$) of the data/MC ratio is attributed to split-offs which occur more often in data than in simulated events, as has been mentioned above and can be seen in Figure 8.3a. A possible explanation for the increase for $N_{\gamma_{add}} \leq 2$ is a larger discrepancy in the description by the simulation of EMC clusters with more than two local maxima[2], i. e., with more than one split-off.

Figure 8.3 shows the distance, d, on the calorimeter surface between the intersection point of the signal track with the EMC and the centroid of the nearest photon cluster. For the $\tau^- \to \mu^- \overline{\nu}_\mu \nu_\tau$ decay mode (Figure 8.3a), the distribution shows two peaks. The peak near $d = 50\,\text{cm}$ is dominated by the $\tau^- \to \pi^- \pi^0 \nu_\tau$ background. The peak at larger values of d is attributed to final-state photons radiated by the tag electron which are

---

[2] The fraction of clusters with more than two local maxima in simulated τ-pair events is $\approx 8\%$

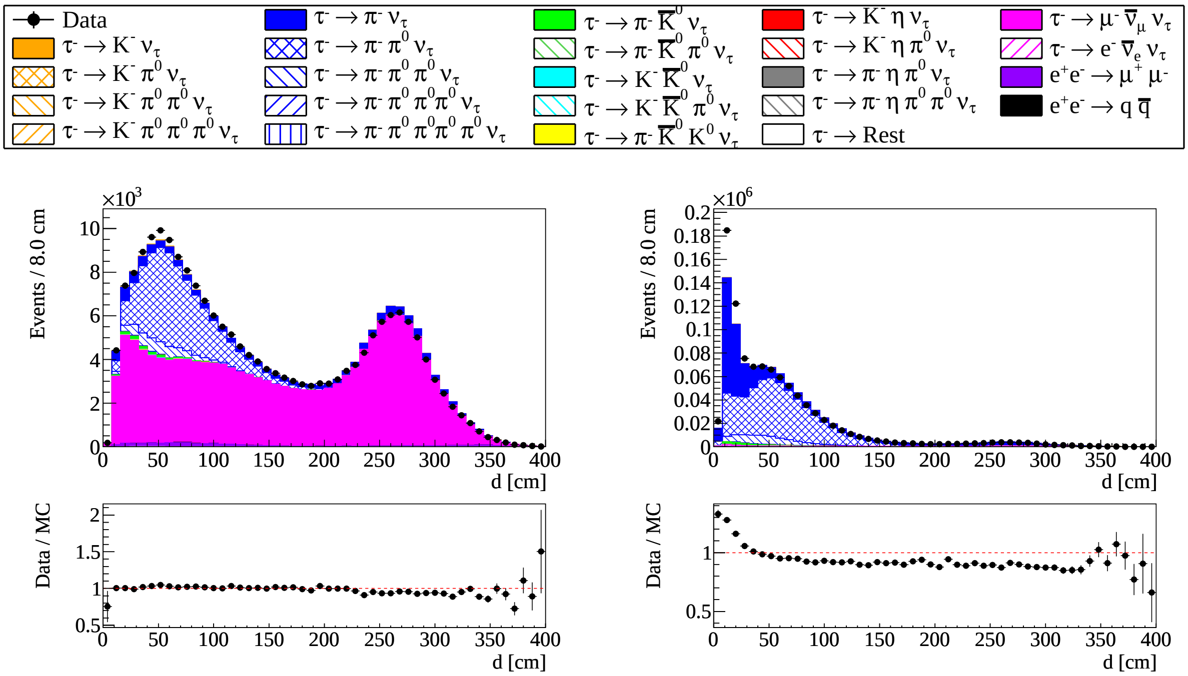

(a) $\tau^- \to \mu^- \overline{\nu}_\mu \nu_\tau$

(b) $\tau^- \to \pi^- \nu_\tau$

Figure 8.3.: The distance, d, between the track intersection point with the EMC and the cluster centroid of the next photon.

reconstructed in the opposite part of the EMC.

The distribution for the $\tau^- \to \pi^- \nu_\tau$ mode (Figure 8.3b) shows an additional large peak at small d values, which is attributed to split-offs. The description of data by the simulation is not good in this region. The number of simulated split-offs is too small. Therefore, this effect has to be corrected, if no additional photons are allowed ($N_{\gamma_{add}} = 0$). The relative data excess, $\eta_{\text{split-off}}$, is defined as

$$\eta_{\text{splitt-off}} = \frac{N^{\text{Data}}(d < 40\,\text{cm}) - N^{\text{MC}}(d < 40\,\text{cm})}{N^{\text{Data}}}, \tag{8.1}$$

where $N^{\text{Data}}(d < 40\,\text{cm})$ and $N^{\text{MC}}(d < 40\,\text{cm})$ are the number of events with $d < 40\,\text{cm}$ in data and simulation, respectively. The value of 40 cm corresponds to the estimated average width of a hadronic shower: The average number of crystals in clusters with multiple local maxima is ≈ 32. Assuming that the crystals correspond to a squared area, and using that the average distance between the crystals centroids is 5 cm one obtains 40 cm as the diagonal of the area.

Table 8.1 shows the values of $\eta_{\text{split-off}}$ for every run. For $d < 40\,\text{cm}$ about half of the selected $\tau^- \to \pi^- \nu_\tau$ candidates are true $\tau^- \to \pi^- \pi^0 \nu_\tau$ events. In these background events split-offs are in principle also produced. However, due to the reconstructed π^0 the split-off effect could be distorted. Therefore, half of the data excess is taken as its systematic uncertainty. The differences between the runs are small compared to this value, therefore a correction averaged over all runs is applied to the simulation. In

Table 8.1.: Observed relative amount of split-offs for each run. The listed uncertainties are statistical. Additionally to the statistical uncertainty a systematic uncertainty of 1.2% is assigned to the split-off correction factor.

Run period	$\eta_{\text{split-off}}[\%]$
1	3.13 ± 0.16
2	2.53 ± 0.09
3	2.56 ± 0.13
4	2.44 ± 0.07
5	2.35 ± 0.06
6	2.18 ± 0.08
1-6	2.42 ± 0.04

this analysis, split-offs are produced by pions and kaons. Since only one pion or kaon is allowed per event, the split-off correction can be applied as an event weight. The correction factor is defined as:

$$\begin{aligned} w_{\text{split-off}} &= 1 - \eta_{\text{split-off}} && (8.2) \\ &= 0.976 \pm 0.012(\text{syst}), && (8.3) \end{aligned}$$

where the systematic uncertainty is half of the average of the $\eta_{\text{split-off}}$ values for the different runs, and the statistical uncertainty is negligible and therefore not taken into account.

9. π^0 reconstruction efficiency correction

9.1. Motivation

The uncertainty of the π^0 reconstruction efficiency is one of the dominant uncertainties in this analysis. Five of the six measured signal decay modes contain at least one π^0. In one decay mode, four π^0's are reconstructed. Thus, it is very important that the π^0 efficiency is well described by the simulation. Deviations between data and simulation can be introduced by shortcomings of the description of electromagnetic shower shapes[1]

Studies have been performed by the *BABAR* collaboration [37, 51] to measure the difference of the π^0 efficiency in data and simulation. A correction of the simulation which is applied to each reconstructed π^0 candidate in dependence of its momentum has been determined to $(-2 \pm 3)\%$. The uncertainty is obtained from a comparison with a correction obtained with the same analysis but with an inclusive π^0 selection not separating the τ final states. In this analysis, an attempt is made to reduce this uncertainty. The π^0 efficiency correction is determined using the same approach as for the standard correction. However, the π^0's for the correction determination are selected in exactly the same way as for the branching fraction measurement. Thus, no systematic uncertainty due to differences in selection criteria has to be taken into account. A detailed study of the remaining systematic effects is performed, and a significant reduction of the uncertainty could be achieved.

This section presents the determination of the π^0 efficiency correction and the study of the associated systematic uncertainties.

9.2. Correction method

The method to determine the π^0 correction has been developed in [37], and is introduced in this section.

The π^0 correction w^{π^0} is defined as the ratio of the π^0 reconstruction efficiency in data, $\epsilon_{\pi^0}^{\mathrm{Data}}$, and in the simulation, $\epsilon_{\pi^0}^{\mathrm{MC}}$:

$$w^{\pi^0} = \frac{\epsilon_{\pi^0}^{\mathrm{Data}}}{\epsilon_{\pi^0}^{\mathrm{MC}}}. \tag{9.1}$$

---

[1] In addition, small effects can arise from the uncertainty of the energy calibration, and from the description of the spacial acceptance of the EMC.

This ratio can be determined in a study of the τ decays

$$\begin{aligned}\tau^- &\to t^-\pi^0\nu_\tau,\\ \tau^- &\to t^-\nu_\tau,\end{aligned} \tag{9.2}$$

where t denotes a charged particle of any type, i. e., t can be either a pion, kaon, muon, or in principle an electron. However, as will be explained later, electrons have to be vetoed . These modes can be used for the determination of the π^0 correction, because the branching fractions $\mathcal{B}(\tau^- \to t^-\pi^0\nu_\tau)$ and $\mathcal{B}(\tau^- \to t^-\nu_\tau)$ with $t = \pi, K, \mu$ are known with a high precision or are small [4]. The $\tau^- \to t^-\pi^0\nu_\tau$ and $\tau^- \to t^-\nu_\tau$ decays are selected by applying the same selection criteria for both modes except of the π^0 reconstruction. The numbers of selected $\tau^- \to t^-\pi^0\nu_\tau$ and $\tau^- \to \pi^-\nu_\tau$ events can be expressed as

$$\begin{aligned}N(\tau^- \to t^-\pi^0\nu_\tau) &= \epsilon_{\tau^-\to t^-\pi^0\nu_\tau}\mathcal{B}(\tau^- \to t^-\pi^0\nu_\tau)N_{\tau\tau},\\ N(\tau^- \to t^-\nu_\tau) &= \epsilon_{\tau^-\to t^-\nu_\tau}\mathcal{B}(\tau^- \to t^-\nu_\tau)N_{\tau\tau},\end{aligned} \tag{9.3}$$

where ϵ_i is the reconstruction efficiency of the mode i and $N_{\tau\tau}$ is the total number of produced τ pairs[2]. The reconstruction efficiencies for both modes are then

$$\begin{aligned}\epsilon_{\tau^-\to t^-\pi^0\nu_\tau} &= \frac{N(\tau^- \to t^-\pi^0\nu_\tau)}{\mathcal{B}(\tau^- \to t^-\pi^0\nu_\tau)N_{\tau\tau}}\\ \epsilon_{\tau^-\to t^-\nu_\tau} &= \frac{N(\tau^- \to t^-\nu_\tau)}{\mathcal{B}(\tau^- \to t^-\nu_\tau)N_{\tau\tau}}.\end{aligned} \tag{9.4}$$

The reconstruction efficiency of the $\tau^- \to t^-\pi^0\nu_\tau$ mode has two contributions: the π^0 reconstruction efficiency, and the efficiency due to all other selection criteria. The latter is assumed to be equal to the reconstruction efficiency of the $\tau^- \to t^-\nu_\tau$ decay mode. Therefore,

$$\epsilon_{\tau^-\to t^-\pi^0\nu_\tau} = \epsilon_{\pi^0}\epsilon_{\tau^-\to t^-\nu_\tau}. \tag{9.5}$$

Using the relations above, the π^0 efficiency correction can then be written as

$$\begin{aligned}w^{\pi^0} = \frac{\epsilon_{\pi^0}^{\text{Data}}}{\epsilon_{\pi^0}^{\text{MC}}} &= \frac{\epsilon^{\text{Data}}_{\tau^-\to t^-\pi^0\nu_\tau}}{\epsilon^{\text{Data}}_{\tau^-\to t^-\nu_\tau}} \Big/ \frac{\epsilon^{\text{MC}}_{\tau^-\to t^-\pi^0\nu_\tau}}{\epsilon^{\text{MC}}_{\tau^-\to t^-\nu_\tau}}\\ &= \frac{N(\tau^- \to t^-\pi^0\nu_\tau)^{\text{Data}}}{N(\tau^- \to t^-\pi^0\nu_\tau)^{\text{MC}}}\frac{N(\tau^- \to t^-\nu_\tau)^{\text{MC}}}{N(\tau^- \to t^-\nu_\tau)^{\text{Data}}}\end{aligned} \tag{9.6}$$

The determination of the π^0 efficiency correction using this *double ratio* has the advantage that systematic effects partially cancel for w^{π^0}, since the decays $\tau^- \to t^-\nu_\tau$ and $\tau^- \to t^-\pi^0\nu_\tau$ are reconstructed with the same selection criteria (except for the reconstructed π^0 in the $\tau^- \to t^-\pi^0\nu_\tau$ decay). For example, the luminosity uncertainty and the tracking efficiency uncertainty contribute to both channels in the same way. The

---

[2] As described in Section 6.2, the number of simulated $e^+e^- \to \tau^+\tau^-$ events is scaled to match the data luminosity.

π^0 efficiency correction depends on the momentum[3] of the π^0, p_{π^0}. Thus, the correction is determined as a function of p_{π^0}:

$$w^{\pi^0}(p_{\pi^0}) = \frac{\frac{N(\tau^- \to t^- \pi^0 \nu_\tau)^{\mathrm{Data}}}{N(\tau^- \to t^- \pi^0 \nu_\tau)^{\mathrm{MC}}}(p_{\pi^0})}{\frac{N(\tau^- \to t^- \nu_\tau)^{\mathrm{Data}}}{N(\tau^- \to t^- \nu_\tau)^{\mathrm{MC}}}}. \tag{9.7}$$

Since the track reconstruction efficiency is independent of the particle momentum (Section 5.1.2), the denominator of the double-ratio is constant.

9.3. Determination of the π^0 efficiency correction

9.3.1. $\tau^- \to t^-\nu_\tau$ and $\tau^- \to t^-\pi^0\nu_\tau$ event samples

The π^0 efficiency correction could in principle be determined from the $\tau^- \to \pi^-\nu_\tau$ and $\tau^- \to \pi^-\pi^0\nu_\tau$ decay modes used as control modes in the main analysis. However, the identification of a charged pion leads to a relatively large systematic uncertainty in the $\tau^- \to \pi^-\nu_\tau$ mode (Section 10.5). Hence, the application of pion identification criteria is omitted for the determination of the π^0 correction to minimize the systematic uncertainty. If the pion is not identified, an electron veto on the signal charged particle is necessary in the e-tag event sample to reject $e^+e^- \to e^+e^-$ events, and accordingly a muon veto has to be applied in the μ-tag sample to reject $e^+e^- \to \mu^+\mu^-$ events. The muon identification is less efficient than the electron identification and the muon-veto uncertainty is relatively large. Therefore, the muon veto is not applied and only the e-tag sample is used. In summary, the $\tau^- \to t^-\nu_\tau$ and $\tau^- \to t^-\pi^0\nu_\tau$ modes with an e-tag are selected where t failed the electron identification criteria and thus can be a charged pion, muon, or kaon.

Figure 9.1 shows the tag electron momentum distribution for both channels, $\tau^- \to t^-\nu_\tau$ and $\tau^- \to t^-\pi^0\nu_\tau$. For the $\tau^- \to t^-\nu_\tau$ mode the data is described very well by the simulation. Table 9.1 lists the composition of the selected samples in the simulation. As expected, the ratio of the selected $\tau^- \to \mu^-\overline{\nu}_\mu\nu_\tau$ and $\tau^- \to \pi^-\nu_\tau$ candidate numbers which amounts to 1.5 is approximately consistent with their branching fraction ratio, $\mathcal{B}(\tau^- \to \mu^-\overline{\nu}_\mu\nu_\tau)/\mathcal{B}(\tau^- \to \pi^-\nu_\tau) = 1.6$, as no particle identification is used. The same is true for the $\tau^- \to K^-\nu_\tau$ candidate number. The small deviation from the branching fraction ratio can be due to different kinematics of the muons, pions, and kaons. For example, the muons tend to have a smaller momentum than the pions, because of the presence of an additional neutrino in $\tau^- \to \mu^-\overline{\nu}_\mu\nu_\tau$ decays. The background fraction in the selected sample of $\tau^- \to t^-\nu_\tau$ events amounts to 3.6%. A systematic uncertainty due to this background is estimated in Section 9.6.

For the $\tau^- \to t^-\pi^0\nu_\tau$ events, the data/MC ratio is constant for the lepton momentum distribution. The deviation from one can be attributed to the differences in the π^0 reconstruction efficiency between data and simulation. The fraction of simulated

---

[3] A more natural quantity for the π^0 correction dependence would be the measured π^0 energy. The π^0 momentum is used instead to allow for a direct comparison with the results of the previous π^0 correction determinations [37, 51].

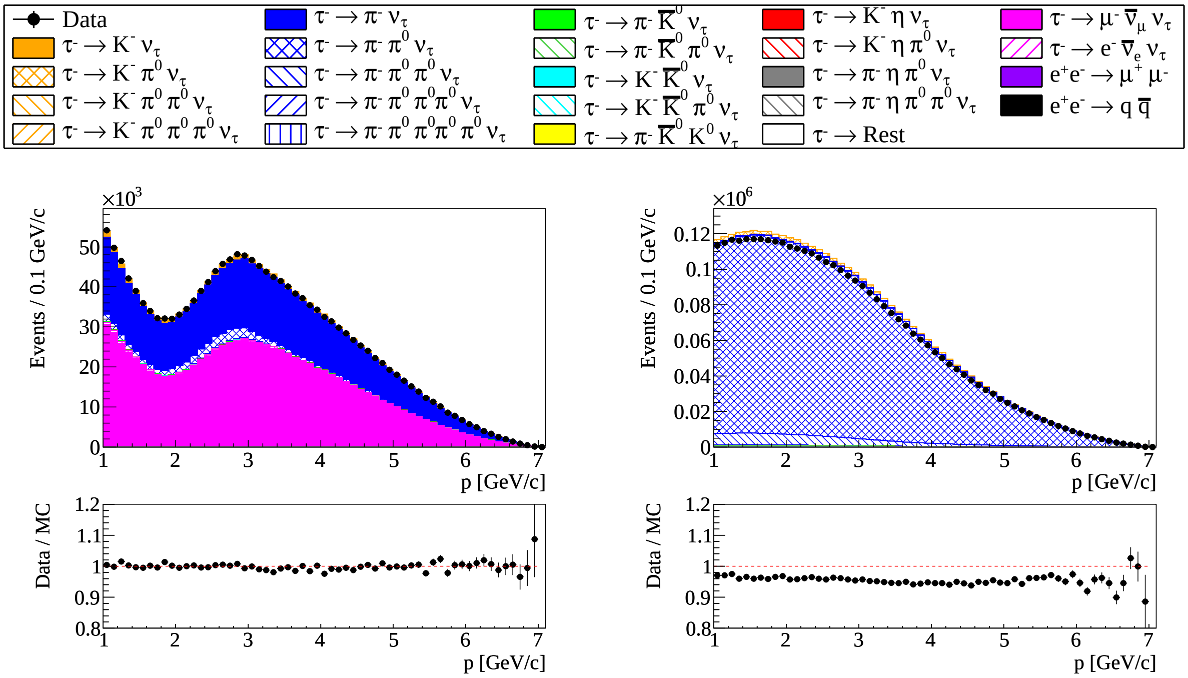

(a) $\tau^- \to t^- \nu_\tau$

(b) $\tau^- \to t^- \pi^0 \nu_\tau$

Figure 9.1.: Momentum of the tag electron. A constant deviation between data and simulation is visible in (b), which is attributed to the imprecise simulation of the π^0 reconstruction efficiency.

Table 9.1.: Composition of the selected $\tau^- \to t^- \nu_\tau$, $\tau^- \to t^- \pi^0 \nu_\tau$, and $\tau^- \to t^-(2\pi^0)\nu_\tau$ modes in simulation.

Decay mode	$\tau^- \to t^- \nu_\tau$ N [%]	$\tau^- \to t^- \pi^0 \nu_\tau$ N [%]	$\tau^- \to t^-(2\pi^0)\nu_\tau$ N [%]
$\tau^- \to \pi^- \nu_\tau$	37.26	0.39	0.06
$\tau^- \to \pi^- \pi^0 \nu_\tau$	3.27	93.02	3.57
$\tau^- \to \pi^-(2\pi^0)\nu_\tau$	0.19	4.37	90.60
$\tau^- \to \pi^-(3\pi^0)\nu_\tau$	0.01	0.09	2.82
$\tau^- \to K^- \nu_\tau$	2.15	0.03	0.00
$\tau^- \to K^- \pi^0 \nu_\tau$	0.05	1.30	0.08
$\tau^- \to K^-(2\pi^0)\nu_\tau$	0.00	0.03	0.58
$\tau^- \to \pi^- \overline{K}^0 \nu_\tau$	0.26	0.11	1.06
$\tau^- \to \pi^- \overline{K}^0 \pi^0 \nu_\tau$	0.01	0.41	0.38
$\tau^- \to \mu^- \overline{\nu}_\mu \nu_\tau$	56.03	0.06	0.00
$\tau^- \to e^- \overline{\nu}_e \nu_\tau$	0.65	0.01	0.00
rest	0.12	0.18	0.85

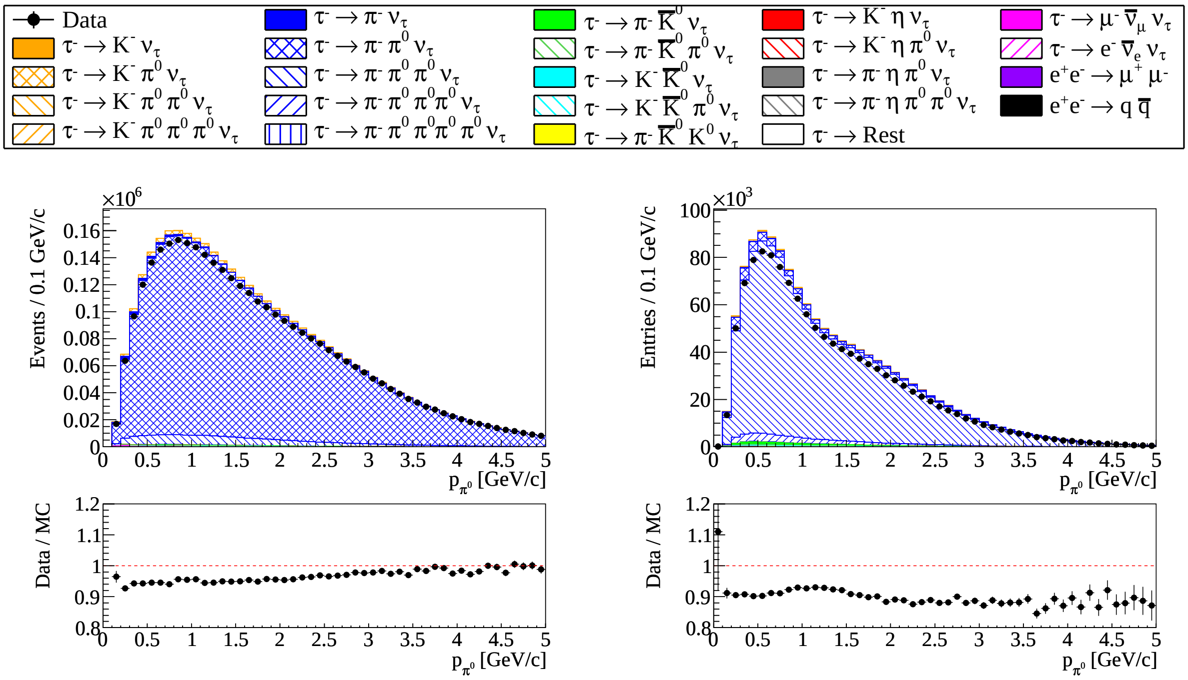

(a) $\tau^- \to t^-\pi^0\nu_\tau$

(b) $\tau^- \to t^-(2\pi^0)\nu_\tau$

Figure 9.2.: Distribution of the π^0 momentum before the application of the π^0 efficiency correction. (b) contains two entries per event, i. e., one entry per reconstructed π^0.

background events is 5.7% as can be seen in Table 9.1. The background is dominated by $\tau^- \to \pi^-(2\pi^0)\nu_\tau$ events. As for the $\tau \to t\nu$ channel, the systematic uncertainty due to this background is discussed in Section 9.6.

The dependence of the data/MC ratio on the π^0 momentum can be seen in Figure 9.2a for the $\tau^- \to t^-\pi^0\nu_\tau$ mode. At high π^0 momenta the deviations are small and increase for smaller momenta. For the $\tau^- \to t^-(2\pi^0)\nu_\tau$ channel (Figure 9.2b) a deviation is visible, which is about twice as large as for the mode with one reconstructed π^0. This observation further confirms that the uncertainty of the π^0 reconstruction is the origin of this deviation. The dependence of the data/MC ratio on the π^0 momentum for this mode does not correspond to the dependence observed in the $\tau^- \to t^-\pi^0\nu_\tau$ mode. This is attributed to the insufficient modeling of the resonance structure in the $\tau^- \to \pi^-(2\pi^0)\nu_\tau$ decay which is the dominant contribution to the $\tau^- \to t^-(2\pi^0)\nu_\tau$ sample (see also Section 6.3.4).

9.4. Determination of the correction values

The correction of the π^0 reconstruction efficiency is determined according to Equation 9.7 using the data and simulated samples described in the previous section. Figure 9.3a shows the obtained π^0 correction values, $w^{\pi^0}_{p,\text{r-av}}$, in dependence of the π^0 momentum p_{π^0}, where the index r-av denotes that the correction factors are averaged over the runs, i. e., they are determined using the whole data sample. The correction factors approach

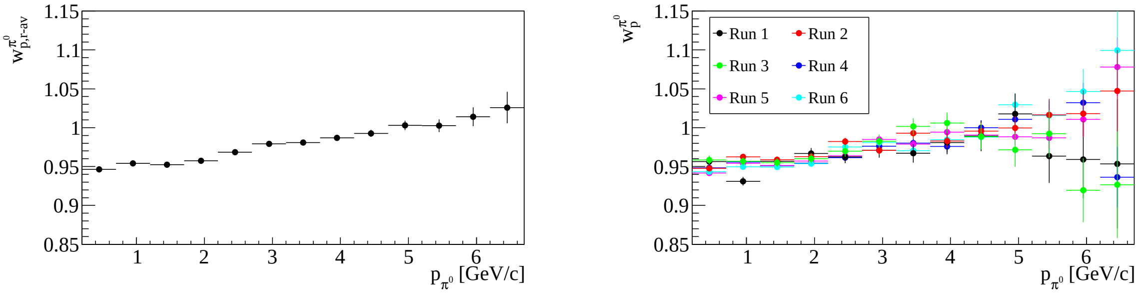

(a) π^0 correction averaged over the run periods

(b) π^0 correction for each run

Figure 9.3.: The π^0 efficiency correction values in dependence of the π^0 momentum. (a) shows the correction for each run period, while the time-averaged correction is displayed in (b). The latter correction values are used in this analysis to improve the description of data by the simulation. The shown error bars correspond to the statistical uncertainties.

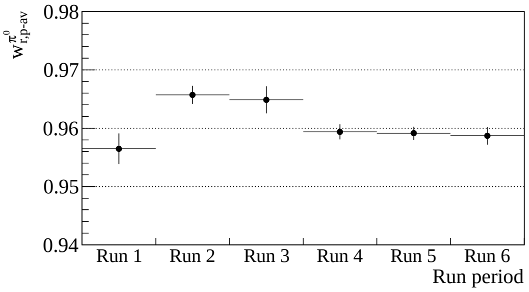

Run period	$w^{\pi^0}_{r,p\text{-}av}$
1	0.956 ± 0.003
2	0.966 ± 0.002
3	0.965 ± 0.002
4	0.959 ± 0.001
5	0.959 ± 0.001
6	0.959 ± 0.001
Av	0.960 ± 0.001

Figure 9.4.: Momentum-averaged π^0 correction values determined for each run period. The shown uncertainties are only statistical. In addition to the graphical exposure the values are also listed in a table.

1 with increasing momentum.

The performance of the electromagnetic calorimeter of the *BABAR* detector changed over the years. Different calibrations and corrections [25] have been applied to the data and the simulation to ensure a good description of the reconstruction efficiency by the simulation over time. Therefore, no significant time dependence of the π^0 efficiency correction is expected. Nevertheless, the π^0 correction values, $w^{\pi^0}_{p}$, are determined separately for each run to exclude this possible source of a systematic effect. The momentum-averaged π^0 correction factors, $w^{\pi^0}_{\mathrm{r,p\text{-}av}}$, for each run are shown in Figure 9.4. The size and shape of the distribution of the correction values (Figure 9.3a) agree very well between the runs. The values for run 4, run 5, and run 6, which correspond to 73% of the total event sample, agree within the very small statistical uncertainty. The values obtained for the data samples of run 1, run 2, and run 3 agree within 0.6% with the average correction value. Therefore, the run-averaged π^0 correction values are used to correct the simulation.

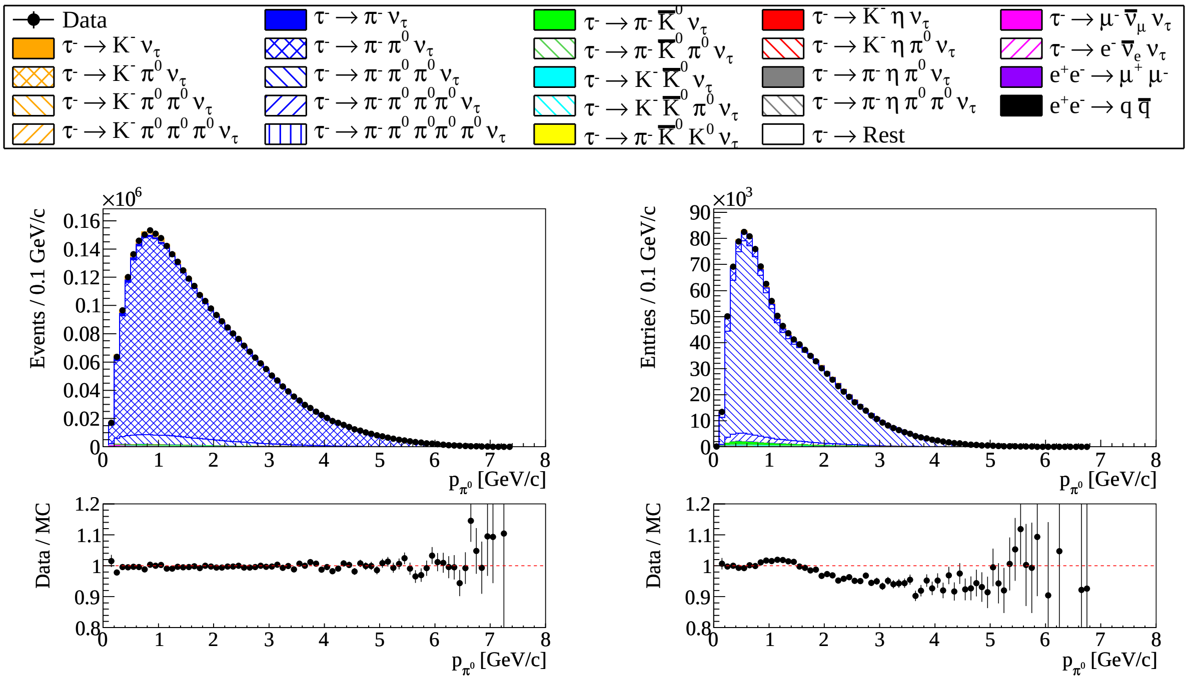

(a) $\tau^- \to t^- \pi^0 \nu_\tau$

(b) $\tau^- \to t^- (2\pi^0) \nu_\tau$

Figure 9.5.: Distribution of the π^0 momentum after the application of the π^0 efficiency correction. (b) contains two entries per event, i. e., one entry per reconstructed π^0.

9.5. Application of the π^0 correction

The simulated π^0 reconstruction efficiency is corrected by applying the weight

$$\eta_{\pi^0} = \prod_{i=1}^{n} w_{p_i,\text{r-av}}^{\pi_i^0} \tag{9.8}$$

to each event, where p_i is the momentum of the i^{th} π_i^0 in an event with n reconstructed π^0's. The weights are taken from Figure 9.3a. Since the width of the bins is rather large, a linear interpolation of the bin centers is used as correction function. Figure 9.5 shows the π^0 momentum in the $\tau^- \to t^- \pi^0 \nu_\tau$ and $\tau^- \to t^- (2\pi^0) \nu_\tau$ decays with a corrected π^0 efficiency. The agreement between data and simulation is significantly improved.

9.6. Uncertainty of the π^0 correction

This section discusses the systematic uncertainties of the π^0 efficiency correction determined by the double ratio of Equation 9.7.

9.6.1. Determination of systematic uncertainties

The contributions to the systematic uncertainty of the π^0 efficiency correction are estimated using the same method as for the branching fractions uncertainties described later in Section 10.4.1. Each quantity X, which affects the determination of the π^0 efficiency correction, e. g., the split-off correction factor, is varied within its uncertainty ΔX. A total of $N = 50$ variations are performed and for each variation k the quantity

$$X_k^{'} = X + r_k \cdot \Delta X, \tag{9.9}$$

where r_k is a random number following a Gaussian distribution, is computed. All sources of systematic uncertainties are assumed to be independent of the π^0 momentum. A test of this assumption is presented in Section 9.6.4. The momentum-averaged π^0 correction, η^{π^0}, is recalculated for each $X_k^{'}$. The root mean square (RMS) of the distribution of the resulting 50 values of the π^0 correction is taken as the estimate for the systematic uncertainty.

9.6.2. Sources of systematic uncertainties

In this section, the systematic uncertainties which affect the selection of the $\tau^- \to t^-\nu_\tau$ and $\tau^- \to t^-\pi^0\nu_\tau$ samples are described. Some of these uncertainties cancel in the double ratio (Equation 9.7), i. e., they do not contribute to the total uncertainty of the π^0 efficiency correction. However, they do contribute to the uncertainties of the branching fractions of the $\tau^- \to \pi^-\nu_\tau$ and $\tau^- \to \pi^-\pi^0\nu_\tau$ decays which are determined as a cross check in Section 9.6.5. In this section, the magnitudes of the uncertainties are determined with respect to the π^0 correction. The uncertainty values for the control branching fractions are given in Section 9.6.5. The systematic uncertainties are discussed briefly in this section, since a detailed description of systematic effects in this analysis is given in the context of the determination of the signal branching fractions in Chapter 10.

Luminosity and τ cross section uncertainty

In this analysis, the number of generated τ-pair events is scaled such that it agrees with the number of $e^+e^- \to \tau^+\tau^-$ processes expected in the e^+e^- collisions. This scaling is performed by applying a weight $w = \frac{\mathcal{L}\cdot\sigma_{\tau^+\tau^-}}{N_{\tau\tau}^{\text{gen}}}$ to each simulated τ-pair event, where $\mathcal{L} \pm \Delta\mathcal{L}$ is the integrated luminosity, $\sigma_{\tau^+\tau^-} \pm \Delta\sigma_{\tau^+\tau^-}$ is the τ-pair production cross section, and $N_{\tau\tau}^{\text{gen}}$ the number of generated $e^+e^- \to \tau^+\tau^-$ processes. This scaling factor enters both the nominator and the denominator of the double ratio through the event numbers $N(\tau^- \to t^-\nu_\tau)^{\text{MC}}$ and $N(\tau^- \to t^-\pi^0\nu_\tau)^{\text{MC}}$. Since the background of non-$e^+e^- \to \tau^+\tau^-$ events is negligible, the scaling factor cancels in the double ratio. Therefore, the uncertainties of $\mathcal{L}$ and $\sigma_{\tau^+\tau^-}$ do not contribute to the systematic uncertainty of the π^0 efficiency correction.

Track reconstruction efficiency

As described in Section 5.1.2, the track reconstruction efficiency is independent of the charges particle momentum. The uncertainty of the track reconstruction therefore only depends on the number of selected tracks in the event. Both decays used for determination of the π^0 efficiency correction are selected in events containing exactly two tracks. Therefore, the track efficiency cancels in the double ratio.

Particle identification uncertainty

Events selected for the π^0 correction determination contain two charged tracks, where the tag track is identified as an electron and the other track is required to fail the electron selection criteria. Therefore, the product of two PID weights has to be applied to each simulated event according to the method described in Section 5.2.5:

$$w_{PID}^{evt} = w_e \cdot w_e^{veto}, \tag{9.10}$$

where w_e is the correction of the identification efficiency of the tag electron, and w_e^{veto} the correction of the signal track t. The PID weights depend on the momentum, polar angle, azimuthal angle, the charge, and the true type of the track.

The distributions of p, θ, and ϕ of the selected tag electron are very similar in both decays. Therefore, the contribution of the tag electron, w_e, largely cancels in the double ratio. However, the correction weights w_e^{veto} are distributed differently for the two decays, because of the different fractions of muons, kaons and pions contributing to the selected $\tau^- \to t^-\nu_\tau$ and $\tau^- \to t^-\pi^0\nu_\tau$ decays. The uncertainties of the veto weights, Δw_e^{veto}, contribute to the total uncertainty of the π^0 efficiency correction. The resulting particle identification uncertainty on the π^0 correction amounts to

$$\Delta\eta_{PID}^{\pi^0} = 0.0002. \tag{9.11}$$

This small contribution is neglected.

Split-off correction uncertainty

A split-off correction (Chapter 8) is applied to each hadron in the simulated event. The selected $\tau^- \to t^-\nu_\tau$ and $\tau^- \to \mu^-\overline{\nu}_\mu\nu_\tau$ samples contain different fractions of hadrons. About two-thirds of the selected $\tau^- \to t^-\nu_\tau$ events contain $\tau^- \to \mu^-\overline{\nu}_\mu\nu_\tau$ decays, i. e., such events are purely leptonic (the other τ in the event is tagged by an electron). For the $\tau^- \to t^-\pi^0\nu_\tau$ sample, the fraction of purely leptonic events is negligible. Therefore, the split-off correction does not cancel in the double ratio resulting in an uncertainty of the double ratio of

$$\Delta\eta_{\text{split-off}}^{\pi^0} = 0.005. \tag{9.12}$$

Branching fractions uncertainties

The π^0 efficiency correction relies on the good knowledge of the branching fractions of the τ decays used for its determination. These branching fractions and their uncertainties are given in Equation 4.3. Their relatively small uncertainties have to be taken into account in the uncertainty of the π^0 efficiency correction. The uncertainty amounts to

$$\Delta\eta_{\mathcal{B}_{\text{MC}}}^{\pi^0} = 0.005. \tag{9.13}$$

Uncertainty due to Bhabha background

The selection criteria which reject this type of events are described in Section 6.2. These criteria have been optimized for events where the signal track is identified as a particle of a certain type by the application of a PID selector sequence (Section 5.2.4). This

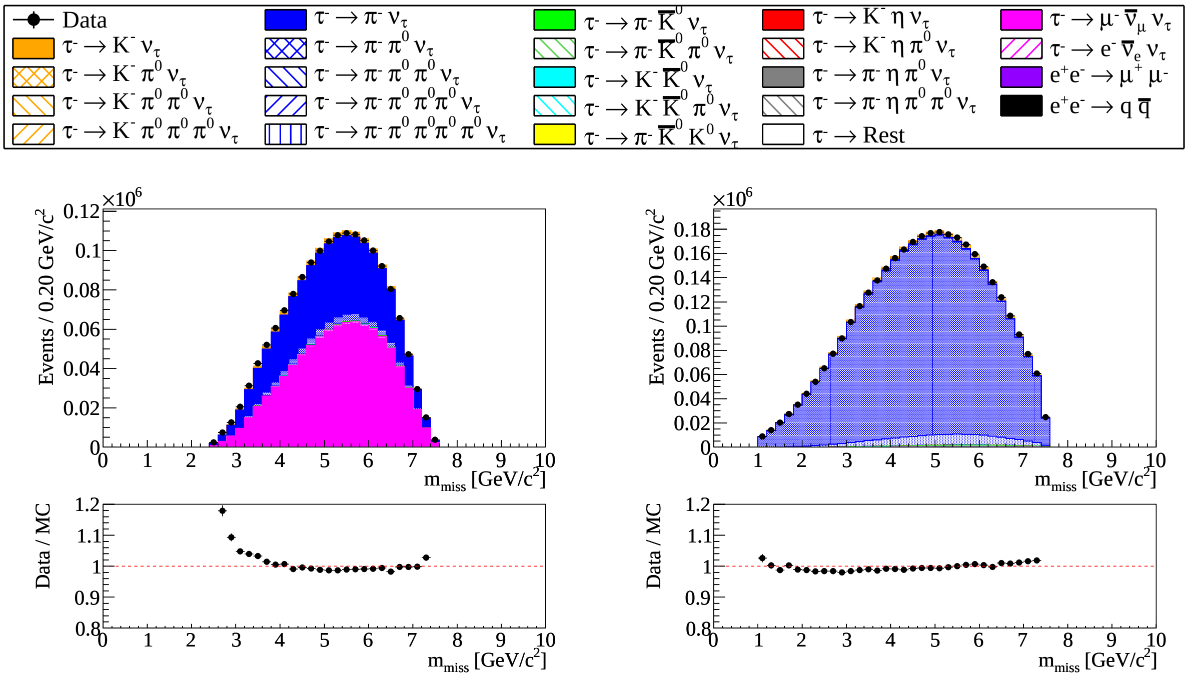

(a) $\tau^- \to t^- \nu_\tau$ **(b)** $\tau^- \to t^- \pi^0 \nu_\tau$

Figure 9.6.: Missing mass in the event.

sequence contains not only an electron veto but also an explicit identification of the particle as a pion, kaon, or muon. In contrast to that, the $\tau^- \to t^- \nu_\tau$ and $\tau^- \to t^- \pi^0 \nu_\tau$ modes are selected by only applying an electron veto to the signal track, i. e., a less efficient suppression of Bhabha events is possible.

Since the simulation does not contain $e^+e^- \to e^+e^-(\gamma)$ events (Section 3.3.2), the Bhabha contamination of the $\tau^- \to t^- \nu_\tau$ and $\tau^- \to t^- \pi^0 \nu_\tau$ sample should appear as a data excess at small values of the missing mass m_{miss}. The distribution of the missing mass is shown in Figure 9.6 for the both samples. A data excess is visible for $m_{\text{miss}} < 3.8\,\text{GeV}/c^2$ for the $\tau^- \to t^- \nu_\tau$ mode, while no excess is observed for the $\tau^- \to t^- \pi^0 \nu_\tau$ mode.

The excess in the distribution for the $\tau^- \to t^- \nu_\tau$ mode is quantified by computing the relative data excess

$$\eta_{m_{\text{miss}}} = \frac{N^{\text{Data}}(m_{\text{miss}}^{<3.8\,\text{GeV}/c^2}) - N^{\text{MC}}(m_{\text{miss}}^{<3.8\,\text{GeV}/c^2})}{N^{\text{Data}}} = 0.0043 \pm 0.0004(\text{stat}) \qquad (9.14)$$

in the m_{miss} region below $3.8\,\text{GeV}/c^2$. The relative uncertainty on the number of selected $\tau^- \to t^- \nu_\tau$ events is assumed to amount to the full size of $\eta_{m_{\text{miss}}}$ resulting in an uncertainty

$$\Delta\eta^{\pi^0}_{Bhabha} = 0.004 \qquad (9.15)$$

of the π^0 correction.

Table 9.2.: Uncertainty of the π^0 efficiency correction. All contributing sources are listed.

Source of uncertainty	Contribution to $\Delta\eta^{\pi^0}$
Data and simulation statistics	0.001
Splitoff correction	0.005
Branching fractions	0.005
Bhabha background	0.004
Total	0.008

9.6.3. Summary of the systematic uncertainties of the π^0 correction

Table 9.2 lists the determined contributions to the total systematic uncertainty of the π^0 efficiency correction. The average π^0 correction determined in this analysis is

$$\eta^{\pi^0} = 0.960 \pm 0.008 \tag{9.16}$$

where all statistical and systematic uncertainties are added in quadrature. The size of the correction is consistent with the value determined in previous *BABAR* studies of the π^0 efficiency correction [37, 51]. The uncertainty is reduced by more than a factor of three. The correction is applied to all simulated events in this analysis as a function of the π^0 momentum.

9.6.4. Tests of possible remaining dependencies of the π^0 correction

In this section, a test is presented to rule out a dependence of the π^0 correction on the π^0 polar angle. In addition, the assumption that the π^0 uncertainty does not depend on the π^0 momentum is validated.

π^0 polar angle dependence of the π^0 correction

π^0's are reconstructed from photons measured in the electromagnetic calorimeter. Calibrations of the EMC are performed as a function of spacial coordinates. Therefore, a possible dependence of the π^0 correction on the polar angle θ_{π^0} is investigated. This dependence can be checked by studying the θ_{π^0} distribution. Figure 9.7 shows the distribution of θ_{π^0} for the $\tau^- \to \pi^-\pi^0\nu_\tau$ and $\tau^- \to \pi^-(2\pi^0)\nu_\tau$ decay modes which are selected according to the criteria discussed in Chapter 6. All corrections to the simulation including the momentum-dependent π^0 correction are applied. The displayed data/MC ratios show that the description of the data by the simulation is very good over the whole polar angle range.

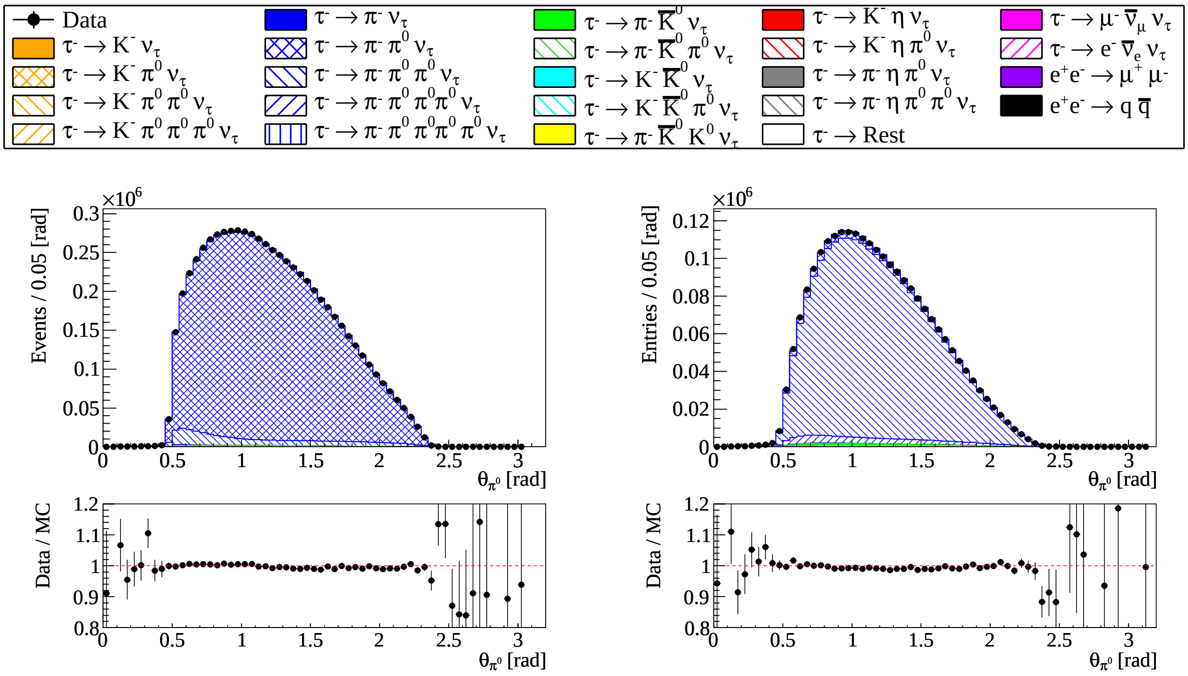

(a) $\tau^- \to \pi^- \pi^0 \nu_\tau$

(b) $\tau^- \to \pi^- (2\pi^0) \nu_\tau$

Figure 9.7.: Distribution of the π^0 polar angle for the $\tau^- \to \pi^- \pi^0 \nu_\tau$ and $\tau^- \to \pi^- (2\pi^0) \nu_\tau$ decay modes. The decays are selected according to the criteria described in Chapter 6. The π^0 efficiency correction is applied. (b) contains two entries per event, i. e., one entry per reconstructed π^0.

π^0 momentum dependence of the π^0 correction uncertainty

The uncertainty of the π^0 correction has been assumed to be independent of the π^0 momentum. The dominant contributions to the systematic uncertainty of the correction are determined in dependence of the π^0 momentum to validate this assumption. Table 9.3 shows the uncertainty arising from the split-off correction and from the uncertainty of τ decay branching fractions used in the simulation. The uncertainties are listed in intervals of the π^0 momentum. The differences of the uncertainties in different intervals are negligible which justifies the assumption of a π^0-momentum independent uncertainty assignment.

Table 9.3.: Largest contributions to the systematic uncertainty of the π^0 efficiency correction determined in intervals of the π^0 momentum p_{π^0}.

p_{π^0} [GeV/c]	0.0 - 1.0	1.0 - 2.0	2.0 - 3.0	3.0 - 4.0	4.0 - 5.0
split-off correction	0.0050	0.0050	0.0051	0.0052	0.0053
branching fractions	0.0047	0.0048	0.0049	0.0050	0.0051

9.6.5. Consistency check: Branching fractions determined in the $\tau^- \to t^-\nu_\tau$, $\tau^- \to t^-\pi^0\nu_\tau$, and $\tau^- \to t^-(2\pi^0)\nu_\tau$ samples

As a consistency check of the π^0 correction determination the branching fractions of the $\tau^- \to \pi^-\nu_\tau$, $\tau^- \to \pi^-\pi^0\nu_\tau$, and $\tau^- \to \pi^-(2\pi^0)\nu_\tau$ decays can be computed from the selected $\tau^- \to t^-\nu_\tau$, $\tau^- \to t^-\pi^0\nu_\tau$, and $\tau^- \to t^-(2\pi^0)\nu_\tau$ samples. The results have to be consistent with the branching fractions of these modes used in the simulation, i. e., the current world averages. Since the π^0 correction is applied twice in the $\tau^- \to \pi^-(2\pi^0)\nu_\tau$ mode, any inconsistency of the correction would be doubled in this mode.

Moreover, the obtained values can be compared with the branching fractions of these decays obtained from the samples selected in the main analysis. In the latter samples a full particle identification is applied. The comparison can be therefore used to cross check the PID performance. This comparison is discussed in Section 10.5.

Figure 9.8 shows the branching fractions determined from the $\tau^- \to t^-\nu_\tau$, $\tau^- \to t^-\pi^0\nu_\tau$, and $\tau^- \to t^-(2\pi^0)\nu_\tau$ samples for each run as well as the run-averaged value. The branching fractions are computed according to Equation 10.8 which is presented in Section 10.2. The branching fractions are compared with the current world average [4] which is used in the simulation. All statistical and systematic uncertainties as listed in the previous section are included in the figure. The uncertainties of the tracking efficiency and of the number of τ pairs are also taken into account. They are a significant contributions to the total uncertainty of the branching fractions. In case of the uncertainty of the π^0 efficiency correction, which is given by a double ratio, these contributions cancel. The obtained branching fractions and uncertainties are summarized in Table 9.4. For all three decay modes the branching fractions determined separately

Table 9.4.: Summary of the measured branching fractions of the control decays. The branching fractions are calculated from the event samples used to determine the π^0 efficiency correction. The total uncertainties are obtained by adding the uncertainties in quadrature.

Control mode	$\tau \to \pi\nu_\tau$	$\tau \to \pi\pi^0\nu_\tau$	$\tau \to \pi\pi^0\pi^0\nu_\tau$
Branching fraction [%]	10.894	25.371	9.214
Total uncertainty [%]	0.335	0.578	0.256
Statistical uncertainty (Data & MC) [%]	0.033	0.021	0.017
Systematic uncertainty [%]	0.333	0.577	0.255
Breakdown of systematic uncertainties			
Background branching fractions [%]	0.044	0.025	0.008
Bhabha background [%]	0.065	0.000	0.000
Number of $\tau^+\tau^-$ pairs [%]	0.253	0.260	0.087
Track efficiency [%]	0.096	0.099	0.033
Splitoff correction [%]	0.177	0.418	0.140
PID (electron + electron veto) [%]	0.014	0.005	0.002
π^0 efficiency correction [%]	0.000	0.284	0.191

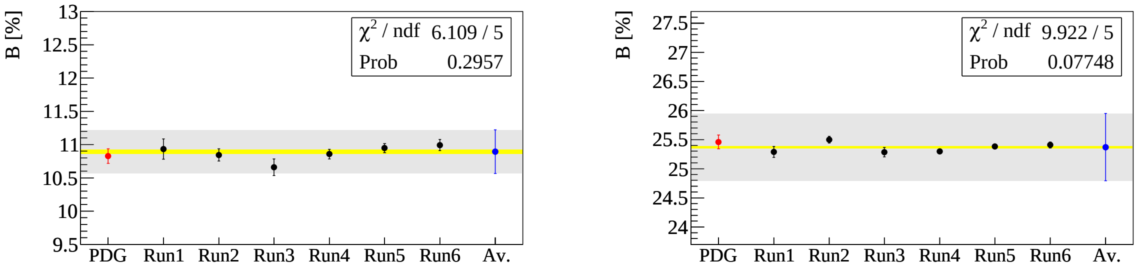

(a) $\tau^- \to \pi^- \nu_\tau$ **(b)** $\tau^- \to \pi^- \pi^0 \nu_\tau$

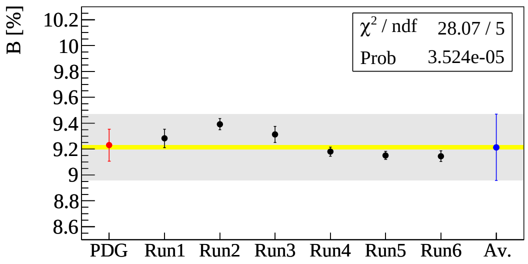

(c) $\tau^- \to \pi^-(2\pi^0)\nu_\tau$

Figure 9.8.: The branching fractions $\mathcal{B}(\tau^- \to \pi^-\nu_\tau)$, $\mathcal{B}(\tau^- \to \pi^-\pi^0\nu_\tau)$, and $\mathcal{B}(\tau^- \to \pi^-(2\pi^0)\nu_\tau)$ determined from the numbers of selected $\tau^- \to t^-\nu_\tau$, $\tau^- \to t^-\pi^0\nu_\tau$, and $\tau^- \to t^-(2\pi^0)\nu_\tau$ decays. The black circles represent the branching fractions determined for each run. The corresponding error bars display the run dependent contributions to the uncertainty, i. e., the uncertainty of the data and simulation event numbers, and of the number of control tracks in the PID control samples. The displayed χ^2 value is calculated with respect to the average branching fraction using the branching fractions for each run and the uncorrelated uncertainties between the runs. The run-averaged value of the branching fraction for each decay is represented by the blue circle with error bars. The yellow band corresponds to the averaged run-dependent uncertainty. The gray band shows the systematic uncertainty contribution which is assumed to be run independent. The measured branching fractions are compared with the world average [4] red circle.

for each run are in good agreement with the world averages.

10. Determination of the branching fractions

In the following sections, the branching fractions of the signal and control decays are computed from the numbers of selected events, and the determination of the uncertainties for both types of decays is presented.

10.1. Number of selected events

The number of selected events for each signal and control mode in data and simulation is listed in Table 10.1 for the total dataset used in this analysis. For the simulated event sample the contribution from the signal and control decays (bold) and the contributions from the various background decays are given.

The selection efficiencies are determined from simulation. For the decay mode i the efficiency is defined as

$$\epsilon_i = \frac{N_i^{\mathrm{sel}}}{N_i^{\mathrm{gen}}}, \tag{10.1}$$

where N_i^{sel} is the number of selected signal or control events and N_i^{gen} is the number of generated events of this type. The efficiencies obtained for all analyzed decay modes are given in Table 10.2. They are relatively small due to the requirement of a tag lepton which limits the efficiencies to at most $\approx 34\%$, corresponding to the branching fractions $\mathcal{B}(\tau^- \to e^-\overline{\nu}_e\nu_\tau) \approx \mathcal{B}(\tau^- \to \mu^-\overline{\nu}_\mu\nu_\tau) \approx 17\%$. Thus, the maximum signal selection efficiency which can be achieved with a lepton tag is approximately 32%. The selection criteria described in Chapter 6 further reduce the efficiency. The efficiency of the π^0-less modes is relatively small compared to the modes with π^0's, because additional selection criteria to suppress $e^+e^- \to l^+l^-(\gamma)$ events are applied. For the decays with π^0's the efficiency decreases with the number of reconstructed π^0's.

10.2. Calculation of the branching fractions

The branching fractions of the signal decays are determined with the same method as in [10]. The method is described in detail in this section.

Table 10.1.: Selected event numbers for each signal decay mode in data and simulation. These numbers are used to determine the branching fractions. All corrections to simulated events are applied leading to non-integer numbers of simulated events. The event numbers obtained in simulation are further subdivided according to the true τ decay mode contained in the event. The selected signal events numbers are bold.

Selected mode	K^-	$K^-\pi^0$	$K^-(2\pi^0)$	$K^-(3\pi^0)$	π^-	$\pi^-\pi^0$	$\pi^-(2\pi^0)$	$\pi^-(3\pi^0)$	$\pi^-(4\pi^0)$	μ^-
data	79279	148327	12399	609	1445918	6786687	1217602	50560	1099	1074053
MC	77602.2	134203.4	12672.4	770.5	1479464.4	6795696.1	1216317.0	43555.5	1091.2	1076260.7
True decay										
K^-	**59255.8**	1032.2	7.4	0.2	3076.4	358.8	15.9	0.0	0.0	974.1
$K^-\pi^0$	1174.2	**80695.7**	404.3	6.7	56.1	4630.0	207.4	4.1	0.0	27.2
$K^-(2\pi^0)$	13.7	1516.5	**4813.2**	20.4	1.6	105.1	395.4	10.7	0.0	0.8
$K^-(3\pi^0)$	1.0	118.9	560.3	**328.6**	0.1	12.8	89.6	30.1	0.7	0.1
π^-	12375.0	592.0	18.8	0.6	**1143012.3**	25660.9	604.9	13.2	0.0	54281.8
$\pi^-\pi^0$	1076.6	42151.1	657.1	16.1	105358.7	**6406842.6**	42074.7	534.1	3.5	5694.7
$\pi^-(2\pi^0)$	58.7	2317.7	4790.2	70.5	6203.6	307031.5	**1114868.6**	6637.6	42.8	333.7
$\pi^-(3\pi^0)$	6.1	44.4	166.4	75.7	223.1	6210.2	35285.9	**29209.1**	194.5	12.6
$\pi^-(4\pi^0)$	0.2	2.1	4.9	8.4	8.7	192.5	1161.3	3057.6	**575.2**	0.2
$\pi^-\eta\pi^0$	0.0	2.3	3.3	3.0	18.1	504.6	881.0	1449.9	180.2	0.2
$\pi^-\eta\pi^0\pi^0$	0.0	0.2	0.3	0.3	0.1	10.0	88.3	98.7	18.1	0.0
$K^-\eta$	6.5	41.4	110.1	14.2	0.3	3.6	14.8	6.8	0.2	0.1
$K^-\eta\pi^0$	0.1	15.5	35.4	16.7	0.0	1.5	4.6	2.3	0.3	0.0
$\pi^-\overline{K}^0$	80.9	65.1	17.8	1.9	8131.7	7352.2	13129.9	92.0	1.8	566.3
$\pi^-\overline{K}^0\pi^0$	2.2	143.8	23.5	2.4	342.6	28435.1	4633.8	2024.1	14.1	24.7
K^+K^0	1341.9	1364.5	365.8	11.0	112.6	124.7	160.7	3.0	0.0	40.0
$K^-\overline{K}^0\pi^0$	44.7	3853.2	652.0	183.2	7.0	299.0	117.9	46.3	1.2	0.9
$\pi^-\overline{K}^0\eta$	0.0	0.2	0.3	0.3	0.1	10.5	29.1	14.3	2.8	0.0
$\pi^-\overline{K}^0K^0$	2.1	10.0	3.4	0.9	99.6	659.2	1586.1	181.4	29.7	24.7
e^-	248.7	15.4	0.0	0.0	17795.6	657.1	1.7	0.0	0.0	34.7
μ^-	1794.1	3.6	0.0	0.0	187800.9	606.7	3.7	0.0	0.0	**1014019.6**
$q\overline{q}$	23.6	155.3	33.6	9.3	120.0	922.8	433.1	116.8	26.0	2.9
$\mu^+\mu^-$	55.7	2.2	0.0	0.0	5538.1	76.2	0.0	0.0	0.0	123.0
rest	40.5	60.1	4.8	0.0	1557.3	4988.6	528.8	23.6	0.0	98.4

Table 10.2.: Selection efficiencies in % of all signal and control decay modes.

Mode	ϵ[%]	Mode	ϵ[%]
$\tau^- \to \pi^- \nu_\tau$	1.27	$\tau^- \to K^- \nu_\tau$	0.99
$\tau^- \to \pi^- \pi^0 \nu_\tau$	3.32	$\tau^- \to K^- \pi^0 \nu_\tau$	2.19
$\tau^- \to \pi^- (2\pi^0) \nu_\tau$	1.46	$\tau^- \to K^- (2\pi^0) \nu_\tau$	0.96
$\tau^- \to \pi^- (3\pi^0) \nu_\tau$	0.35	$\tau^- \to K^- (3\pi^0) \nu_\tau$	0.10
$\tau^- \to \pi^- (4\pi^0) \nu_\tau$	0.06	$\tau^- \to \mu^- \overline{\nu}_\mu \nu_\tau$	0.74

10.2.1. Definition of signal events for the branching fraction calculation

The branching fraction of a signal τ decay is defined as the ratio of the width of a signal decay, $\Gamma(\tau\to\ \mathit{signal})$, and the total decay width, Γ_τ. It can be obtained from the ratio of the number of signal decays, $N(\tau\to\ \mathit{signal})$, and the total number of τ decays, N_τ:

$$\mathcal{B}(\tau\to\ \mathit{signal}) = \frac{\Gamma(\tau\to\ \mathit{signal})}{\Gamma_\tau} = \frac{N(\tau\to\ \mathit{signal})}{N_\tau}. \tag{10.2}$$

For the calculation of the branching fraction it has to be taken into account that events which contain two τ's are selected. One or both of the two τ's can decay into a signal final state. A *signal event* is defined as an event which contains at least one signal decay[1]. The number of produced signal events, $N^{\mathrm{prod}(i)}$, for a signal decay i can be written as:

$$\begin{aligned} N^{\mathrm{prod}} &= N(\tau^-\to\ \mathit{signal}, \tau^+\not\to\ \mathit{signal}) \\ &+ N(\tau^-\not\to\ \mathit{signal}, \tau^+\to\ \mathit{signal}) \\ &+ N(\tau^-\to\ \mathit{signal}, \tau^+\to\ \mathit{signal}), \end{aligned} \tag{10.3}$$

where $N(\tau^-\to\ \mathit{signal}, \tau^+\not\to\ \mathit{signal})$ and $N(\tau^-\not\to\ \mathit{signal}, \tau^+\to\ \mathit{signal})$ are the numbers of events where only one τ decays into a signal final state, and $N(\tau^-\to\ \mathit{signal}, \tau^+\to\ \mathit{signal})$ is the number of events with two signal decays. These numbers are related to $\mathcal{B}(\tau\to\ \mathit{signal})$ through

$$\begin{aligned} N(\tau^-\to\ \mathit{signal}, \tau^+\not\to\ \mathit{signal}) &= N(\tau^-\not\to\ \mathit{signal}, \tau^+\to\ \mathit{signal}) \\ &= \mathcal{B}(\tau\to\ \mathit{signal}) \cdot (1-\mathcal{B}(\tau\to\ \mathit{signal})) \cdot N_{\tau\tau}, \end{aligned} \tag{10.4}$$

and

$$N(\tau^-\to\ \mathit{signal}, \tau^+\to\ \mathit{signal}) = (\mathcal{B}(\tau\to\ \mathit{signal}))^2 \cdot N_{\tau\tau}, \tag{10.5}$$

---

[1] In principle, a signal event could be defined as $(\tau^-\to\ \mathit{signal},\ \tau^- \to l^-\overline{\nu}_l\nu_\tau)$. However, this results in a dependence of the measured branching fraction on itself. The branching fraction is obtained by subtracting $N^{\mathrm{sel}}_{\mathrm{bkg}}$ from data. $N^{\mathrm{sel}}_{\mathrm{bkg}}$ is taken from the simulation, and depends on the branching fractions of the background decays. With the above definition, events with two signal τ decays are background. They can contribute to $N^{\mathrm{sel}}_{\mathrm{bkg}}$ if one of the two signal decays is misidentified as a $\tau^- \to l^-\overline{\nu}_l\nu_\tau$ decay, which leads to a dependence on the branching fraction to be measured.

where $N_{\tau\tau}$ is the total number of produced τ-pair events given by the product of the integrated luminosity and the τ-pair production cross section at the BABAR center-of-mass energy:

$$N_{\tau\tau} = \mathcal{L} \cdot \sigma_{\tau\tau}. \tag{10.6}$$

With the above relations N^{prod} can be written as

$$N^{\text{prod}} = (2\mathcal{B}(\tau\!\rightarrow \textit{signal}) - \mathcal{B}(\tau\!\rightarrow \textit{signal})^2)N_{\tau\tau}. \tag{10.7}$$

The branching fraction is then[2]

$$\mathcal{B}(\tau\!\rightarrow \textit{signal}) = 1 - \sqrt{1 - \frac{N^{\text{prod}}}{\mathcal{L} \cdot \sigma_{\tau\tau}}}. \tag{10.8}$$

For the signal modes, cross feed between the different signal modes has to be taken into account. Therefore, the branching fractions of the signal decays and those of the control decays are determined using two different approaches. The two approaches are described in the next sections.

10.2.2. Branching fraction determination for control decays

The branching fractions of the control decays $\tau^- \rightarrow \pi^-\nu_\tau$, $\tau^- \rightarrow \pi^-\pi^0\nu_\tau$, $\tau^- \rightarrow \pi^-(2\pi^0)\nu_\tau$, and $\tau^- \rightarrow \mu^-\overline{\nu}_\mu\nu_\tau$ are well known. Therefore, the fraction of cross feed between the selected control modes is correctly simulated. The number of selected signal[3] events, $N^{\text{sel}(i)}_{\text{sig}}$, where the index i corresponds to the selected control mode, is then given by

$$N^{\text{sel}(i)}_{\text{sig}} = N^{\text{sel}(i)} - \sum_j N^{\text{sel}(i)}_{\text{bkg}(j)}. \tag{10.9}$$

where $N^{\text{sel}(i)}$ is the number of selected events, and $N^{\text{sel}(i)}_{\text{bkg}(j)}$ are the numbers of selected background events j, where j can be any type of event, except of events which contain the control decay i. The number of produced signal events, $N^{\text{prod}(i)}$, is related to $N^{\text{sel}(i)}_{\text{sig}}$ through

$$N^{\text{prod}(i)} = \frac{N^{\text{sel}(i)}_{\text{sig}}}{\epsilon_i}, \tag{10.10}$$

where ϵ_i is the signal selection efficiency defined in Equation 10.1.

The number of selected background events as well as the signal efficiency (Table 10.2) are estimated from simulation:

$$\begin{aligned} N^{\text{sel}(i)}_{\text{bkg}(j)} &= N^{\text{sel}(i),\text{MC}}_{\text{bkg}(j)}, \\ \epsilon_i &= \epsilon_i^{\text{MC}}. \end{aligned} \tag{10.11}$$

---

[2] Equation 10.7 contains a quadratic term of the $\mathcal{B}(\tau\!\rightarrow \textit{signal})$ leading to two solution for $\mathcal{B}(\tau\!\rightarrow \textit{signal})$. The second solution is unphysical, because $\mathcal{B}(\tau\!\rightarrow \textit{signal}) > 1$, and is not considered.

[3] In this thesis the term *signal* usually denotes one of the six decays which are measured. Here it refers to the analyzed control decay.

This leads to

$$N^{\mathrm{prod}(i)} = \frac{N^{\mathrm{sel}(i)} - N^{\mathrm{sel}(i),\mathrm{MC}}_{\mathrm{bkg}(j)}}{\epsilon_i}. \tag{10.12}$$

$N^{\mathrm{sel}(i),\mathrm{MC}}_{\mathrm{bkg}(j)}$ is obtained by scaling the number of selected simulated events for each of the processes $e^+e^- \to \tau^+\tau^-$, $e^+e^- \to \mu^+\mu^-$, and $e^+e^- \to q\overline{q}$ $(q = u, d, s, c, b)$ to match the integrated luminosity. The branching fraction is then given by

$$\mathcal{B}(\tau \to \ \mathit{signal}(i)) = 1 - \sqrt{1 - \frac{N^{\mathrm{sel}(i)} - N^{\mathrm{sel}(i),\mathrm{MC}}_{\mathrm{bkg}(j)}}{\epsilon_i^{\mathrm{MC}} \mathcal{L} \sigma_{\tau\tau}}}. \tag{10.13}$$

The statistical uncertainties of the data and simulated event samples are assumed to be Poisson distributed. The resulting uncertainties of the branching fractions are given in Section 10.3.1.

10.2.3. Branching fraction determination for the signal decays

The six signal decays can be mutual backgrounds, i. e., a signal decay can be wrongly reconstructed as a different signal decay. As the branching fractions are not known, this migration for a signal mode to another is taken into account in the calculation of the branching fractions by using the following method. As given in Equation 10.9 the number of selected signal events, $N^{\mathrm{sel}(i)}_{\mathrm{sig}}$, is

$$N^{\mathrm{sel}(i)}_{\mathrm{sig}} = N^{\mathrm{sel}(i)} - \sum_m N^{\mathrm{sel}(m)}_{\mathrm{bkg}(m)}. \tag{10.14}$$

Due to the migration of signal events, two different contributions to the number of background events have to be considered:

$$\sum_m N^{\mathrm{sel}(i)}_{\mathrm{bkg}(m)} = \sum_k N^{\mathrm{sel}(i)}_{\mathrm{xfeed}(k)} + \sum_l N^{\mathrm{sel}(i)}_{\mathrm{rest}(l)} \tag{10.15}$$

where the first term is the number of migrated signal events from the $k \neq i$ modes , and the second term is the sum of events from all remaining background modes[4]. The event numbers for this remaining modes are taken from the simulation.

The probabilities M_{ij} to reconstruct a true event of type j as an event of type i, which are estimated from simulated events, are defined as

$$M_{ij} = \frac{N^{\mathrm{sel}(j\text{-as-}i),\mathrm{MC}}}{N^{\mathrm{gen,MC}}_j}. \tag{10.16}$$

The number of selected events in decay mode i can then be written as

$$N^{\mathrm{sel}(i)} = M_{ii} N^{\mathrm{prod}(i)} + \sum_{k \neq i} M_{ik} N^{\mathrm{prod}(k)} + \sum_l N^{\mathrm{sel}(i)}_{\mathrm{rest}(l)}, \tag{10.17}$$

---

[4] The number of these background events is scaled to match the data luminosity.

where the probabilities M_{ii} correspond to the signal selection efficiencies as defined in Equation 10.1. This can be used to write

$$N^{\mathrm{sel}(i)}_{(\mathrm{w/o\ rest})} = \sum_{j=0}^{n} M_{ij} N^{\mathrm{prod}(j)}, \tag{10.18}$$

where $N^{\mathrm{sel}(i)}_{(\mathrm{w/o\ rest})} = N^{\mathrm{sel}(i)} - \sum_{l} N^{\mathrm{sel}(i)}_{\mathrm{rest}(l)}$, and $n = 6$ is the number of all signal modes, or in matrix form:

$$\mathbf{N}^{\mathrm{sel}}_{(\mathrm{w/o\ rest})} = \mathbf{M} \cdot \mathbf{N}^{\mathrm{prod}}. \tag{10.19}$$

where

$$\mathbf{N}^{\mathrm{sel}}_{(\mathrm{w/o\ rest})} = \begin{pmatrix} N^{\mathrm{sel}(1)}_{\mathrm{sig}} + \sum_{k} N^{\mathrm{sel}(1)}_{\mathrm{xfeed(k)}} \\ N^{\mathrm{sel}(2)}_{\mathrm{sig}} + \sum_{k} N^{\mathrm{sel}(2)}_{\mathrm{xfeed(k)}} \\ \dots \end{pmatrix} \tag{10.20}$$

and

$$\mathbf{N}^{\mathrm{prod}} = \begin{pmatrix} N^{\mathrm{prod}(1)} \\ N^{\mathrm{prod}(2)} \\ \dots \end{pmatrix} \tag{10.21}$$

The matrix $\mathbf{M}$ is denoted as *migration matrix.*

The number of produced events is obtained from the number of selected signal events by inverting the migration matrix:

$$\mathbf{N} = \mathbf{M^{-1}} \cdot \mathbf{N}^{\mathrm{sel}}_{\mathrm{sig}}. \tag{10.22}$$

The branching fractions of the signal decays j are then calculated according to

$$\mathcal{B}(\tau \to j) = 1 - \sqrt{1 - \frac{N^{\mathrm{prod}(j)}}{\mathcal{L}\sigma_{\tau\tau}}}. \tag{10.23}$$

10.2.4. Statistical uncertainty of the signal branching fractions

The statistical uncertainties of the selected signal event numbers, $N^{\mathrm{sel}(i)}_{\mathrm{sig}}$, are uncorrelated for the various signal modes. The covariances of the $N^{\mathrm{sel}(i)}_{\mathrm{sig}}$ are therefore

$$V^{\mathrm{sel}}_{ij} = \delta_{ij} N^{\mathrm{sel}(i)}_{\mathrm{sig}} \quad \text{with} \quad \delta_{ij} = \begin{cases} 0 \text{ if } i \neq j \\ 1 \text{ if } i = j \end{cases}, \tag{10.24}$$

assuming a Poisson distribution of the $N^{\mathrm{sel}(i)}_{\mathrm{sig}}$.

The number of produced signal events $N^{\mathrm{sel}(i)}$ is related to $N^{\mathrm{sel}(i)}_{\mathrm{sig}}$ trough the migration matrix $\mathbf{M}$ (Equation 10.22). The covariance matrix $\mathbf{V}$ of the produced signal event numbers is then obtained from

$$\mathbf{V} = \mathbf{M^{-1}} \mathbf{V}^{\mathrm{sel}} (\mathbf{M^{-1}})^{\mathrm{T}} \tag{10.25}$$

where $\mathbf{V}^{\text{sel}} = (V_{ij}^{\text{sel}})$. The covariance matrix $V_{\mathcal{B}}$ for the measured branching fractions is determined by error propagation:

$$\mathbf{V}^{\boldsymbol{\mathcal{B}}} = \mathbf{J}\mathbf{V}\mathbf{J}^T, \tag{10.26}$$

where $\mathbf{J}$ is the Jacobian matrix with the elements

$$J_{ij} = \frac{\partial \mathcal{B}_i}{\partial N_j}. \tag{10.27}$$

The elements are derived from Equation 10.13:

$$J_{ij} = \delta_{ij} \cdot \frac{1}{2\mathcal{L}\sigma_{\tau\tau}} \sqrt{1 - \frac{N_j}{\mathcal{L}\sigma_{\tau\tau}}} \quad \text{with} \quad \delta_{ij} = \begin{cases} 0 \text{ if } i \neq j \\ 1 \text{ if } i = j \end{cases}. \tag{10.28}$$

The elements of the correlation matrix $\boldsymbol{\rho}_{\boldsymbol{\mathcal{B}}}$ for the branching fractions are given by

$$\rho_{ij} = \frac{V_{ij}^{\mathcal{B}}}{\sigma_i^{\mathcal{B}} \sigma_j^{\mathcal{B}}} \tag{10.29}$$

where

$$\sigma_i^{\mathcal{B}} = \sqrt{V_{ii}^{\mathcal{B}}} =: \Delta\mathcal{B}_i^{\text{stat}}. \tag{10.30}$$

is the statistical uncertainty of the branching fraction $\mathcal{B}_i$ of the signal mode i.

10.3. Measured branching fractions

The branching fractions of the analyzed decays are determined by averaging the branching fraction values obtained separately for each run. Some of the branching fraction uncertainties, i. e., the statistical uncertainty of the selected data and simulated event sample, and the systematic uncertainty of the particle identification performance, are uncorrelated between the data taking periods. The average branching fraction is computed taking this uncertainty contributions into account. Other systematic uncertainties which are independent of the run are determined only for the whole data sample. The reason to first determine the branching fractions for each run, and then compute the average is that this procedure allows for a test of the consistency of the measured values for the statistically independent samples. The determination of all uncertainties is described in the following sections.

10.3.1. Control decays

The branching fractions of the control decays are calculated from Equation 10.13. The values obtained in the total event sample are

$$\begin{aligned}
\mathcal{B}(\tau^- \to \pi^-\nu_\tau) &= (10.542 \pm 0.016(\mathrm{stat}_{(\mathrm{Data\&MC})}) \times 10^{-2} \\
\mathcal{B}(\tau^- \to \pi^-\pi^0\nu_\tau) &= (25.366 \pm 0.015(\mathrm{stat}_{(\mathrm{Data\&MC})}) \times 10^{-2} \\
\mathcal{B}(\tau^- \to \pi^-(2\pi^0)\nu_\tau) &= (9.236 \pm 0.012(\mathrm{stat}_{(\mathrm{Data\&MC})}) \times 10^{-2} \\
\mathcal{B}(\tau^- \to \mu^-\overline{\nu}_\mu\nu_\tau) &= (17.225 \pm 0.924(\mathrm{stat}_{(\mathrm{Data\&MC})}) \times 10^{-2}.
\end{aligned} \tag{10.31}$$

The uncertainty is the combined[5] statistical uncertainty of the data sample and the simulated event sample.

10.3.2. Signal decays

The signal branching fractions are determined with the migration matrix method described in Section 10.2.3. The values obtained according to Equation 10.22 for run 1–6 are

$$\begin{aligned}
\mathcal{B}(\tau^- \to K^-\nu_\tau) &= (7.100 \pm 0.033(\mathrm{stat})) \times 10^{-3} \\
\mathcal{B}(\tau^- \to K^-\pi^0\nu_\tau) &= (5.000 \pm 0.020(\mathrm{stat})) \times 10^{-3} \\
\mathcal{B}(\tau^- \to K^-(2\pi^0)\nu_\tau) &= (5.654 \pm 0.144(\mathrm{stat})) \times 10^{-4} \\
\mathcal{B}(\tau^- \to K^-(3\pi^0)\nu_\tau) &= (1.642 \pm 0.279(\mathrm{stat})) \times 10^{-4} \\
\mathcal{B}(\tau^- \to \pi^-(3\pi^0)\nu_\tau) &= (1.216 \pm 0.010(\mathrm{stat})) \times 10^{-2} \\
\mathcal{B}(\tau^- \to \pi^-(4\pi^0)\nu_\tau) &= (1.041 \pm 0.067(\mathrm{stat})) \times 10^{-3}.
\end{aligned} \tag{10.32}$$

The uncertainty is the statistical uncertainty of the selected data event sample. The determination of statistical uncertainty of the simulated event sample is described in the next section. The corresponding correlation matrix is

$$\boldsymbol{\rho}^{\mathcal{B}}_{(\mathrm{stat})} = \begin{array}{c} \\ K \\ K\pi^0 \\ K2\pi^0 \\ K3\pi^0 \\ \pi3\pi^0 \\ \pi4\pi^0 \end{array} \!\!\begin{array}{c} \begin{array}{rrrrrr} K & K\pi^0 & K2\pi^0 & K3\pi^0 & \pi3\pi^0 & \pi4\pi^0 \end{array} \\ \left(\begin{array}{rrrrrr}
1.000 & -0.033 & 0.001 & -0.000 & -0.000 & 0.000 \\
-0.033 & 1.000 & -0.104 & 0.012 & 0.000 & -0.000 \\
0.001 & -0.104 & 1.000 & -0.370 & -0.005 & 0.007 \\
-0.000 & 0.012 & -0.370 & 1.000 & -0.023 & -0.002 \\
-0.000 & 0.000 & -0.005 & -0.023 & 1.000 & -0.652 \\
0.000 & -0.000 & 0.007 & -0.002 & -0.652 & 1.000
\end{array}\right) \end{array}. \tag{10.33}$$

10.4. Systematic uncertainties

The branching fractions are calculated from the numbers of events selected in data and simulation. These numbers depend on various quantities which have been determined with a limited accuracy. In this section, systematic effects in the branching fraction

---

[5] Throughout the thesis, uncertainties are combined by adding them in quadrature.

measurement are discussed, and the resulting branching fraction uncertainties are determined. Furthermore, the uncertainty due to the limited number of simulated events is also computed.

10.4.1. Determination method of systematic uncertainties

The systematic uncertainties considered in this analysis are estimated using a variation method which is summarized in this section, and is applied in the following.

The systematic uncertainty of the branching fraction resulting from an uncertainty ΔX of a quantity X is determined simultaneously for all signal mode branching fractions, $\mathcal{B}_i$, as follows:

The quantity X is varied N times within its uncertainty according to

$$X_k' = X + r_k \cdot \Delta X, \quad \text{with} \;\; k = 1...N, \tag{10.34}$$

where the r_k are random numbers generated according to a Gaussian function

$$f(x) = \tfrac{1}{\sqrt{2\pi\sigma^2}}\, e^{-\frac{(x-\mu)^2}{2\sigma^2}} \tag{10.35}$$

with mean $\mu = 0$ and variance $\sigma^2 = 1$. In this analysis, the quantity X is varied $N = 50$ times. The branching fractions $\mathcal{B}_i$ are recalculated for each X_k' ($k = 1, ..., 50$). The branching fraction uncertainty is then determined from the resulting branching fraction values $\mathcal{B}_i^k$ by

$$\Delta\mathcal{B}_i = \sqrt{\operatorname{cov}(\mathcal{B}_i, \mathcal{B}_i)} = \sqrt{\frac{1}{N}\sum_{k=1}^{N}(\mathcal{B}_i^k - \overline{\mathcal{B}}_i)^2} \tag{10.36}$$

where

$$\overline{B}_i = \frac{1}{N}\sum_{k=1}^{N}\mathcal{B}_i^k. \tag{10.37}$$

For all uncertainties also the correlation matrices are determined according to:

$$\boldsymbol{\rho} = (\rho)_{ij} = \frac{\operatorname{cov}(\mathcal{B}_i, \mathcal{B}_j)}{\sqrt{\operatorname{cov}(\mathcal{B}_i, \mathcal{B}_i)}\sqrt{\operatorname{cov}(\mathcal{B}_j, \mathcal{B}_j)}} \tag{10.38}$$

This variation method has the advantage that a systematic effect which is the result of a combination of many uncertainties, can be computed in a single variation cycle k by generating different random numbers $r_k(i)$ for the different quantities i. This leads to a significant reduction of computational time. An example is the total particle identification uncertainty obtained from the uncertainties of PID weights (Section 5.2.5). The number of different PID weights applied in this analysis is of the order $\mathcal{O}(1000)$. For each of the PID weights a different random number is generated and all the PID weights can be varied in a single variation cycle k.

10.4.2. Statistical uncertainty of the simulated event sample

In addition to the uncertainty of the number of data events, the statistical uncertainty of the number of selected simulated events has to be taken into account in the calculation of the branching fractions uncertainties. Selected simulated events are either signal or background events. The statistical uncertainties of these two event categories have to be determined separately for the signal modes[6], because signal event numbers are related through the migration matrix used to calculate the signal decay branching fractions. Correlations between the migration matrix elements therefore have to be considered when calculating the statistical uncertainties of simulated signal events. In contrast, the numbers of selected simulated background events, which are subtracted from the data in the branching fraction calculation, are assumed to be uncorrelated. Both contributions to the branching fraction uncertainties are determined in the following paragraphs.

Signal events

The uncertainty of the number of selected signal events in the simulation enters the calculation of the branching fractions trough the uncertainty of the migration matrix elements M_{ij} defined as

$$M_{ij} = \frac{N_{ij}}{N_j^{gen}} \tag{10.39}$$

where the matrix elements M_{ij} are the efficiencies to select a true signal event of type j as an event of type i. The method to determine the ΔM_{ij} is presented in this section.

An event which is generated as a signal event of type k is either correctly reconstructed and therefore contributes to the matrix element M_{kk}, or is misidentified as another signal event l contributing to M_{lk}. The matrix elements for a certain true event type are therefore anti-correlated. For different true event types they are statistically independent.

For the case of only two reconstructed modes a and b, the matrix elements M_{ak} and M_{bk} for the true type $k = a, b$ would be fully anti-correlated. In this analysis, however, six different modes are selected, i. e., the size of the correlations between the matrix elements cannot be easily estimated. A method to account for these correlations was developed in [10]. The matrix elements M_{ik} for a certain true type k are expressed as a combination of fully anti-correlated efficiencies. The following diagram illustrates the definition of these efficiencies:

$$\begin{tikzcd}
N_k^{gen} \arrow[r, "1-\epsilon_0"] \arrow[d, "\epsilon_0"] & N_{rejected} & & & & \\
N_{hn\pi^0} \arrow[r, "1-\epsilon_1"] \arrow[d, "\epsilon_1"] & N_{\cancel{K}} \arrow[r, "1-\epsilon_2"] \arrow[d, "\epsilon_2"] & N_{\cancel{K\pi^0}} \arrow[r, "1-\epsilon_3"] \arrow[d, "\epsilon_3"] & N_{\cancel{K2\pi^0}} \arrow[r, "1-\epsilon_4"] \arrow[d, "\epsilon_4"] & N_{\cancel{K3\pi^0}} \arrow[r, "1-\epsilon_5"] \arrow[d, "\epsilon_5"] & N_{\cancel{\pi3\pi^0}} \arrow[d, "\epsilon_6=1.0"] \\
N_K & N_{K\pi^0} & N_{K2\pi^0} & N_{K3\pi^0} & N_{\pi3\pi^0} & N_{\pi4\pi^0}
\end{tikzcd}$$

---

[6] The statistical uncertainties for the control modes have already been presented in Section 10.3.1. For the control decays the selected simulated event numbers have been assumed to be Poisson distributed and their uncertainties to be uncorrelated between the different modes.

The first efficiency, $\epsilon_0 = \frac{N_{hn\pi^0}}{N_k^{gen}}$, is defined as the efficiency to select a true event of type k as any of the signal events, i. e., as the efficiency not to reject a signal event. In the next step, the efficiency, $\epsilon_1 = \frac{N_K}{N_{hn\pi^0}}$ to select a $\tau^- \to K^- \nu_\tau$ event from a sample of selected signal events is determined. The efficiency to select events of true type k, which are not reconstructed $\tau^- \to K^- \nu_\tau$ events (denoted as $\not K$ in the diagram) is then given by $\epsilon^{'} = \epsilon_0 \cdot (1 - \epsilon)$. The procedure is continued by determining the efficiency $\epsilon_2 = \frac{N_{K\pi^0}}{N_{\not K}}$ to select $\tau^- \to K^- \pi^0 \nu_\tau$ events from a sample of signal events not containing the already selected $\tau^- \to K^- \nu_\tau$ events. The steps are repeated for all signal modes in the same way. The efficiency ϵ_6 to select the last event type in the sequence is equal to one by construction[7]. The chosen order of the signal modes in this scheme is arbitrary because any possible order leads to the same final result for the branching fraction uncertainties.

With the above efficiency definitions the migration matrix elements for the true decay k can be then expressed as

$$\begin{aligned}
M_{K,k} &= \epsilon_0 \cdot \epsilon_1 \\
M_{K\pi^0,k} &= \epsilon_0 \cdot (1 - \epsilon_1) \cdot \epsilon_2 \\
M_{K2\pi^0,k} &= \epsilon_0 \cdot (1 - \epsilon_1) \cdot (1 - \epsilon_2) \cdot \epsilon_3 \\
M_{K3\pi^0,k} &= \epsilon_0 \cdot (1 - \epsilon_1) \cdot (1 - \epsilon_2) \cdot (1 - \epsilon_3) \cdot \epsilon_4 \\
M_{\pi3\pi^0,k} &= \epsilon_0 \cdot (1 - \epsilon_1) \cdot (1 - \epsilon_2) \cdot (1 - \epsilon_3) \cdot (1 - \epsilon_4) \cdot \epsilon_5 \\
M_{\pi4\pi^0,k} &= \epsilon_0 \cdot (1 - \epsilon_1) \cdot (1 - \epsilon_2) \cdot (1 - \epsilon_3) \cdot (1 - \epsilon_4) \cdot (1 - \epsilon_5) \cdot \epsilon_6.
\end{aligned} \tag{10.40}$$

The uncertainties of the efficiencies ϵ_i are given by the binomial uncertainty:

$$\Delta\epsilon_i = \sqrt{\frac{N_i(N_{i-1} - N_i)}{N_{i-1}^3}}, \tag{10.41}$$

where N_i is the number of selected events in the i^{th} step of the above diagram, e. g.,

$$\Delta\epsilon_2 = \sqrt{\frac{N_{K\pi^0}(N_{\not K} - N_{K\pi^0})}{N_{\not K}^3}}. \tag{10.42}$$

The resulting branching fraction uncertainties are determined according to the variation method described in Section 10.4.1. The ϵ_i in Equation 10.40 are replaced with the corresponding efficiencies varied within their uncertainties:

$$\epsilon_i \longrightarrow \epsilon_i^{'} = \epsilon_i + r_i \Delta\epsilon_i, \tag{10.43}$$

where r_i are random numbers generated according to a Gaussian distribution. A different number r_i is used for each of the six efficiencies for a true decay mode k. Therefore, $6 \times 6 = 36$ random numbers are used in total for each variation cycle. Table 10.3 shows

---

[7] The possible presence of $\tau^- \to \pi^-(5\pi^0)\nu_\tau$ and $\tau^- \to K^-(4\pi^0)\nu_\tau$ events, or events with even more π^0's, is ignored in this definition.

the obtained uncertainties for the signal mode branching fractions. The correlation matrix calculated according to Equation 10.29 is

$$\boldsymbol{\rho}^{\mathcal{B}}_{(\Delta N^{MC}_{\text{sig}})} = \begin{array}{c} \\ K \\ K\pi^0 \\ K2\pi^0 \\ K3\pi^0 \\ \pi3\pi^0 \\ \pi4\pi^0 \end{array} \begin{array}{c} \begin{array}{rrrrrr} K & K\pi^0 & K2\pi^0 & K3\pi^0 & \pi3\pi^0 & \pi4\pi^0 \end{array} \\ \begin{pmatrix} 1.000 & -0.092 & -0.156 & -3.662 & 1.296 & -0.278 \\ -0.092 & 1.000 & 0.059 & 2.214 & -0.250 & 0.224 \\ -0.156 & 0.059 & 1.000 & -0.148 & -0.312 & 0.284 \\ -3.662 & 2.214 & -0.148 & 1.000 & 0.664 & 0.145 \\ 1.296 & -0.250 & -0.312 & 0.664 & 1.000 & -0.568 \\ -0.278 & 0.224 & 0.284 & 0.145 & -0.568 & 1.000 \end{pmatrix} \end{array}.$$

Table 10.3.: Absolute and relative systematic uncertainties of the measured branching fractions due to the uncertainties of the number of simulated signal events.

Signal decay	$\Delta\mathcal{B}$	$\frac{\Delta\mathcal{B}}{\mathcal{B}}[\%]$
$\tau^- \to K^-\nu_\tau$	0.021×10^{-3}	0.30
$\tau^- \to K^-\pi^0\nu_\tau$	0.012×10^{-3}	0.23
$\tau^- \to K^-(2\pi^0)\nu_\tau$	0.056×10^{-4}	1.00
$\tau^- \to K^-(3\pi^0)\nu_\tau$	0.090×10^{-4}	5.48
$\tau^- \to \pi^-(3\pi^0)\nu_\tau$	0.005×10^{-2}	0.41
$\tau^- \to \pi^-(4\pi^0)\nu_\tau$	0.028×10^{-3}	2.69

Background events

The branching fractions are calculated from the numbers of selected signal events (Equation 10.13). They are obtained by subtracting the number of background events[8], N^{bkg}, in the selected signal mode sample from the number of selected data events, N^{Data}:

$$N^{\text{Data}}_{\text{sig}} = N^{\text{Data}} - N^{\text{bkg}}. \tag{10.44}$$

The latter number, N^{bkg}, is determined by estimating in simulation the efficiency to select a background event as a signal event.

As has been discussed in previous sections events of different types can contribute to the background of a signal mode. Each of these types has a different selection efficiency, i. e.,

$$\epsilon_{ij} = \frac{N_{ij}}{N_{gen,j}}, \tag{10.45}$$

where i is the selected signal mode, and j denotes the true type of the background

---

[8] Note that in this context also the control decays are considered as background decays.

Table 10.4.: τ decay modes which contribute to the background of the signal modes. The table specifies the branching fractions and their relative uncertainties in % as summarized in [4].

Decay	$\mathcal{B}[\%]$	$\frac{\Delta\mathcal{B}}{\mathcal{B}}[\%]$
$\tau^- \to \pi^-\nu_\tau$	10.828 ± 0.105	1.0
$\tau^- \to \pi^-\pi^0\nu_\tau$	25.46 ± 0.12	0.5
$\tau^- \to \pi^-(2\pi^0)\nu_\tau$	9.239 ± 0.124	1.3
$\tau^- \to \pi^-\eta\pi^0\nu_\tau$	0.138 ± 0.009	6.5
$\tau^- \to \pi^-\eta\pi^0\pi^0\nu_\tau$	0.015 ± 0.005	33
$\tau^- \to K^-\eta\nu_\tau$	0.0161 ± 0.0010	6.2
$\tau^- \to K^-\eta\pi^0\nu_\tau$	0.0048 ± 0.0012	25
$\tau^- \to \pi^-\overline{K}^0\nu_\tau$	0.831 ± 0.030	3.6
$\tau^- \to \pi^-\overline{K}^0\pi^0\nu_\tau$	0.36 ± 0.04	11
$\tau^- \to K^-\overline{K}^0\nu_\tau$	0.158 ± 0.017	11
$\tau^- \to K^-\overline{K}^0\pi^0\nu_\tau$	0.144 ± 0.023	16
$\tau^- \to \pi^-\overline{K}^0\eta\nu_\tau$	0.0093 ± 0.0015	16
$\tau^- \to \pi^-\overline{K}^0K^0\nu_\tau$	0.153 ± 0.034	22
$\tau^- \to e^-\overline{\nu}_e\nu_\tau$	17.83 ± 0.05	0.3
$\tau^- \to \mu^-\overline{\nu}_\mu\nu_\tau$	17.33 ± 0.05	0.3

events with $i \neq j$. The uncertainty of the efficiency ϵ_{ij} is given by

$$\Delta\epsilon_{ij} = \sqrt{\frac{N_{ij}(N_j^{gen} - N_{ij})}{N_{gen,j}^3}}, \tag{10.46}$$

similarly to Equation 10.41.

Table 10.1 lists the numbers of events selected in this measurement. The fraction of background events containing processes other than $e^+e^- \to \tau^+\tau^-$ is very small and their contribution is neglected. The number of remaining $e^+e^- \to e^+e^-$ events, which are not simulated, is estimated from the missing mass distribution in Figure 6.6b in the $\tau^- \to \pi^-\nu_\tau$ mode in the same manner as in Section 9.6 for the $\tau^- \to t^-\nu_\tau$ mode. The remaining relative contribution amounts to 0.1%. Since this contribution is small and the Bhabha background is expected to be even smaller in modes with additional π^0's this uncertainty is neglected. Also the contribution of τ decays into more than one charged track is neglected.

The various τ decays which contribute to the background of the selected signal modes are listed in Table 10.4. The selection efficiency of each of the listed decays is determined in the simulation. Following the procedure described in Section 10.4.1, the efficiency is varied within its uncertainty. A different random number is used for each of the background decays listed in Table 10.4, i. e., the numbers of selected events for the different background modes are assumed to be uncorrelated. The branching fractions of the signal decays are recalculated for 50 variations of the background selection efficiencies. The resulting uncertainties are listed in Table 10.5 and the correlation matrix is

$$\boldsymbol{\rho}^{\mathcal{B}}_{(\Delta N^{\mathrm{MC}}_{\mathrm{bkg}})} = \begin{array}{c} \\ K \\ K\pi^0 \\ K2\pi^0 \\ K3\pi^0 \\ \pi3\pi^0 \\ \pi4\pi^0 \end{array} \begin{array}{c} \begin{array}{rrrrrr} K & K\pi^0 & K2\pi^0 & K3\pi^0 & \pi3\pi^0 & \pi4\pi^0 \end{array} \\ \begin{pmatrix} 1.000 & 0.236 & 0.180 & 0.216 & 0.034 & 0.102 \\ 0.236 & 1.000 & 0.346 & 0.424 & 0.199 & 0.128 \\ 0.180 & 0.346 & 1.000 & 0.588 & 0.721 & 0.271 \\ 0.216 & 0.424 & 0.588 & 1.000 & 0.371 & 0.377 \\ 0.034 & 0.199 & 0.721 & 0.371 & 1.000 & -0.000 \\ 0.102 & 0.128 & 0.271 & 0.377 & -0.000 & 1.000 \end{pmatrix} \end{array} .$$

Table 10.5.: Absolute and relative systematic uncertainties of the measured branching fractions due to the uncertainties of the numbers of simulated background events.

Signal decay	$\Delta\mathcal{B}$	$\frac{\Delta\mathcal{B}}{\mathcal{B}}$[%]
$\tau^- \to K^-\nu_\tau$	0.010×10^{-3}	0.14
$\tau^- \to K^-\pi^0\nu_\tau$	0.008×10^{-3}	0.16
$\tau^- \to K^-(2\pi^0)\nu_\tau$	0.052×10^{-4}	0.92
$\tau^- \to K^-(3\pi^0)\nu_\tau$	0.131×10^{-4}	7.98
$\tau^- \to \pi^-(3\pi^0)\nu_\tau$	0.002×10^{-2}	0.16
$\tau^- \to \pi^-(4\pi^0)\nu_\tau$	0.023×10^{-3}	2.21

10.4.3. Uncertainty of the background decays branching fractions

The uncertainties of the background branching fractions, $\Delta\mathcal{B}_{\mathrm{bkg}(j)}$, which are known from other measurements [4], have to be considered. The $\Delta\mathcal{B}_{\mathrm{bkg}(j)}$ enter the calculation of the branching fractions in the same way as the statistical uncertainties of the numbers of selected background events (Section 10.4.2).

The background decay branching fractions are varied within their uncertainties listed in Table 10.4 to determine the resulting uncertainties of the signal decay branching fractions. The results for the signal decays are listed in Table 10.6 together with the uncertainties observed for the control modes. The correlation matrix is:

$$\boldsymbol{\rho}^{\mathcal{B}}_{(\Delta\mathcal{B}_{\mathrm{bkg}})} = \begin{array}{c} \\ K \\ K\pi^0 \\ K2\pi^0 \\ K3\pi^0 \\ Pi3\pi^0 \\ Pi4\pi^0 \end{array} \begin{array}{c} \begin{array}{rrrrrr} K & K\pi^0 & K2\pi^0 & K3\pi^0 & \pi3\pi^0 & \pi4\pi^0 \end{array} \\ \begin{pmatrix} 1.000 & -0.076 & 0.317 & -0.221 & 0.020 & 0.265 \\ -0.076 & 1.000 & 0.538 & 0.932 & -0.081 & 0.001 \\ 0.317 & 0.538 & 1.000 & 0.462 & 0.327 & 0.021 \\ -0.221 & 0.932 & 0.462 & 1.000 & -0.110 & -0.042 \\ 0.020 & -0.081 & 0.327 & -0.110 & 1.000 & 0.158 \\ 0.265 & 0.001 & 0.021 & -0.042 & 0.158 & 1.000 \end{pmatrix} \end{array}$$

Table 10.6.: Absolute and relative systematic uncertainties of the measured branching fractions due to the uncertainties of the background decay branching fractions used in the simulation.

Signal decay	$\Delta\mathcal{B}$	$\frac{\Delta\mathcal{B}}{\mathcal{B}}[\%]$	Control decay	$\Delta\mathcal{B}$	$\frac{\Delta\mathcal{B}}{\mathcal{B}}[\%]$
$\tau^- \to K^-\nu_\tau$	0.024×10^{-3}	0.34	$\tau^- \to \pi^-\nu_\tau$	0.008×10^{-2}	0.07
$\tau^- \to K^-\pi^0\nu_\tau$	0.031×10^{-3}	0.62	$\tau^- \to \pi^-\pi^0\nu_\tau$	0.028×10^{-2}	0.11
$\tau^- \to K^-(2\pi^0)\nu_\tau$	0.104×10^{-4}	1.84	$\tau^- \to \pi^-(2\pi^0)\nu_\tau$	0.006×10^{-2}	0.07
$\tau^- \to K^-(3\pi^0)\nu_\tau$	0.289×10^{-4}	17.60	$\tau^- \to \mu^-\overline{\nu}_\mu\nu_\tau$	0.011×10^{-2}	0.06
$\tau^- \to \pi^-(3\pi^0)\nu_\tau$	0.009×10^{-2}	0.77			
$\tau^- \to \pi^-(4\pi^0)\nu_\tau$	0.026×10^{-3}	2.54			

The largest uncertainty, $\Delta\mathcal{B}_{K3\pi^0} = 17\%$, is obtained for the $\tau^- \to K^-(3\pi^0)\nu_\tau$ signal mode. The source of this uncertainty is the large background contribution of the $\tau^- \to K^-\overline{K}^0\pi^0\nu_\tau$ decay which amounts to 24% of the selected $\tau^- \to K^-(3\pi^0)\nu_\tau$ candidates. The $\tau^- \to K^-\overline{K}^0\pi^0\nu_\tau$ branching fraction is known with a relative uncertainty of 16%. The decay is misidentified as a $\tau^- \to K^-(3\pi^0)\nu_\tau$ decay if the K_S^0 decays into two π^0's ($\mathcal{B}(K_S^0 \to \pi^0\pi^0) = (30.69 \pm 0.05)\%$). The signature for this decay in the detector is very similar to that of the signal decay. A reduction of this background is therefore difficult.

10.4.4. Particle identification uncertainty

Events selected in this measurement contain exactly two charged tracks. The types of both tracks have to be identified to assign the selected event to a signal mode. The identification is performed using PID selectors which have already been described.

The identification efficiencies of a PID selector differ for data and simulated events. Correction factors are applied to simulated events to account for these deviations. PID selectors can be used to identify particles or to veto particles of a certain type. The corresponding correction factors are called *PID weights* and *PID veto weights*, respectively (Section 5.2.5). In the following, the latter type is included in the term *PID weight* for simplicity.

PID weights are determined with an uncertainty which arises from the limited number of events in control samples and which contributes to the uncertainty of the branching fraction measurement performed in this analysis.

Two groups of PID weights are applied in this measurement. The first group of PID weights is provided by the *BABAR* PID Group. These PID weights are used to correct for deviations between data and simulation in the lepton identification and misidentification, and also for the misidentification of kaons as pions. The latter is a minor effect in this analysis. The second group of PID weights is determined with control τ decays with three charged particles in the final state (Chapter 7). These correction factors are used to correct the pion and kaon identification, and the misidentification of pions as kaons.

PID weights from BABAR PID tables

The PID weights for a certain reconstructed particle type are provided in dependence of the true type of the particle. For example, a PID weight table exists for true electrons which have been correctly identified as electrons. A further table contains correction factors for a true electron misidentified as a pion. The tables are determined separately for each run. Each table contains correction factors in intervals of the particle momentum p, polar angle θ and azimuthal angle ϕ.

The uncertainties of the signal decay branching fractions are determined assuming that the PID weights in different tables and intervals are uncorrelated. Following the method described in Section 10.4.1, the PID weights are varied within their uncertainties. A different random number is generated for each table (i. e., for each run , particle charge, and true type), and for each interval of the three variables p, θ, and ϕ of the table. The results for the branching fraction uncertainties are listed in Table 10.7 and the correlation matrix results to

$$\boldsymbol{\rho}^{\mathcal{B}}_{(\Delta\mathrm{PID}_{tab})} = \begin{array}{c} \\ K \\ K\pi^0 \\ K2\pi^0 \\ K3\pi^0 \\ \pi3\pi^0 \\ \pi4\pi^0 \end{array} \begin{array}{c} \begin{array}{rrrrrr} K & K\pi^0 & K2\pi^0 & K3\pi^0 & \pi3\pi^0 & \pi4\pi^0 \end{array} \\ \begin{pmatrix} 1.000 & 0.588 & 0.363 & 0.048 & 0.270 & -0.159 \\ 0.588 & 1.000 & 0.627 & 0.174 & 0.622 & 1.782 \\ 0.363 & 0.627 & 1.000 & 0.175 & 0.471 & 0.197 \\ 0.048 & 0.174 & 0.175 & 1.000 & 0.025 & -0.050 \\ 0.270 & 0.622 & 0.471 & 0.025 & 1.000 & 1.053 \\ -0.159 & 1.782 & 0.197 & -0.050 & 1.053 & 1.000 \end{pmatrix} \end{array} .$$

Table 10.7.: Absolute and relative systematic uncertainties of the measured branching fractions due to the uncertainties of the particle identification weights.

Signal decay	$\Delta\mathcal{B}$	$\frac{\Delta\mathcal{B}}{\mathcal{B}}$[%]	Control decay	$\Delta\mathcal{B}$	$\frac{\Delta\mathcal{B}}{\mathcal{B}}$[%]
$\tau^- \to K^-\nu_\tau$	0.010×10^{-3}	0.14	$\tau^- \to \pi^-\nu_\tau$	0.018×10^{-2}	0.17
$\tau^- \to K^-\pi^0\nu_\tau$	0.005×10^{-3}	0.10	$\tau^- \to \pi^-\pi^0\nu_\tau$	0.019×10^{-2}	0.07
$\tau^- \to K^-(2\pi^0)\nu_\tau$	0.009×10^{-4}	0.16	$\tau^- \to \pi^-(2\pi^0)\nu_\tau$	0.007×10^{-2}	0.08
$\tau^- \to K^-(3\pi^0)\nu_\tau$	0.012×10^{-4}	0.73	$\tau^- \to \mu^-\overline{\nu}_\mu\nu_\tau$	0.023×10^{-2}	0.13
$\tau^- \to \pi^-(3\pi^0)\nu_\tau$	0.001×10^{-2}	0.08			
$\tau^- \to \pi^-(4\pi^0)\nu_\tau$	0.003×10^{-3}	0.29			

PID weights from τ control decays

The determination of PID weights from τ control samples is described in Chapter 7. The weights are available for true pions and kaons which are identified correctly, and for true pions which are misidentified as kaons. The weights are determined separately for each run and in intervals of the particle momentum p.

The determination of the signal decay branching fractions is performed by varying the PID weights within their uncertainties using a random number (Section 10.4.1) for each true and reconstructed particle type, run, and momentum interval. Table 10.8

lists the obtained uncertainties and the correlation matrix is

$$\boldsymbol{\rho}^{\mathcal{B}}_{(\Delta\mathrm{PID}^{\pi}_{K})} = \begin{array}{c} \\ K \\ K\pi^0 \\ K2\pi^0 \\ K3\pi^0 \\ \pi3\pi^0 \\ \pi4\pi^0 \end{array} \begin{array}{c} \begin{array}{rrrrrr} K & K\pi^0 & K2\pi^0 & K3\pi^0 & \pi3\pi^0 & \pi4\pi^0 \end{array} \\ \begin{pmatrix} 1.000 & 0.878 & 0.673 & 0.586 & -0.089 & -0.290 \\ 0.878 & 1.000 & 0.907 & 0.799 & 0.047 & -0.056 \\ 0.673 & 0.907 & 1.000 & 0.910 & -0.002 & -0.094 \\ 0.586 & 0.799 & 0.910 & 1.000 & -0.145 & -0.192 \\ -0.089 & 0.047 & -0.002 & -0.145 & 1.000 & 0.969 \\ -0.290 & -0.056 & -0.094 & -0.192 & 0.969 & 1.000 \end{pmatrix} \end{array}.$$

Table 10.8.: Absolute and relative systematic uncertainties of the measured branching fractions due to the uncertainties of the pion and kaon PID correction factors.

Signal decay	$\Delta\mathcal{B}$	$\frac{\Delta\mathcal{B}}{\mathcal{B}}$[%]	Control decay	$\Delta\mathcal{B}$	$\frac{\Delta\mathcal{B}}{\mathcal{B}}$[%]
$\tau^- \to K^-\nu_\tau$	0.083×10^{-3}	1.17	$\tau^- \to \pi^-\nu_\tau$	0.023×10^{-2}	0.22
$\tau^- \to K^-\pi^0\nu_\tau$	0.047×10^{-3}	0.94	$\tau^- \to \pi^-\pi^0\nu_\tau$	0.033×10^{-2}	0.13
$\tau^- \to K^-(2\pi^0)\nu_\tau$	0.067×10^{-4}	1.19	$\tau^- \to \pi^-(2\pi^0)\nu_\tau$	0.011×10^{-2}	0.11
$\tau^- \to K^-(3\pi^0)\nu_\tau$	0.023×10^{-4}	1.40	$\tau^- \to \mu^-\overline{\nu}_\mu\nu_\tau$	0.000×10^{-2}	0.00
$\tau^- \to \pi^-(3\pi^0)\nu_\tau$	0.002×10^{-2}	0.16			
$\tau^- \to \pi^-(4\pi^0)\nu_\tau$	0.002×10^{-3}	0.19			

10.4.5. Uncertainty of the number of τ pairs

The number of produced τ pairs, $N_{\tau\tau}$, enters the calculation of the signal decay branching fractions (Equation 10.13) in two ways. On the one hand, a branching fraction is defined as the number of selected signal events relative to $N_{\tau\tau}$. On the other hand, $N_{\tau\tau}$ is used to normalize the simulated τ-pair background to the integrated luminosity of the data. These τ background events are subtracted from selected data events. $N_{\tau\tau}$ is given by the product of the integrated luminosity, $\mathcal{L}$, and the τ pair production cross section, $\sigma_{\tau\tau}$:

$$N_{\tau\tau} = \mathcal{L} \cdot \sigma_{\tau\tau}. \tag{10.47}$$

The uncertainties of both quantities have to be considered.

- **Integrated luminosity:** The *BABAR* collaboration provides luminosity uncertainty values for two different periods. The first value, $\Delta\mathcal{L}_{123}$, is the luminosity uncertainty for the runs 1, 2, and 3. The second value, $\Delta\mathcal{L}_{456}$, is determined for the larger data sample corresponding to the runs 4, 5, and 6. The two values are treated as partially correlated following the recommendations of the *BABAR* Tau Analysis Working Group. The uncorrelated contributions are

$$\begin{aligned} \Delta\mathcal{L}^{uncorr}_{123} &= 0.80\% \\ \Delta\mathcal{L}^{uncorr}_{456} &= 0.49\%, \end{aligned} \tag{10.48}$$

whereas the fully correlated contribution is

$$\Delta\mathcal{L}^{corr} = 0.50\%. \tag{10.49}$$

All three uncertainties are relative uncertainties.

The branching fraction uncertainties due to the luminosity are determined taking the described correlations into account. The luminosity is varied using three different random numbers for the relative uncertainty contributions:

$$\begin{aligned} \mathcal{L}'_{123} &= \mathcal{L}_{123} + \mathcal{L}_{123} \cdot (r_1^{uncorr}\Delta\mathcal{L}_{123}^{uncorr} + r_{corr}\Delta\mathcal{L}^{corr}) \\ \mathcal{L}'_{456} &= \mathcal{L}_{456} + \mathcal{L}_{456} \cdot (r_2^{uncorr}\Delta\mathcal{L}_{456}^{uncorr} + r_{corr}\Delta\mathcal{L}^{corr}) \end{aligned} \tag{10.50}$$

- **τ-pair production cross section:** The cross section $\sigma_{\tau\tau}$ was determined in [29] with a relative uncertainty of

  $$\frac{\Delta\sigma_{\tau\tau}}{\sigma_{\tau\tau}} = 0.31\%. \tag{10.51}$$

  The branching fraction uncertainties due to the cross section are fully correlated for all runs, i. e., only one random number is generated for each variation of this quantity.

The branching fraction uncertainties determined in 50 variations of the luminosity and τ-pair cross section due to the uncertainty of $N_{\tau\tau}$ combined from the luminosity and cross section uncertainties are listed in Table 10.9. The relative sizes of the uncertainties are different for the decay modes due to the different fractions of background events contributing to the selected event samples. The relation between the relative branching fraction uncertainty and the background fraction is given in Appendix C.

Table 10.9.: Absolute and relative systematic uncertainties of the measured branching fractions due to the uncertainty of the number of $\tau^+\tau^-$ pairs.

Signal decay	$\Delta\mathcal{B}$	$\frac{\Delta\mathcal{B}}{\mathcal{B}}$[%]	Control decay	$\Delta\mathcal{B}$	$\frac{\Delta\mathcal{B}}{\mathcal{B}}$[%]
$\tau^- \to K^-\nu_\tau$	0.063×10^{-3}	0.89	$\tau^- \to \pi^-\nu_\tau$	0.102×10^{-2}	0.97
$\tau^- \to K^-\pi^0\nu_\tau$	0.053×10^{-3}	1.06	$\tau^- \to \pi^-\pi^0\nu_\tau$	0.220×10^{-2}	0.89
$\tau^- \to K^-(2\pi^0)\nu_\tau$	0.090×10^{-4}	1.59	$\tau^- \to \pi^-(2\pi^0)\nu_\tau$	0.074×10^{-2}	0.80
$\tau^- \to K^-(3\pi^0)\nu_\tau$	0.034×10^{-4}	2.07	$\tau^- \to \mu^-\overline{\nu}_\mu\nu_\tau$	0.142×10^{-2}	0.83
$\tau^- \to \pi^-(3\pi^0)\nu_\tau$	0.011×10^{-2}	0.90			
$\tau^- \to \pi^-(4\pi^0)\nu_\tau$	0.011×10^{-3}	1.04			

The uncertainties are fully correlated for all signal modes, i. e., all entries of the correlation matrix are equal to one:

$$\boldsymbol{\rho}^{\mathcal{B}}_{(\Delta N_{\tau\tau})} = \begin{array}{c|cccccc} & K & K\pi^0 & K2\pi^0 & K3\pi^0 & \pi3\pi^0 & \pi4\pi^0 \\ \hline K & 1.000 & 1.000 & 1.000 & 1.000 & 1.000 & 1.000 \\ K\pi^0 & 1.000 & 1.000 & 1.000 & 1.000 & 1.000 & 1.000 \\ K2\pi^0 & 1.000 & 1.000 & 1.000 & 1.000 & 1.000 & 1.000 \\ K3\pi^0 & 1.000 & 1.000 & 1.000 & 1.000 & 1.000 & 1.000 \\ \pi3\pi^0 & 1.000 & 1.000 & 1.000 & 1.000 & 1.000 & 1.000 \\ \pi4\pi^0 & 1.000 & 1.000 & 1.000 & 1.000 & 1.000 & 1.000 \end{array}$$

10.4.6. Uncertainty of the track efficiency

The efficiency to reconstruct a charged track in data and simulation is discussed in Section 5.1.2. The efficiency ratio

$$\frac{\epsilon_t^{\mathrm{Data}}}{\epsilon_t^{\mathrm{MC}}} = 0.9996 \pm 0.0017 \tag{10.52}$$

is consistent with one, i. e., the track reconstruction efficiency is well described by the simulation within its uncertainty. Therefore, no simulation correction is applied in this analysis, i. e., the correction factor η_t is set to one. However, the uncertainty of η_t is taken into account in the calculation of the signal mode branching fractions.

The factor $\eta_t = 1 \pm 0.0017$ is varied within its uncertainty:

$$\eta_t^{'} = \eta_t + r \cdot \Delta\eta_t, \tag{10.53}$$

where r is a random number (see Section 10.4.1).

Since each event contains exactly two tracks, a track efficiency correction would have to be applied twice in each event. As the corrections for the two tracks are assumed to be fully correlated, the same random number r is used for both tracks. The correction factor for the whole event is then given by

$$\eta_{2\ tracks}^{'} = (\eta_t + 2r \cdot \Delta\eta_t). \tag{10.54}$$

The obtained branching fraction uncertainties (Table 10.10) are of similar size for all decay modes. The largest value is obtained for the $\tau^- \to K^-(3\pi^0)\nu_\tau$ mode because of the large fraction of background events which have to be subtracted from the number of data events in the calculation of the branching fraction.

The resulting uncertainties of the branching fractions are fully correlated, i. e., the

Table 10.10.: Absolute and relative systematic uncertainties of the measured branching fractions due to the uncertainty of the track efficiency correction.

Signal decay	$\Delta\mathcal{B}$	$\frac{\Delta\mathcal{B}}{\mathcal{B}}[\%]$	Control decay	$\Delta\mathcal{B}$	$\frac{\Delta\mathcal{B}}{\mathcal{B}}[\%]$
$\tau^- \to K^-\nu_\tau$	0.028×10^{-3}	0.39	$\tau^- \to \pi^-\nu_\tau$	0.045×10^{-2}	0.42
$\tau^- \to K^-\pi^0\nu_\tau$	0.023×10^{-3}	0.46	$\tau^- \to \pi^-\pi^0\nu_\tau$	0.096×10^{-2}	0.38
$\tau^- \to K^-(2\pi^0)\nu_\tau$	0.039×10^{-4}	0.69	$\tau^- \to \pi^-(2\pi^0)\nu_\tau$	0.032×10^{-2}	0.35
$\tau^- \to K^-(3\pi^0)\nu_\tau$	0.015×10^{-4}	0.91	$\tau^- \to \mu^-\overline{\nu}_\mu\nu_\tau$	0.062×10^{-2}	0.36
$\tau^- \to \pi^-(3\pi^0)\nu_\tau$	0.005×10^{-2}	0.39			
$\tau^- \to \pi^-(4\pi^0)\nu_\tau$	0.005×10^{-3}	0.45			

correlation matrix is

$$\boldsymbol{\rho}^{\mathcal{B}}_{(\Delta\eta_{track})} = \begin{array}{c} \\ K \\ K\pi^0 \\ K2\pi^0 \\ K3\pi^0 \\ \pi3\pi^0 \\ \pi4\pi^0 \end{array} \begin{array}{c} \begin{array}{cccccc} K & K\pi^0 & K2\pi^0 & K3\pi^0 & \pi3\pi^0 & \pi4\pi^0 \end{array} \\ \begin{pmatrix} 1.000 & 1.000 & 1.000 & 1.000 & 1.000 & 1.000 \\ 1.000 & 1.000 & 1.000 & 1.000 & 1.000 & 1.000 \\ 1.000 & 1.000 & 1.000 & 1.000 & 1.000 & 1.000 \\ 1.000 & 1.000 & 1.000 & 1.000 & 1.000 & 1.000 \\ 1.000 & 1.000 & 1.000 & 1.000 & 1.000 & 1.000 \\ 1.000 & 1.000 & 1.000 & 1.000 & 1.000 & 1.000 \end{pmatrix} \end{array}$$

10.4.7. Uncertainty of the split-off correction

The hadronic split-off correction determined in Chapter 8 is applied to each simulated event which contains a true charged pion or kaon. The correction factor is

$$w_{\text{split-off}} = 0.976 \pm 0.012. \tag{10.55}$$

It is varied within its uncertainty. The results are listed in Table 10.11.

Table 10.11.: Absolute and relative systematic uncertainties of the measured branching fractions due to the uncertainty of the split-off correction.

Signal decay	$\Delta\mathcal{B}$	$\frac{\Delta\mathcal{B}}{\mathcal{B}}[\%]$	Control decay	$\Delta\mathcal{B}$	$\frac{\Delta\mathcal{B}}{\mathcal{B}}[\%]$
$\tau^- \to K^-\nu_\tau$	0.107×10^{-3}	1.51	$\tau^- \to \pi^-\nu_\tau$	0.152×10^{-2}	1.44
$\tau^- \to K^-\pi^0\nu_\tau$	0.092×10^{-3}	1.84	$\tau^- \to \pi^-\pi^0\nu_\tau$	0.383×10^{-2}	1.51
$\tau^- \to K^-(2\pi^0)\nu_\tau$	0.156×10^{-4}	2.76	$\tau^- \to \pi^-(2\pi^0)\nu_\tau$	0.129×10^{-2}	1.40
$\tau^- \to K^-(3\pi^0)\nu_\tau$	0.058×10^{-4}	3.53	$\tau^- \to \mu^-\overline{\nu}_\mu\nu_\tau$	0.014×10^{-2}	0.08
$\tau^- \to \pi^-(3\pi^0)\nu_\tau$	0.019×10^{-2}	1.56			
$\tau^- \to \pi^-(4\pi^0)\nu_\tau$	0.188×10^{-3}	1.81			

The uncertainty of the $\tau^+ \to \mu^+\nu_\mu\overline{\nu}_\tau$ branching fraction is small compared to the uncertainties of all other modes because hadrons can only enter this mode if they are misidentified as a lepton. The fraction of such misidentified hadrons is small in this mode.

The obtained uncertainties are fully correlated for all signal modes:

$$\boldsymbol{\rho}^{\mathcal{B}}_{(\Delta\eta_{\text{split-off}})} = \begin{array}{c} \\ K \\ K\pi^0 \\ K2\pi^0 \\ K3\pi^0 \\ \pi3\pi^0 \\ \pi4\pi^0 \end{array} \begin{array}{c} \begin{array}{cccccc} K & K\pi^0 & K2\pi^0 & K3\pi^0 & \pi3\pi^0 & \pi4\pi^0 \end{array} \\ \begin{pmatrix} 1.000 & 1.000 & 1.000 & 1.000 & 1.000 & 1.000 \\ 1.000 & 1.000 & 1.000 & 1.000 & 1.000 & 1.000 \\ 1.000 & 1.000 & 1.000 & 1.000 & 1.000 & 1.000 \\ 1.000 & 1.000 & 1.000 & 1.000 & 1.000 & 1.000 \\ 1.000 & 1.000 & 1.000 & 1.000 & 1.000 & 1.000 \\ 1.000 & 1.000 & 1.000 & 1.000 & 1.000 & 1.000 \end{pmatrix} \end{array}$$

10.4.8. Uncertainty of the π^0 reconstruction efficiency

The determination of the π^0 reconstruction efficiency correction is presented in Chapter 9. A correction factor is applied for each reconstructed π^0 in the event in dependence of the π^0 momentum, e. g., three correction factors are applied to a selected $\tau^- \to \pi^-(3\pi^0)\nu_\tau$ candidate.

The uncertainties of the signal mode branching fractions resulting from the uncertainty of the π^0 correction are determined according to the method presented in Section 10.4.1. Each of the correction factors is varied within the uncertainty of the average π^0 correction, $\Delta\eta_{\pi^0} = 0.008$. The uncertainties of all correction factors are considered to be fully correlated, i. e., the same random number is used for their variations.

The resulting values of the branching fraction uncertainties are given in Table 10.12. As expected, the uncertainty increases with the number of reconstructed π^0's. The branching fraction uncertainty of a decay with $(n+1)\pi^0$'s is however not twice as large as the uncertainty for a decay with $n\pi^0$'s due to the different fractions of background events in the various signal samples.

Table 10.12.: Absolute and relative systematic uncertainties of the measured branching fractions due to the uncertainty of the π^0 efficiency correction.

Signal decay	$\Delta\mathcal{B}$	$\frac{\Delta\mathcal{B}}{\mathcal{B}}[\%]$	Control decay	$\Delta\mathcal{B}$	$\frac{\Delta\mathcal{B}}{\mathcal{B}}[\%]$
$\tau^- \to K^-\nu_\tau$	0.002×10^{-3}	0.03	$\tau^- \to \pi^-\nu_\tau$	0.000×10^{-2}	0.00
$\tau^- \to K^-\pi^0\nu_\tau$	0.065×10^{-3}	1.30	$\tau^- \to \pi^-\pi^0\nu_\tau$	0.274×10^{-2}	1.08
$\tau^- \to K^-(2\pi^0)\nu_\tau$	0.221×10^{-4}	3.91	$\tau^- \to \pi^-(2\pi^0)\nu_\tau$	0.186×10^{-2}	2.01
$\tau^- \to K^-(3\pi^0)\nu_\tau$	0.131×10^{-4}	7.98	$\tau^- \to \mu^-\overline{\nu}_\mu\nu_\tau$	0.000×10^{-2}	0.00
$\tau^- \to \pi^-(3\pi^0)\nu_\tau$	0.039×10^{-2}	3.24			
$\tau^- \to \pi^-(4\pi^0)\nu_\tau$	0.059×10^{-3}	5.63			

The uncertainties of all branching fractions of decays with π^0's in the final state are fully anti-correlated with the uncertainty of the π^0-less $\tau^- \to K^-\nu_\tau$ decay as can be seen from the computed correlation matrix:

$$\boldsymbol{\rho}^{\mathcal{B}}_{(\Delta\eta_{\pi^0})} = \begin{array}{c}\\ \\ K\pi^0 \\ K2\pi^0 \\ K3\pi^0 \\ \pi3\pi^0 \\ \pi4\pi^0\end{array} \begin{array}{cccccc} K & K\pi^0 & K2\pi^0 & K3\pi^0 & \pi3\pi^0 & \pi4\pi^0 \\ 1.000 & -1.000 & -1.000 & -1.000 & -1.000 & -1.000 \\ -1.000 & 1.000 & 1.000 & 1.000 & 1.000 & 1.000 \\ -1.000 & 1.000 & 1.000 & 1.000 & 1.000 & 1.000 \\ -1.000 & 1.000 & 1.000 & 1.000 & 1.000 & 1.000 \\ -1.000 & 1.000 & 1.000 & 1.000 & 1.000 & 1.000 \\ -1.000 & 1.000 & 1.000 & 1.000 & 1.000 & 1.000 \end{array}$$

10.4.9. Uncertainty due to $\tau^- \to \pi^-(5\pi^0)\nu_\tau$ and $\tau^- \to K^-(4\pi^0)\nu_\tau$ background decays.

Motivation

The decays $\tau^- \to \pi^-(5\pi^0)\nu_\tau$ and $\tau^- \to K^-(4\pi^0)\nu_\tau$ are not included in the background simulation because their branching fractions have not been measured [4]. Their branching fractions are expected to be very small. However, these decays can contribute to the background of a signal mode if one or more π^0's are not reconstructed. To determine the systematic uncertainty of the signal branching fractions due to this effect, first upper limits on the numbers of $\tau^- \to \pi^-(5\pi^0)\nu_\tau$ and $\tau^- \to K^-(4\pi^0)\nu_\tau$ events are determined, and then the fractions of $\tau^- \to \pi^-(5\pi^0)\nu_\tau$ and $\tau^- \to K^-(4\pi^0)\nu_\tau$ events migrating into a signal mode are determined by using an estimate of the π^0 reconstruction efficiency. This procedure was already applied in [10] to estimate this systematic uncertainty.

Determination of the upper limits on the numbers of $\tau^- \to \pi^-(5\pi^0)\nu_\tau$ and $\tau^- \to K^-(4\pi^0)\nu_\tau$ events

The upper limits, $N^{UL}_{\pi5\pi^0}$ and $N^{UL}_{K4\pi^0}$, on the numbers of selected $\tau^- \to \pi^-(5\pi^0)\nu_\tau$ and $\tau^- \to K^-(4\pi^0)\nu_\tau$ events are determined by selecting $\tau^- \to \pi^-(5\pi^0)\nu_\tau$ and $\tau^- \to K^-(4\pi^0)\nu_\tau$ events in data and in simulation. The number of selected events in data, N^{Data}, consists of signal events and background events, i. e., $N^{\text{Data}} = N_{\text{sig}} + N_{\text{bkg}}$. The number of selected simulated events, N^{MC}, only contains background events $N^{\text{MC}} = N_{\text{bkg}}$.

The selection criteria are the same as for the $\tau^- \to \pi^-(4\pi^0)\nu_\tau$ and $\tau^- \to K^-(3\pi^0)\nu_\tau$ modes, and one additional π^0 is required. The selected event numbers in data and simulation are

$$\begin{aligned} \tau^- \to \pi^-(5\pi^0)\nu_\tau : &\qquad N^{\text{Data}}_{sel,\pi5\pi^0} = 51, \quad N^{\text{MC}}_{sel,\pi5\pi^0} = 36.8, \\ \tau^- \to K^-(4\pi^0)\nu_\tau : &\qquad N^{\text{Data}}_{sel,K4\pi^0} = 18, \quad N^{\text{MC}}_{sel,K4\pi^0} = 12.3. \end{aligned} \tag{10.56}$$

The upper limit, S^{CL}, on the number of selected events of a certain type at a confidence level CL can be determined according to

$$CL := \frac{\int_0^{S^{\text{CL}}} P_S \, \mathrm{d}S}{\int_0^{\infty} P_S \, \mathrm{d}S} \tag{10.57}$$

where P_S is the probability to observe S signal events, with S being the (unknown) true number of signal events. P_S is obtained from a combination of the probability to observe $N_{\text{sig}} + N_{\text{bkg}}$ events in the selected data sample, $P_{S+B}(N_{\text{sig}} + N_{\text{bkg}})$, and the probability to find N_{bkg} events in the simulated event sample, $P_B(N_{\text{bkg}})$:

$$P_S(N_{\text{sig}} + N_{\text{bkg}}, N_{\text{bkg}}) = \int_0^\infty P_{S+B}(N_{\text{sig}} + N_{\text{bkg}}) P_B(N_{\text{bkg}}) \, \mathrm{d}B, \tag{10.58}$$

where B is the true number of background events.

The events are assumed to be distributed according to a Poisson distribution. Therefore

$$P_{S+B}(N_{\text{sig}} + N_{\text{bkg}}) = \frac{(S+B)^{(N_{\text{sig}}+N_{\text{bkg}})}}{(N_{\text{sig}} + N_{\text{bkg}})!} e^{-(S+B)}, \tag{10.59}$$

and

$$P_B(N_{\text{bkg}}) = \frac{B^{N_{\text{bkg}}}}{(N_{\text{bkg}})!} e^{-B}. \tag{10.60}$$

Using this relations with Equation 10.57 leads to

$$CL := \frac{\int_0^{S^{\text{CL}}} \int_0^\infty \frac{(S+B)^{(N_{\text{sig}}+N_{\text{bkg}})}}{(N_{\text{sig}}+N_{\text{bkg}})!} e^{-(S+B)} \cdot \frac{B^{N_{\text{bkg}}}}{(N_{\text{bkg}})!} e^{-B} \, \mathrm{d}B \, \mathrm{d}S}{\int_0^\infty \int_0^\infty \frac{(S+B)^{(N_{\text{sig}}+N_{\text{bkg}})}}{(N_{\text{sig}}+N_{\text{bkg}})!} e^{-(S+B)} \cdot \frac{B^{N_{\text{bkg}}}}{(N_{\text{bkg}})!} e^{-B} \, \mathrm{d}B \, \mathrm{d}S} \tag{10.61}$$

which is used to determine the upper limits $S^{CL} = (N^{UL}_{\pi 5\pi^0},\ N^{UL}_{K4\pi^0})$, by a numerical evaluation of the integrals. The upper limits obtained at a confidence level of $CL = 68\%$ with the selected event numbers given in Equation 10.56 are:

$$\begin{aligned} N^{UL}_{\pi 5\pi^0} &= 19.2 \\ N^{UL}_{K4\pi^0} &= 9.2. \end{aligned} \tag{10.62}$$

Estimation of the number of migrating $\tau^- \to \pi^-(5\pi^0)\nu_\tau$ and $\tau^- \to K^-(4\pi^0)\nu_\tau$ events

Table 10.1 gives the numbers of selected events for each signal mode. For the simulation the numbers are split up according to the true decay. Two observations are made with respect to the selected background decays with missed π^0's:

1. The contribution of true decays with $(n+m)\pi^0$ to a decay mode with n π^0's is largest for $m = 1$, i. e., for decays where one π^0 is not detected. The fraction of true decays with a larger number of missed π^0 is significantly smaller.

2. The background contribution of $(n+1)\pi^0$ decays is dominated by decays with the same charged hadron type as the signal decay under study.

As a result of these two observations, the contribution of the $\tau^- \to \pi^-(5\pi^0)\nu_\tau$ decay is estimated only for the $\tau^- \to \pi^-(4\pi^0)\nu_\tau$ signal mode. The number of these events is denoted as $N_{\pi 5\pi^0 \to \pi 4\pi^0}$ in the following . The contribution of these decays to the $\tau^- \to \pi^-(n\pi^0)\nu_\tau$ modes with $n < 4$ and all $\tau^- \to K^-(n\pi^0)\nu_\tau$ modes are assumed to be negligible. Accordingly, only the contribution, $N_{K4\pi^0\to K3\pi^0}$, of $\tau^- \to K^-(4\pi^0)\nu_\tau$ decays to the $\tau^- \to K^-(3\pi^0)\nu_\tau$ mode is estimated.

The number of $\tau^- \to \pi^-(5\pi^0)\nu_\tau$ events contributing to the background of the $\tau^- \to \pi^-(4\pi^0)\nu_\tau$ mode, $N_{\pi5\pi^0\to\pi4\pi^0}$, and the corresponding number, $N_{K4\pi^0\to K3\pi^0}$, for the $\tau^- \to K^-(3\pi^0)\nu_\tau$ mode are both determined with the same method. Therefore, both numbers are denoted as $N_{(n+1)\to n}$ is the following description of the method.

The number of selected events containing a decay with (n+1)π^0's is

$$N^{sel}_{(n+1)} = (\epsilon_{\pi^0})^{n+1} N_{(n+1)}, \tag{10.63}$$

where ϵ_{π^0} is the π^0 reconstruction efficiency, and $N_{(n+1)}$ is the number of events containing the decay with $(n+1)$ π^0's where all selection criteria but the π^0 reconstruction have been applied. The number of events, $N_{(n+1)\to n}$, which migrate from a decay mode with $(n+1)\pi^0$ into a decay mode with $n\pi$ is given by

$$N_{(n+1)\to n} = (n+1)(1-\epsilon_{\pi^0})(\epsilon_{\pi^0})^n N_{(n+1)}, \tag{10.64}$$

where $(1-\epsilon_{\pi^0})$ is the probability to lose one π^0. The factor $(n+1)$ takes into account that any of the $(n+1)$ π^0's can be missed. Using Equation 10.63, $N_{(n+1)\to n}$ can be written as

$$N_{(n+1)\to n} = \frac{(n+1)(1-\epsilon_{\pi^0})}{\epsilon_{\pi^0}} N^{sel}_{(n+1)}. \tag{10.65}$$

For the number of selected events in a decay mode with $(n+1)\pi^0$'s, $N^{sel}_{(n+1)}$, the upper limits determined in the last paragraph are used:

$$\begin{aligned} N^{\pi4\pi^0}_{\pi5\pi^0} &= \frac{(n+1)(1-\epsilon_{\pi^0})}{\epsilon_{\pi^0}} N^{UL}_{\pi5\pi^0}, \\ N^{K3\pi^0}_{K4\pi^0} &= \frac{(n+1)(1-\epsilon_{\pi^0})}{\epsilon_{\pi^0}} N^{UL}_{K4\pi^0}. \end{aligned} \tag{10.66}$$

An estimate for the π^0 reconstruction efficiency is determined in simulated events containing the $\tau^- \to \pi^-(4\pi^0)\nu_\tau$ decay. The obtained value is

$$\epsilon_{\pi^0} = 81\,\%\,. \tag{10.67}$$

The value arises from the photon selection criteria, i. e., π^0's with low-energy daughter photons are not reconstructed, and from photon losses due to the EMC acceptance[9]. The resulting values of $N^{\pi4\pi^0}_{\pi5\pi^0}$ and $N^{K3\pi^0}_{K4\pi^0}$ are

$$\begin{aligned} N^{\pi4\pi^0}_{\pi5\pi^0} &= 23.9, \\ N^{K3\pi^0}_{K4\pi^0} &= 9.1. \end{aligned} \tag{10.68}$$

The numbers $N^{\pi4\pi^0}_{\pi5\pi^0}$ and $N^{K3\pi^0}_{K4\pi^0}$ are used as an estimate for the uncertainty of the number of selected $\tau^- \to \pi^-(4\pi^0)\nu_\tau$ and $\tau^- \to K^-(3\pi^0)\nu_\tau$ decays, i. e., $\Delta N_{\pi4\pi^0} = 23.9$

---

[9] The photons can be lost in gaps between the EMC crystals.

and $\Delta N_{K3\pi^0} = 9.1$. The selected event numbers are varied within these uncertainties according to Equation 10.34 to obtain the systematic contribution to the branching fraction uncertainty. The resulting values are listed in Table 10.13 and Table 10.14. This systematic effect mainly contributes to the uncertainty of the $\tau^- \to \pi^-(4\pi^0)\nu_\tau$ and $\tau^- \to K^-(3\pi^0)\nu_\tau$ branching fractions. As expected, the effect is found to be negligible for the other signal modes. The correlation matrices are also determined:

$$\boldsymbol{\rho}^{\mathcal{B}}_{(\Delta N_{\pi 4\pi^0})} = \begin{array}{c} \\ K \\ K\pi^0 \\ K2\pi^0 \\ K3\pi^0 \\ \pi3\pi^0 \\ \pi4\pi^0 \end{array} \begin{array}{c} \begin{array}{cccccc} K & K\pi^0 & K2\pi^0 & K3\pi^0 & \pi3\pi^0 & \pi4\pi^0 \end{array} \\ \begin{pmatrix} 1.000 & 0.000 & 0.441 & 0.000 & 0.000 & 0.441 \\ 0.000 & 1.000 & 0.000 & 0.705 & 0.705 & 0.000 \\ 0.441 & 0.000 & 1.000 & 0.000 & 0.000 & 1.000 \\ 0.000 & 0.705 & 0.000 & 1.000 & 1.000 & 0.000 \\ 0.000 & 0.705 & 0.000 & 1.000 & 1.000 & 0.000 \\ 0.441 & 0.000 & 1.000 & 0.000 & 0.000 & 1.000 \end{pmatrix} \end{array}$$

$$\boldsymbol{\rho}^{\mathcal{B}}_{(\Delta N_{K3\pi^0})} = \begin{array}{c} \\ K \\ K\pi^0 \\ K2\pi^0 \\ K3\pi^0 \\ \pi3\pi^0 \\ \pi4\pi^0 \end{array} \begin{array}{c} \begin{array}{cccccc} K & K\pi^0 & K2\pi^0 & K3\pi^0 & \pi3\pi^0 & \pi4\pi^0 \end{array} \\ \begin{pmatrix} 1.000 & 0.000 & 0.000 & 0.000 & 0.000 & 0.000 \\ 0.000 & 1.000 & 0.000 & 0.999 & 0.000 & 0.000 \\ 0.000 & 0.000 & 1.000 & 0.000 & 0.992 & 0.994 \\ 0.000 & 0.999 & 0.000 & 1.000 & 0.000 & 0.000 \\ 0.000 & 0.000 & 0.992 & 0.000 & 1.000 & 0.982 \\ 0.000 & 0.000 & 0.994 & 0.000 & 0.982 & 1.000 \end{pmatrix} \end{array}$$

Table 10.13.: Absolute and relative systematic uncertainties of the measured branching fractions due to the contribution of $\tau^- \to \pi^-(5\pi^0)\nu_\tau$ events to the background of the $\tau^- \to \pi^-(4\pi^0)\nu_\tau$ decay mode.

Signal decay	$\Delta\mathcal{B}$	$\frac{\Delta\mathcal{B}}{\mathcal{B}}$[%]
$\tau^- \to K^-\nu_\tau$	0.000×10^{-3}	0.00
$\tau^- \to K^-\pi^0\nu_\tau$	0.000×10^{-3}	0.00
$\tau^- \to K^-(2\pi^0)\nu_\tau$	0.001×10^{-4}	0.01
$\tau^- \to K^-(3\pi^0)\nu_\tau$	0.000×10^{-4}	0.02
$\tau^- \to \pi^-(3\pi^0)\nu_\tau$	0.004×10^{-2}	0.33
$\tau^- \to \pi^-(4\pi^0)\nu_\tau$	0.047×10^{-3}	4.51

10.4.10. Summary of systematic uncertainties

Control modes

The branching fractions of the control decays, which have been used to develop the selection criteria and the corrections of the simulated events, are obtained as a consis-

Table 10.14.: Absolute and relative systematic uncertainties of the measured branching fractions due to the contribution of $\tau^- \to K^-(4\pi^0)\nu_\tau$ events to the background of the $\tau^- \to K^-(3\pi^0)\nu_\tau$ decay mode.

Signal decay	$\Delta\mathcal{B}$	$\frac{\Delta\mathcal{B}}{\mathcal{B}}[\%]$
$\tau^- \to K^-\nu_\tau$	0.000×10^{-3}	0.00
$\tau^- \to K^-\pi^0\nu_\tau$	0.000×10^{-3}	0.00
$\tau^- \to K^-(2\pi^0)\nu_\tau$	0.018×10^{-4}	0.32
$\tau^- \to K^-(3\pi^0)\nu_\tau$	0.097×10^{-4}	5.91
$\tau^- \to \pi^-(3\pi^0)\nu_\tau$	0.000×10^{-2}	0.00
$\tau^- \to \pi^-(4\pi^0)\nu_\tau$	0.000×10^{-3}	0.00

tency check of the analysis. As expected, they are consistent with the current world averages from [4] within their uncertainties. The determined values are

$$\begin{aligned}
\mathcal{B}(\tau^- \to \pi^-\nu_\tau) &= (10.542 \pm 0.192) \times 10^{-2} \\
\mathcal{B}(\tau^- \to \pi^-\pi^0\nu_\tau) &= (25.366 \pm 0.531) \times 10^{-2} \\
\mathcal{B}(\tau^- \to \pi^-(2\pi^0)\nu_\tau) &= (9.236 \pm 0.241) \times 10^{-2} \\
\mathcal{B}(\tau^- \to \mu^-\overline{\nu}_\mu\nu_\tau) &= (17.225 \pm 0.160) \times 10^{-2}.
\end{aligned} \tag{10.69}$$

The listed uncertainties are the total uncertainties which include all statistical and systematic effects presented in Section 10.4. The separate contributions are summarized in Table 10.15.

Signal modes

The measured branching fractions for the signal modes are

$$\begin{aligned}
\mathcal{B}(\tau^- \to K^-\nu_\tau) &= (7.100 \pm 0.160) \times 10^{-3} \\
\mathcal{B}(\tau^- \to K^-\pi^0\nu_\tau) &= (5.000 \pm 0.141) \times 10^{-3} \\
\mathcal{B}(\tau^- \to K^-(2\pi^0)\nu_\tau) &= (5.654 \pm 0.354) \times 10^{-4} \\
\mathcal{B}(\tau^- \to K^-(3\pi^0)\nu_\tau) &= (1.642 \pm 0.468) \times 10^{-4} \\
\mathcal{B}(\tau^- \to \pi^-(3\pi^0)\nu_\tau) &= (1.216 \pm 0.048) \times 10^{-2} \\
\mathcal{B}(\tau^- \to \pi^-(4\pi^0)\nu_\tau) &= (1.041 \pm 0.112) \times 10^{-3}.
\end{aligned} \tag{10.70}$$

The quoted uncertainty is the total uncertainty which includes all statistical and systematic contributions. The separate contributions are listed in Table 10.16. The correlation matrix for the statistical uncertainties is given in Equation 10.33. The

Table 10.15.: Summary of the measured branching fractions of the control decays. All uncertainties are relative uncertainties in % with respect to the branching fractions. The total uncertainties are obtained by adding the uncertainties in quadrature.

Control mode	$\tau \to \pi\nu_\tau$	$\tau \to \pi\pi^0\nu_\tau$	$\tau \to \pi\pi^0\pi^0\nu_\tau$	$\tau \to \mu\nu_\mu\nu_\tau$
Branching fraction [%]	10.542	25.366	9.236	17.225
Total uncertainty [%]	1.82	2.09	2.61	0.93
Statistical uncertainty (Data & MC)[%]	0.15	0.06	0.13	0.14
Systematic uncertainty [%]	1.82	2.09	2.61	0.93
Breakdown of the systematic uncertainties				
Background $\mathcal{B}$'s [%]	0.07	0.11	0.07	0.06
Number of $\tau^+\tau^-$ pairs [%]	0.97	0.89	0.80	0.83
Track efficiency [%]	0.42	0.38	0.35	0.36
Splitoff correction [%]	1.44	1.51	1.40	0.08
PID efficiency (tables) [%]	0.17	0.07	0.07	0.13
Pion and kaon ID [%]	0.22	0.13	0.11	0.00
π^0 efficiency correction [%]	0.00	1.08	2.01	0.00

Table 10.16.: Summary of the measured branching fractions and their uncertainties. All uncertainties are relative uncertainties in % with respect to the branching fractions. The total uncertainties are obtained by adding the uncertainties in quadrature.

	$\tau \to K\nu_\tau$	$\tau \to K\pi^0\nu_\tau$	$\tau \to K(2\pi^0)\nu_\tau$	$\tau \to K(3\pi^0)\nu_\tau$	$\tau \to \pi(3\pi^0)\nu_\tau$	$\tau \to \pi(4\pi^0)\nu_\tau$
Branching fraction	7.100×10^{-3}	5.000×10^{-3}	5.654×10^{-4}	1.642×10^{-4}	1.216×10^{-2}	1.041×10^{-3}
Total uncertainty [%]	2.25	2.82	6.26	28.50	3.95	10.76
Statistical uncertainty [%]	0.46	0.40	2.55	16.99	0.82	6.44
Systematic uncertainty [%]	2.20	2.78	5.71	22.84	3.87	8.65
Breakdown of systematic uncertainties						
Signal efficiencies [%]	0.30	0.23	1.00	5.48	0.41	2.69
Background efficiency [%]	0.14	0.16	0.92	7.98	0.16	2.21
Background $\mathcal{B}$'s[%]	0.34	0.62	1.84	17.6	0.77	2.54
Number of $\tau^+\tau^-$ pairs [%]	0.89	1.06	1.59	2.07	0.90	1.04
Track efficiency [%]	0.39	0.46	0.69	0.91	0.39	0.45
Splitoff correction [%]	1.51	1.84	2.76	3.53	1.56	1.81
PID efficiency (tables) [%]	0.14	0.10	0.16	0.73	0.08	0.29
Pion and kaon ID [%]	1.17	0.94	1.19	1.40	0.16	0.19
π^0 efficiency correction [%]	0.03	1.30	3.91	7.98	3.24	5.63
$\pi 5\pi^0 \to \pi 4\pi^0$ migration [%]	0.00	0.00	0.01	0.02	0.35	4.49
$K4\pi^0 \to K3\pi^0$ migration [%]	0.00	0.00	0.31	5.88	0.00	0.00

matrix for the systematic uncertainty is:

$$\boldsymbol{\rho}^{\mathcal{B}}_{(\mathrm{syst})} = \begin{array}{c|cccccc} & K & K\pi^0 & K2\pi^0 & K3\pi^0 & \pi3\pi^0 & \pi4\pi^0 \\ \hline K & 1.000 & 0.786 & 0.545 & 0.025 & 0.398 & 0.190 \\ K\pi^0 & 0.786 & 1.000 & 0.871 & 0.535 & 0.761 & 0.504 \\ K2\pi^0 & 0.545 & 0.871 & 1.000 & 0.484 & 0.867 & 0.614 \\ K3\pi^0 & 0.025 & 0.535 & 0.484 & 1.000 & 0.388 & 0.306 \\ \pi3\pi^0 & 0.398 & 0.761 & 0.867 & 0.388 & 1.000 & 0.606 \\ \pi4\pi^0 & 0.190 & 0.504 & 0.614 & 0.306 & 0.606 & 1.000 \end{array} .$$

The total correlation matrix for the measured branching fraction amounts to

$$\boldsymbol{\rho}^{\mathcal{B}}_{((\mathrm{tot}))} = \begin{array}{c|cccccc} & K & K\pi^0 & K2\pi^0 & K3\pi^0 & \pi3\pi^0 & \pi4\pi^0 \\ \hline K & 1.000 & 0.761 & 0.488 & 0.019 & 0.382 & 0.149 \\ K\pi^0 & 0.761 & 1.000 & 0.781 & 0.425 & 0.737 & 0.401 \\ K2\pi^0 & 0.488 & 0.781 & 1.000 & 0.264 & 0.776 & 0.453 \\ K3\pi^0 & 0.019 & 0.425 & 0.264 & 1.000 & 0.301 & 0.197 \\ \pi3\pi^0 & 0.382 & 0.737 & 0.776 & 0.301 & 1.000 & 0.398 \\ \pi4\pi^0 & 0.149 & 0.401 & 0.453 & 0.197 & 0.398 & 1.000 \end{array} .$$

10.5. Stability checks of the results

In this section, the stability of the results for the control and signal modes with respect to the data taking periods and the two lepton tag categories is studied.

As has been described in Section 10.3, the branching fractions are obtained by averaging branching fractions measured separately for each run. The uncertainties considered in the calculation of the average branching fraction are the statistical uncertainties of data and the simulated samples, and the particle identification uncertainty. These uncertainties are assumed to be uncorrelated between the runs. All other uncertainty contributions are calculated only for the whole data sample.

The branching fractions are presented in figures similar to the Figure 10.1 which shows the control decays determined for each run (black circles), the average branching fraction (blue circle), and the current world average (red circle) taken from [4]. All uncertainty contributions discussed in Section 10.4 are considered in the figure. The uncertainty which is assigned to a branching fraction determined for a certain run (black error bars) is the quadratic sum of the statistical uncertainty of the data and the simulated event sample, and of the particle identification uncertainties. The yellow band shows the uncorrelated uncertainty of the average branching fraction. The gray band shows the systematic uncertainty which is correlated between the runs, and thus not determined separately for each run. The total branching fraction value is displayed with the corresponding statistical and systematic uncertainty contribution added in quadrature (blue error bar).

The statistical agreement between the branching fractions determined for a subsample (for one of the six runs, for the e-tag-sample, or the μ-tag-sample) is tested by

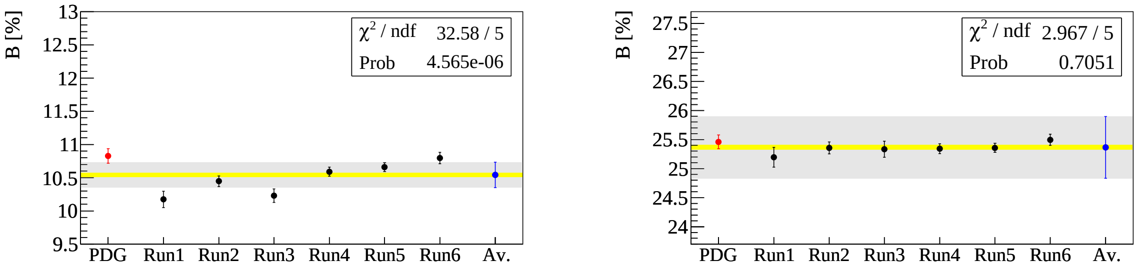

(a) $\tau^- \rightarrow \pi^- \nu_\tau$ **(b)** $\tau^- \rightarrow \pi^- \pi^0 \nu_\tau$

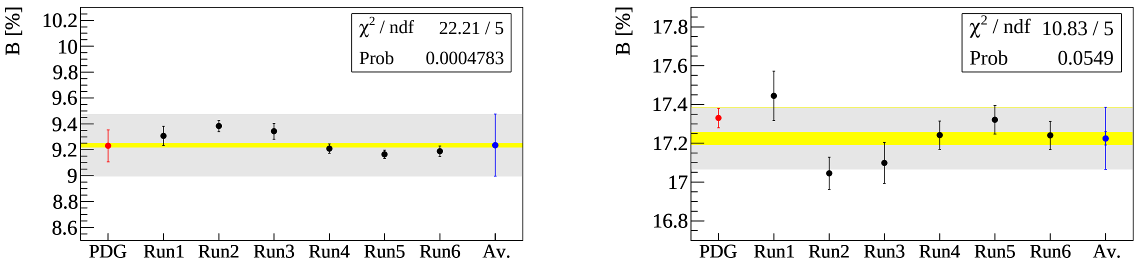

(c) $\tau^- \rightarrow \pi^- (2\pi^0) \nu_\tau$ **(d)** $\tau^- \rightarrow \mu^- \overline{\nu}_\mu \nu_\tau$

Figure 10.1.: Branching fraction of the control decays obtained as a cross check of the analysis. The black circles represent the branching fractions determined for each run. The corresponding error bars display the run dependent contributions to the uncertainty, i. e., the uncertainty of the data and simulation event numbers, and of the number of control tracks in the PID control samples. The displayed χ^2 value is calculated with respect to the average branching fraction using the branching fractions for each run and the uncorrelated uncertainties between the runs. The run-averaged value of the branching fraction for each decay is represented by the blue circle with error bars. The yellow band corresponds to the averaged run-dependent uncertainty. The gray band shows the systematic uncertainty contribution which is assumed to be run independent. The measured branching fractions are compared with the world average [4] red circle.

calculating the χ^2 for the n branching fractions $\mathcal{B}_i$ in n subsamples:

$$\chi^2 = \sum_1^n \frac{(\overline{\mathcal{B}} - \mathcal{B}_i)^2}{(\Delta\mathcal{B}_i)^2}, \tag{10.71}$$

where $\overline{\mathcal{B}}$ is the average of the $\mathcal{B}_i$ $(i = 1, .., n)$. The χ^2 is compared with the number of degrees of freedom, ndf. The determined numbers are shown in Figure 10.1 together with the corresponding probability, $Prob$, to observe a larger χ^2 than the computed χ^2.

10.5.1. Stability checks for the control modes

The branching fractions of the control modes determined for each run and for each tag sample are expected to agree with the world average branching fractions used in the simulation. This comparison is described in this section.

Agreement between the results for different runs

For the $\tau^- \to \pi^-\nu_\tau$ decay sizable deviations of the branching fractions determined separately for the runs are observed (Figure 10.1). They are clearly systematic and are discussed below in the last paragraph of this section. The branching fractions of the $\tau^- \to \pi^-\pi^0\nu_\tau$ and $\tau^- \to \mu^-\overline{\nu}_\mu\nu_\tau$ decays determined for each run agree well with each other. Their average is consistent with the world average. For the $\tau^- \to \pi^-(2\pi^0)\nu_\tau$ decay the χ^2 probability amounts to 0.047% indicating that the uncertainty contributions for each run might be too small. Every of the six branching fractions obtained for the different runs is consistent with the world average.

Agreement between the results for the e-tag and μ-tag

In Figure 10.2 the branching fractions determined separately for the e-tag and μ-tag samples are shown for the control modes $\tau^- \to \pi^-\nu_\tau$, $\tau^- \to \pi^-\pi^0\nu_\tau$, and $\tau^- \to \pi^-(2\pi^0)\nu_\tau$. A good agreement is observed for the $\tau^- \to \pi^-\pi^0\nu_\tau$, and $\tau^- \to \pi^-(2\pi^0)\nu_\tau$ modes. For the $\tau^- \to \pi^-\nu_\tau$ mode, the χ^2 probability is small.

Discussion of $\tau^- \to \pi^-\nu_\tau$ branching fraction result

The observed deviation between the $\tau^- \to \pi^-\nu_\tau$ branching fractions determined separately for each run are attributed to the difficult separation of muons and pions in the $\tau^- \to \pi^-\nu_\tau$ mode. In contrast to all other decay modes studied in this analysis, this mode contains a significant fraction of $\tau^- \to \mu^-\overline{\nu}_\mu\nu_\tau$ background, i. e., run-dependent deviations between data and simulation of the probability to misidentify a muon as a pions can be sizable. The muon background is small in all modes with π^0's due to a small probability to reconstruct a π^0 from background photons. The decay $\tau^- \to K^-\nu_\tau$ is not affected due to much better separation of muons and kaons compared to the separation of muons and pions. The values of the Cherenkov angle measured in the DIRC are similar for muons and pions, whereas significantly larger values are obtained for kaons (Figure 5.1b).

The above assumption is validated by a comparison of the control decay branching fractions discussed in this section with the branching fractions obtained from the $\tau^- \to t^-\nu_\tau$, and $\tau^- \to t^-\pi^0\nu_\tau$ $(t = \text{not } e)$ samples described in Section 9.6.5. In these

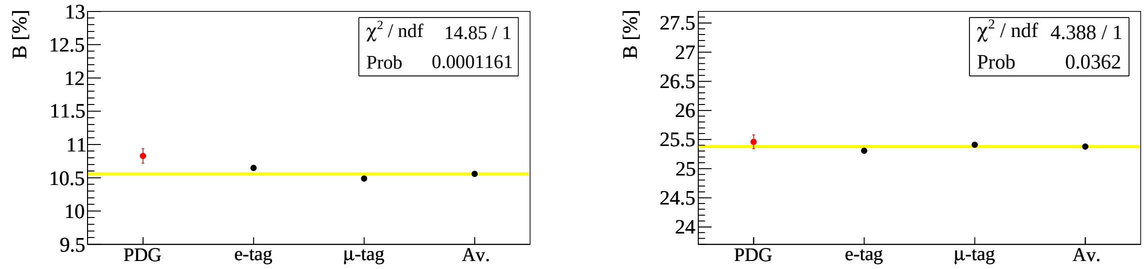

(a) $\tau^- \to \pi^- \nu_\tau$

(b) $\tau^- \to \pi^- \pi^0 \nu_\tau$

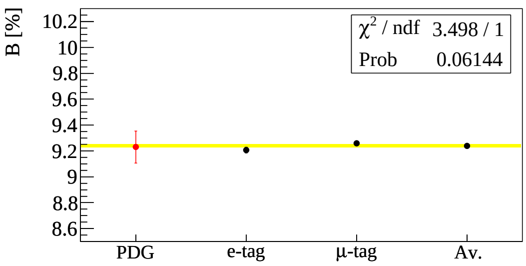

(c) $\tau^- \to \pi^- (2\pi^0) \nu_\tau$

Figure 10.2.: Branching fractions of the control decays. The values are determined separately for the e-tag and μ-tag sample. The statistical uncertainties of the data sample and simulated event sample, and the systematic uncertainty of the electron and muon identification are displayed and used in the χ^2 calculation.

samples, only minimal particle identification criteria are applied. Instead of the full PID selector sequence described in Section 5.2.4, the selected signal track in Figure 9.8 is only required to fail the selection criteria of an electron. A further difference is that only electron-tagged events are considered. As can be seen in Figure 9.8, the agreement of the $\tau^- \to \pi^-\nu_\tau$ branching fractions determined for each run is very good for these minimal PID requirements. This means that the observed deviations between the runs originate from the applied particle identification.

The identification of the tag muon can be ruled out as a possible source of the deviations, since no deviations are observed for the other two control modes with a μ-tag, the $\tau^- \to \pi^-\pi^0\nu_\tau$ and the $\tau^- \to \pi^-(2\pi^0)\nu_\tau$ modes. As an additional check, the branching fractions are compared for each run and for the e-tag and μ-tag sample. The obtained values are displayed in Figure 10.3. The same run dependence is visible in both tag samples.

Muons are identified with the IFR. This detector component was subject to significant changes during the data taking periods, and showed a degrading performance of the RPC's from run 1 to run 4, which were then partially replaced by LST's. This means, that a run-dependent performance of the muon identification is expected. If in the simulation a true muon is misidentified as a pion the following PID weight combination (Section 5.2.5) is applied to the signal track

$$w_{\text{signal track}} = w_{\mu\text{-as-}\pi} \cdot w^{veto}_{\mu\text{-as-e}} \cdot w^{veto}_{\mu\text{-as-}\mu}. \tag{10.72}$$

The weights $w_{\mu\text{-as-}\pi}$ correct the probability to misidentify a muon as a pion. Since muons and pions are difficult to separate in the tracking detectors and the calorimeter, they are separated with quantities measured in the IFR, i. e., a run dependence of the separation performance is expected, and thus is also likely to be observed for the $w_{\mu\text{-as-}\pi}$. The probability to misidentify a muon as an electron, which is corrected by the veto weights $w^{veto}_{\mu\text{-as-}e}$, is not expected to be run dependent, since muons and electrons are mainly separated by comparing their signature in the calorimeter, which did not change much with time. The veto weights $w^{veto}_{\mu\text{-as-}\mu}$ can be regarded as reliable since this weights are only applied in muon-tagged events, and a good agreement is found between the μ-tag and the e-tag for all other control modes. Therefore, the observed deviations between the runs are attributed to the $w_{\mu\text{-as-}\pi}$. The corresponding systematic uncertainty is regarded as underestimated. Since the $\tau^- \to \pi^-\nu_\tau$ mode is a control mode and other modes are much less influenced by this systematic effect, no attempt is made to estimate this uncertainty.

10.5.2. Stability checks for the signal modes

In this section, a comparison of the signal branching fractions obtained for the different runs, and the e-tag and μ-tag are presented. The shown figures correspond to the figures presented in the last section for the control decays.

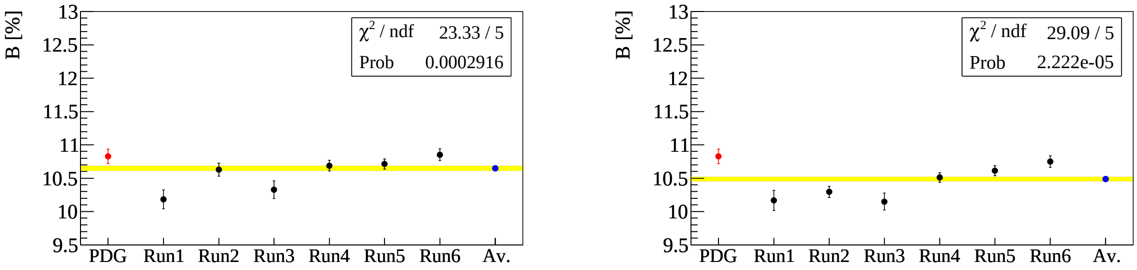

(a) $\tau^- \to \pi^- \nu_\tau$, e-tag

(b) $\tau^- \to \pi^- \nu_\tau$, μ-tag

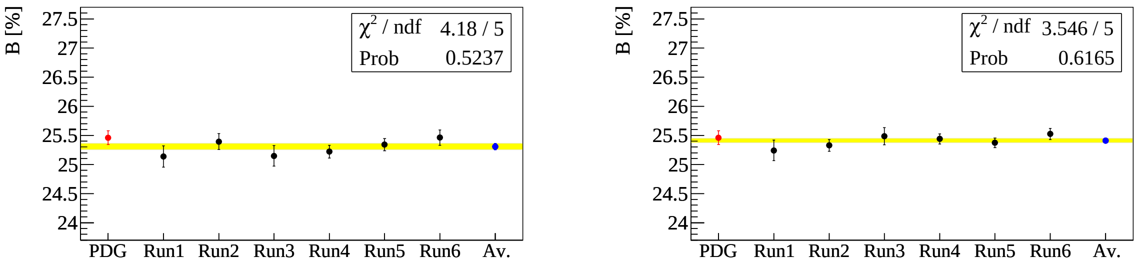

(c) $\tau^- \to \pi^- \pi^0 \nu_\tau$,$e$-tag

(d) $\tau^- \to \pi^- \pi^0 \nu_\tau$, μ-tag

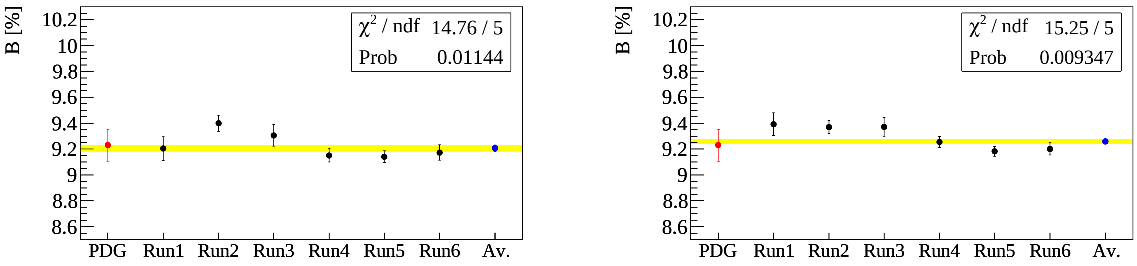

(e) $\tau^- \to \pi^- (2\pi^0) \nu_\tau$, e-tag

(f) $\tau^- \to \pi^- (2\pi^0) \nu_\tau$, μ-tag

Figure 10.3.: Branching fractions of the control decays. The values are determined separately for each run, and for the e-tag and μ-tag sample. A description of the figures can be found in the caption of Figure 10.1. The run independent uncertainty contributions are not displayed.

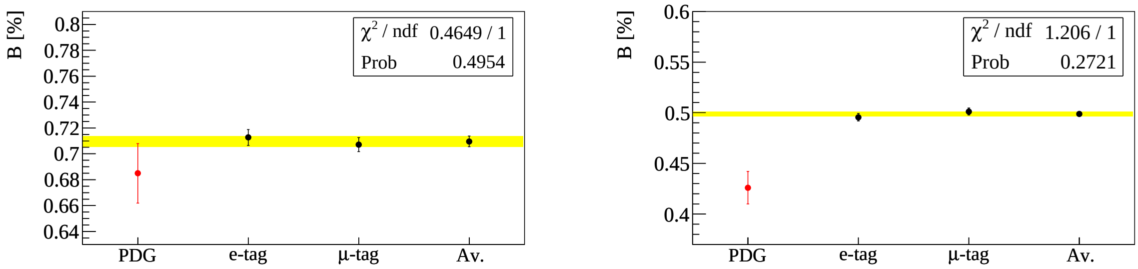

(a) $\tau^- \to K^- \nu_\tau$

(b) $\tau^- \to K^- \pi^0 \nu_\tau$

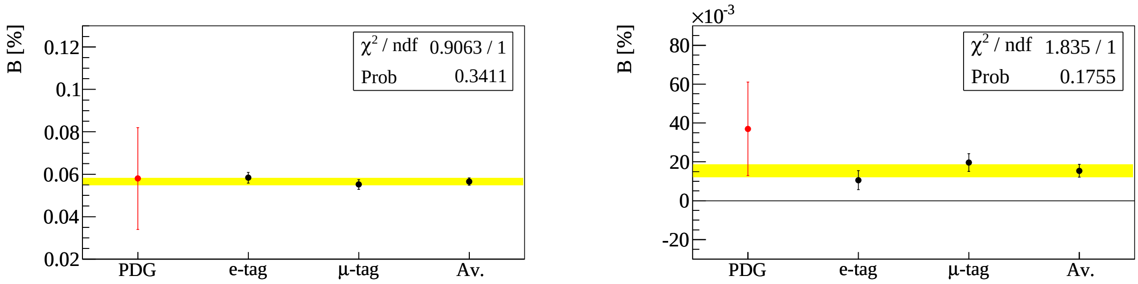

(c) $\tau^- \to K^- (2\pi^0) \nu_\tau$

(d) $\tau^- \to K^- (3\pi^0) \nu_\tau$

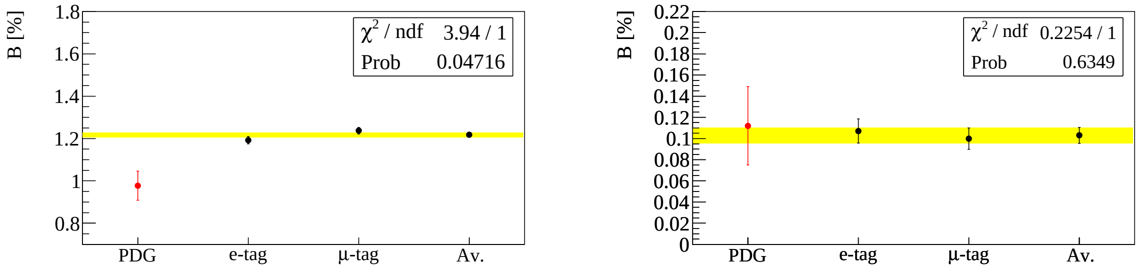

(e) $\tau^- \to \pi^- (3\pi^0) \nu_\tau$

(f) $\tau^- \to \pi^- (4\pi^0) \nu_\tau$

Figure 10.4.: Branching fractions of the measured signal decays. The values are determined separately for the e-tag and μ-tag sample. Only the statistical uncertainties of the data sample and simulated event sample, and the systematic uncertainty of the electron and muon identification are displayed and used in the χ^2 calculation.

Agreement between the results for the e-tag and μ-tag

Figure 10.4 shows the branching fractions determined separately for the e-tag and μ-tag tag samples. The agreement is good for all signal modes.

Agreement between the results for different runs

Figure 10.5 shows the branching fractions determined for each run.

For the $\tau^- \to K^-\pi^0\nu_\tau$, $\tau^- \to K^-(2\pi^0)\nu_\tau$, and $\tau^- \to K^-(3\pi^0)\nu_\tau$ modes, the obtained χ^2 probabilities show that the branching fractions for each run are in a good agreement with each other.

For the $\tau^- \to K^-\nu_\tau$ and $\tau^- \to \pi^-(4\pi^0)\nu_\tau$ modes, the χ^2 probabilities are large, 99.2% and 98.9%, respectively. Possibly this could indicate an overestimated systematic uncertainty for this modes. Besides the statistical uncertainty of the selected data and simulated event samples, only the charged particle identification uncertainties are considered in the χ^2 calculation. As has been mentioned above, the agreement between the the e-tag and μ-tag tag is good for these signal modes, i. e., an overestimated uncertainty of the lepton identification can be ruled out. Therefore, only the kaon and pion identification uncertainty might be overestimated for this signal modes. However, these uncertainties are determined in the same manner for all signal modes, where no such large χ^2 probabilities are observed. As an additional check, Figures 10.6 and 10.7 show a comparison of the branching fractions for the runs and for the two tag samples. For the $\tau^- \to \pi^-(4\pi^0)\nu_\tau$ mode a large value is obtained only for the μ-tag, and not for the e-tag. This means the high χ^2 probability for the $\tau^- \to \pi^-(4\pi^0)\nu_\tau$ mode is probably due to a statistical fluctuation ("data is too good"). For the $\tau^- \to K^-\nu_\tau$ mode large χ^2 probabilities are obtained for both samples which leads to the conclusion that the uncertainty assigned to the kaon identification might be too large for this mode.

For the $\tau^- \to \pi^-(3\pi^0)\nu_\tau$ branching fractions obtained in different runs, the χ^2 probability is only 0.45% which might indicate an underestimated run-dependent uncertainty.

In summary, one can say that the run dependent and the tag-lepton dependent branching fractions agree very well with their averages.

The figures shown in this section also display the current world average values [4] of the measured branching fractions. A detailed comparison of the results of this analysis with previously published measurements is given in the next chapter.

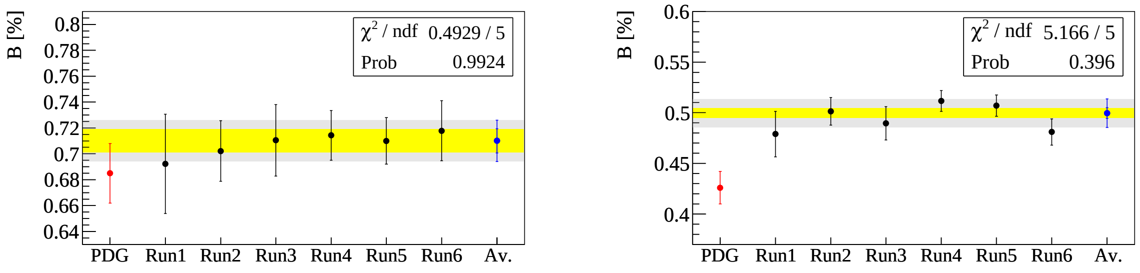

(a) $\tau^- \to K^- \nu_\tau$

(b) $\tau^- \to K^- \pi^0 \nu_\tau$

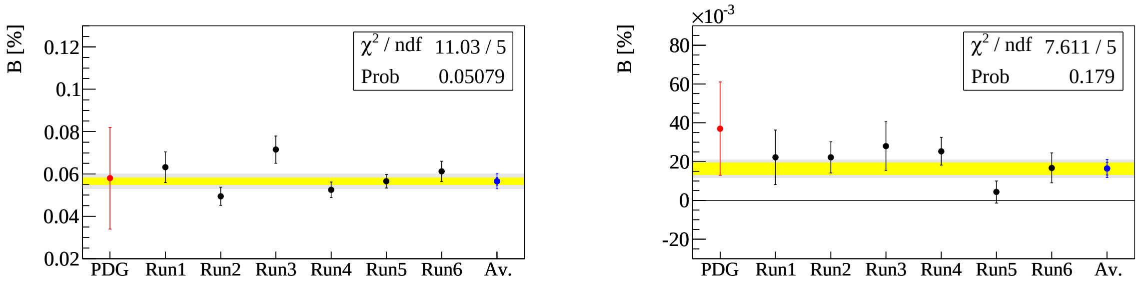

(c) $\tau^- \to K^- (2\pi^0) \nu_\tau$

(d) $\tau^- \to K^- (3\pi^0) \nu_\tau$

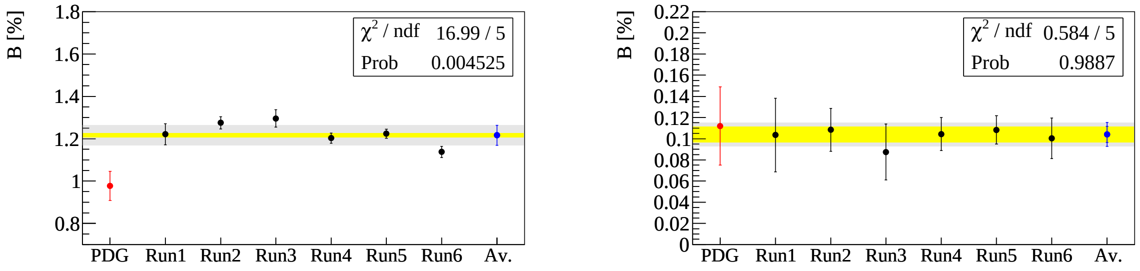

(e) $\tau^- \to \pi^- (3\pi^0) \nu_\tau$

(f) $\tau^- \to \pi^- (4\pi^0) \nu_\tau$

Figure 10.5.: Branching fractions of the measured signal decays. The values are determined separately for each run. A description of the figures can be found in the caption of Figure 10.1.

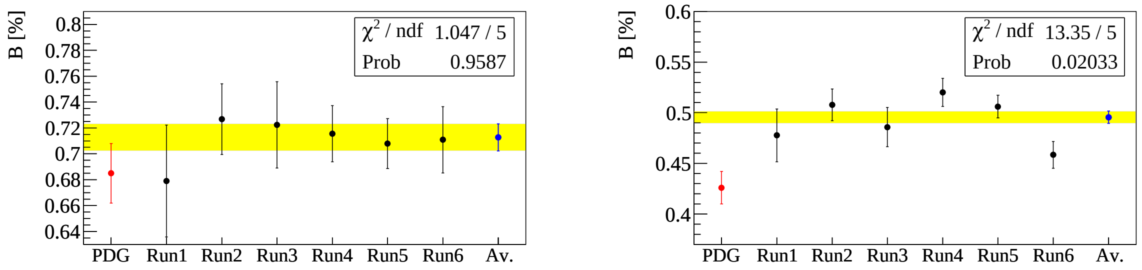

(a) $\tau^- \to K^- \nu_\tau$

(b) $\tau^- \to K^- \pi^0 \nu_\tau$

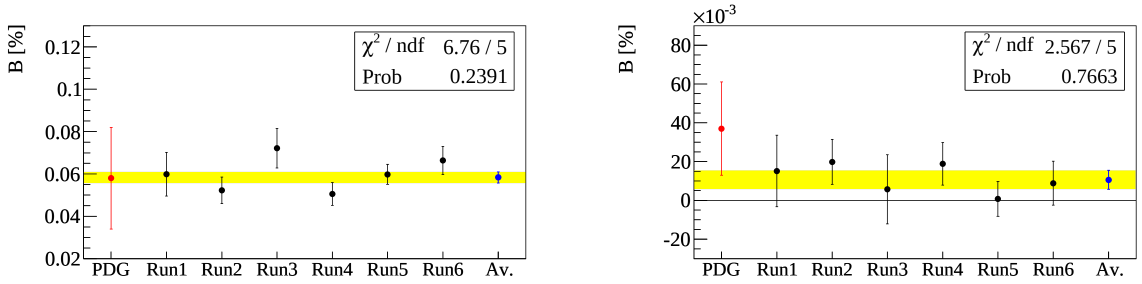

(c) $\tau^- \to K^- (2\pi^0) \nu_\tau$

(d) $\tau^- \to K^- (3\pi^0) \nu_\tau$

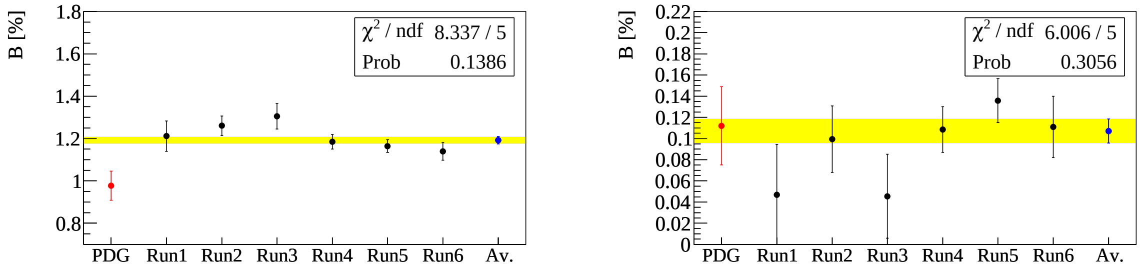

(e) $\tau^- \to \pi^- (3\pi^0) \nu_\tau$

(f) $\tau^- \to \pi^- (4\pi^0) \nu_\tau$

Figure 10.6.: Branching fractions of the measured signal decays determined in the e-tag sample. The values are determined separately for each run. A description of the figures can be found in the caption of Figure 10.1. The run independent uncertainty contributions are not displayed.

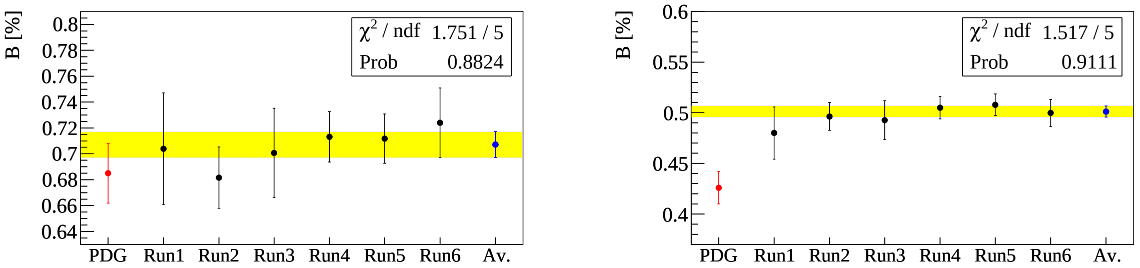

(a) $\tau^- \to K^- \nu_\tau$ **(b)** $\tau^- \to K^- \pi^0 \nu_\tau$

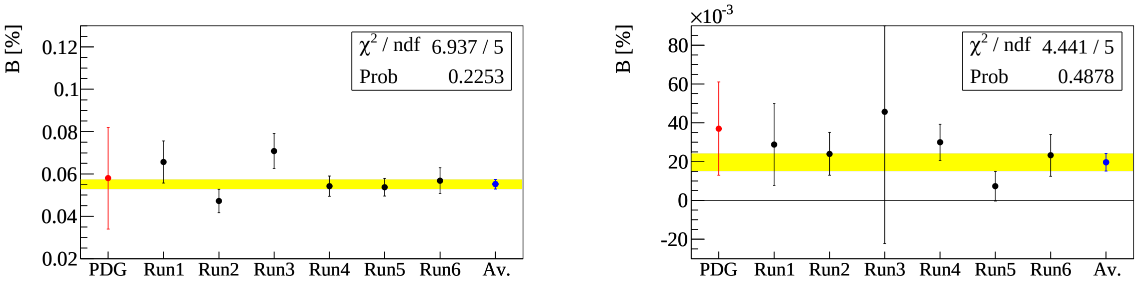

(c) $\tau^- \to K^- (2\pi^0) \nu_\tau$ **(d)** $\tau^- \to K^- (3\pi^0) \nu_\tau$

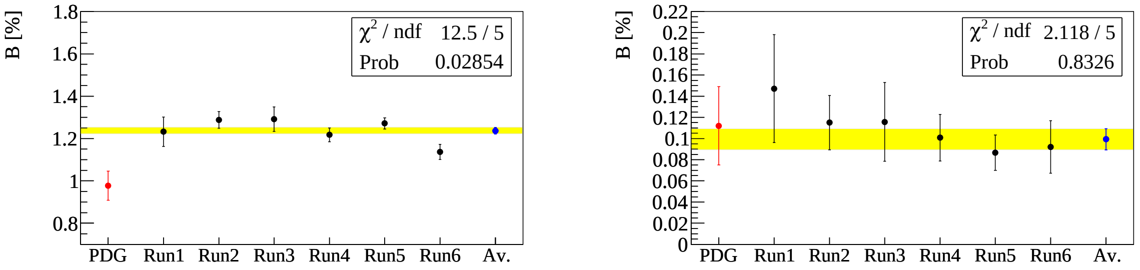

(e) $\tau^- \to \pi^- (3\pi^0) \nu_\tau$ **(f)** $\tau^- \to \pi^- (4\pi^0) \nu_\tau$

Figure 10.7.: Branching fractions of the measured signal decays determined in the μ-tag sample. The values are determined separately for each run. A description of the figures can be found in the caption of Figure 10.1. The run independent uncertainty contributions are not displayed.

11. Summary, discussion of results, and determination of $|V_{us}|$

In the first part of this chapter the measured branching fractions are discussed and, if available, compared with earlier results published by *BABAR* and with results from other experiments. In the second part, the results are used to determine the magnitude of the CKM matrix element V_{us}. In the last section the conclusion of this analysis is presented.

11.1. Summary of the branching fraction measurements

Using the data sample of 435.5×10^6 τ-pairs recorded by the *BABAR* experiment from 1999–2008 in e^+e^- collisions at the center-of-mass energy of 10.58 GeV and 40 MeV below the following τ branching fractions have been determined

$$\begin{aligned}
\mathcal{B}(\tau^- \to K^-\nu_\tau) &= (7.100 \pm 0.033(\text{stat}) \pm 0.156(\text{syst})) \times 10^{-3} && (\pm 2.3\%),\\
\mathcal{B}(\tau^- \to K^-\pi^0\nu_\tau) &= (5.000 \pm 0.020(\text{stat}) \pm 0.139(\text{syst})) \times 10^{-3} && (\pm 2.8\%),\\
\mathcal{B}(\tau^- \to K^-(2\pi^0)\nu_\tau) &= (5.654 \pm 0.144(\text{stat}) \pm 0.323(\text{syst})) \times 10^{-4} && (\pm 6.3\%),\\
\mathcal{B}(\tau^- \to K^-(3\pi^0)\nu_\tau) &= (1.642 \pm 0.279(\text{stat}) \pm 0.375(\text{syst})) \times 10^{-4} && (\pm 29\%),\\
\mathcal{B}(\tau^- \to \pi^-(3\pi^0)\nu_\tau) &= (1.216 \pm 0.010(\text{stat}) \pm 0.047(\text{syst})) \times 10^{-2} && (\pm 4.0\%),\\
\mathcal{B}(\tau^- \to \pi^-(4\pi^0)\nu_\tau) &= (1.041 \pm 0.067(\text{stat}) \pm 0.090(\text{syst})) \times 10^{-3} && (\pm 10.9\%),
\end{aligned}$$

where the first uncertainty is the statistical uncertainty of the data and the second is the total systematic uncertainty which includes the statistical uncertainty of the simulated events. In brackets the relative total uncertainties are given.

The consistency of the analysis has been checked with several well known τ control modes. The control modes have also been used to develop corrections of simulated events to improve the description of the data by the simulation which has been used to develop the selection criteria and to estimate the signal and background selection efficiencies.

The branching fraction uncertainties of the $\tau^- \to K^-\nu_\tau$, $\tau^- \to K^-\pi^0\nu_\tau$, $\tau^- \to K^-(2\pi^0)\nu_\tau$, and $\tau^- \to \pi^-(3\pi^0)\nu_\tau$ decays are dominated by the systematic contributions. For the $\tau^- \to K^-(3\pi^0)\nu_\tau$ and $\tau^- \to \pi^-(4\pi^0)\nu_\tau$ decays the statistical uncertainty is of similar size as the systematic uncertainty.

The $\tau^- \to K^-(3\pi^0)\nu_\tau$ branching fraction has the largest relative uncertainty of 29%. As can be seen in Table 10.16 the dominant systematic uncertainty in this mode results from the uncertainty of τ background events. The background is dominated by the

$\tau^- \rightarrow K^-\overline{K}^0\pi^0\nu_\tau$ decay with a branching fraction known with a relative precision of 16% [4]. This decay has not yet been measured by the B Factories leaving room for improvement. The dominant systematic effects for all other signal modes are related to the reconstruction of photons and π^0's, i. e., to the reconstruction of electromagnetic clusters in the electromagnetic calorimeter of the *BABAR* detector.

11.2. Comparison of the obtained branching fractions with earlier published results

In Figure 11.1 the measured branching fractions (blue circles) are compared with previously published results (black circles). The comparison is discussed below separately for each signal decay. The values of the published branching fractions are taken from [7], [52], [53], [54], [55], [56], [57], [17]. The same measurements are considered as are used by the Particle Data Group when calculating the current world averages [4]. Here, new average branching fractions are computed by including the results of this analysis. They are shown in Figure 11.1 as red circles with an uncertainty indicated by the yellow band. To compute an average branching fraction, $\overline{\mathcal{B}}$, from the results of N different measurements, the same method is applied as is used by the Particle Data Group. The average branching fractions are determined by

$$\overline{\mathcal{B}} \pm \Delta\overline{\mathcal{B}} = \frac{\sum\limits_{i=1}^{N} \frac{1}{(\Delta\mathcal{B}_i)^2} \cdot \mathcal{B}_{i=1}^{N}}{\sum\limits_{i=1}^{N} \frac{1}{(\Delta\mathcal{B}_i)^2}} \pm (\sum_{i=1}^{N} \frac{1}{(\Delta\mathcal{B}_i)^2})^{-\frac{1}{2}} \qquad (11.1)$$

where $\mathcal{B}_i \pm \Delta\mathcal{B}_i$ is the result of the i^{th} measurement. If

$$\chi^2 > (N+1) \quad \text{where} \quad \chi^2 = \sum_{i=1}^{N} \frac{(\overline{\mathcal{B}} - \mathcal{B}_i)^2}{(\Delta\mathcal{B}_i)^2} \qquad (11.2)$$

then the uncertainty of the average branching fraction is increased by a factor S:

$$\Delta\overline{\mathcal{B}} \longrightarrow S \cdot \Delta\overline{\mathcal{B}} \quad \text{where} \quad S = \left(\frac{\chi^2}{N-1}\right)^{\frac{1}{2}}. \qquad (11.3)$$

The obtained value of S is also shown in Figure 11.1 for each signal decay. The new average branching fractions are compared in Table 11.1 with the current world averages, and the results of the Heavy Flavor Averaging Group (HFAG) [23] obtained in fit of all available hadronic τ branching fraction results[1].

---

[1] As mentioned in Section 2.4.7, the HFA-Group uses the branching fraction results given in the PDG listings and additional recent results from the B factories. In the fit the sum of the measured branching fractions is constrained to one, and correlations between the different measurements are taken into account.

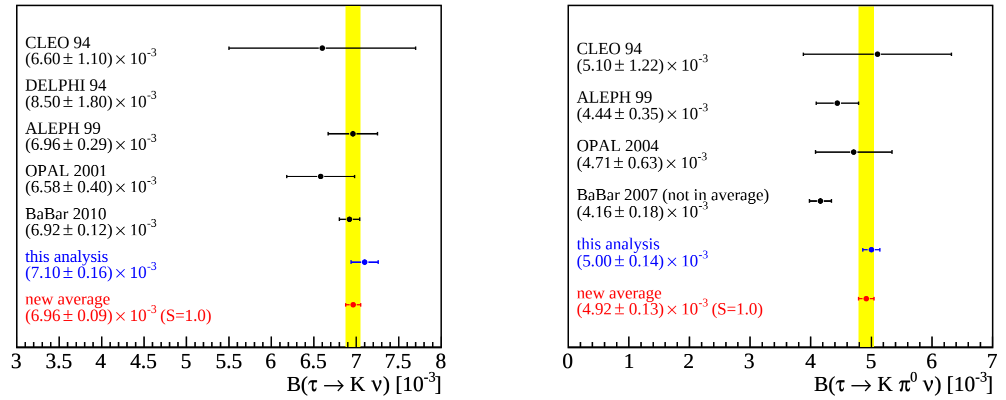

(a) $\tau^- \to K^-\nu_\tau$ **(b)** $\tau^- \to K^-\pi^0\nu_\tau$

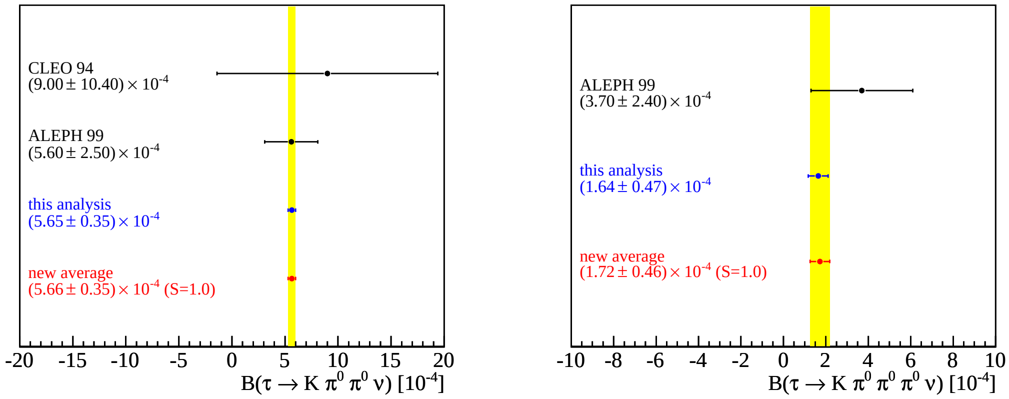

(c) $\tau^- \to K^-(2\pi^0)\nu_\tau$ **(d)** $\tau^- \to K^-(3\pi^0)\nu_\tau$

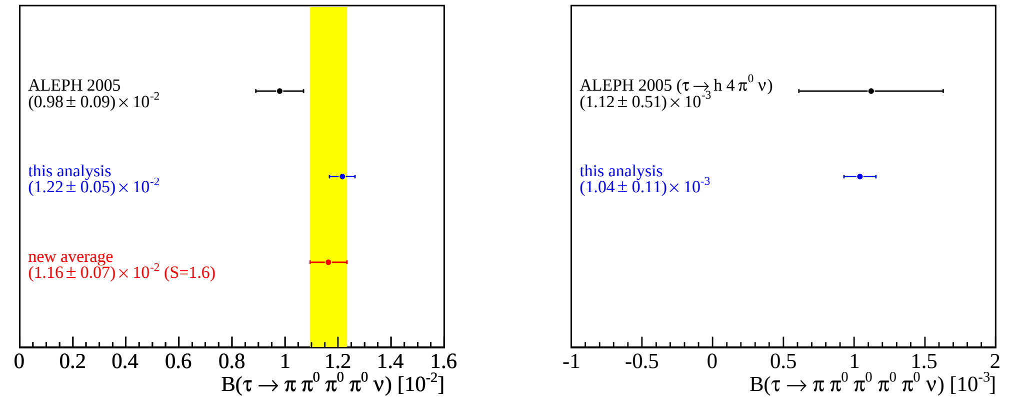

(e) $\tau^- \to \pi^-(3\pi^0)\nu_\tau$ **(f)** $\tau^- \to \pi^-(4\pi^0)\nu_\tau$

Figure 11.1.: Comparison of the measured branching fractions with earlier published results from *BABAR* and other experiments (References are given in the text). The new average which includes the result obtained in this analysis is displayed as red circle. The yellow band shows the uncertainy of the average. The $\tau^- \to K^-\pi^0\nu_\tau$ branching fraction result obtained in 2007 by *BABAR* is superseded by the result of this analysis, and therefore not included in the new average.

Table 11.1.: Average signal branching fractions. The first column lists the average branching fractions obtained by the Heavy Flavor Averaging τ-Group [23]. The second column lists the current world averaged taken from [4]. The last column contains the average branching fractions computed from the results of this analysis and the world averages.

	$\mathcal{B}$ [%]		
Decay	HFAG	PDG	PDG + this
$\tau^- \to K^-\nu_\tau$	0.697 ± 0.010	0.685 ± 0.023	0.696 ± 0.009
$\tau^- \to K^-\pi^0\nu_\tau$	0.431 ± 0.015	0.426 ± 0.016	0.492 ± 0.013
$\tau^- \to K^-(2\pi^0)\nu_\tau$	0.060 ± 0.022	0.058 ± 0.024	0.057 ± 0.004
$\tau^- \to K^-(3\pi^0)\nu_\tau$	0.039 ± 0.022	0.037 ± 0.024	0.017 ± 0.005
$\tau^- \to \pi^-(3\pi^0)\nu_\tau$	1.046 ± 0.074	0.977 ± 0.090	1.163 ± 0.069
$\tau^- \to \pi^-(4\pi^0)\nu_\tau$	0.107 ± 0.039	0.112 ± 0.051	0.104 ± 0.011

11.2.1. $\tau^- \to K^-\nu_\tau$

The branching fraction of the $\tau^- \to K^-\nu_\tau$ decay has been measured by CLEO, by three LEP experiments (DELPHI, ALEPH, OPAL), and also by *BABAR*. The result of this analysis is consistent with all other measurements, and has a significantly smaller uncertainty than the results of the LEP experiments and CLEO. The other *BABAR* result has a smaller uncertainty. The obtained $\mathcal{B}(\tau^- \to K^-\nu_\tau)$ is also consistent with the $\tau^- \to K^-\nu_\tau$ branching fraction computed from the $K^- \to \mu^-\overline{\nu}_\mu$ branching fraction under the assumption of τ-μ universality (Equation 2.36).

The other *BABAR* result was obtained from a measurement of the branching fraction ratio $\mathcal{B}(\tau^- \to K^-\nu_\tau)/\mathcal{B}(\tau^- \to e^-\overline{\nu}_e\nu_\tau)$ with a data sample corresponding to approximately the same integrated luminosity as used in this analysis. The selected $e^+e^- \to \tau^+\tau^-$ events were tagged with a tagging technique which uses τ decays into three charged particles, i. e., events with a 1-3 topology were selected, whereas in this analysis events with a 1-1 topology have been studied. Due to this difference the data samples used for this and the other *BABAR* analysis are statistically independent.

In both analyses similar systematic effects are considered. However, the size of most of the resulting branching fraction uncertainties is different for the two measurements. For example, the same track reconstruction efficiency uncertainty applies to both analyses. The resulting branching fraction uncertainty is larger for the other result, since four tracks are reconstructed (to be compared with two track in this analysis). Another example is the uncertainty of the integrated luminosity. The effect of the luminosity is smaller in the other measurement because it partially cancels in the $\mathcal{B}(\tau^- \to K^-\nu_\tau)/\mathcal{B}(\tau^- \to e^-\overline{\nu}_e\nu_\tau)$ ratio.

Despite a partial correlation of the systematic uncertainties of this and the other *BABAR* measurement, a new average of the $\tau^- \to K^-\nu_\tau$ branching fraction is calculated assuming that all measurements are uncorrelated. The new average is

$$\mathcal{B}^{\text{average}}_{\tau^-\to K^-\nu_\tau} = (0.696 \pm 0.009) \times 10^{-2}. \tag{11.4}$$

11.2.2. $\tau^- \to K^-\pi^0\nu_\tau$

The branching fraction of the $\tau^- \to K^-\pi^0\nu_\tau$ decay was also measured by CLEO, ALEPH, OPAL, and *BABAR*. The branching fraction obtained in this analysis is consistent with the results of the first three experiments which have significantly larger uncertainties. However, there exists a 3.7σ deviation between this result and the previous *BABAR* measurement.

The previous *BABAR* measurement was performed with the run 1–4 data sample which corresponds to approximately 49% of the integrated luminosity used in this thesis. Since a lepton tag was used to reconstruct the $e^+e^- \to \tau^+\tau^-$ events, i. e., events with a 1–1 topology were used, the statistical uncertainties of this and the previous measurement are partially correlated. The same is true for the systematic uncertainties because the applied selection criteria are based on the same variables in both measurements.

The essential differences between the two analysis arise from the corrections that have been applied to the simulation. In this analysis, a π^0 efficiency correction and a split-off correction have been determined with exactly the same selection criteria for the neutral particles as in the branching fraction measurement. In the previous *BABAR* measurement the standard *BABAR* π^0 correction was applied, and effects due to hadronic split-offs were not considered. Moreover, in this analysis charged particle identification correction factors have been determined in events with a similar topology as the studied signal events. The other analysis used correction factors from multihadron events, which are provided by the *BABAR* collaboration, without correcting for the different event topologies.

Due to the significantly larger data sample and the improved corrections for the simulation this $\tau^- \to K^-\nu_\tau$ result supersedes the previous *BABAR* measurement. The latter is therefore not used in the calculation of a new average which amounts to

$$\mathcal{B}^{\text{average}}_{\tau^- \to K^-\pi^0\nu_\tau} = (0.492 \pm 0.013) \times 10^{-2}. \tag{11.5}$$

11.2.3. $\tau^- \to K^-(2\pi^0)\nu_\tau$

The branching fraction of the $\tau^- \to K^-(2\pi^0)\nu_\tau$ decay was already measured by the CLEO and ALEPH collaborations. The value obtained in this analysis has a significantly smaller uncertainty and is consistent with the other measurements. The updated average branching fraction amounts to

$$\mathcal{B}^{\text{average}}_{\tau^- \to K^-(2\pi^0)\nu_\tau} = (0.057 \pm 0.004) \times 10^{-2}. \tag{11.6}$$

While the central value of this average is in good agreement with the previous average, the relative uncertainty is reduces from 41% to 7%.

11.2.4. $\tau^- \to K^-(3\pi^0)\nu_\tau$

The branching fraction of the $\tau^- \to K^-(3\pi^0)\nu_\tau$ was only measured by the ALEPH collaboration. The result of this analysis is consistent with the ALEPH result, and the relative uncertainty is smaller by more than a factor of two. The average branching fraction amounts to

$$\mathcal{B}^{\text{average}}_{\tau^-\to K^-(3\pi^0)\nu_\tau} = (0.017 \pm 0.005) \times 10^{-2}. \tag{11.7}$$

and is dominated by the result of this analysis.

11.2.5. $\tau^- \to \pi^-(3\pi^0)\nu_\tau$

The branching fraction of the $\tau^- \to \pi^-(3\pi^0)\nu_\tau$ decay was also only measured by the ALEPH experiment. The relative uncertainty of the branching fraction obtained in this analysis is more than a factor of two smaller than the relative uncertainty of the ALEPH result. However, the two measurements differ by 2.3σ. The average branching fraction is

$$\mathcal{B}^{\text{average}}_{\tau^-\to \pi^-(3\pi^0)\nu_\tau} = (1.163 \pm 0.069) \times 10^{-2}, \tag{11.8}$$

where the uncertainty is scaled with $S = 1.6$.

11.2.6. $\tau^- \to \pi^-(4\pi^0)\nu_\tau$

The branching fraction of the $\tau^- \to \pi^-(4\pi^0)\nu_\tau$ decay has not yet been measured. The result of this analysis is compared in Figure 11.1 with the $\tau^- \to h^-(4\pi^0)\nu_\tau$ branching fraction measured by the ALEPH collaboration. Typically, branching fractions with kaons are on the order of 10–100 smaller than the corresponding branching fractions with a pion. Assuming that this also applies to the ratio of the $\tau^- \to \pi^-(4\pi^0)\nu_\tau$ and $\tau^- \to K^-(4\pi^0)\nu_\tau$ decays, $\mathcal{B}(\tau^- \to \pi^-(4\pi^0)\nu_\tau)$ is expected to be 1–10% smaller than $\mathcal{B}(\tau^- \to h^-(4\pi^0)\nu_\tau)$. The measured value is consistent with this expectation.

11.2.7. Summary

The measured branching fractions are consistent with almost all earlier published results. A deviation is observed between an earlier *BABAR* measurement of the $\tau^- \to K^-\pi^0\nu_\tau$ branching fraction and the result of this analysis which supersedes the previous measurement. The $\tau^- \to \pi^-(3\pi^0)\nu_\tau$ result differs by 2.3σ from the earlier ALEPH measurement.

The uncertainties of the measured branching fractions have been significantly reduced with respect to the ALEPH, DELPHI, OPAL, and CLEO measurements of this decays, and, for the $\tau^- \to K^-\nu_\tau$ and $\tau^- \to K^-\pi^0\nu_\tau$ results, are of similar size as the uncertainties of previous *BABAR* results [4].

The obtained result for the $\tau^- \to K^-\nu_\tau$ branching fraction is consistent with the value predicted from the $K^- \to \mu^-\overline{\nu}_\mu$ branching fraction under the assumption of τ-μ universality (Section 2.3.5).

11.3. Determination of $|V_{us}|$

In this section, the measured branching fractions of the $\tau^- \to K^-\nu_\tau$, $\tau^- \to K^-\pi^0\nu_\tau$, $\tau^- \to K^-(2\pi^0)\nu_\tau$, and $\tau^- \to K^-(3\pi^0)\nu_\tau$ decays are used to determine the CKM matrix element $|V_{us}|$ with two different methods. The results are compared with $|V_{us}|$ values obtained in other measurements in Figure 11.2

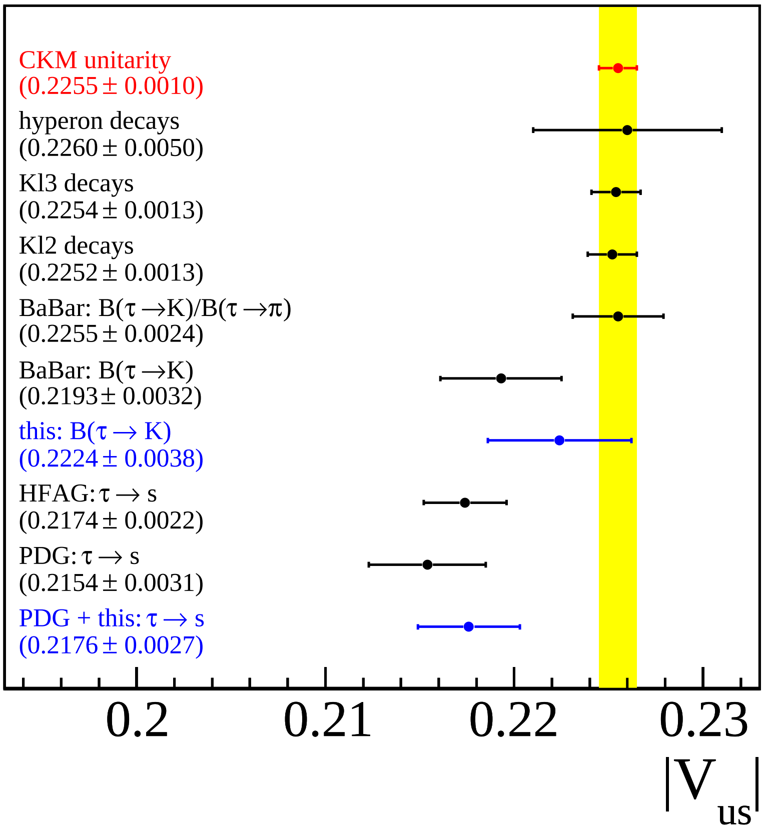

Figure 11.2.: Comparison of different $|V_{us}|$ measurements. The $|V_{us}|$ value obtained from the unitarity condition of the CKM matrix is shown as red circle. The uncertainty of this value is displayed as the yellow band. The black circles show $|V_{us}|$ values measured with different methods which are described in Section 2.4. The blue circle labeled with this:$\mathcal{B}(\tau \to K)$ is the $|V_{us}|$ value computed from $\mathcal{B}(\tau^- \to K^-\nu_\tau)$ measured in this analysis. The second blue circle (PDG+this:$\tau \to s$) is the $|V_{us}|$ value from the inclusive sum of strange τ decays where the results of this analysis is taken into account.

11.3.1. $|V_{us}|$ from the $\tau^- \to K^-\nu_\tau$ decay

The CKM matrix element $|V_{us}|$ can be determined from the branching fraction of the $\tau^- \to K^-\nu_\tau$ decay by using the following relation (see also Section 2.3.5) [5]:

$$\mathcal{B}(\tau^- \to K^-\nu_\tau) = \frac{G_F^2 f_K^2 |V_{us}|^2 m_\tau^3 \tau_\tau}{16\pi\hbar}\left(1 - \frac{m_K^2}{m_\tau^2}\right)^2 S_{EW} \tag{11.9}$$

where $G_F^2 = (1.16637 \pm 0.00001) \times 10^{-5}\,\mathrm{GeV}^{-2}$ [4] is the Fermi coupling constant, $f_K = 157 \pm 2\,\mathrm{MeV}$ [21] is the kaon decay constant, $m_\tau = 1776.82 \pm 0.16\,\mathrm{MeV}/c^2$ and $\tau_\tau = (290.6 \pm 1.0) \times 10^{-15}\,\mathrm{s}$ [4] are the τ mass and lifetime, $m_K = 493.677 \pm 0.013\,\mathrm{MeV}/c^2$ [58] is the kaon mass, $S_{EW} = 1.0201 \pm 0.0003$ [4] is an electroweak correction, and $\hbar = 6.58211899 \times 10^{-22}\,\mathrm{MeV/\,s}$ [4] is the Planck constant.

Using the $\tau^- \to K^-\nu_\tau$ branching fraction obtained in this analysis $|V_{us}|$ amounts to

$$|V_{us}| = 0.2224 \pm 0.0025(\mathrm{exp}) \pm 0.0029(\mathrm{theo}). \tag{11.10}$$

which is consistent with $|V_{us}|$ obtained from the CKM matrix unitarity condition $|V_{us}|^2 = \sqrt{1 - |V_{ud}|^2 - |V_{ub}|^2} = 0.2255 \pm 0.0010$, where $|V_{ud}|$ is known with a high precision from superallowed beta decays and $|V_{ub}|$ is neglected (Section 2.4.1).

This result is also consistent with the $|V_{us}|$ measurements from hyperon, $Kl3$, and $Kl2$ decays. It also agrees with the $|V_{us}|$ value which has been determined in Reference [7] from the earlier BABAR measurement of the $\tau^- \to K^-\nu_\tau$ branching fraction and which differs by almost 2σ from the $|V_{us}|$ predicted from CKM matrix unitarity.

11.3.2. $|V_{us}|$ from the inclusive sum of strange τ decays

The CKM matrix element $|V_{us}|$ can also be determined from the sum of exclusive strange decays by evaluating the relation [8]:

$$|V_{us}| = \sqrt{\frac{R_\mathrm{s}}{\frac{R_\mathrm{ns}}{|V_{ud}|^2} - \delta R_\tau}}, \tag{11.11}$$

which is described in Section 2.4.7. The value of the CKM matrix element $|V_{ud}| = 0.97425 \pm 0.00022$ is taken from [14], and $\delta R_\tau = 0.240 \pm 0.032$ is taken from [8]. $R_{\tau,\mathrm{s}}$ is obtained from

$$R_\mathrm{s} = \frac{\mathcal{B}_\mathrm{s}}{\mathcal{B}(\tau^- \to e^-\overline{\nu}_e\nu_\tau)}, \tag{11.12}$$

where $\mathcal{B}_\mathrm{s}$ is the sum of the exclusive branching fraction of τ decays with strangeness $|S| = 1$.

Four of the exclusive decays which contribute to $\mathcal{B}_\mathrm{s}$ are measured in this analysis. This are the decays $\tau^- \to K^-\nu_\tau$, $\tau^- \to K^-\pi^0\nu_\tau$, $\tau^- \to K^-(2\pi^0)\nu_\tau$, and $\tau^- \to K^-(3\pi^0)\nu_\tau$. For the calculation of $\mathcal{B}_\mathrm{s}$ the average of the branching fractions obtained in this analysis with previously published results is used. The average values are given in Table 11.1. For all other decays with $|S| = 1$ the current world average (Table 2.5) is used. $\mathcal{B}_\mathrm{s}$

amounts to

$$\mathcal{B}_\mathrm{s} = (2.894 \pm 0.066)\%, \tag{11.13}$$

where the relative uncertainty is improved from 2.7% to 2.3% by including the results of this analysis. This leads to a strange hadronic width ratio of

$$R_\mathrm{s} = \frac{\mathcal{B}_\mathrm{s}}{B(\tau^- \to e^-\overline{\nu}_e\nu_\tau)_\mathrm{uni}} = 0.162 \pm 0.004, \tag{11.14}$$

where $B(\tau^- \to e^-\overline{\nu}_e\nu_\tau)_\mathrm{uni} = 17.817 \pm 0.031$ is the lepton-universality improved $\tau^- \to e^-\overline{\nu}_e\nu_\tau$ branching fraction as described in Section 2.2. The relative uncertainty of R_s is 2.3% to be compared with 2.7% without the results of this analysis (Section 2.4.7).

The hadronic τ decay width ratio with $|S| = 0$, R_ns, can be than calculated from

$$R_\mathrm{ns} = R_\mathrm{had} - R_\mathrm{s} = 3.478 \pm 0.010, \tag{11.15}$$

where $R_{had} = 3.6401 \pm 0.010$ is the total hadronic τ decay width ratio determined in Section 2.3.3. Using the above values the CKM matrix element $|V_{us}|$ amounts to

$$|V_{us}| = 0.2176 \pm 0.0025(\mathrm{exp}) \pm 0.0010(\mathrm{theo}), \tag{11.16}$$

where the relative uncertainty has been slightly improved from 1.4% to 1.2%, but is still dominated by the experimental uncertainty of $\mathcal{B}_\mathrm{s}$.

The obtained $|V_{us}|$ value is 0.5σ larger than $|V_{us}|$ computed from the branching fraction world averages listed by the Particle Data Group in 2010 [4]. It is 1.2σ smaller than $|V_{us}| = 0.2224 \pm 0.0038$ obtained from the $\tau^- \to K^-\nu_\tau$ decay.

The result differs by 2.9σ from $|V_{us}|$ derived from the unitarity condition of the CKM matrix, and also deviates from the $|V_{us}|$ values obtained in the hyperon, $Kl3$, and $Kl2$ decay measurements. It has to be noted that the 2.9σ deviation is reduced to 2.6σ if the recently published result for the $\tau^- \to K^-\pi^+\pi^-\nu_\tau$ branching fraction, which has already been mentioned in Section 2.3.4, is included[2] in the $|V_{us}|$ calculation. This new $\tau^- \to K^-\pi^+\pi^-\nu_\tau$ measurement is taken into account in the HFAG $|V_{us}|$ result shown in Figure 11.2.

11.4. Conclusion and outlook

The six measured hadronic τ branching fractions are in good agreement with earlier published measurements. The $|V_{us}|$ value obtained from the inclusive sum of strange τ decays is 2.9σ lower that the $|V_{us}|$ prediction from the unitarity conditions of the CKM matrix, whereas the $|V_{us}|$ value determined from the $\tau^- \to K^-\nu_\tau$ decay is consistent with this prediction. This indicates that a systematic uncertainty of the $|V_{us}|$ determination from the inclusive sum of strange τ decays could be underestimated.

The understanding of the observed deviation could be improved by further mea-

---

[2] Instead of the world average, $\mathcal{B}(\tau^- \to K^-\pi^+\pi^-\nu_\tau) = (0.280 \pm 0.019)\%$, taken from [4], the HFAG average $\mathcal{B}(\tau^- \to K^-\pi^+\pi^-\nu_\tau) = (0.291 \pm 0.016)\%$ which includes the Belle result is used.

surements of strange τ decays by *BABAR* and Belle. Especially, a measurement of the $\tau^- \to \pi^- \overline{K}^0 \nu_\tau$ and $\tau^- \to \pi^- \overline{K}^0 \pi^0 \nu_\tau$ branching fractions is important, since these branching fractions are relatively large and are currently known with a relative precision of 3.6% and 11.1% [4]. The $\tau^- \to \pi^- \overline{K}^0 \nu_\tau$ branching fraction has already been published by the Belle experiment [59]. *BABAR* has presented preliminary results for both decays, and final results are expected soon [15].

The relative contribution of other strange τ decays to the total strange branching fraction B_s is $\approx 6\%$. These contributions are known with a relative precision of only $\approx 20\%$. Thus, a measurement of these less frequent decays is also important. Moreover, since non-strange τ decays contribute to the background of the strange τ decay measurements, new high-precision measurements of these decays would also lead to an improved precision of $\mathcal{B}_\mathrm{s}$. For example, the precision of the $\tau^- \to K^-(3\pi^0)\nu_\tau$ branching fraction measured in this analysis could be improved by a better knowledge of the $\tau^- \to K^- \overline{K}^0 \pi^0 \nu_\tau$ branching fraction which currently limits this measurement.

A further possible source of the observed deviation is the CKM matrix element V_{ud} which enters the $|V_{us}|$ determination. In addition to the very precise $|V_{ud}|$ result from superallowed beta decays [14], which has been used in this analysis, $|V_{ud}|$ can also be determined from the lifetime of the neutron. The neutron lifetime measurement presented in [60] is inconsistent with the world average, and leads to a larger $|V_{ud}|$ value. To resolve the $|V_{us}|$ puzzle also further theoretical investigations of the $SU(3)_L$-symmetry breaking correction δR_τ [8] could be necessary.

Besides the contribution to the determination of $|V_{us}|$, the presented analysis is also an important step towards the measurement of the invariant mass spectra of the hadronic final states in the studied decays, and thus, of the strange spectral functions.

A. Missing mass in τ decays

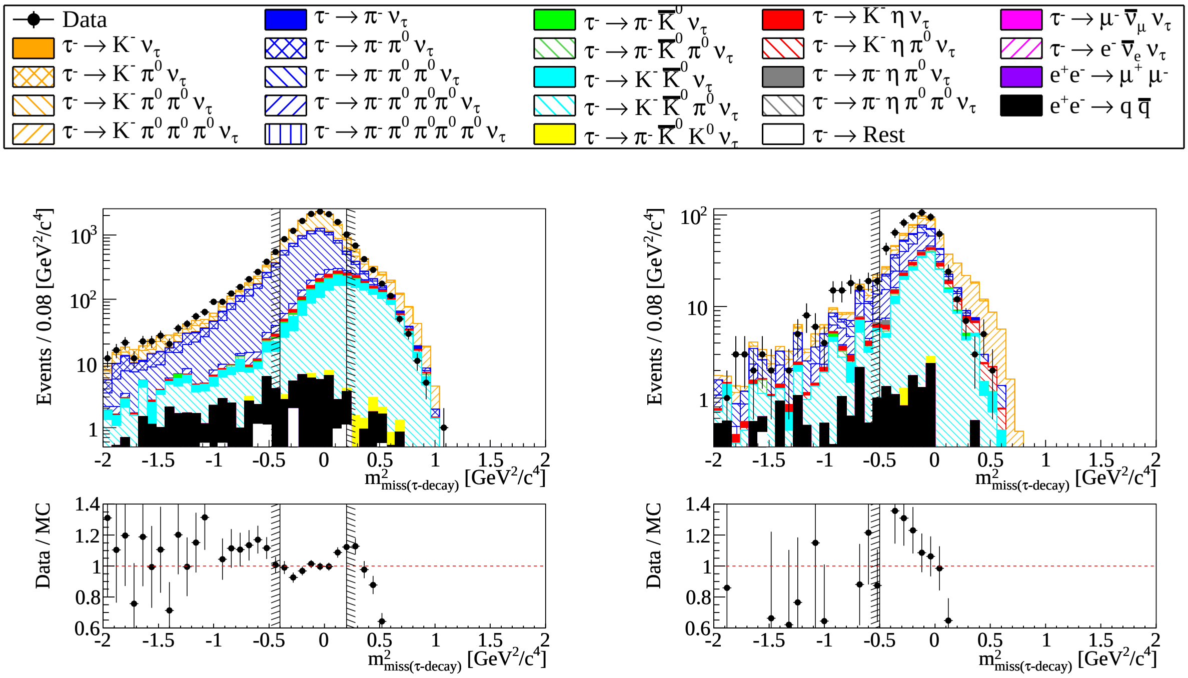

(a) $\tau^- \to K^-(2\pi^0)\nu_\tau$

(b) $\tau^- \to K^-(3\pi^0)\nu_\tau$

Figure A.1.: Distribution of the squared missing mass in the τ decay, $m_{\text{miss}(\tau-decay)}$ for selected $\tau^- \to K^-(2\pi^0)\nu_\tau$, and $\tau^- \to K^-(3\pi^0)\nu_\tau$ candidates.

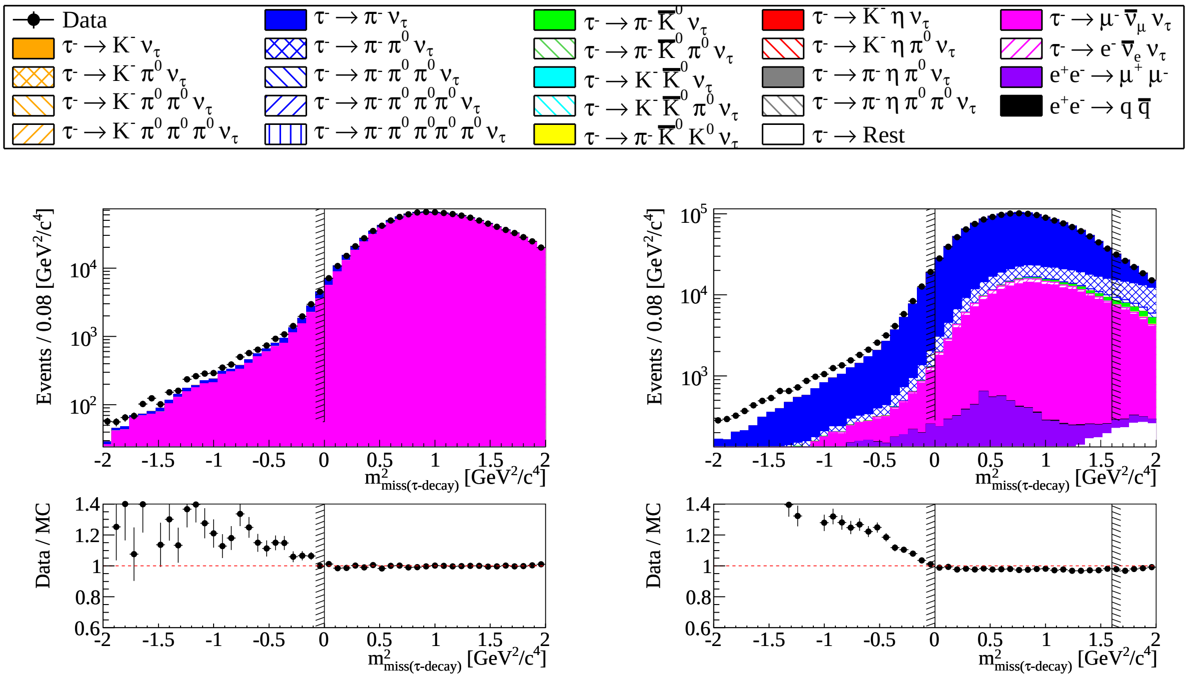

(a) $\tau^+ \to e^+\nu_e\overline{\nu}_\tau$, $\tau^- \to \mu^-\overline{\nu}_\mu\nu_\tau$ **(b)** $\tau^- \to \pi^-\nu_\tau$

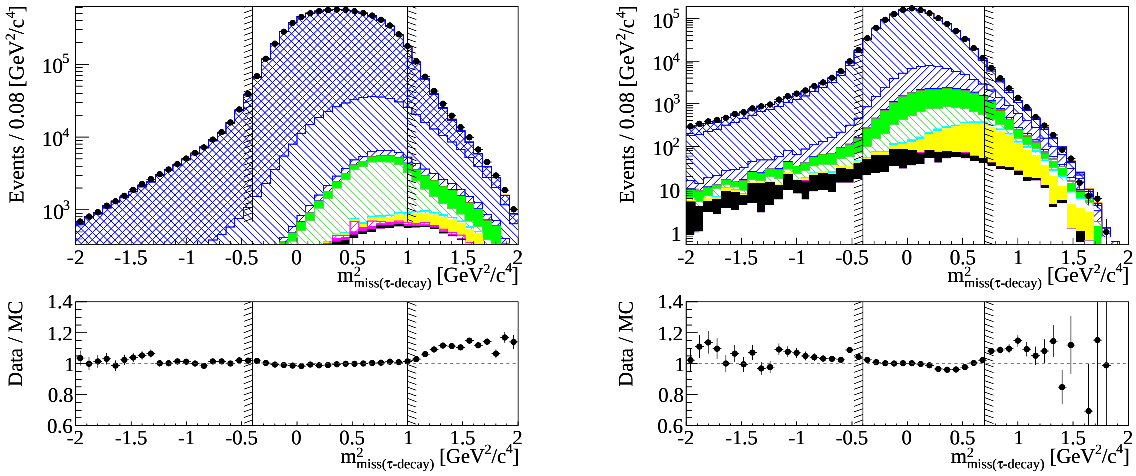

(c) $\tau^- \to \pi^-\pi^0\nu_\tau$ **(d)** $\tau^- \to \pi^-(2\pi^0)\nu_\tau$

Figure A.2.: Distribution of the squared missing mass in the τ decay, $m_{\text{miss}(\tau-decay)}$ in the selected control modes.

B. Pion and kaon identification correction weights

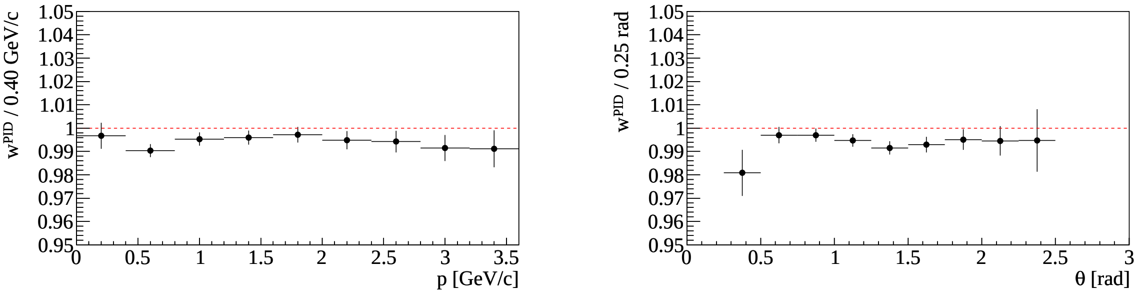

(a) Momentum p_{control} **(b)** Polar angle $\theta_{\mathrm{control}}$

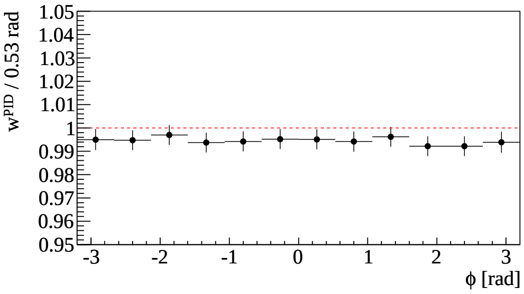

(c) Azimuthal angle ϕ_{control}

Figure B.1.: Pion identification weights, $w^{PID}_{\pi\text{-}as\text{-}\pi}$ in dependence of the control track momentum, polar angle and azimuthal angle. The whole data sample, i. e., runs 1-6, is used to obtain the shown weights. The error bars correspond to the statistical uncertainties of the weights.

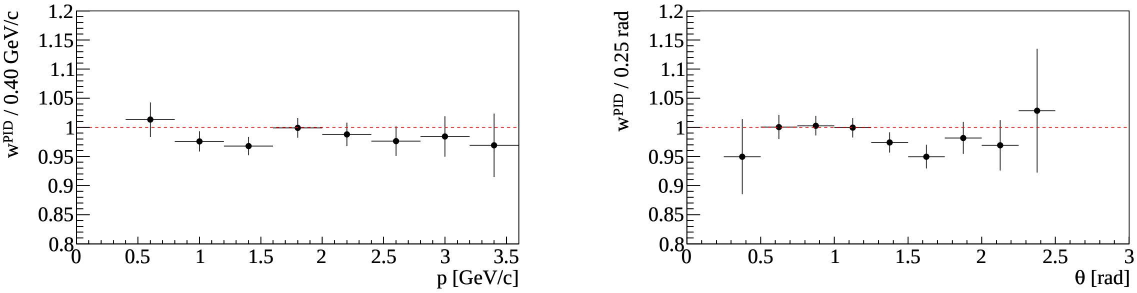

(a) Momentum p_{control}

(b) Polar angle θ_{control}

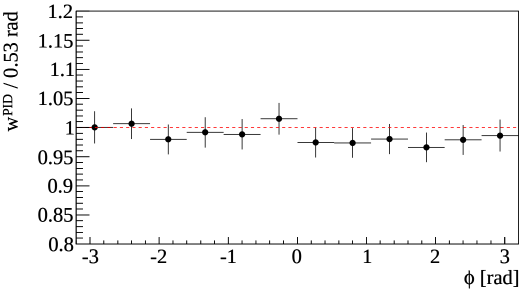

(c) Azimuthal angle ϕ_{control}

Figure B.2.: Kaon identification weights, $w^{PID}_{K\text{-}as\text{-}K}$ in dependence of the control track momentum, polar angle and azimuthal angle. The whole data sample, i. e., runs 1-6, is used to obtain the shown weights. The error bars correspond to the statistical uncertainties of the weights.

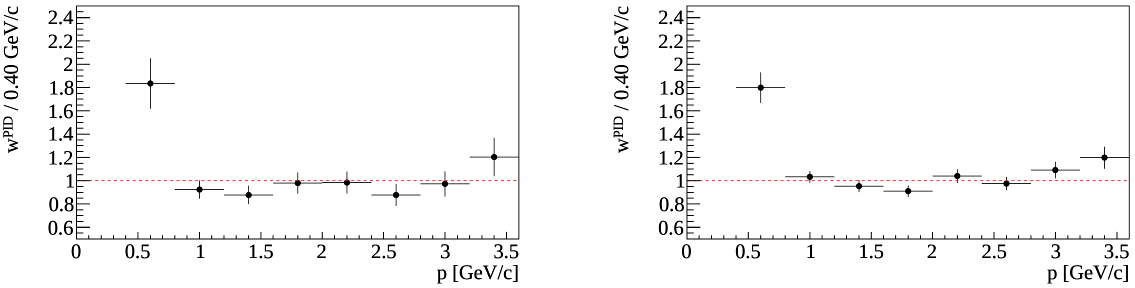

(a) Run 1 **(b)** Run 2

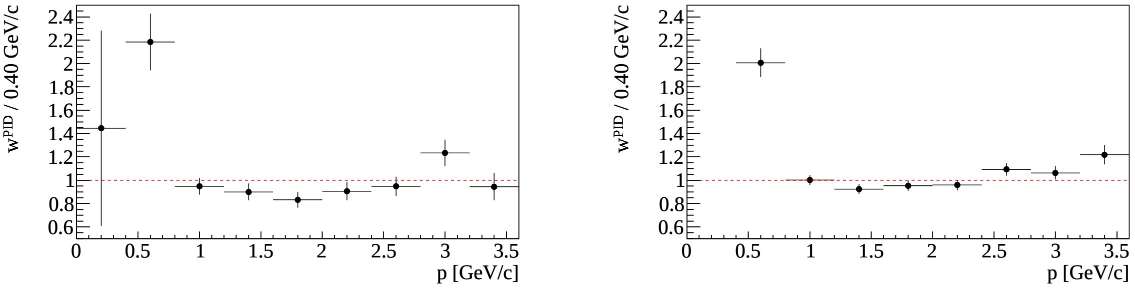

(c) Run 3 **(d)** Run 4

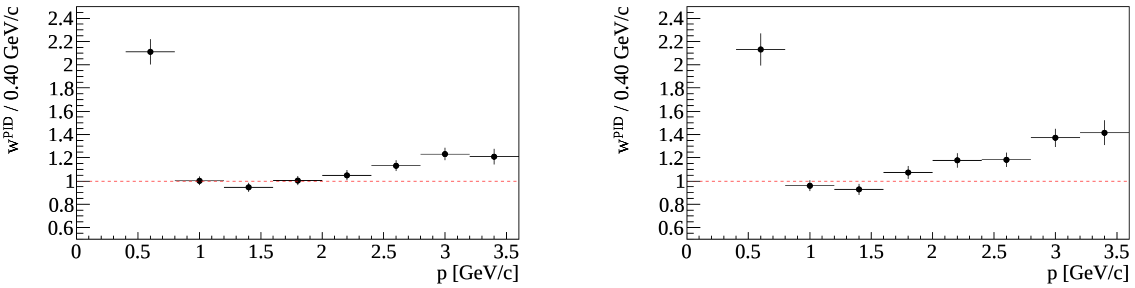

(e) Run 5 **(f)** Run 6

Figure B.3.: Misidentification weights for a pion misidentified as a kaon, $w^{PID}_{\pi\text{-}as\text{-}K}$ in dependence of the control track momentum for each run period. The error bars correspond to the statistical uncertainties of the weights.

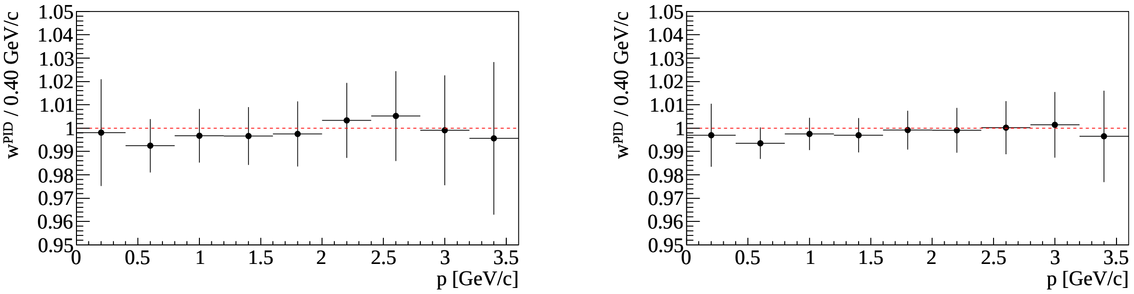

(a) Run 1 **(b)** Run 2

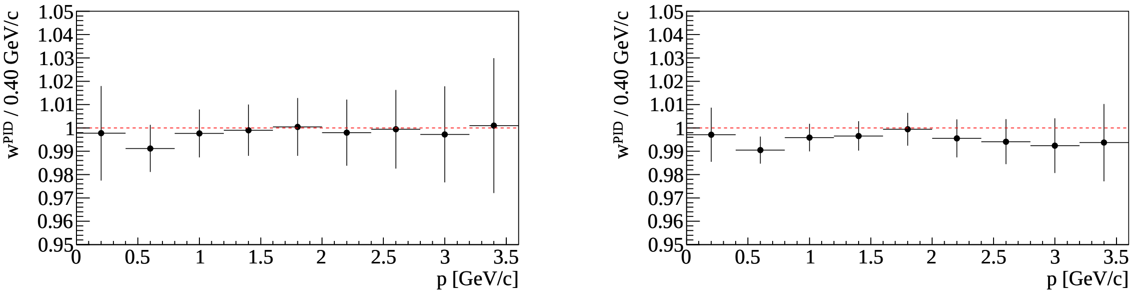

(c) Run 3 **(d)** Run 4

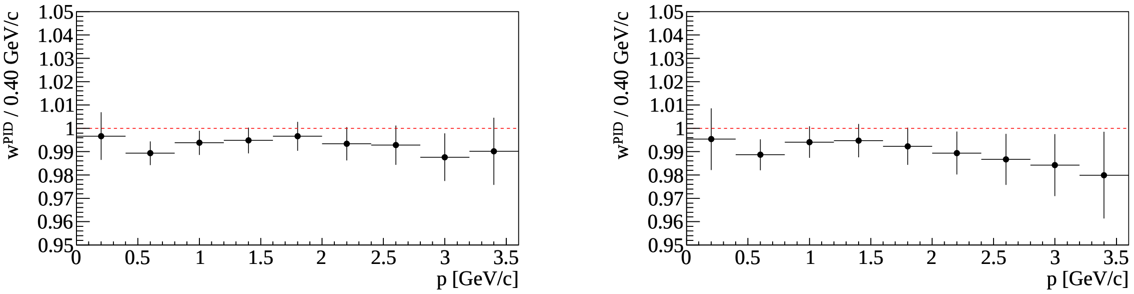

(e) Run 5 **(f)** Run 6

Figure B.4.: Pion identification weights, $w^{PID}_{\pi\text{-}as\text{-}\pi}$ in dependence of the control track momentum for each run period. The error bars correspond to the statistical uncertainties of the weights.

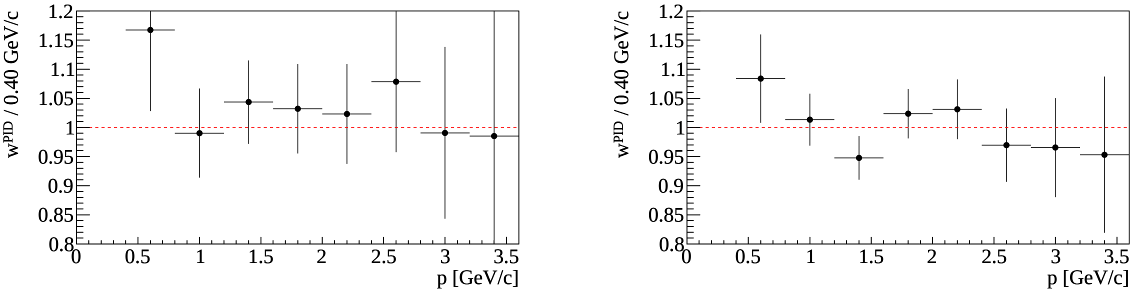

(a) Run 1 **(b)** Run 2

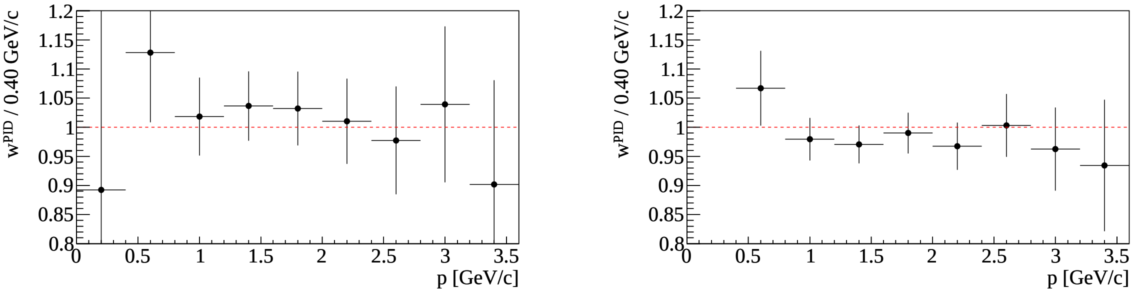

(c) Run 3 **(d)** Run 4

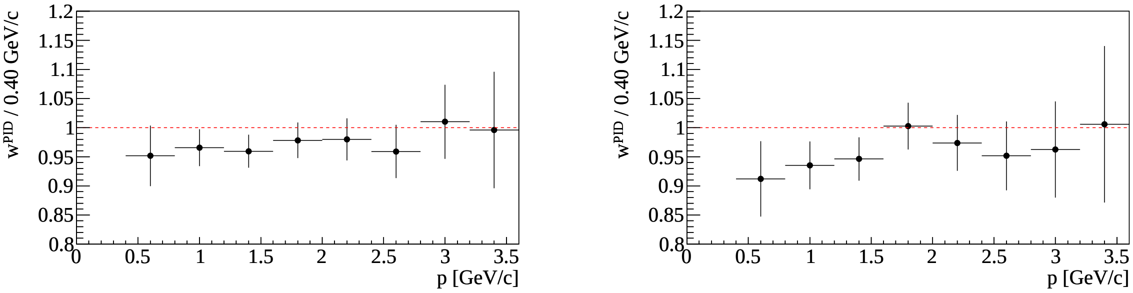

(e) Run 5 **(f)** Run 6

Figure B.5.: Kaon identification weights, $w^{PID}_{K\text{-}as\text{-}K}$ in dependence of the control track momentum for each run period. The error bars correspond to the statistical uncertainties of the weights.

C. Effect of background in the branching fraction calculation

This section illustrates the effect of background on the uncertainty $\Delta\mathcal{B}$ of a branching fraction computed according to Equation 10.8:

$$\mathcal{B} = 1 - \sqrt{1 - \frac{N_{\text{sel}} - N_{\text{bkg}}}{\epsilon_{\text{sig}} \cdot N_{\tau\tau}}} \underbrace{\approx}_{\mathcal{B} \ll 1} \frac{N_{\text{sel}} - N_{\text{bkg}}}{2\epsilon_{\text{sig}} \cdot N_{\tau\tau}}, \tag{C.1}$$

where N_{bkg} and ϵ_{sig} are estimated from simulation. The index MC is dropped to improve the readability. The second term is a simplification of the formula using that $\mathcal{B} \ll 1$.

The uncertainty of the branching fraction is calculated from

$$\Delta\mathcal{B}^2 = \frac{1}{\mathcal{B}^2} \cdot \left[\left(\frac{\partial\mathcal{B}}{\partial N_{\text{sel}}} \Delta N_{\text{sel}} \right)^2 + \left(\frac{\partial\mathcal{B}}{\partial N_{\text{bkg}}} \Delta N_{\text{bkg}} \right)^2 + \left(\frac{\partial\mathcal{B}}{\partial \epsilon_{\text{sig}}} \Delta \epsilon_{\text{sig}} \right)^2 + \left(\frac{\partial\mathcal{B}}{\partial N_{\tau\tau}} \Delta N_{\tau\tau} \right)^2 \right].$$

Using the simplified formula in Equation C.1 the relative uncertainty is than

$$\begin{aligned} \left(\frac{\Delta\mathcal{B}}{\mathcal{B}} \right)^2 &= \left(\frac{1}{1 - f_{\text{bkg}}} \right)^2 \cdot \left(\frac{\Delta N_{\text{sel}}}{N_{\text{sel}}} \right)^2 + \left(\frac{f_{\text{bkg}}}{1 - f_{\text{bkg}}} \right)^2 \cdot \left(\frac{\Delta N_{\text{bkg}}}{N_{\text{bkg}}} \right)^2 \\ &+ \quad \cdot \left(\frac{\Delta\epsilon_{\text{sig}}}{\epsilon_{\text{sig}}} \right)^2 + \quad \cdot \left(\frac{\Delta N_{\tau\tau}}{N_{\tau\tau}} \right)^2 \end{aligned} \tag{C.2}$$

where f_{bkg} is the fraction of background events in the selected event sample:

$$f_{\text{bkg}} = \frac{N_{\text{bkg}}}{N_{\text{sel}}}. \tag{C.3}$$

Equation C.2 shows why the relative branching fraction uncertainties of different modes which arise from the same systematic effect can have different values:

1. The relative uncertainty of the background, $\frac{\Delta N_{\text{bkg}}}{N_{\text{bkg}}}$, which corresponds the statistical uncertainty of the simulated background sample as well as systematic contributions is scaled by the factor $\frac{f_{\text{bkg}}}{1-f_{\text{bkg}}}$. For example, the uncertainty contribution of the τ pair cross section, $\frac{\Delta\sigma_{\tau\tau}}{\sigma_{\tau\tau}} = 0.31\%$, enters $\frac{\Delta\mathcal{B}}{\mathcal{B}}$ as $\left(\frac{f_{\text{bkg}}}{1-f_{\text{bkg}}} \cdot 0.31\% \right)$.

2. The relative uncertainty of the selected events, $\frac{\Delta N_{\text{sel}}}{N_{\text{sel}}}$, which is of statistical nature, is increased by the factor $\frac{1}{1-f_{\text{bkg}}}$. For example, a background fraction of 50% doubles the contribution of $\frac{\Delta N_{\text{sel}}}{N_{\text{sel}}}$.

List of Figures

1.1. Feynman diagram of the hadronic τ decay into a final state with $|S| = 1$. 1

2.1. Feynman diagrams of hadronic charged current transitions in τ decays. 7
2.2. Feynman diagram of the leptonic τ decay $\tau^- \to l^- \overline{\nu}_l \nu_\tau$ with $l^- = e^-, \mu^-$. 8
2.3. Feynman diagram of the $\tau^- \to K^- \pi^0 \nu_\tau$ decay. 10
2.4. Comparison of $|V_{us}|$ values obtained with different methods. 18

3.1. Schematic view of the PEP-II collider 24
3.2. Integrated luminosity as a function of the time. 24
3.3. Schematic longitudinal view of the *BABAR* detector 26
3.4. Schematic view of the SVT 27
3.5. Schematic longitudinal view of the DCH 28
3.6. Schematic view of the DIRC 29
3.7. Working principle of the DIRC 29
3.8. Schematic longitudinal view of the EMC 31
3.9. Schematic view of the IFR 32

5.1. Specific energy loss and Cherenkov angle for different particle types. . . 41
5.2. Electron and muon PID selector efficiencies. 46
5.3. Kaon PID selector efficiencies. 47
5.4. Pion PID selector efficiencies. 48

6.1. *BABAR* event displays: An $e^+e^- \to \tau^+\tau^-$ event and $e^+e^- \to B^0\ \overline{B}^0$ event. 56
6.2. Feynman graphs: $e^+e^- \to l^+l^-\gamma$ and $e^+e^- \to e^+e^- f\bar{f}$. 56
6.3. Distribution of the tag lepton momentum. 61
6.4. Schematic illustration of a $e^+e^- \to \tau^+\tau^-$ event. 62
6.5. Distribution of the thrust. 63
6.6. Distribution of the missing mass. 65
6.7. Distribution of the kaon momentum. 68
6.8. Distribution of the angle between hadron and next π^0. 69
6.9. Distribution of the number of additional photons in the event. 70
6.10. Distribution of the total transverse momentum over missing energy. . . 72
6.11. Distribution of the acoplanarity. 73
6.12. Distributions of the 2-π^0 and 3-π^0 invariant mass. 74
6.13. Distribution of the missing mass in the τ decay. 76
6.14. Distribution of the pion and kaon momentum. 78
6.15. Tag lepton momentum in selected events. 79
6.16. Tag lepton momentum in selected events. 80

6.17. Signal track momentum in selected events. 83
6.18. Signal track momentum in selected events. 84
6.19. Signal track polar angle in selected events. 85
6.20. Signal track polar angle in selected events. 86

7.1. PID control track momentum. 92
7.2. Pion-as-kaon misidentification weights. 94

8.1. Illustration of split-offs. 96
8.2. Number of additional photon in an event. 97
8.3. Distance between signal track and next photon. 98

9.1. Tag electron momentum in event sample for the π^0 efficiency correction study. 103
9.2. π^0 momentum before application of the π^0 efficiency correction. 104
9.3. π^0 efficiency correction values. 105
9.4. π^0 efficiency correction values for each run period. 105
9.5. π^0 momentum after application of the π^0 efficiency correction. 106
9.6. Missing mass in event sample for the π^0 efficiency correction study. . . 109
9.7. Polar angle of the reconstructed π^0. 111
9.8. $\mathcal{B}(\tau^- \to \pi^-\nu_\tau)$, $\mathcal{B}(\tau^- \to \pi^-\pi^0\nu_\tau)$, and $\mathcal{B}(\tau^- \to \pi^-(2\pi^0)\nu_\tau)$ determined in event sample for the π^0 efficiency study. 113

10.1. Measured branching fractions of control decays 143
10.2. Branching fractions of control decays measured separately in e-tag and μ-tag sample. 145
10.3. Branching fraction of control decays measured separately for e-tag and μ-tag sample, and for each run. 147
10.4. Branching fractions of signal decays measured separately for e-tag and μ-tag samples. 148
10.5. Measured signal decay branching fractions. 150
10.6. Branching fractions of signal decays measured in e-tag sample for each run. 151
10.7. Branching fractions of signal decays measured in μ-tag sample for each run. 152

11.1. Comparison of measured $\mathcal{B}$'s with previously published results. 155
11.2. Comparison of obtained $|V_{us}|$ with other measurements. 159

A.1. Distribution of the missing mass in τ decay. 163
A.2. Distribution of the missing mass in τ decay. 164

B.1. Pion identification weights. 165
B.2. Kaon identification weights. 166
B.3. Pion-as-kaon misidentification weights for each run period. 167
B.4. Pion identification weights for each run period. 168
B.5. Kaon identification weight for each run period. 169

List of Tables

2.1. Fundamental forces 3
2.2. Fundamental particles 4
2.3. Fundamental particles 5
2.4. Branching fractions of the five most frequent hadronic τ decays. 15
2.5. Branching fractions of strage τ decays. 15

3.1. Integrated lumiminosity recorded by the *BABAR* experiment. 33
3.2. Cross sections and numbers of generated events. 34
3.3. Branching fractions and generated signal and background samples. . . . 34

5.1. Neutral particle reconstruction criteria. 54

6.1. Selection criteria applied to all decay modes. 81
6.2. Decay-specific selection criteria applied in this analysis. 82

7.1. Data and simulation agreement in kaon and pion PID control samples. 93
7.2. Composition of selected τ^- PID control samples in simulation 93

8.1. Relative amount of split-offs in each run. 99

9.1. Composition of the simulated samples used for the π^0 correction determination. 103
9.2. Systematic uncertainties of the π^0 efficiency correction. 110
9.3. Systematic uncertainties of the π^0 efficiency correction in dependence of π^0 momentum. 111
9.4. Measured control branching fractions with all uncertainty contributions in event sample for the π^0 efficiency correction study. 112

10.1. Numbers of selected events. 115
10.2. Selection efficiencies. 116
10.3. Systematic uncertainties due to signal decay efficiencies. 125
10.4. Background τ decay branching fractions. 126
10.5. Systematic uncertainties due to background decay efficiencies. 127
10.6. Systematic uncertainties due to the background decay branching fractions. 128
10.7. Systematic uncertainties due to the PID weights. 129
10.8. Systematic uncertainties due to the kaon and pion identification. 130
10.9. Systematic uncertainties due to the uncertainty of the number of τ pairs. 131
10.10Systematic uncertainties due to the track efficiency correction. 133
10.11Systematic uncertainties due to the split-off correction. 133

10.12Systematic uncertainties due to the π^0 efficiency correction. 134
10.13Systematic uncertainties due to π^0 downfeed in $\tau^- \to \pi^-(4\pi^0)\nu_\tau$. . . . 138
10.14Systematic uncertainties due to π^0 downfeed in $\tau^- \to K^-(3\pi^0)\nu_\tau$. . . . 139
10.15Measured control branching fractions with all uncertainty contributions. 140
10.16Measured signal branching fractions with all uncertainty contributions. 141

11.1. Average signal branching fractions 156

Bibliography

[1] Glashow, S. L., Partial-symmetries of weak interactions, Nuclear Physics 22 (4) (1961) 579 – 588. doi:10.1016/0029-5582(61)90469-2.

[2] Salam, A. and Ward, J. C., Electromagnetic and weak interactions, Phys. Lett. 13 (1964) 168–171. doi:10.1016/0031-9163(64)90711-5.

[3] Weinberg, S., A Model of Leptons, Phys. Rev. Lett. 19 (1967) 1264–1266. doi:10.1103/PhysRevLett.19.1264.

[4] Nakamura, K. et al., Review of Particle Physics, J. Phys. G 37 075021.

[5] Davier, M. and Hocker, A. and Zhang, Z., The physics of hadronic τ decays, Rev. Mod. Phys. 78 (2006) 1043–1109. arXiv:hep-ph/0507078, doi:10.1103/RevModPhys.78.1043.

[6] Kobayashi, M. and Maskawa, T., CP Violation in the Renormalizable Theory of Weak Interaction, Prog. Theor. Phys. 49 (1973) 652–657. doi:10.1143/PTP.49.652.

[7] Aubert, B. et al., Measurements of Charged Current Lepton Universality and $|V_{us}|$ Using Tau Lepton Decays to $e^-\overline{\nu}_e\nu_\tau$, $\mu^-\overline{\nu}_\mu\nu_\tau$, $K^-\nu_\tau$, $\pi^-\nu_\tau$, Phys. Rev. Lett. 105 (5) (2010) 051602. doi:10.1103/PhysRevLett.105.051602.

[8] Gamiz, E. and Jamin, M. and Pich, A. and Prades, J. and Schwab, F., $|V_{us}|$ and $m(s)$ from hadronic τ decays, Nucl. Phys. Proc. Suppl. 169 (2007) 85–89. arXiv:hep-ph/0612154, doi:10.1016/j.nuclphysbps.2007.02.053.

[9] Antonelli, M. et al., An evaluation of $|V_{us}|$ and precise tests of the Standard Model from world data on leptonic and semileptonic kaon decays, Eur. Phys. J. C69 (2010) 399–424. arXiv:1005.2323, doi:10.1140/epjc/s10052-010-1406-3.

[10] Schenk, S., Measurement of Cabibbo-suppressed τ decays and the determination of $|V_{us}|$, Ph.D. thesis, Ruprecht-Karls-Universität Heidelberg (2008).

[11] Valle, J. W. F., Neutrino physics overview, J. Phys. Conf. Ser. 53 (2006) 473–505. arXiv:hep-ph/0608101, doi:10.1088/1742-6596/53/1/031.

[12] Halzen, F. and Martin, A. D., Quarks & Leptons - An introductory Course in Modern Particle Physics, John Wiley & Sons, 1984.

[13] Maki, Z. and Nakagawa, M. and Sakata, S., Remarks on the unified model of elementary particles, Prog. Theor. Phys. 28 (1962) 870–880. doi:10.1143/PTP.28.870.

[14] Hardy, J. C. and Towner, I. S., Superallowed $0^+ \to 0^+$ nuclear β decays: A new survey with precision tests of the conserved vector current hypothesis and the standard model, Phys. Rev. C 79 (5) (2009) 055502. doi:10.1103/PhysRevC.79.055502.

[15] Paramesvaran, S., Selected topics in τ physics from *BABAR*. arXiv:0910.2884.

[16] Maltman, K. and Wolfe, C. E., $|V_{us}|$ From Hadronic Tau Decays. arXiv:hep-ph/0703314.

[17] Schael, S. et al., Branching ratios and spectral functions of τ decays: Final aleph measurements and physics implications, Physics Reports 421 (5-6) (2005) 191 – 284. doi:10.1016/j.physrep.2005.06.007.

[18] Aubert, B. et al., Exclusive branching fraction measurements of semileptonic τ decays into three charged hadrons, $\tau^- \to \phi\pi^-\nu_\tau$ and $\tau^- \to \phi K^-\nu_\tau$, Phys. Rev. Lett. 100 (2008) 011801. arXiv:0707.2981, doi:10.1103/PhysRevLett.100.011801.

[19] Lee, M. J. et al., Measurement of the branching fractions and the invariant mass distributions for $\tau^- \to h^-h^+h^-\nu_\tau$ decays, Phys. Rev. D81 (2010) 113007. arXiv:1001.0083, doi:10.1103/PhysRevD.81.113007.

[20] Mateu, V. and Pich, A., $|V_{us}|$ determination from hyperon semileptonic decays, JHEP 10 (2005) 041. arXiv:hep-ph/0509045, doi:10.1088/1126-6708/2005/10/041.

[21] Follana, E. and Davies, C. T. H. and Lepage, G. P. and Shigemitsu, J., High-Precision Determination of the π, K, D, and D_s Decay Constants from Lattice QCD, Phys. Rev. Lett. 100 (6) (2008) 062002. doi:10.1103/PhysRevLett.100.062002.

[22] Lusiani, A., Measurements of $|V_{us}|$ and Searches for Violation of Lepton Universality and CPT in Tau Decays at *BABAR*, PoS (ICHEP 2010) 251.

[23] Asner, D. et al., Averages of b-hadron, c-hadron, and τ-lepton Properties. arXiv:1010.1589.

[24] Hardy, J. C. and Towner, I. S., Superallowed beta decay: the role of nuclear structure in standard-model tests, Acta Physica Polonica B 40 (3).

[25] Aubert, B. et al., The *BABAR* detector, Nucl. Instrum. Methods Phys. Res., Sect. A **479** (2002) 1–116arXiv:hep-ex/0105044.

[26] PEP-II: An Asymmetric B Factory. Conceptual Design Report.SLAC-418.

[27] *BABAR* collaboration, *BABAR* Detector Operations, `http://www.slac.stanford.edu/BFROOT/www/Detector/Operations/Operations.html` (2008).

[28] Harrison, P. F., ed. and Quinn, H. R., ed., The *BABAR* Physics Book: Physics at an Asymmetric B Factory, papers from Workshop on Physics at an Asymmetric B Factory (*BABAR* collaboration Meeting), Rome, Italy, 11-14 Nov 1996, Princeton,

NJ, 17-20 Mar 1997, Orsay, France, 16-19 Jun 1997 and Pasadena, CA, 22-24 Sep 1997.

[29] Banerjee, S. and Pietrzyk, B. and Roney, J. M. and Was, Z. , Tau and muon pair production cross sections in electron-positron annihilations at $\sqrt{s} = 10.58\,\mathrm{GeV}$, Phys. Rev. D 77 (5) (2008) 054012. doi:10.1103/PhysRevD.77.054012.

[30] Accelerator Systems Division: PEP-II: Asymmetric *B* Factory, PEP-II Records, `http://www.slac.stanford.edu/BFROOT/www/Organization/PubBoard/OfficialPlots/index.html` (2008).

[31] The *BABAR* collaboration, The Pub Board Page of Official Plots: PEP-II plots, `http://www.slac.stanford.edu/BFROOT/www/Organization/PubBoard/OfficialPlots/index.html#PEPIIplots` (2011).

[32] R. Gamet, C. Touramanis, Luminosity Measurement for the Runs 1, 2 and 3 data sample using Release 12 and SP5 Simulation, *BABAR* Analysis Document **1312**, SLAC (2005).

[33] Ward, B. F. L. and Jadach, S. and Was, Z., Precision calculation for $e^+e^- \to 2f$: The KK MC project, Nucl. Phys. Proc. Suppl. 116 (2003) 73–77. arXiv:hep-ph/0211132, doi:10.1016/S0920-5632(03)80147-0.

[34] Jadach, S. and Was, Z. and Decker, R. and Kuhn, Johann H., The τ decay library `TAUOLA`: Version 2.4, Comput. Phys. Commun. 76 (1993) 361–380. doi:10.1016/0010-4655(93)90061-G.

[35] David, J. L., The `EvtGen` particle decay simulation package, Nuclear Instruments and Methods in Physics Research Section A: Accelerators, Spectrometers, Detectors and Associated Equipment 462 (1-2) (2001) 152 – 155. doi:10.1016/S0168-9002(01)00089-4.

[36] Agostinelli, S. et al., Geant4 — a simulation toolkit, Nuclear Instruments and Methods in Physics Research A (506) (2003) 250–303.

[37] Allen, M., Naisbit, M., Roodman, A. and Banerjee, S., A Measurement of the π^0 Efficiency Using $\tau \to \rho\nu$ and $\tau \to \pi\nu$ Decays, *BABAR* Analysis Document **870v3**, SLAC (2004).

[38] The Charged Particles Identifcation Working Group, Inventory of PidSelectors for "r24c", `http://www.slac.stanford.edu/BFROOT/www/Physics/Tools/Pid/Selectors/r24c/selectors.html` (2011).

[39] The *BABAR* collaboration, Tracking Efficiency for Run 1 - Run 7 in R24 , `http://www.slac.stanford.edu/BFROOT/www/Physics/TrackEfficTaskForce/TrackingTaskForce-2009-R24.html` (2010).

[40] The *BABAR* collaboration, The Pub Board Page of Official Plots, `http://www.slac.stanford.edu/BFROOT/www/Organization/PubBoard/OfficialPlots/index.html` (2011).

[41] Electron Identification Working Group, Cut-Based Electron Identification, *BABAR* Analysis Document **90v5**, SLAC (2001).

[42] Brandt, T., Likelihood Based Electron Identification, *BABAR* Analysis Document **391v1**, SLAC (2002).

[43] Mohapatra, A. and Holler, J. and Band, H., Studies of A Neural Net Based Muon Selector for the BaBar Experiment, *BABAR* Analysis Document **474v3**, SLAC (2004).

[44] Vuosalo, C. O. and Telnov, A. V. Flood, K. T, Muon Identification Using Decision Trees, *BABAR* Analysis Document **1853v3**, SLAC (2010).

[45] Ongmongkolkul, P. and Mishra, K. and Telnov, A. and Gaz, A., Particle Identification Using Error Correction Output Code 3 Multiclass Classifier, *BABAR* Analysis Document **2199v2**, SLAC (2009).

[46] Telnov, A., Detailed Track-Level dE/dx Calibration for The *BABAR* Drift Chamber and Silicon Vertex Tracker, *BABAR* Analysis Document **1500v5**, SLAC (2008).

[47] Brandt, T, Measurement of Inclusive Electron Spectrum, Moments and Branching Fraction for Semileptonic B Meson Decays, *BABAR* Analysis Document **636v7**, SLAC (2003).

[48] Asner, D. M. et al. , Hadronic structure in the decay $\tau^- \to \nu_\tau \pi^- \pi^0 \pi^0$ and the sign of the tau neutrino helicity, Phys. Rev. D 61 (1) (1999) 012002. doi:10.1103/PhysRevD.61.012002.

[49] Nugent, I. and Banerjee, S. and Roney, M., Measurment of $\frac{\mathcal{B}(\tau^-\to K^-\nu_\tau)}{\mathcal{B}(\tau^-\to e^-\overline{\nu}_e\nu_\tau)}, \frac{\mathcal{B}(\tau^-\to\pi^-\nu_\tau)}{\mathcal{B}(\tau^-\to e^-\overline{\nu}_e\nu_\tau)}, \frac{\mathcal{B}(\tau^-\to\mu^-\overline{\nu}_\mu\nu_\tau)}{\mathcal{B}(\tau^-\to e^-\overline{\nu}_e\nu_\tau)}$, *BABAR* Analysis Document **1905**, SLAC (2005).

[50] Banerjee, S. et al., CM2 skims for $e^+e^- \to \mu^+\mu^-$ and $e^+e^- \to \tau^+\tau^-$ events (TAUQED2), *BABAR* Analysis Document **760**, SLAC (2003).

[51] Latham, T. and Gershon, T. and Puccio, E., Study of Neutral Pion Efficiency Using τ Lepton Decays in the *BABAR* detector, *BABAR* Analysis Document **1897v1**, SLAC (2005).

[52] Battle, M. et al., Measurement of Cabibbo-Suppressed Decays of the τ Lepton, Phys. Rev. Lett. 73 (8) (1994) 1079–1083. doi:10.1103/PhysRevLett.73.1079.

[53] Abreu, P., Charged kaon production in tau decays at LEP, Physics Letters B 334 (3-4) (1994) 435 – 449. doi:10.1016/0370-2693(94)90711-0.

[54] Barate et al., Study of τ decays involving kaons, spectral functions and determination of the strange quark mass, The European Physical Journal C - Particles and Fields 11 (1999) 599–618, 10.1007/s100529900208.

[55] Abbiendi et al., A study of one-prong τ decays with a charged kaon, The European Physical Journal C - Particles and Fields 19 (2001) 653–665, 10.1007/s100520100632.

[56] Abbiendi et al., Measurement of the strange spectral function in hadronic τ decays, The European Physical Journal C - Particles and Fields 35 (2004) 437–455, 10.1140/epjc/s2004-01877-2.

[57] Aubert, B. et al. , Measurement of the $\tau^- \to k^-\pi^0\nu_\tau$ branching fraction, Phys. Rev. D 76 (5) (2007) 051104. doi:10.1103/PhysRevD.76.051104.

[58] Erler, J., Electroweak radiative corrections to semileptonic τ decays, Rev.Mex.Fis. 50 (2004) 200.

[59] Epifanov, D. et al., Study of $\tau^- \to K_S^0\pi^-\nu_\tau$ decay at Belle, Phys. Lett. B654 (2007) 65–73. arXiv:0706.2231, doi:10.1016/j.physletb.2007.08.045.

[60] Serebrov, A., Measurement of the neutron lifetime using a gravitational trap and a low-temperature fomblin coating, Physics Letters B 605 (1-2) (2005) 72 – 78. doi:DOI: 10.1016/j.physletb.2004.11.013.

Acknowledgments

Mein herzlicher Dank gilt meinem Doktorvater Herrn Prof. Dr. Ulrich Uwer für die intensive Betreuung und Unterstützung bei der Bearbeitung des interessanten Themas.
Herrn Prof. Dr. Hans-Christian Schultz-Coulon danke ich für die freudliche Übernahme der Zweitkorrekur dieser Arbeit.
Mein Dank gilt auch Dr. Jörg Marks, nicht nur für die fachlichen Ratschläge, sondern auch für seine Freundlichkeit und die Ermutigungen immer dran zu bleiben.
Dr. Stefan Schenk danke ich für die freundschaftliche Zusammenarbeit in der ersten Phase dieser Arbeit.
Bedanken möchte ich mich auch bei der ganzen HE-Gruppe für die nette Arbeitsatmosphäre, ganz besonders bei Manuel Schiller, der nicht nur gelegentlich mit technischen Tipps half, sondern auch die Arbeit Korrektur gelesen hat.
Ein herzlicher Dank gilt auch meinen Eltern für die Unterstützung nicht nur in den letzten Jahren, sondern auch während meines Physikstudiums.
Ganz besonders danke ich Jochen für das Verständnis und den Rückhalt.

I hereby declare that I have written the submitted dissertation myself and in this process have used no other sources or materials than those expressly indicated.

Heidelberg, 26. April 2011